Nonlinear Magnetomechanical Modeling and Characterization of Galfenol and System-Level Modeling of Galfenol-Based Transducers

Dissertation

Presented in Partial Fulfillment of the Requirements for the Degree Doctor of Philosophy in the Graduate School of The Ohio State University

By

Phillip Gordon Evans, B.S.

Graduate Program in Mechanical Engineering

The Ohio State University

2009

Dissertation Committee:

Marcelo Dapino, Advisor

Joseph Heremans

Ahmet Kahraman

Chia-Hsiang Menq

ABSTRACT

Magnetostrictive materials have the ability to transfer energy between the magnetic and mechanical domains. They deform in response to magnetic fields and magnetize in response to stresses. Further, their stiffness and permeability depend on both magnetic field and stress. Galfenol, an alloy of iron and gallium, is an emerging magnetostrictive material which is unique for its combination of high magnetomechanical coupling and steel-like structural properties. Although its energy density and coupling factor is less than that of other materials like Terfenol-D and piezoelectric materials, this is compensated by its ease of packaging and manufacturability. In terms of reliability, it is far superior and makes possible a new class of devices with innovative geometries capable of combined sensing and actuation in 3-D. Unique among smart materials, Galfenol can serve both as a structural element and as an actuator or sensor. Motivated by the need to utilize the full-scale, i.e., nonlinear, range of Galfenol transduction, this work presents nonlinear characterization and modeling of magnetization and strain from magnetic field and stress, and details the incorporation of the material model into system-level models for Galfenol-based transducers. The system-level modeling is carried out in 3-D and is an enabling tool for creating Galfenol-based systems with innovative 3-D geometries.

Magnetomechanical measurements are presented which reveal that Galfenol constitutive behavior is kinematically reversible and thermodynamically irreversible. Magnetic hysteresis resulting from thermodynamic irreversibilities is shown to arise from a common mechanism for both magnetic field and stress application. Linear regions in constant-stress magnetization curves are identified as promising for force sensing applications. It is shown that the slope of these linear regions, or the magnetic susceptibility, is highly sensitive to stress. This observation can be used for force sensing; the 19-22 at. % Ga range is identified as a favorable Galfenol composition for sensing, due to its low anisotropy with moderate magnetostriction and saturation magnetization.

A thermodynamic framework is constructed to describe the magnetization and strain with special attention to hysteresis properties. An elementary hysteron, derived from the first and second laws, describes the underlying nature of the nonlinearities and hysteresis. Minimization of the energy of a single magnetic domain, the microscopic unit responsible for magnetization and magnetostriction, gives analytic expressions for the states of the hysteron and accurately describes certain features of the constitutive behavior, including the stress dependence in the magnetization regions identified for force sensing and the stress dependence of the location of the burst magnetization region. The switching of the hysteron, or domain orientation change, is characterized by a coercive energy, an energy loss analogous to overcoming dry-friction. The energy loss in major magnetization hysteresis loops of research grade Galfenol is found to be 873 J/m^3 and for production grade it is 1149 J/m^3. Stochastic homogenization of certain parameters in the hysteron yields a homogenized energy model for the bulk magnetization and strain that agrees with the measurements, including the hysteresis properties.

An alternate model is developed with special attention given to achieving high accuracy at minimal computational expense. The model is shown to be 100 times faster than previous models for Galfenol. While the homogenized energy model bridges the gap between the domain scale and the macroscopic scale through stochastic homogenization, the efficient model does this with energy-weighted averaging. The enabling feature for faster computation is careful choice of which domain orientations to include in the averaging scheme. The orientations are the same as those derived from energy principles in the homogenized energy model. Both models utilize a new energy formulation for magnetic anisotropy, the form of which depends explicitly on the energetically preferred magnetization directions. This new formulation can describe any anisotropy symmetry which is important for Galfenol, given that its anisotropy can be manipulated through post-processing techniques such as stress-annealing.

The efficient model is adopted in a transducer-level model implemented with the finite element method. The transducer-level model consists of Maxwell's equations describing eddy currents and flux leakage and the force balance equations from the conservation of linear momentum. These equations are solved over a geometry that includes a current carrying coil, an air volume, a magnetic circuit of steel, Galfenol and additional structural materials. The efficient constitutive model based on energy-weighted averaging is used for Galfenol. A broad range of effects are described such as energy losses affecting device efficiency, dynamic magnetostructural effects, delay and remanence from hysteresis, and eddy currents. This framework enables design optimization of efficient and innovative Galfenol-based devices which take advantage of the full transduction range of Galfenol.

To my wife and children

and their future siblings may they be many and happy.

ACKNOWLEDGMENTS

I want to thank my advisor Dr. Marcelo Dapino and committee members Dr. Joseph Heremans, Dr. Chia-Hsiang Menq, and Dr. Ahmet Kahraman for the time and effort they have devoted to my betterment. Dr. Dapino has provided excellent technical direction and motivation throughout my research. He has especially helped me to better understand the art of communication. His advice will be remembered throughout my career.

I am grateful to Dr. Alison Flatau and the rest of the Galfenol MURI team, funded by Jan Lindberg at the Office of Naval Research (Grant N000140610530) for supporting my education and research. I also benefited enormously from a Summer spent at the Naval Surface Warfare Center with mentors Marilyn Wun-Fogle and Dr. Jim Restorff from the Magnetic Materials Group. I very much appreciate the support and friendship of that group. The measurements I conducted with their assistance proved invaluable for my model development.

Working with Dr. Ralph Smith at North Carolina State University and Dr. Billy Oates at Florida State University was a pleasure and I benefited from my discussions with them as well as from studying their published works. I also appreciate my conversations with Eric Summers at Etrema Products as well the material and hardware that I received from that company including a Galfenol beam actuator provided to us developed by Dr. Julie Slaughter.

I want to thank my colleagues of the Smart Materials and Structures Laboratory for their support and friendship. Arjun Mahadevan, Liang Shu and Craig Poeppelman provided great assistance in collecting measurements and fishing with Liang Shu and Jian Xu brought me out of the lab for much needed breaks.

I give a special thanks to my family, especially my wife, for their moral support and patience during my graduate work. Their encouragement and love has kept me going and perhaps more importantly kept me sane. Finally, I owe my love of learning to the inspiration and example from my parents.

VITA

November 8, 1980	Born - Cedar Falls, IA USA
2005	B.S. Mechanical Engineering
2005-present	Graduate Research Associate, Ohio State University Columbus, OH

PUBLICATIONS

Journal Publications

P.G. Evans and M.J. Dapino, "State-space constitutive model for magnetization and magnetostriction of Galfenol alloys," *IEEE Transactions on Magnetics*, Vol. 44, No. 7, pp. 1711–1720, 2008.

P.G. Evans and M.J. Dapino, "Efficient model for field-induced magnetization and magnetostriction of Galfenol," *Journal of Applied Physics*, Vol. 105, p. 113901, 2009.

W.S. Oates, P.G. Evans, R.C. Smith, and M.J. Dapino, "Experimental implementation of a hybrid nonlinear control design for magnetostrictive actuators," *Journal of Dynamic Systems, Measurement, and Control*, Vol. 131, No. 4, p. 041004, 2009.

S. Bashash, J. Nader, P. Evans, and M Dapino, "Recursive memory-based hysteresis modeling for solid-state smart actuators," *Journal of Intelligent Material Systems and Structures*, Vol. 20, No. 18, pp. 2161–2171, 2009.

Conference Publications

P.G. Evans, M.J. Dapino, and J.B. Restorff, "Free energy model for magnetization and magnetostriction in stressed Galfenol alloys," *in Proceedings of SPIE*, Vol. 6526, April 2007.

W.S. Oates, P.G. Evans, R.C. Smith, and M.J. Dapino, "Open loop nonlinear optimal tracking control of a magnetostrictive Terfenol-D actuator," *in Proceedings of SPIE*, Vol. 6526, April 2007.

W.S. Oates, P.G. Evans, R.C. Smith, and M.J. Dapino, "Experimental implementation of a nonlinear control method for magnetostrictive transducers," *in Proceedings of the American Control Conference*, pp. 43094314, 9-13 July 2007.

P.G. Evans, M.J. Dapino, and J.B. Restorff, "Thermodynamic model for magnetization and magnetostriction in stressed $Fe_{1x}Ga_x$," *in 13th International Symposium on Applied Electromagnetics and Mechanics*, September 2007.

P.G. Evans and M.J. Dapino, "Fully-coupled model for the direct and inverse effects in cubic magnetostrictive materials," *in Proceedings of SPIE*, Vol. 6929, April 2008.

P.G. Evans and M.J. Dapino, "Fully-coupled magnetoelastic model for Galfenol alloys incorporating eddy current losses and thermal relaxation," *in Proceedings of SPIE*, Vol. 6929, April 2008.

P.G. Evans and M.J. Dapino, "Continuum thermodynamic model for magnetostrictive Galfenol alloys," *in Mathematical Aspects of Materials Science, in Proceedings of SIAM*, May 2008.

P.G. Evans and M.J. Dapino, "Constitutive modeling for design and control of magnetostrictive Galfenol devices," *Advances in Science and Technology*, Vol. 54, pp. 13-18, June 2008.

S. Bashash, K. Vora, N. Jalili, P.G. Evans, M.J. Dapino, and J. Slaughter, "Modeling major and minor hysteresis loops in Galfenol-driven micro-positioning actuators using a memory-based hysteresis framework," *in Proceedings of the ASME Dynamic Systems and Control Conference*, October 2008.

P.G. Evans and M.J. Dapino, "Fully-coupled model for 3-D induction and strain of Galfenol with geometry effects and applied currents," *in Proceedings of the ASME Conference on Smart Materials*, October 2008.

P.G. Evans and M.J. Dapino, "Measuresment and modeling of magnetomechanical coupling in magnetostrictive Iron-Gallium alloys," *in Proceedings of SPIE*, Vol. 2789, 9-13 April 2009.

FIELDS OF STUDY

Major Field: Mechanical Engineering

Studies in:

Smart Materials and Structures
Finite element method
Nonlinear dynamics and control

TABLE OF CONTENTS

Page

LIST OF FIGURES

Figure **Page**

LIST OF TABLES

CHAPTER 1

Introduction

1.1 Overview

Magnetostrictive materials undergo dimensional changes in response to magnetic fields and change magnetic state in response to stresses. These effects have been used to create actuators and sensors that deliver superior performance with less weight, size and moving parts than traditional electromagnetic devices [30]. Material and modeling limitations have limited magnetostrictive devices to unidirectional loading applications with either constant field or constant stress. Galfenol (Fe-Ga) is a recent magnetostrictive material that enables a new class of transducers with 3-D functionality and the capability to withstand harsh environments. A ductile material with high yield strength, it can be machined into intricate 3-D geometries, welded onto passive structures, and serve simultaneously as a structural element and an actuator/sensor. This work enables robust magnetostrictive devices and structures with 3-D functionality by developing a modeling framework for both Galfenol constitutive behavior and Galfenol-based devices and structures. Furthermore, measurements are performed to characterize the full nonlinear magnetization and strain constitutive behavior of Galfenol.

Magnetostrictive materials are smart or adaptive materials which convert one form of energy to another. Common examples of smart materials are electrostrictives and piezoceramics which provide transduction between electrical and mechanical energy and shape-memory alloys which provide transduction between thermal and mechanical energy. This transduction can be used to do mechanical work with non-mechanical inputs and to sense mechanical quantities of stress and strain or the related quantities, displacement and force. It can also be used to introduce tunable stiffness or damping into structures and devices. Magnetostrictives provide transduction between mechanical and magnetic energy. The transduction bandwidth is around 30 kHz, lower than the 1 MHz bandwidth of electrostrictives and piezoceramics and higher than the 100 Hz bandwidth of shape memory alloys [43]. The advantage of magnetostrictives over electrostrictives and piezoceramics is its superior mechanical and thermal robustness. The advantage over shape memory alloys, which produce a much larger strain, is its higher bandwidth and lower hysteresis. These advantages can be exploited for actuation and sensing or even combined applications like self-sensing actuators requiring high frequency operation and reliability.

Galfenol alloys of iron and gallium with 12-29 atomic percent (at. %) gallium. It has both high magnetically induced strain or magnetostriction ($\sim$ 400 microstrain) and ductility similar to steel. Furthermore, the variation in its properties with temperature is small. Prior to the advent of Galfenol, magnetostrictive materials included mechanically robust materials with low magnetostriction such as iron ($\sim$20 microstrain) and nickel ($\sim$40 microstrain) and brittle materials with giant magnetostriction such as Terfenol-D ($\sim$2000 microstrain.) The unique combination of mechanical robustness and high magnetostriction of Galfenol makes it ideal for creating sensors

and actuators that can take tension, bending, torsion and shock loads in harsh environments. Furthermore, it can be machined, welded, extruded, and deposited into complex geometries.

The full-scale magnetization $\mathbf{M}$, or related quantity flux density $\mathbf{B} = \mu_0(\mathbf{H} + \mathbf{M})$, and strain $\mathbf{S}$ response to magnetic field $\mathbf{H}$ and stress $\mathbf{T}$ of Galfenol, and of magnetostrictive materials in general, is nonlinear and depends on material history. The major nonlinearities in the constitutive behavior are saturation (both magnetization and magnetostriction), and anisotropy. For example, the magnetostriction at saturation in the $\langle 100 \rangle$ crystal direction λ_{100} of Terfenol-D is 90 microstrain and in the $\langle 111 \rangle$ crystal direction λ_{111}, it is 1200 microstrain. Also, it is more difficult to magnetize or requires much higher fields to reach saturation in the $\langle 100 \rangle$ direction than in the $\langle 111 \rangle$ direction. Galfenol is also anisotropic both in it magnetization and magnetostriction but λ_{100} is greater than λ_{111} and it is easier to magnetize in the $\langle 100 \rangle$ direction.

To avoid these nonlinear complexities, transducers are often limited to small-signal operating regimes. For small-signal operating ranges about a bias field and stress, the constitutive behavior can be expressed as

$$\begin{aligned} \mathbf{B} &= \boldsymbol{\mu}^{\mathbf{T}}\mathbf{H} + \mathbf{d}\mathbf{T}, \\ \mathbf{S} &= \mathbf{d}^{T}\mathbf{H} + \mathbf{s}^{\mathbf{H}}\mathbf{T}. \end{aligned} \tag{1.1}$$

The permeability tensor $\boldsymbol{\mu}^{\mathbf{T}}$ is measured at constant stress and the compliance tensor $\mathbf{s}^{\mathbf{H}}$ is measured at constant field; $\mathbf{d}$ is the piezomagnetic tensor.

Linear transduction properties defined from (1.1) serve as figures of merit for evaluating the performance of a magnetostrictive material. The piezomagnetic tensor $\mathbf{d}$ determines the maximum available strain or free strain which occurs under the mechanically-free condition $\mathbf{T} = 0$; the free strain is $\mathbf{d}^{T}\mathbf{H}$. The piezomagnetic tensor

and the compliance tensor together determine the maximum possible stress or blocked stress which occurs under the mechanically-blocked condition $\mathbf{S} = 0$; the blocked stress is $(\mathbf{s^H})^{-1}\mathbf{dH}$. Another figure of merit is the relative change in stiffness or ΔE effect in the magnetically-blocked condition, $\mathbf{B} = 0$. From (1.1), the magnetically-blocked stress-strain relation is

$$\mathbf{S} = \left(\mathbf{s^H} - \mathbf{d}^T(\boldsymbol{\mu}^\mathbf{T})^{-1}\mathbf{d}\right)\mathbf{T}. \tag{1.2}$$

Magnetically blocking the material effectively reduces the compliance by $\mathbf{d}^T(\boldsymbol{\mu}^\mathbf{T})^{-1}\mathbf{d}$. For 1-D loading, the effective Young's modulus in the magnetically-free condition $H = 0$ is the soft modulus and in the magnetically-blocked condition $B = 0$ it is the hard modulus.

The energy density or work capacity is half the product of the free strain and blocked stress. The coupling coefficient k quantifies the efficiency of transduction. The free energy is

$$\begin{aligned} G =& \frac{1}{2}\left(\mathbf{T}\cdot\mathbf{S} + \mathbf{H}\cdot\mathbf{B}\right) \\ =& \frac{1}{2}\mathbf{T}\cdot\mathbf{s^H}\mathbf{T} + \frac{1}{2}\left(\mathbf{T}\cdot\mathbf{d}^T\mathbf{H} + \mathbf{H}\cdot\mathbf{dT}\right) + \frac{1}{2}\mathbf{H}\cdot\boldsymbol{\mu}^\mathbf{T}\mathbf{H} \\ :=& G_{mechanical} + 2G_{coupling} + G_{magnetic}. \end{aligned} \tag{1.3}$$

The coupling coefficient is

$$k = \frac{G_{coupling}}{\sqrt{G_{mechanical}G_{magnetic}}}. \tag{1.4}$$

For 1-D loading it is simply $d/\sqrt{\mu^T s^H}$. A good transduction material therefore has high piezomagnetic coefficient, low permeability and low compliance resulting in high free strain, blocked stress, ΔE, and transduction efficiency. However, when considering the electrical domain as well, it is desirable to have high permeability for effective

electromagnetic transduction where lower voltage is required to create the magnetic field.

The figures of merit for electrostrictives and piezoceramics are derived in an analogous fashion replacing magnetic field with electric field, magnetic flux density with electric flux density, permeability with permittivity, and piezomagnetic with piezoelectric. The figures of merit offer a means to compare active materials of different mechanisms. Comparing magnetostrictives to electrostrictives and piezoceramics in particular is prudent given their similar figures of merit at comparable bandwidths, especially since the latter have received wide use in a broad range of applications from buzzers inside pagers and cell phones to ultrasonic cleaners and ultra-precise positioning. Energy density or work capacity, coupling coefficient, free strain, and blocked stress are shown for Terfenol-D, Galfenol, and PZT-5H (a common piezo-ceramic) in Table 1.1 for 1-D application.

Terfenol-D and PZT-5A have similar figures of merit. Transducers using the former can achieve greater displacement but with less force since the two have nearly the same energy density. Galfenol lags in terms of figures of merit related to transduction, but there is more to be considered for transducer applications. Galfenol has clear advantages in terms of reliability, manufacturability, and packaging which are important considerations for transducer design.

Reliability

The properties of electrostrictives and piezoceramics degrade over time and change irreversibly at elevated temperatures. Magnetostrictive materials have been shown to go through millions of cycles with zero degradation. Both Terfenol-D and Galfenol exhibit little change with temperature if operated below the curie temperature T_C,

Table 1.1: Figures of merit for Terfenol-D, Galfenol, and PZT-5H.

	Energy (kJ/m^3)	Coupling	Strain ($\times 10^{-6}$)	Stress (MPa)
Terfenol-D[(a)]	25	0.75	1200	42
PZT-5H[(b)]	24	0.75	1000	48
Galfenol[(c)]	2.4	0.60	247	19

[(a)] Etrema Products Inc.
[(b)] Wilkie et al. [110]
[(c)] Single-crystal 16 at. % Ga, reported by Datta and Flatau [33]

380 oC for Terfenol-D and 500 oC for Galfenol. Even if the temperature is elevated above T_C, the properties assume their previous values when the temperature is lowered; irreversible changes do not occur. Only temperatures sufficient to cause melting will irreversibly affect the properties, since re-crystallization occurs. A chief advantage of Galfenol is its mechanical reliability. Electrostrictives, piezo-electrics, and Terfenol-D are all brittle and have little tolerance for shock, bending, and tensile loads.

Manufacturability

Because of their brittle nature, electrostrictives, piezo-electrics, and Terfenol-D cannot be machined with conventional methods. Complex shapes are generally of little use anyway since 3-D loads will usually lead to mechanical failure. Ueno et al. [107] have shown that Galfenol can be machined with conventional milling tools with no change to its transduction properties. Ueno et al. [108] have also showed that it can be welded. Summers, Meloy, and Na [98] have shown that polycrystalline Galfenol can be rolled to produce a textured material with 154×10^{-6} free strain.

Packaging

Piezoceramics require high voltage power supplies and the placement of electrodes for electric field generation while magnetostrictive materials require a drive solenoid for magnetic field generation and permanent magnets for a bias field. An advantage of Galfenol is that the drive solenoid and bias magnet can be small since its permeability is ten to twenty times larger than that of Terfenol-D. It is even possible to eliminate the bias magnet and apply the bias field through the solenoid since only low fields are needed. An additional advantage resulting from the high permeability is that both the magnetic circuit and active element can be made of Galfenol. Terfenol-D and piezoceramics require a pre-compression mechanism to ensure it is operated only in tension and to achieve maximum strain. Galfenol does not have this restriction because it can be operated in tension and maximum strain can be achieved without pre-compression through a process called stress annealing.

In general, Galfenol devices can be smaller, lighter, and more robust than traditional electromagnetic devices or smart material devices using piezoelectric materials and Terfenol-D. Ueno et al. [105, 108, 109, 106, 117] have already exploited these in the area of miniature robotics for medical devices—creating actuators with an unprecedented combination of small size, high bandwidth, and reliability. A novel displacement amplification concept that requires a ductile material was used to create spherical and linear motors that achieve large strokes, on the order of millimeters. The key advantage of Galfenol is that it is both a structural and an active material. It can serve simultaneously as a structural element and an actuator/sensor. Both fasteners and structural supports can be made of Galfenol and at the same time be

used for health monitoring using Galfenol's sensing capabilities and for active control of the structure or system using its actuation capabilities.

This work develops a 3-D and full-scale, i.e. nonlinear, modeling framework for Galfenol and Galfenol-based transducers in order to enable use of its full transduction capabilities and take advantage of its unique status as both an active and a structural material. Such a modeling framework is especially important for Galfenol applications because of its comparatively low transduction properties. The framework can be used to optimize device efficiency in order to compensate for the low coupling factor. It can be used in model-based control schemes to utilize the full nonlinear range of its work capacity. Finally, it can be used to design for 3-D functionality which, to date, has not been done.

1.2 Literature Survey

Early work regarding Fe-Ga alloys focused primarily on material characterization, including measurement of the saturation values of magnetostriction and magnetization as a function of temperature and stoichiometry. The anisotropy constants and elastic coefficients were also been measured. In addition to measuring these bulk properties, investigations were carried-out to understand the physical mechanism whereby the introduction of non-magnetic gallium leads to a tenfold increase in the magnetostriction over pure iron. This involved identifying the material phases and lattice structure of Fe-Ga alloys as affected by stoichiometry and heat treatment. Linear characterization of the material constitutive behavior was performed by identifying the linear coefficients and the coupling factor at different bias fields and stresses.

In addition to the early work on material characterization, statistical models based on energy-weighted averaging have been used to describe some nonlinear aspects of the magnetization and strain constitutive behavior for applied magnetic field and stress, including anisotropy, saturation, magnetostriction and hysteresis during magnetic field application in the $\langle 100 \rangle$ and $\langle 110 \rangle$ directions. A limited number of transducer models have also been developed including for nonlinear, quasi-static operation of beam and plate actuators and sensors.

Researchers have developed actuators and sensors that make capital of the unique properties of Galfenol. This development has taken place with a test and measurement approach without modeling for optimization. To date, the proposed actuators and sensors use Galfenol in unidirectional loading only, operated in the linear regime of its constitutive behavior. While they do not take advantage of the 3-D functionality or full nonlinear operating regime of Galfenol, they do benefit from its machinability and mechanical robustness, specifically, its ability to withstand impact, bending, and tensile loads.

Little attention has been given to modeling dynamic effects, both at the material level like thermal relaxation and at the transducer level like eddy currents and inertial loads. Dynamic effects have been studied for other materials like Terfenol-D but these studies and accompanying models have been limited to 1-D applications. Hysteresis in Galfenol has also received little attention both from a modeling and from an experimental viewpoint, especially for combined stress and magnetic field loading. Additionally, while the models that have been proposed for magnetization and strain lead to a better understanding of the material behavior, they are less useful for transducer development because they rely exclusively on statistical methods or

energy-weighted averaging, which is computationally cumbersome and does not give analytic expressions for the constitutive behavior. This dissertation is undertaken to address these issues.

A survey of the literature regarding Fe-Ga alloys and magnetostrictive material and transducer modeling follows. This chapter concludes with the research objectives and outline of the dissertation.

1.2.1 Galfenol material characterization

Clark et al. [23] were the first to report on the large magnetomechanical coupling of Galfenol alloys with a Ga content of 15-20 at. %. They measured saturation magnetization and magnetostriction, anisotropy, and the soft and stiff elastic moduli of various Fe-Ga and Fe-Ga-Al single crystals from 180 K to room temperature. In a separate study Clark et al. [25] found that quenched Galfenol exhibits magnetostrictions 25% higher than when furnace-cooled, the maximum exceeding 300 microstrain. They proposed that the great increase of magnetostriction above that of Fe in FeGa alloys is due to the substitutive presence of asymmetrically shaped clusters of the Ga atoms. Clark et al. [24] reported the greatest magnetostriction for Galfenol at 19 at. % Ga, 400 microstrain. Clark et al. [22] observed that in Galfenol with concentrations of Ga between 4 and 27 at. % Ga, the maximum magnetostriction exhibits two peaks as a function of Ga content. This unusual magnetostrictive behavior is interpreted on the basis of a single maximum in the magnetomechanical coupling of Fe with increasing amounts of non-magnetic Ga, combined with a strongly temperature dependent elastic shear modulus.

Cullen et al. [27] measured the saturation magnetostriction of Galfenol with 21-35 at. % Ga. They reported anomalous behaviors for the magnetostriction and shear elastic modulus versus at. % Ga, which they attributed to internal stresses associated with short-range atomic ordering. Wuttig, Dai, and Cullen [114] reported continuous-wave measurements of the shear elastic constants of Galfenol. They concluded that Galfenol is inhomogeneous and contains clusters consisting of embryos of a martensitic phase. A model was proposed assuming that the clusters are centered around next-nearest Ga pairs which reproduced the known composition dependence of the magnetostriction in the composition range 0-23 at. % Ga. Lograsso et al. [66, 67] investigated the effect of thermal history on the lattice structure with X-ray diffraction. Wu [111] investigated the phase stability, magnetism and magnetostriction using the full potential linearized augmented plane wave method. This investigation showed that the magnetostrictive coefficients strongly depend on the atomic arrangement. The electronic origin of the enhancement in magnetostriction was discussed in terms of density of states and band structures.

Kellogg et al. [58] measured the temperature and stress dependence of both the magnetostriction and magnetization from -21 deg C to +80 deg C under compressive stresses ranging from 14.4 MPa to 87.1 MPa. Constant temperature tests showed that compressive stresses greater than 14.4 MPa were needed to achieve the maximum magnetostriction. The well-behaved temperature response reported in their study illustrates that Galfenol is particularly valuable for industrial and military smart actuator, transducer, and active damping applications. They also measured the Youngs modulus and found it to be almost temperature independent.

Kellogg et al. [59] tested Galfenol with 17 at. % Ga in tension at room temperature. Specimens with a [110] tensile axis orientation exhibited $110\langle 111\rangle$ slip and an ultimate tensile strength of 580 MPa through 1.6% elongation. The Young's modulus was 160 GPa in the loading direction with a Poisson's ratio of -0.37 on the (100) major face. A specimen with a [100] tensile axis orientation exhibited $211\langle 111\rangle$ slip and discontinuous yielding. A maximum tensile strength of 515 MPa was observed with fracture occurring after 2% elongation. The Young's modulus was 65 GPa in the loading direction with a Poisson's ratio of 0.45 on the (001) major face. Petculescu et al. measured [80] measured the elastic shear moduli of Galfenol single crystals via resonant ultrasound spectroscopy with and without a magnetic field and within a $4 - 300$ K temperature range. Rafique et al. [83] measured the magnetic anisotropy for Galfenol with 0.05, 0.125, 0.14, 0.18, and 0.20 at. % Ga.

Kellogg et al. [57] measured the nonlinear magneto-elastic transduction properties of single-crystal and textured polycrystalline Galfenol for applied field at constant stress and applied stress at constant field. Atulasimha et al. [9] studied the effect of stoichiometry on the nonlinear magneto-elastic transduction properties. Yoo and Flatau [115] measured the linear transduction and elastic properties at different bias magnetic field levels.

Restorff et al. [86] and Wun-Fogle et al. [112, 113] investigated stress-annealing of Galfenol. Applying stress at elevated temperatures changes the magnetic anisotropy by introducing an internal stress. The linear transduction properties of stress annealed Galfenol were reported.

1.2.2 Galfenol transducer applications

Downey and Flatau [34] investigated the behavior of Galfenol in elastic bending to facilitate design concepts for using Galfenol in novel sensor applications at the macro to nano-scale. A series of experiments were conducted on the magnetic response of cantilevered beams to dynamic bending loads. McGary et al. [69] presented a method for growing Galfenol nano-wires to mimic the hairlike sensors or cilia which play an important role in biological sensors such as the human ear.

Ueno et al. [105, 108, 109, 106, 117] have designed a number of novel actuators based on Galfenol, including a bending actuator, a sonic transducer, a two-DOF bending actuator, a miniature spherical motor, and a linear motor. These compact devices were shown to have high bandwidths ($\sim$ 30kHz) and good mechanical robustness and required low operating voltages. Each uses Galfenol with 1-D loading. Displacement amplification is done by utilizing the ability of Galfenol to sustain bending and impact loads. The spherical and linear motors achieve mm scale motion.

1.2.3 Galfenol constitutive and transducer modeling

Atulasimha, Flatau, and Summers [10] modeled the actuation and sensing behavior of polycrystalline Galfenol. The magnetomechanical behavior was modeled as the sum of the volume fraction-weighted, single-crystal behavior along the [100], [110], [210], [310], [111], [211] and [311] directions, which were modeled using an energy-weighted average modeling approach. The energy includes terms for magnetic anisotropy, magnetomechanical coupling, and magnetic work. The weighting functions is the Boltzmann distribution. The model is anhysteretic and describes the

nonlinear shape of magnetization and strain curves for applied magnetic field at constant stress and applied stress at constant magnetic field. Atulasimha, Akhras, and Flatau [7] combined the energy-weighted average modeling approach with a hysteresis model for magnetic field application to describe the magnetization and strain of $\langle 110 \rangle$ oriented Galfenol with applied magnetic field at constant stress.

Mudivarthi et al. [70] developed a quasi-static transducer model for stress application. The model couples Gauss' law for magnetism with the conservation of linear momentum using a nonlinear constitutive model based on energy-weighted averaging. It was implemented with the finite-element method for a unimorph beam. Datta et al. [31, 32, 88] developed nonlinear models for Galfenol beams and composite plates by including magnetostriction in classical Euler beam theory and laminated plate theory. The energy-weighted average model was again used for the constitutive behavior relating magnetostriction to magnetic field and stress.

1.2.4 Constitutive modeling of magnetostrictive materials

The literature encompassing constitutive models for magnetization/strain versus field/stress tends to focus on the field and stress dependence of the magnetization. It has been assumed that the strain is simply the sum of a purely elastic, linear component from Hooke's law and the magnetostriction where the magnetostriction is a simple quadratic function of the magnetization [61]. Thus, once the field and stress dependence of the magnetization is known, the magnetostriction and total strain directly follow. Various macroscopic models for magnetization have been proposed which address effects such as hysteresis, anisotropy, and stress. However, a complete 3-D framework for magnetization due to any applied stress (in the elastic region) and

field with these combined effects has not been developed. A summary of the current state-of-the art macroscopic magnetization models follows. Micromagnetics models, while very accurate, are not addressed because the focus of this work is on macroscopic models for understanding bulk material behavior as well as transducer-level behavior.

Preisach

The Preisach model [82] was originally a purely mathematical approach to model ferromagnetic hysteresis. Its major contribution is the idea that smooth hysteresis curves obtained from macroscopic measurements are actually the result of a large number of elementary hysterons. The hysterons are bistable, having a value $\pm M_s$ (saturation magnetization.) Each hysteron switches to the up state ($+M_s$) and back to the down state ($-M_s$) at different field values. The macroscopic magnetization is then calculated as the weighted average of the elementary hysterons (see Fig 1.1.) Scalar in its original formulation, Mayergoyz and Friedman [68] extended the approach to higher dimensions as an isotropic vector model and Cardelli et al. [19] as an anisotropic vector model. The Preisach model does lend itself to physical interpretation where each hysteron represents a magnetic moment which can be oriented either up or down and switches its orientation when the field reaches the coercive field value. The weighted summation essentially calculates the expected value of all the moment orientations in the material thus giving the total magnetization. Using this physical interpretation, Della Torre included accommodation effects [102], Della Torre et al. [103] included thermally-induced rate dependence and Suzuki and Matsumoto [99] included stress dependence.

The afore mentioned extensions all add complexity to the weights which are either experimentally determined or are represented by a probability density function

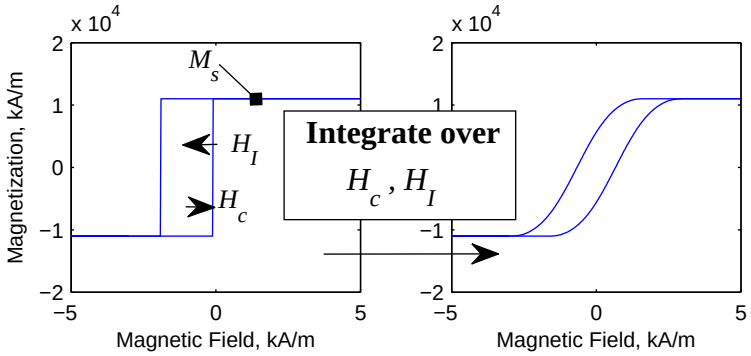

Figure 1.1: Preisach kernel and total magnetization.

assumed *a priori*. Finding a suitable density function or measuring the weights becomes quite challenging with each added feature. Even with this added complexity, the Preisach model can only be used for materials which have macroscopic constitutive relationships similar to the basic Preisach hysteron. Most ferromagnetic materials are only slightly magnetostrictive and even when stress is applied have magnetization versus field curves that are similar to the elementary hysteron. Giant magnetostrictive materials however, do not. In particular, as stress is applied, kinking occurs. An alternate hysteron developed by Reimers and Della Torre [85] has successfully modeled giant magnetostrictives with relatively benign kinking such as Terfenol-D, but the approach is phenomenological, making it inaccurate for materials with significant kinking.

Jiles-Atherton

The Jiles-Atherton model [49] was first formulated for isotropic ferromagnetic hysteresis. The magnetization is calculated as the sum of the reversible component from domain wall bowing and an irreversible component from domain wall motion impeded

by material impurities. The nonlinear shape of the magnetization versus field curve is dictated by an anhysteretic function which can be either purely phenomenological or derived from energy principles. The irreversible losses leading to hysteresis are calculated from an energy balance.

Extensions to the model to include anisotropy or stress dependence simply use different anhysteretic functions that include contributions from these effects [53, 50]. The model was also extended to include hysteresis in the magnetization versus stress curve and dynamic losses from eddy currents [48, 50]. Both these extensions were made by including additional terms in the energy balance. The original model and noted extensions are scalar but a simple extension to 3-D was made by Bergqvist [14]. While the original model produces minor loops—magnetization due to field cycled around a bias point—inconsistent with measurements, the inconsistencies were eliminated by a scaling determined from *a priori* knowledge of the field turning points. This technique however cannot be applied to the 3-D extension [14]. This model has been widely used for power-electronics and has also been used by Dapino et al. [30] to model Terfenol-D based actuators.

Homogenized energy

Smith's homogenized energy framework [94] has broad application to ferroic materials having been applied to magnetostrictives, piezoelectrics, and shape-memory alloys. The framework applied to ferromagnetic materials [91] is scalar and derives an elementary hysteron or kernel by considering the exchange energy and the work from a magnetic field at the lattice scale. Rate dependence is introduced into the kernel with Boltzmann statistics and the total magnetization is calculated through stochastic homogenization of certain parameters that define the kernel (see Fig. 1.2.)

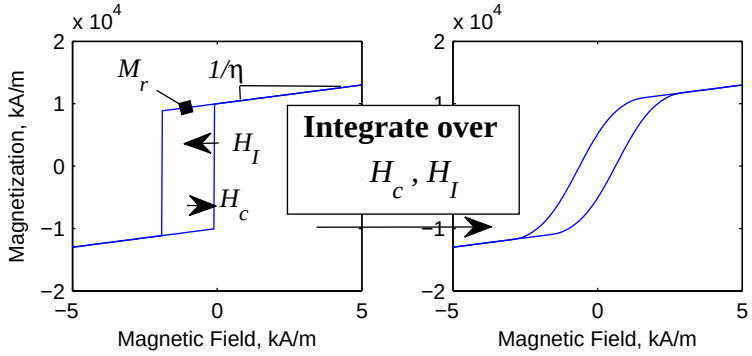

Figure 1.2: Smith kernel and total magnetization.

Stress dependence is incorporated in the kernel through an additional energy term in the balance that defines the kernel.

The framework has mathematical similarities to the classical Preisach model and its extensions in that macroscopic hysteresis curves are assumed to be the result of a statistically distributed, elementary hysteron. The differences may largely be attributed to the thermodynamic basis of Smith's framework. The hysteresis properties of Smith's framework are in better agreement with experiments as compared to the classical Preisach model. Specifically, the model includes (i) minor loops that are not closed in operating regimes where thermal relaxation is significant (ii) noncongruency exhibited by certain materials (iii) both reversible and irreversible behavior (iv) certain accommodation processes and (v) stress and temperature dependence. Extensions to the Preisach model also address these issues; the advantage of Smith's homogenized energy model is that additional physical effects are included in the kernel rather than the weights or density function and thus fewer experiments are required to

identify the model parameters. While the framework is scalar and isotropic, Oates [73] made an extension to 3-D.

Other researchers have also used physics-based kernels with stochastic homogenization, including Ossart et al. [76] and Appino et al. [4]. The formulation of their kernels is done at the microscopic scale rather than the lattice scale. In other words, the energy from the magnetization of groups of atoms called magnetic domains is used to describe the underlying behavior rather than the energy of a single atom. Magnetomechanical coupling was not considered in their formulations.

Energy-weighted averaging

The Armstrong model [6] applies statistical mechanics to calculate magnetization and magnetostriction of magnetostrictives with cubic anisotropy. It was formulated as an anhysteretic model that calculates any bulk quantity as an energy-weighted average. The density function dictates that lower energy states are more likely, similar to Boltzmann statistics. It is postulated that material impurities cause a spread in the distribution of energy states about the minima rather than thermal-induced disorder as in Boltzmann statistics. Stress and anisotropy terms are included in the energy formulation.

A hysteretic variant of the model was used for major loops of Terfenol-D [5]. Major loops are hysteresis loops caused by cycling the field between positive and negative saturation. Hysteresis was introduced in a similar manner to the Jiles-Atherton model. First, the number of possible energy states was reduced by only allowing the local internal energy minima, with volume fraction of material in these energy states determined by using a discrete version of the probability density function. Finally, irreversible losses are introduced in the evolution of the volume fractions under a

changing field by considering the energy losses associated with impediments to domain wall motion. Losses are not accounted for when stress is applied so hysteresis is only included for magnetization/magnetostriction versus applied field.

Atulasimha et al. [7] mitigated inaccuracies associated with limiting the possible energy states to the internal energy minima by expanding the number of possible energy states; this extension was used to model major loops of $\langle 110 \rangle$ oriented, single-crystal Galfenol. The anhysteretic model was extended by Restorff et al. [86] to include the effect of stress-annealing in Galfenol while Atulasimha et al. [10] included the effect of material texture.

1.2.5 Modeling of magnetostrictive transducers

Models for magnetostrictive transducers have been focused on devices that are operated with Terfenol-D in unidirectional loading. Dapino, Smith, and Flatau [30] modeled 1-D constitutive behavior of Terfenol-D with the Jiles-Atherton model, including an effective field due to pre-stress. In their transducer-level description, the magnetostriction calculated from the constitutive model is used as input to the wave equation for the structural dynamics of a rod. Huang et al. [46] also used the Jiles-Atherton model for 1-D characterization of a Terfenol-D actuator but included eddy current losses in the energy formulation and used a lumped parameter model for the structural dynamics; the effect of dynamic stress was not included in their constitutive model. Sarawate and Dapino [87] also developed a decoupled model but included time delay from eddy currents through solution of the magnetic field diffusion equation with constant permeability. Engdahl and Bergqvist [37] calculated

dynamic losses in a 1-D actuator by fully coupling the magnetic field diffusion equation, the wave equation for structural dynamics, and a lumped parameter model for the magnetic circuit with constitutive behavior obtained both from measurement and from a Stoner-Wohlfarth hysteresis model. Bottauscio et al. [17] modeled losses from eddy currents using the field diffusion equation along with the Preisach model to calculate the nonlinear permeability and stress-induced flux density changes. All of the works referenced above have as input, externally applied magnetic field.

Some attention has also been given to higher dimension models. Datta et al. [32, 88] used classical laminated plate theory with the Armstrong magnetomechanical model to characterize laminated sensors and actuators in the absence of current-induced magnetic field. Zhou and Zhou [118] developed a dynamic finite element model for a unimorph actuator with one-way magnetomechanical coupling. The magnetostatic finite element model formulated by Kannan and Dasgupta [56] is 2-D, uses nonlinear constitutive behavior for bi-directional coupling and includes current-induced magnetic fields and electromagnetic body forces. Mudivarthi et al. [70] used a fully-coupled, magnetostatic formulation for stress-induced flux density changes in Galfenol with no current-induced fields. The 3-D model of Kim and Jung [60] employs one-way coupling with force due to magnetostriction driving a coupled fluid-structural model for a sonar transducer. Aparicio and Sosa [79] describe a 3-D, fully-coupled finite element model including dynamic effects and give a simple implementation for a magnetostrictive material using a single element.

1.3 Research objectives and dissertation outline

The objectives of this research are to

- study the nonlinear and hysteretic constitutive behavior of Galfenol through experiments,
- construct a constitutive modeling framework for understanding and describing this behavior,
- develop a transducer-level modeling framework for describing a broad range effects such as energy losses affecting device efficiency, dynamic magnetostructural effects, transducer-level consequences of using hysteretic materials, and eddy currents.

Prior to the presentation of the main body of research, Chapter 2 introduces key concepts from the two disciplines most important to the study of magnetostrictive materials and devices: electromagnetics and mechanics of materials. Definitions of electric flux density, electric field, magnetic flux density, and magnetic field are given along with the equations describing their spatial and temporal dependence. The various forms of magnetism are discussed with special attention given to ferromagnetic materials; Galfenol exhibits this form of magnetism. The stress and strain tensors are introduced—specifically, the Lagrangian definitions are given as well as their reduction to infinitesimal strains, used throughout the dissertation. Finally, the origin of magnetomechanical coupling in magnetostrictive materials is discussed along with the classical energy and magnetostriction formulations for cubic materials. With these concepts properly defined, presentation of the main research effort proceeds as follows. Chapters 3-5 each follow the same format. A preamble introduces two sections, each of which constitutes the body of a journal publication complete with literature review, research presentation, and conclusion.

Constitutive modeling: Part I

Chapter 3 details an initial effort to model the magnetization and strain constitutive response of Galfenol under magnetic field loading at constant stress. The first section presents a 1-D model employing Boltzmann statistics. The bulk magnetization and strain are calculated from the expected value of the orientation of a continuum of magnetic moments, atomic scale quantities which are discussed in the background chapter. An energy formulation is used in conjunction with the Boltzmann probability function to model the distribution of magnetic moments as well as the rate at which moments flip between adjacent energy wells. Direct energy minimization yields analytic functions for certain features of the measurements while Boltzmann statistics are used to give the overall behavior. Hysteresis is interpreted as the time-delay in the transition of moments between energy wells, occurring as stress and field change the energy of magnetic moments. The model is implemented in state-space form which facilitates its adoption into transducer-level models.

The second section of Chapter 3 extends the energy and statistical principles presented in the first section to 3-D, with two critical differences. An alternate interpretation of hysteresis is given which is rate-independent. Additionally, key simplifications enable efficient 3-D implementation. A finite number of magnetic moment orientations, determined through direct energy minimization, is considered in place of a continuum. The bulk anhysteretic behavior is calculated by assuming a Boltzmann distribution of these moment orientations. Hysteresis is interpreted as the result of energy loss that occurs when magnetic moments are impeded by material defects. Polycrystallinity is also investigated; material texture is described by the probability

density of grain orientations and its effects on the magnetization and magnetostriction are demonstrated.

Constitutive modeling: Part II

Chapter 4 presents a two-tiered modeling framework, motivated by additional magnetization and strain measurements. The first is for a detailed understanding of hysteresis in Galfenol and the second is better suited for adoption in device-level models. The measurements are reported in the first section and shed light on the nature of magnetization and strain hysteresis in Galfenol. Magnetization and strain are measured in two grades of Galfenol by applying both magnetic field at constant stress and stress at constant magnetic field. Special attention is given to the history and order of application.

Following the measurements, the first tier model, a new homogenized energy model is developed. It is derived from the first and second laws of thermodynamics. Anisotropy, magnetomechanical coupling, strain, and magnetic energy densities are included in the energy formulation and provide a physical basis for the construction of a 3-D hysteron for magnetostrictive materials. As in Smith's homogenized energy model, a statistically distributed interaction field is superimposed on the applied field to account for material defects. An improvement is made to the homogenized energy class of models and to Preisach-type models in general by using a coercive energy rather than coercive field to determine the switching of the hysteron. This approach satisfies the second law and reduces the required integration order from six to four. The model satisfies the hysteresis properties observed in the measurements.

The second section of Chapter 4 presents the second tier model, a refinement of the efficient modeling framework developed in Chapter 3 in light of the additional

measurements. It again employs concepts from Boltzmann statistics, using an energy-weighted average of a discrete number of domain orientations to relate micro-scale behavior to macro-scale behavior. A new formulation is used for the anisotropy energy which is applicable to materials of any symmetry. This is particularly useful for Galfenol since stress annealing, applying stress at elevated temperatures, can change the crystal symmetry. Additionally, the hysteresis model is extended for 3-D magnetic field and stress loading. The model gives an accurate representation of magnetization and strain with minimal computational expense and is adopted Chapter 5 for transducer modeling.

Application of Galfenol to force sensing and 3-D dynamic transducer modeling

In Chapter 5 the application of Galfenol to force sensing is investigated and a general framework for transducer-level modeling is constructed. Particular attention is given to the quantities of interest in transducers: voltage, current, force, and displacement.

The first section investigates a force sensing concept based on Galfenol which is motivated by the presence of linear regions in the measured magnetization versus magnetic field curves. These regions are described through a simple rotational model using only the saturation magnetization and magnetostriction and the anisotropy constant. This model motivates a force sensing principle based on stress dependent susceptibility—the slope of the magnetization versus field curve. A Ga content range is identified which yields alloys having properties that best leverage the proposed force sensing principle.

In the second section, a framework is developed for the study of magnetostrictive transducers operated in dynamic and nonlinear regimes and having complex geometries. The finite element method is employed in the modeling strategy which is implemented for a variety of cases in order to study various transducer-level effects. A 1-D implementation is used to study the effect of eddy currents on the dynamic actuation and sensing ability of Galfenol transducers. A 2-D implementation is considered to describe the effect of hysteretic magnetostrictive materials on the device-level behavior. A 2-D and dynamic implementation is done for composite beam actuators in order to study the structural dynamics which are induced by nonlinear magnetostriction. Finally, a fully 3-D and dynamic finite element model is used to study the entire input-output relationship of a Galfenol-based micro-positioner, from the voltage applied to a solenoid to the output displacement. Measures are proposed to quantify the transduction efficiency of the entire device as well as the magnetomechanical transduction efficiency of the Galfenol element.

Summary

Chapters 3-5 are intended to be self-contained studies of topics ranging from material to device-level behavior. Chapter 6 is the concluding chapter and summarizes the important contributions that were made to the field of magnetostrictive materials and devices with specific application to Galfenol. It also identifies future areas of work that are possible in light of the research presented in this dissertation.

CHAPTER 2

Background

2.1 Preamble

The study of magnetostrictive materials is inherently interdisciplinary. The coupling between electromagnetic and mechanical domains present in these materials requires understanding of two disciplines, electromagnetism and mechanics of materials. The first is the study of electric and magnetic fields and their work conjugates electric flux density and magnetic flux density. The second is the study of the work conjugates stress and strain. A concise background in the principles of electromagnetism is given in Section 2.2 and of mechanics of materials in Section 2.3. Magnetostrictive materials exhibit magnetomechanical coupling with unusual work conjugates of magnetic flux density and stress as well as strain and magnetic field. Section 2.4 discusses magnetomechanical coupling and includes a derivation of the energy and magnetostriction formulations used for cubic materials.

2.2 Electromagnetism

This background in electromagnetism describes the electrical and magnetic quantities of interest in magnetostrictive materials, structures, and devices. An overview

of the field equations for electromagnetics is given, followed by a description of magnetization in ferromagnetic materials. Further descriptions can be found in recent texts on magnetism from O'Handley [75] and Jiles [49] as well as classical texts from Chikazumi [21], Bozorth [18], and Cullity [28].

2.2.1 Electromagnetic field equations

Electric flux density $\mathbf{D}$ is a measure of the strength of electric field $\mathbf{E}$ created by free charges q. It is essentially the number of field lines which pass through an area. Electric fields are detectable by virtue of the fact that they generate a force on electric charge acting along the field lines. Magnetic flux density or magnetic induction $\mathbf{B}$ is a measure of the strength of a magnetic field $\mathbf{H}$ created by charge in motion. Magnetic fields are detectable by virtue of the fact that they generate a force on moving charge which causes a change in the curvature of the charge path.

Coulomb's law gives the differential electric field created by a differential charge

$$d\mathbf{E} = \frac{1}{4\pi\epsilon_0}\frac{dq\hat{\mathbf{r}}}{r^2}. \tag{2.1}$$

This is the electric field in free space where the relationship between field and flux density is linear, $\mathbf{D} = \epsilon_0\mathbf{E}$. Additionally, the electric field associated with flowing charging in conductors is governed by Ohm's law $\mathbf{E} = \rho_E\mathbf{J}$, where ρ_E is the electrical resistivity. While (2.1) suggests that the field is independent of the medium, in reality the problem of determining $\mathbf{D}$ and $\mathbf{E}$ is more complex. When a charge creates an electric field, this field causes polarization $\mathbf{P}$ in dielectric materials. The polarization is the density of electric dipoles which act like paired charges. The total electric flux density then is that seen in free space in addition to the flux density contributed by the polarization, $\mathbf{D} = \epsilon_0(\mathbf{E} + \mathbf{P})$.

The Biot-Savart law gives the differential magnetic field element $d\mathbf{H}$ for a differential current $Id\hat{\mathbf{l}}$ at a distance $r\hat{\mathbf{r}}$

$$d\mathbf{H} = \frac{1}{4\pi}\frac{Id\hat{\mathbf{l}} \times \hat{\mathbf{r}}}{r^2}. \tag{2.2}$$

The field at a point is found by integrating (2.2) around a current loop with $\mathbf{r}$ a unit vector pointing from $\mathbf{dI}$ to the point of interest. The approximation (2.2) is valid when the conductor can be approximated as infinitely narrow. If there is some thickness to the conductor, current density $\mathbf{J}$ is used and the proper formulation is

$$d\mathbf{H} = \frac{1}{4\pi}\frac{\mathbf{J}dV \times \hat{\mathbf{r}}}{r^2}. \tag{2.3}$$

From (2.3) it is observed that the field applied by a current carrying conductor is independent of the properties of the surrounding medium. However, the medium affects the total field because all media has some form of magnetism. Electron spins and orbital motion act as charge in motion, creating magnetic field. They can be thought of as microscopic magnets and in combination with the motion of electron orbits create magnetic moments—analogous to electric dipoles. Magnetic field created by a current carrying wire or by a permanent magnet causes reorientation of these magnetic moments or magnetization $\mathbf{M}$, which contributes to the magnetic flux density in the same manner that polarization contributes to electric flux density. The magnetic flux density is the sum of that seen in free-space and the contribution from the involved materials, $\mathbf{B} = \mu_0(\mathbf{H} + \mathbf{M})$.

To create a complete description of $\mathbf{D}$, $\mathbf{E}$, $\mathbf{B}$, and $\mathbf{H}$, Maxwell's equations along with constitutive relations are needed. A conceptual explanation of Maxwell's equations follows:

- **Gauss' law for electricity** describes how divergence of electric flux density is affected by electric charge density ρ_q. Field lines diverge from positive charges and are drawn towards negative charges. Furthermore, the total electric flux through a Gaussian surface must be zero unless it contains free charge.

- **Gauss' law for magnetism** states that the total magnetic flux $\oint_S \mathbf{B} \cdot d\mathbf{A}$ through a Gaussian surface is zero. This is due to the apparent absence of magnetic monopoles in nature. Magnetic charges always come in pairs which have divergences that cancel. This fact creates an asymmetry in the laws of electromagnetism with respect to the electric and magnetic variables.

- **Faraday's law of induction** describes how a changing magnetic field creates an electric field. This is the origin of eddy-currents and the basis for electric power generation.

- **Ampère's law with Maxwell's correction** describes how magnetic fields can be be generated by both electric current and by changing electric fields or displacement currents.

In equation form these laws are,

$$\nabla \cdot \mathbf{D} = \rho_q, \tag{2.4}$$

$$\nabla \cdot \mathbf{B} = 0, \tag{2.5}$$

$$\nabla \times \mathbf{E} = -\frac{\partial \mathbf{B}}{\partial t}, \tag{2.6}$$

$$\nabla \times \mathbf{H} = \mathbf{J} + \epsilon_0 \frac{\partial \mathbf{E}}{\partial t}. \tag{2.7}$$

Gauss' law for magnetism and Ampère's law (no displacement current) can be derived from the Biot-Savart law.

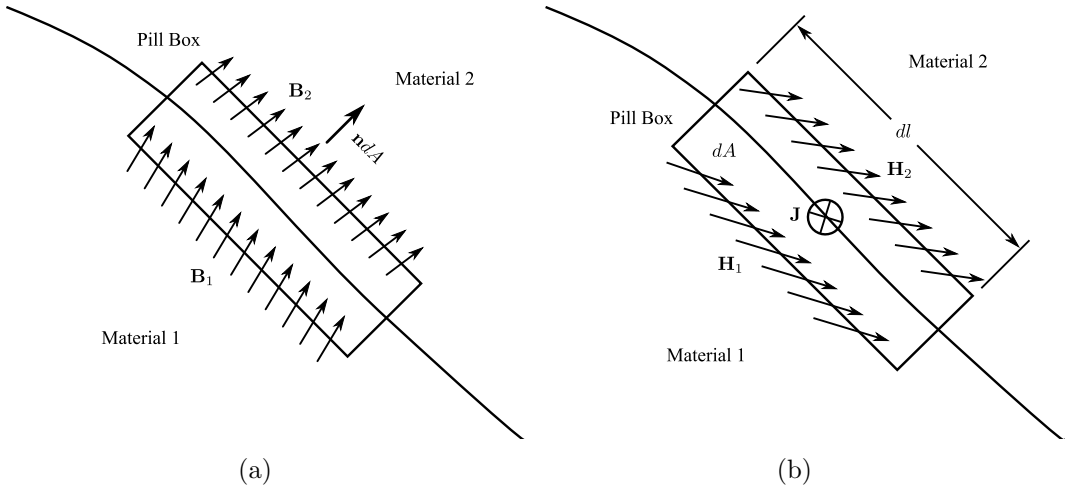

Figure 2.1: Demonstration of (a) flux density continuity and (b) field continuity.

Continuity conditions

Gauss' law for magnetism (2.5) enforces continuity of the normal flux component across a boundary and the Ampére-Maxwell law (2.7) enforces continuity of the tangential component of the magnetic field. Continuity of one results in discontinuity of the other since $\mathbf{B}$ is a continuous function of $\mathbf{H}$ within a material and the function changes abruptly at the boundary.

Continuity of the normal component of $\mathbf{B}$ through a material boundary is readily shown from the integral form of Gauss' law

$$\int_S \mathbf{B} \cdot d\mathbf{A} = 0, \tag{2.8}$$

which states that the total flux through a Gaussian (closed) surface is zero. Taking a thin pill box around the boundary (see Figure 2.1(a),) as the height of the box goes to zero, closing in on the boundary, and considering an infinitesimal area dA with $\mathbf{N}$

a unit vector normal to dA, Gauss' law becomes

$$(\mathbf{B}_2 - \mathbf{B}_1) \cdot \mathbf{n} dA = 0 \rightarrow \mathbf{B_2} \cdot \mathbf{n} = \mathbf{B_1} \cdot \mathbf{N}, \tag{2.9}$$

where the subscripts denote for which side of the boundary the flux density is calculated. Boundary conditions for the **H** field can be found from the integral form of the Ampére-Maxwell law

$$\oint_{\partial S} \mathbf{H} \cdot d\mathbf{l} = \int_S \mathbf{J} \cdot d\mathbf{A}. \tag{2.10}$$

With an infinitesimal length $d\mathbf{l} = \mathbf{t}dl$ tangent to the boundary and infinitesimal area $\mathbf{N}dA$ enclosing the boundary (see Fig. 2.1(b),) the equation becomes

$$(\mathbf{H}_2 - \mathbf{H}_1) \cdot \mathbf{t} dl = \mathbf{J} \cdot \mathbf{N} dA = dI. \tag{2.11}$$

In the absence of an inter-facial current

$$(\mathbf{H}_2 - \mathbf{H}_1) \cdot \mathbf{t} = 0, \tag{2.12}$$

which states that the tangential components of the field must be continuous across the boundary.

Continuity of flux density and discontinuity of field for the normal component across a boundary is illustrated in Figure 2.1(b). Continuity of field and discontinuity of flux density for the tangential component across a boundary is illustrated in Figure 2.1(a). A typical measurement setup involves a sample subject to a magnetic field from a coil. The field over the cross section of the sample is uniform since there is no current in the sample during quasi-static testing (eddy-currents will create non-uniformity in the field.) Furthermore, since the permeability is constant in the material, the flux density is also uniform over the cross-section.

The boundary conditions on flux density and field can be understood in the following practical terms when magnetic systems are viewed as consisting of lumped elements having different properties:

- Elements in series have the same flux
- Elements in parallel have the same field

These characteristics are analogous to electrical circuits. Flux is like current and field is like voltage. Conductance is like permeability. Magnetic circuits should therefore have an element property analogous to resistance which takes into account both the material properties and the geometry of the element. For magnetic circuits this property is called reluctance and it resists flux. Reluctance takes into account both the permeability and the geometry of the element. Just as resistance relates voltage to current in an element, reluctance relates field to flux.

For measurement purposes, flux should be measured with a device in series with the element of interest and field should be measured in parallel. To mitigate the effects of the instruments on the magnetic circuit, flux sensors should have low reluctance and field sensors should have high reluctance. This is analogous to electrical sensors where current sensor should have low resistance and voltage sensors should have high resistance.

Electromagnetic potentials

A description of the boundary conditions for electrical quantities will not be given here because the electrical and magnetic domains can be decoupled through introduction of auxiliary quantities or potentials. Various choices for electric and magnetic potentials exist and selection is based on assumptions made on the problem to be

solved [47]. For magnetostrictive systems in quasi-static operation with applied currents, the appropriate potentials are the scalar electric potential or voltage ϕ and the vector magnetic potential $\mathbf{A}$. Before describing these quantities, Ampére's law is simplified in accordance with the quasi-static assumption. For operation frequencies below 30 MHz (consistent with the operating regime of magnetostrictive devices,) the displacement current term in Ampére's law may be omitted. This reduced form of the electromagnetic field equations does not describe electromagnetic radiation but does account for the important effects of demagnetizing fields, described by Gauss' law for $\mathbf{B}$, and eddy currents, described by Ampére's law.

Chief intent of introducing potentials is to reduce the number of equations to be solved while satisfying the continuity conditions on $\mathbf{H}$ and $\mathbf{B}$. First, the vector magnetic potential is introduced,

$$\mathbf{B} = \nabla \times \mathbf{A}. \tag{2.13}$$

This statement is implied by (2.5) which is now automatically satisfied since the divergence of the curl of a field is zero. The scalar electric potential, or voltage, is now introduced,

$$\mathbf{E} = -\nabla\phi - \frac{\partial \mathbf{A}}{\partial t}. \tag{2.14}$$

This relation is implied by (2.6). The curl of the gradient of a scalar is always zero, this ensures that the curl of the electric field is equal to the time rate of change of magnetic induction. The remaining equations (2.4) and (2.7) are decoupled through inclusion of Ohm's law and decomposition of the current density. Magnetostrictive systems are typically composed entirely of Ohmic materials which exhibit a linear relationship

between current density and electric field, characterized by the conductivity σ,

$$\mathbf{J} = \sigma \mathbf{E}. \tag{2.15}$$

The current density is decomposed into a known, source current density $\mathbf{J}_s$ and the part resulting from eddy currents; this is motivated by (2.14), which combined with (2.15) gives

$$\begin{aligned} \mathbf{J} &= -\sigma \nabla \phi - \sigma \frac{\partial \mathbf{A}}{\partial t}, \\ &:= \mathbf{J}_s - \sigma \frac{\partial \mathbf{A}}{\partial t}. \end{aligned} \tag{2.16}$$

The magnetic initial-boundary-value problem

Incorporating the electromagnetic potentials and Ohm's law, the initial boundary value problem describing magnetic quantities is now

$$\nabla \times \mathbf{H} = \mathbf{J}_s - \sigma \frac{\partial \mathbf{A}}{\partial t}. \tag{2.17}$$

The dependent variable to be solved for is $\mathbf{A}$ with input or source $\mathbf{J}_s$. For solution, initial and boundary conditions are needed as well as a constitutive law relating $\mathbf{H}$ to $\mathbf{B}$ which has already been defined as the curl of $\mathbf{A}$. The boundary conditions are of two types. The Dirichlet type is simply specified $\mathbf{A}$ and may consist of part or all of the boundary,

$$\mathbf{A}(\Gamma_A, t) = \mathbf{A}_{\Gamma_A}. \tag{2.18}$$

A typical system to be solved consists of electromagnetic components such as steel, copper, and magnetostrictive materials, surrounded by an air volume, sufficiently large to assume that the the boundary of the air volume is magnetically insulated, $\mathbf{A}_\Gamma = 0$. The Neumann type boundary condition is the specified magnetic field tangent to

the boundary, $\mathbf{H} \times \mathbf{N}$. The tangent component is specified because it is this component that is continuous across material boundaries. This is implied by the fact that the curl of $\mathbf{H}$ appears in (2.17). This is a Neumann condition because $\mathbf{H}$ is related to $\mathbf{A}$ through first derivatives. On the boundary Γ_H, the following condition holds,

$$\begin{aligned} \mathbf{H}(\mathbf{B}) \times \mathbf{N} &= \mathbf{H}(\nabla \times \mathbf{A}) \times \mathbf{N} \\ &= \mathbf{H}_{T,\Gamma_H}. \end{aligned} \tag{2.19}$$

The boundary then is $\Gamma = \Gamma_A \cup \Gamma_H,\ \Gamma_A \cap \Gamma_H = 0$.

2.2.2 Ferromagnetism

To solve the magnetic initial boundary value problem (2.17) a constitutive law is needed to relate $\mathbf{B}$ and $\mathbf{H}$. As stated previously, the flux density is the sum of the contribution from the magnetic field in free space $\mu_0\mathbf{H}$ and the contribution from magnetizable materials $\mu_0\mathbf{M}$. The magnetization is a function of magnetic field and for certain materials, ferromagnetic materials, it can be quite large. The tangent matrix of the $\mathbf{M} - \mathbf{H}$ relationship is called magnetic susceptibility $\boldsymbol{\chi}$. Since the flux density is $\mathbf{B} = \mu_0(\mathbf{H} + \mathbf{M})$, the tangent matrix of the $\mathbf{B} - \mathbf{H}$ curve, or the magnetic permeability, is $\mu_0(1 + \boldsymbol{\chi})$. To summarize, small increments of magnetic flux density due to small increments of magnetic field are linearly related according to

$$\Delta\mathbf{B} = \boldsymbol{\mu}\Delta\mathbf{H} = \mu_0(\Delta\mathbf{H} + \Delta\mathbf{M}) = \mu_0(1 + \boldsymbol{\chi})\Delta\mathbf{H}. \tag{2.20}$$

In general, a magnetic field can magnetize a material in two ways. The first is by affecting electron orbits. Electron orbits may be thought of as charges in motion and hence generate a magnetic field. Additionally, since a magnetic field imparts acceleration on moving charges, a magnetic field will change an electron orbit and thereby

change the magnetization in the material. Magnetization from this effect tends to be very small and is termed diamagnetism. For diamagnetic materials the relationship between **M** and **H** is nearly linear with a very small magnetic susceptibility.

The other possibility for magnetism comes from the electron spin which may also be thought of as charge in motion. Ferromagnetic materials have unpaired electrons which do not participate in bonding. For paired electrons the opposite spins cancel and no magnetism results. In most materials, electrons are either paired with opposite spins in the native atom or become paired when they participate in bonding. Iron has a large number of unpaired electrons which do not participate in bonding and is ferromagnetic. The combined effect of the unpaired spin and the orbital motion is called a magnetic moment since an external field creates a torque on the magnetic moment. Unpaired electrons alone do not result in ferromagnetism because the torque which neighboring magnetic moments exert on each other causes them to align opposite resulting in zero net magnetization. Furthermore, thermal energy causes vibratory motion of the magnetic moment which contributes to randomness in the moment orientations. An external magnetic field can orient the magnetic moments and generate a small amount of macroscopic magnetism termed paramagnetism.

In ferromagnetic materials a spontaneous ordering of magnetic moments occurs below the Curie temperature. The Curie temperature marks the transition from disorder to order where exchange energy, an energy resulting from quantum constraints on the states taken by nearest neighbor electrons, overcomes the thermal energy. Spontaneous order of magnetic moments occurs at the micro-scale; in the absence of an external magnetic field this yields no net macro-scale magnetization. At the micro-scale magnetic moments are ordered in domains. Each domain has a uniform

magnetization M_s, or magnetic moment per volume, from its ordered magnetic moments, however, the domains are ordered so as to produce no net magnetization. This domain ordering reduces the overall energy. Magnetic flux density and field have an associated energy $(1/2)\mathbf{B}\cdot\mathbf{H}$ called the magnetostatic energy. Suppose that domains in an infinite plate of a ferromagnetic material are all aligned, in the absence of a magnetic field, and point towards one side of the plate. The magnetization of the plate is then M_s and the field inside the plate is zero. However, Gauss' law for flux density dictates that the flux density is continuous across material boundaries and therefore

$$\begin{aligned} \mathbf{B}_{plate} &= \mu_0(\mathbf{H}_{plate} + \mathbf{M}_{plate}) = \mu_0 M_s \\ &= \mathbf{B}_{air} = \mu_0 \mathbf{H}_{air}, \\ \rightarrow \mathbf{H}_{air} &= M_s. \end{aligned} \tag{2.21}$$

Even though $\mathbf{H}$ is zero in the plate, a field is generated outside of the plate and results in an energy density $(1/2)\mu_0 M_s^2$. It is therefore more energetically favorable for domains to align in opposing directions so as to produce no net magnetization in the absence of magnetic field. For certain geometries, alignment of domains does not produce an external magnetic field and hence alignment can occur without an internal magnetic field. These geometries have a closed magnetic circuit. For example, a ring can be magnetized circumferentially without generating an external field since no air boundaries are crossed.

Magnetization process for ferromagnetic materials

Below the curie temperature, competition between the exchange and thermal energies results in magnetic domains. The magnetization process $\mathbf{M}(\mathbf{H})$ occurs as an externally applied magnetic field does work $-\mu_0\mathbf{M}\cdot\mathbf{H}$ to order the domains. In

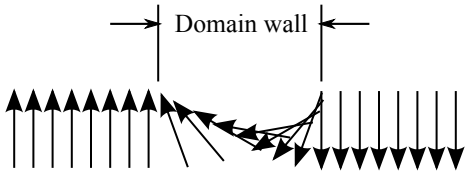

Figure 2.2: 180 degree domain wall.

general, three processes occur in the magnetization curve $\mathbf{M} - \mathbf{H}$: (1) domain wall motion, (2) domain rotation, and (3) further alignment of magnetic moments within domains.

The first process, which typically occurs at low magnetic fields where there are many differently oriented domains, proceeds as the size of domains oriented close to the field direction grow at the expense of domains which are oriented further from the field direction. This growth occurs through motion of the boundary, called a domain wall, that separates two differently oriented domains (see Figure 2.2.) In domain wall motion, the exchange and anisotropy energies are important and the process minimizes energy—domains with lower energy grow in size at the expense of domains with higher energy. Exchange energy encourages neighboring moments to align. Domain wall motion rotates neighboring moments with respect to each other and hence requires overcoming the exchange energy. Furthermore, moments have preferred or easy crystallographic orientations manifested in the anisotropy energy, a consequence of the combination of spin-orbit coupling and orbit-lattice coupling. Domains aligned in easy directions nearer the field direction have lower energy than those aligned in easy directions further from the field direction. The anisotropy energy also plays a significant role in the next process.

The second process is dominant once domain wall motion has created a single domain of the entire material. This domain may not be aligned with the field direction because of the anisotropy energy. Further work from the magnetic field is required to rotate a domain away from its preferred crystallographic direction.

The final process is the forced magnetization region where high magnetic fields improve the moment alignment within the now single domain material. In this process, the magnetic work improves moment alignment resulting in an increase in the domain magnetization M_s.

In general the magnetization process is hysteretic, depending on the magnetization history. During domain wall motion, magnetic moments at times are pinned by material defects. Overcoming the energy associated with these pinning sites is an irreversible, friction-like process. Additionally, the anisotropy energy has multiple energy minima since crystal symmetry dictates that magnetic moments prefer more than one crystallographic direction. Which of the possible orientations are taken by domains thus depends on their history. Since energy principles will be utilized extensively through the rest of this work, the classical form of the anisotropy energy is given here. The form depends on the crystal symmetry and it is expressed in terms of $\mathbf{m}$, the direction of the magnetization vector, through a series expansion omitting high-order terms. For example, uniaxial anisotropy can be expressed as,

$$E_A = -K_2 m_1^2. \tag{2.22}$$

The subscript refers to the order of the energy. For $K_2 > 0$ this expression is minimum at $\mathbf{m} = [\pm 1, 0, 0]$, hence these are the easy directions. For a cubic material, one or both of the direction families $\langle 100 \rangle$ and $\langle 111 \rangle$ are easy and the anisotropy energy can

be expressed

$$E_A = K_4(m1^2m_2^2 + m_2^2m_3^2 + m_3^2m_1^2) + K_6m_1^2m_2^2m_3^2. \tag{2.23}$$

The easy directions depend on the values of K_4 and K_6. Since all moments within a domain have the same orientation (neglecting thermal precession), these energies also define the energy density of a magnetic domain due to anisotropy.

2.3 Mechanics of materials

Mechanics of materials is the study of stress and strain in deformable bodies. Since these quantities are of great interest in the study of magnetostrictive materials, precise definitions for the concepts of stress and strain are needed. More detailed explanations can be found in the book by Boresi and Chong [16].

2.3.1 Strain

The concept of strain is purely geometric; it does not depend on the material under consideration. Strain is the study of transformations that occur with infinitesimal line segments in a body that undergoes deformation.

Deformation gradient tensor

In order to define strain for a 3-D body, consider a body with initial configuration $\mathcal{K}(\mathcal{B})_0$ which undergoes a deformation to a new configuration $\mathcal{K}(\mathcal{B})$ with coordinate systems $\mathbf{X}$ and $\mathbf{x}$, respectively (see Fig. 2.3.) The deformed and undeformed coordinate systems are chosen to have the same basis $\mathbf{e}_j$. The transformation $\mathcal{K}(\mathcal{B})_0$ to $\mathcal{K}(\mathcal{B})$ is given by a one-to-one mapping $\mathbf{x} = \chi(\mathbf{X})$. Now consider point P located at $\mathbf{X}$ in $\mathcal{K}(\mathcal{B})_0$ and a neighboring point Q located at $\mathbf{X} + d\mathbf{X}$, where $d\mathbf{X}$ is a straight,

infinitesimal line segment. After deformation, P is displaced by an amount $\mathbf{u}(\mathbf{X})$ to p and Q is displaced to q by an amount $\mathbf{u}(\mathbf{X}+d\mathbf{X})$. Since Q is in the neighborhood of P in the undeformed body, q is in the neighborhood of p in the deformed body. In other words, p is located at $\mathbf{x}$ and q is at $\mathbf{x}+d\mathbf{x}$ where $d\mathbf{x}$ is a straight, infinitesimal segment. The displacement is defined as $\mathbf{u}=\mathbf{x}-\mathbf{X}$ and from Figure 2.3 it is observed that

$$\mathbf{x}+d\mathbf{x}=\mathbf{X}+d\mathbf{X}+\mathbf{u}(\mathbf{X}+d\mathbf{X}) \tag{2.24}$$

$$\rightarrow d\mathbf{x}=d\mathbf{X}+\mathbf{u}(\mathbf{X}+d\mathbf{X})-\mathbf{x}+\mathbf{X} \tag{2.25}$$

$$=d\mathbf{X}+\mathbf{u}(\mathbf{X}+d\mathbf{X})-\mathbf{u}(\mathbf{X}) \tag{2.26}$$

$$=d\mathbf{X}+d\mathbf{u}. \tag{2.27}$$

Since the segments $d\mathbf{x}$ and $d\mathbf{X}$ are infinitesimal,

$$d\mathbf{u}=\frac{\partial \mathbf{u}}{\partial \mathbf{X}}d\mathbf{X},$$

and from (2.27)

$$d\mathbf{x}=d\mathbf{X}+\frac{\partial \mathbf{u}}{\partial \mathbf{X}}d\mathbf{X}, \tag{2.28}$$

$$=\left(\mathbf{I}+\frac{\partial \mathbf{u}}{\partial \mathbf{X}}\right)d\mathbf{X}, \tag{2.29}$$

$$=\mathbf{F}d\mathbf{X}. \tag{2.30}$$

The deformation gradient tensor $\mathbf{F}$ can also be found as the gradient of the mapping $\chi(\mathbf{X})$, recalling that $\mathbf{x}=\chi(\mathbf{X})$.

Normal strain

The normal strain is a measure of how much stretch is undergone by a differential line segment directed in the $\mathbf{N}$ direction (a unit vector.) The original segment can

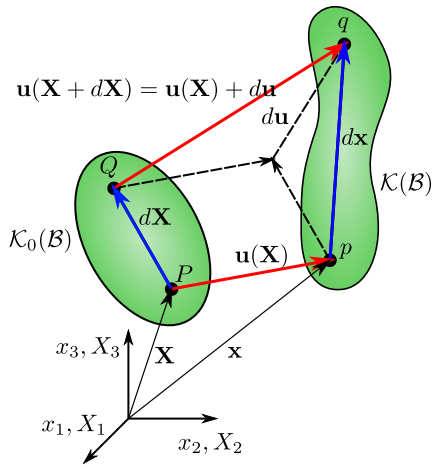

Figure 2.3: Finite deformation of a body.

be represented by its magnitude dX and direction according to $d\mathbf{X} = dX\mathbf{N}$. After deformation, the magnitude of the segment is dx and has an orientation $\mathbf{n}$ which is not in general the same as $\mathbf{N}$. The normal or engineering strain in the $\mathbf{N}$ direction is the percentage change in length of an infinitesimal line segment $d\mathbf{X}$ in this direction,

$$S_{\mathbf{N}} = \frac{dx - dX}{dX}. \tag{2.31}$$

It is beneficial to relate strain to displacement when analyzing deformable bodies. While the deformation gradient $\mathbf{F}$ relates line segments in the deformed and undeformed body, it carries information for both the change in length and the rotation of line segments. To obviate this, a measure using the square of the segment magnitudes is typically used; a common measure is the Lagrangian finite strain tensor $\mathbf{E}$ which

is derived from the magnification factor

$$M_{\mathbf{N}} = \frac{1}{2}\frac{dx^2 - dX^2}{dX^2}, \tag{2.32}$$

$$= \frac{d\mathbf{x}^T d\mathbf{x} - d\mathbf{X}^T d\mathbf{X}}{d\mathbf{X}^T d\mathbf{X}}, \tag{2.33}$$

$$= \frac{d\mathbf{X}^T \left(\mathbf{F}^T\mathbf{F} - \mathbf{I}\right) d\mathbf{X}}{d\mathbf{X}^T d\mathbf{X}}, \tag{2.34}$$

$$= \frac{dX^2 d\mathbf{N}^T \left(\mathbf{F}^T\mathbf{F} - \mathbf{I}\right) d\mathbf{N}}{dX^2 d\mathbf{N}^T d\mathbf{N}}, \tag{2.35}$$

$$= \mathbf{N}^T \left(\mathbf{F}^T\mathbf{F} - \mathbf{I}\right) d\mathbf{N}, \tag{2.36}$$

$$:= \mathbf{N}^T \mathbf{E} \mathbf{N}. \tag{2.37}$$

The finite strain tensor can be related to displacement since it is a function of the deformation gradient tensor which was previously shown to be related to the displacement gradient (2.30),

$$\mathbf{E} = \frac{1}{2}\left(\mathbf{F}^T\mathbf{F} - \mathbf{I}\right), \tag{2.38}$$

$$= \frac{1}{2}\left(\frac{\partial \mathbf{u}}{\partial \mathbf{X}}\right)^T + \frac{1}{2}\frac{\partial \mathbf{u}}{\partial \mathbf{X}} + \frac{1}{2}\left(\frac{\partial \mathbf{u}}{\partial \mathbf{X}}\right)^T \left(\frac{\partial \mathbf{u}}{\partial \mathbf{X}}\right). \tag{2.39}$$

The diagonal components of the finite strain tensor give the magnification factor in the basis directions since,

$$M_{\mathbf{e}_j} = \mathbf{e}_j^T \mathbf{E} \mathbf{e}_j = E_{jj}. \tag{2.40}$$

The magnification factor is related to the normal strain,

$$M_{\mathbf{N}} = \frac{1}{2}\frac{dx^2 - dX^2}{dX^2}, \tag{2.41}$$

$$= \frac{dx - dX}{dX} + \frac{1}{2}\left(\frac{dx - dX}{dX}\right)^2, \tag{2.42}$$

$$= S_{\mathbf{N}} + \frac{1}{2}S_{\mathbf{N}}^2. \tag{2.43}$$

Thus for small strains, the magnification factor is the normal strain and the diagonal components of $\mathbf{E}$ are the normal strains along the basis components $\mathbf{e}_j$.

Shear strain

Shear strain is defined as the change in angle ϕ_{jk} that occurs between two line segments $d\mathbf{X}_j$ and $d\mathbf{X}_k$, perpendicular in the undeformed body, as they are deformed to $d\mathbf{x}_j$ and $d\mathbf{x}_k$ in the deformed body. Before deformation the angle is $\pi/2$ and after deformation the angle is θ_{jk} and thus $\cos\theta_{jk} = \sin\phi_{jk}$. The off-diagonal components of the finite strain tensor are related to the shear strain of segments in the basis directions,

$$d\mathbf{x}_j^T d\mathbf{x}_k = dx_j dx_k \cos\theta_{jk} = dx_j dx_k \sin\phi_{jk}, \tag{2.44}$$

$$= \sqrt{d\mathbf{X}_j^T \mathbf{F}^T \mathbf{F} d\mathbf{X}_j}\sqrt{d\mathbf{X}_k^T \mathbf{F}^T \mathbf{F} d\mathbf{X}_k}\sin\phi_{jk}, \tag{2.45}$$

$$= dX_j dX_k \sqrt{\mathbf{e}_j^T (2\mathbf{E}+\mathbf{I})\,\mathbf{e}_j}\sqrt{\mathbf{e}_k^T (2\mathbf{E}+\mathbf{I})\,\mathbf{e}_k}\sin\phi_{jk}, \tag{2.46}$$

$$= d\mathbf{X}_j^T \mathbf{F}^T \mathbf{F} d\mathbf{X}_k, \tag{2.47}$$

$$= dX_j dX_k \mathbf{e}_j^T (2\mathbf{E}+\mathbf{I})\,\mathbf{e}_k, \tag{2.48}$$

$$\rightarrow \mathbf{e}_j^T (2\mathbf{E}+\mathbf{I})\,\mathbf{e}_k = \sqrt{\mathbf{e}_j^T (2\mathbf{E}+\mathbf{I})\,\mathbf{e}_j}\sqrt{\mathbf{e}_k^T (2\mathbf{E}+\mathbf{I})\,\mathbf{e}_k}\sin\phi_{jk}, \tag{2.49}$$

$$\rightarrow 2E_{jk} = \sqrt{2E_{jj}+1}\sqrt{2E_{kk}+1}\sin\phi_{12}. \tag{2.50}$$

Thus for small strains, $2E_{jj} << 1$ and $\sin\phi_{jk} \approx \phi_{jk}$, the off-diagonal components give half the shear strain, $E_{jk} = (1/2)\phi_{jk}$.

Infinitesimal strain tensor

It is deduced from the relationship between the displacement gradient and the finite strain tensor that strains will be small if the displacement gradient is small, for

in this case,

$$\mathbf{E} = \frac{1}{2}\left(\frac{\partial \mathbf{u}}{\partial \mathbf{X}}\right)^T + \frac{1}{2}\frac{\partial \mathbf{u}}{\partial \mathbf{X}} + \frac{1}{2}\left(\frac{\partial \mathbf{u}}{\partial \mathbf{X}}\right)^T \left(\frac{\partial \mathbf{u}}{\partial \mathbf{X}}\right), \tag{2.51}$$

$$\approx \frac{1}{2}\left(\frac{\partial \mathbf{u}}{\partial \mathbf{X}}\right)^T + \frac{1}{2}\frac{\partial \mathbf{u}}{\partial \mathbf{X}}, \tag{2.52}$$

$$= \mathbf{S}. \tag{2.53}$$

The diagonal components of the infinitesimal strain tensor $\mathbf{S}$ are the normal strains, or the fractional change in length of an infinitesimal line segment, and the off-diagonal components are the shear strains, or the change in angle between perpendicular, infinitesimal line segments. Since the diagonal components are half the shear strain, or the change in angle between line segments in two different basis directions, $\mathbf{S}$ is symmetric. In other words, it does not matter whether it is said change in angle between $\mathbf{e}_j$ and $\mathbf{e}_k$ or change in angle between $\mathbf{e}_k$ and $\mathbf{e}_j$, exactly half the change is given in S_{jk} and S_{kj}. The symmetry is also clear when considering the strain-displacement relationship,

$$\mathbf{S} = \frac{1}{2}\left(\frac{\partial \mathbf{u}}{\partial \mathbf{X}}\right)^T + \frac{1}{2}\frac{\partial \mathbf{u}}{\partial \mathbf{X}} \tag{2.54}$$

$$= \begin{bmatrix} \dfrac{\partial u_1}{\partial X_1} & \dfrac{1}{2}\left(\dfrac{\partial u_2}{\partial X_1} + \dfrac{\partial u_1}{\partial X_2}\right) & \dfrac{1}{2}\left(\dfrac{\partial u_1}{\partial X_3} + \dfrac{\partial u_3}{\partial X_1}\right) \\ \dfrac{1}{2}\left(\dfrac{\partial u_2}{\partial X_1} + \dfrac{\partial u_1}{\partial X_2}\right) & \dfrac{\partial u_2}{\partial X_2} & \dfrac{1}{2}\left(\dfrac{\partial u_2}{\partial X_3} + \dfrac{\partial u_3}{\partial X_2}\right) \\ \dfrac{1}{2}\left(\dfrac{\partial u_1}{\partial X_3} + \dfrac{\partial u_3}{\partial X_1}\right) & \dfrac{1}{2}\left(\dfrac{\partial u_2}{\partial X_3} + \dfrac{\partial u_3}{\partial X_2}\right) & \dfrac{\partial u_3}{\partial X_3} \end{bmatrix} \tag{2.55}$$

Since there are only six independent components, a compact notation can be devised where the strain tensor is stored in a vector with the first three components being the normal strains and the last three are the total shear strains. Furthermore, defining

the gradient operator

$$\nabla_S = \begin{bmatrix} \partial/\partial X_1 & 0 & 0 \\ 0 & \partial/\partial X_2 & 0 \\ 0 & 0 & \partial/\partial X_3 \\ \partial/\partial X_2 & \partial/\partial X_1 & 0 \\ 0 & \partial/\partial X_3 & \partial/\partial X_2 \\ \partial/\partial X_3 & 0 & \partial/\partial X_1 \end{bmatrix}, \tag{2.56}$$

the strain-displacement relationship can be represented

$$\mathbf{S} = \nabla_S \mathbf{u}. \tag{2.57}$$

For infinitesimal strains, the coordinate systems $\mathbf{x}$ and $\mathbf{X}$ can be interchanged. This means that the Lagrangian description and the Eulerian description are essentially the same or that the deformed configuration is very close to the undeformed configuration.

In the development of constitutive models for Galfenol as well as transducer-level models for Galfenol-based devices in this work, infinitesimal strain theory will be employed.

2.3.2 Stress

The concept of stress relates to the internal forces developed in deformable bodies when acted upon by external loads. External loads may be point forces, distributed loads on the surface, or body-type forces that act on the entire volume such as gravity or inertia. For magnetostrictive materials, internal forces can develop due to the simultaneous action of magnetic field-induced strain and an external constraint on the deformation. The constraint causes internal force build-up from reaction forces.

To define stress, a cutting plane is inserted into the body. The plane maintains equilibrium of the body by balancing the internal forces $\mathbf{F}$. Now consider the increment of force $\Delta\mathbf{F}$ acting on area ΔA (see Figure 2.4.) The stress vector or traction

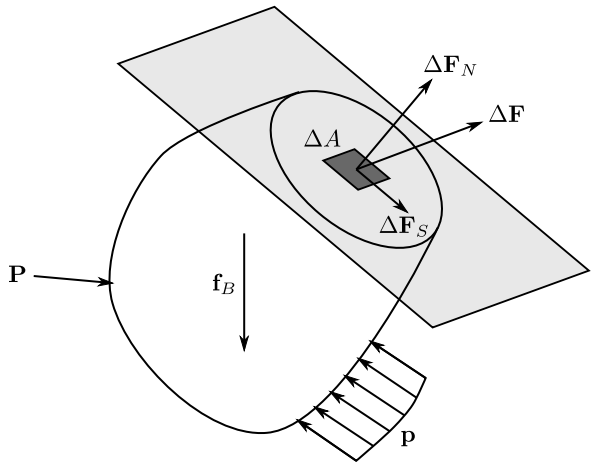

Figure 2.4: Cross-section of a deformable body with external loads.

force is then defined as

$$\mathbf{t} = \lim_{\Delta A \to 0} \frac{\Delta \mathbf{F}}{\Delta A}. \tag{2.58}$$

The component normal to the area is the normal stress vector or traction and the component parallel to the area is the shear stress vector or traction. Tractions on one side of the cutting plane are designated positive and on the other side negative. The sign convention can also be understood to mean that traction forces direct outwards from the plane are positive and towards the plane, negative. Tensile stresses are therefore positive. Traction force $\mathbf{t_N}$ acts on an infinitesimal area with unit normal $\mathbf{N}$. The stress at a point is tensor $\mathbf{T}$ whose columns are the tractions acting on three perpendicular planes passing through the point. Each plane, with unit normal one of the bases of the coordinate system, $\mathbf{e}_j$, has an associated 3-D traction $\mathbf{t}_j$. Thus the stress has nine components. The three components of each traction are the components directed along each of the three basis directions. The component T_{jk} of

the stress is the component of the traction $\mathbf{t}_j$ (acting on the area perpendicular to $\mathbf{e}_j$) directed along $\mathbf{e}_k$.

The diagonal entries of the stress tensor T_{jj} are called normal stresses because they are the normal components of the tractions acting on the planes perpendicular to the coordinate axes. For example, in a coordinate system $\mathbf{x}$, the stress T_{11} is the component of the traction force acting on the $2-3$ plane (perpendicular to x_1) which is directed toward x_1. The off-diagonal entries T_{jk} are the shear stresses because they act parallel to the plane. For example, the T_{12} stress component acts on the $2-3$ plane in a parallel manner, directed towards x_2.

The stress tensor is typically symmetric. Asymmetries only arise when pure moments are applied. Pure moments are torque loads which cannot be decomposed into a force acting on a moment arm. It can be shown from angular momentum is conserved in the absence of pure moments when $\mathbf{T}_{jk} = \mathbf{T}_{kj}$. The torques due to shear stresses in opposing diagonal entries are understood to balance each other. As in the case with the symmetric strain tensor, a compact vector notation can be used for stress where the six independent stress components are stored in a vector with the first three components the normal stresses, or diagonal components, and the second three components the shear stresses, or independent off-diagonal components.

Transformation of a stress

The stress tensor can be interpreted as a mapping between the unit normal $\mathbf{N}$ of an arbitrary plane and the traction acting on that plane $\mathbf{t_N} = \mathbf{TN}$. This relation is important in continuum mechanics because it connects conditions at the boundary of a body to the internal stress of the body. It is also useful for understanding how to transform a stress from one coordinate system to another.

Suppose the stress $\mathbf{T}$ is known in one coordinate system $\mathbf{x}$ having bases $\mathbf{e}_k$ and it is desired to find the stress $\mathbf{T}'$ in another coordinate system $\mathbf{x}'$ having bases $\mathbf{e}'_k$. Recall that the stress is fully defined when all the tractions are known on each of the three perpendicular planes defined by unit normals $\mathbf{e}'_j$. To find T'_{jk}, first find the traction on the plane defined by $\mathbf{I}'_k$, $\mathbf{t}'_j = \mathbf{T}\mathbf{e}'_k$. Then the nine components of stress are the three components of each of these three tractions, so the stress components in the new coordinate system are $T'_{jk} = \mathbf{e}'^T_j \mathbf{T}\mathbf{e}'_k$. The strain tensor transforms in the same fashion.

Applying this transformation process, suppose that in a certain coordinate system $\mathbf{x}$ with bases $\mathbf{e}_j$ that the complete stress state is attributed to a single traction with magnitude T acting normal to a plane with unit normal $\mathbf{N} = [\gamma_1, \gamma_2, \ \gamma_3]$. The 3-D stress tensor in the $\mathbf{x}$ coordinate system is then $T_{jk} = \gamma_j \gamma_k T$. This relation is used in the Armstrong magnetomechanical model [6] which is thus limited to uniaxial stresses.

2.3.3 Stress-strain relations

The materials comprising typical active structures and magnetostrictive devices have linear elastic behavior over the entire operating regime. The only exception is the magnetostrictive element which typically has a nonlinear stress-strain relationship. However, the strain in the magnetostrictive element can be decomposed into the sum of a strain due to purely mechanical energy and a strain due to the energy of the magnetomechanical coupling. The strain due to purely mechanical energy is linear elastic. The operating regime refers to the frequency and magnitude of the mechanical forces and displacements as well as electrical voltages applied to the system.

The linear-elastic stress-strain relationship is represented by Hooke's law, $\mathbf{T} = \mathbf{cS}$ with stiffness $\mathbf{c}$. For asymmetric stress and strain tensors, $\mathbf{c}$ is a fourth-order tensor with eighty-one components since it maps a second-order tensor to a second-order tensor. As discussed previously, kinematic considerations show that the strain tensor is always symmetric. Since there are only six independent components of strain, the number of independent components in the stiffness tensor is reduced fifty-four. In the absence of pure moments, the stress tensor is also symmetric. Since there are only six independent components of stress, the number of independent components in the stiffness tensor is reduced to thirty-six. In compact notation, stress and strain are vectors with six components each and the stiffness tensor is a second-order tensor having thirty-six components.

Energy considerations can further reduce the number of independent coefficients in the stiffness tensor because it can be shown to be symmetric. Stress and strain are work conjugates and the internal energy U is a function of strain; according to the first law of thermodynamics under adiabatic conditions, the variation of the work W and the internal energy are balanced,

$$\delta W = \delta U(\mathbf{S}), \tag{2.59}$$

$$\mathbf{T} \cdot \delta\mathbf{S} = \frac{\partial U}{\partial \mathbf{S}} \cdot \delta\mathbf{S}. \tag{2.60}$$

Since $\delta\mathbf{S}$ is arbitrary,

$$\frac{\partial U}{\partial \mathbf{S}} = \mathbf{T} \tag{2.61}$$

$$= \mathbf{cS}. \tag{2.62}$$

As long as the internal energy is twice differentiable, the coefficients of the stiffness tensor can now be found from the internal energy

$$\frac{\partial^2 U}{\partial S_j \partial S_k} = c_{jk}. \tag{2.63}$$

Since switching the indices $j,\ k$ on the left has no effect, $c_{jk} = c_{kj}$ and the stiffness tensor is symmetric.

The final form of the stiffness matrix can be deduced by considering material symmetries at the lattice level. Common magnetostrictive materials have a crystal lattice with cubic symmetry. Galfenol for example has a body-centered cubic structure [22]. The type of symmetry in the stiffness matrix observed for cubic materials is called isentropic symmetry and has the structure,

$$\mathbf{c} = \begin{bmatrix} c_{11} & c_{12} & c_{12} & 0 & 0 & 0 \\ c_{12} & c_{11} & c_{12} & 0 & 0 & 0 \\ c_{12} & c_{12} & c_{11} & 0 & 0 & 0 \\ 0 & 0 & 0 & c_{44} & 0 & 0 \\ 0 & 0 & 0 & 0 & c_{44} & 0 \\ 0 & 0 & 0 & 0 & 0 & c_{44} \end{bmatrix}. \tag{2.64}$$

2.3.4 Equations of motion

The equations of motion governing mechanical quantities such as $\mathbf{u}$, $\mathbf{S}$, and $\mathbf{T}$ are governed by Newtons' second law or the conservation of linear momentum. As discussed previously, conservation of angular momentum simply leads to the conclusion that the stress tensor is symmetric. The equations of motion can be derived by considering an infinitesimal volume of material acted upon by the three traction vectors $\mathbf{t}_j$ comprising the stress tensor, the body force, and the inertial or dÁlembert force. Summing the forces and dividing by the material volume leads to the system

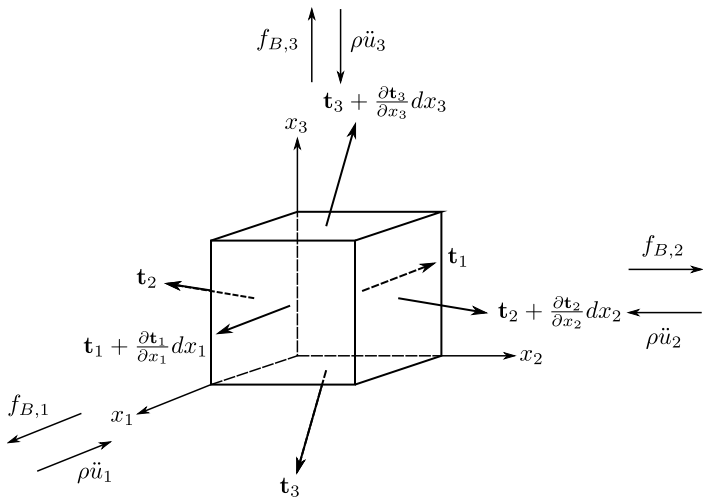

Figure 2.5: Infinitesimal material volume in mechanical equilibrium.

of equations,

$$\frac{\partial \mathbf{t}_1}{\partial x_1} + \frac{\partial \mathbf{t}_2}{\partial x_2} + \frac{\partial \mathbf{t}_3}{\partial x_3} + \mathbf{f}_B = \rho \ddot{\mathbf{u}}. \tag{2.65}$$

Recalling that the tractions $\mathbf{t}_j$ contain the stress components, the mechanical equations of motion can be compactly represented by using the six-element, vector representation of stress and the nabla operator previously defined (2.56)

$$\nabla_S^T \mathbf{T} + \mathbf{f}_B = \rho \ddot{\mathbf{u}}. \tag{2.66}$$

To solve (5.104), the following are needed

- Initial conditions on $\mathbf{u}$
- Boundary conditions
- Stress-strain constitutive law
- Strain-displacement kinematic relationship

The initial condition for displacements is given as $\mathbf{u}(\mathbf{x}, 0) = \mathbf{u}(0)$. Boundary conditions are of two kinds. The first consists of specified displacements,

$$\mathbf{u}(\Gamma_u, t) = \mathbf{u}_{\Gamma_u}, \tag{2.67}$$

where Γ_u is a subset of the boundary of the body where displacements are specified. The other type of boundary condition is that of specified tractions,

$$\mathbf{T}(\Gamma_T, t)\mathbf{N}_{\Gamma_T} = \mathbf{t}_{\Gamma_T} \tag{2.68}$$

where $\mathbf{N}$ is the unit normal of the boundary and $\mathbf{t}_{\Gamma_T}$ is the traction force applied to Γ_T, a subset of the boundary of the body. This form of the traction boundary condition necessitates the use of the second-order tensor representation of the stress rather than the vector representation. The traction boundary condition clearly shows how forces applied to the surface of a body result in internal forces governed by (5.104) and illustrates that stress is a tensor that maps surface normal to surface traction. The traction boundary condition can be represented using the compact stress notation as follows,

$$\mathbf{N}_T\mathbf{T}(\Gamma_T, t) = \mathbf{t}_{\Gamma_T} \tag{2.69}$$

$$\mathbf{N}_T = \begin{bmatrix} N_1 & 0 & 0 & N_2 & 0 & N_3 \\ 0 & N_2 & 0 & N_1 & N_3 & 0 \\ 0 & 0 & N_3 & 0 & N_2 & N_1 \end{bmatrix}. \tag{2.70}$$

For a passive system (no magnetomechanical coupling)and utilizing linear elastic materials as well as the strain-displacement relation, the initial boundary value

problem governing displacements is

$$\nabla_S^T \mathbf{c} \nabla_S \mathbf{u} + \mathbf{f}_B = \rho \ddot{\mathbf{u}} \tag{2.71}$$

$$\mathbf{u}(\mathbf{x}, 0) = \mathbf{u}_0 \tag{2.72}$$

$$\mathbf{u}(\Gamma_u, t) = \mathbf{u}_{\Gamma_u} \tag{2.73}$$

$$\mathbf{N}_T \mathbf{c} \nabla_S \mathbf{u}(\Gamma_T, t) = \mathbf{t}_{\Gamma_T}. \tag{2.74}$$

In Chapter 5, this system will be solved using the finite-element method for passive mechanical elements in systems having magnetostrictive materials.

2.4 Magnetomechanical coupling

Thus far, the fields of electromagnetism and mechanics of materials have been treated separately. The spatial and temporal dependence of electromagnetic quantities can be described by Maxwell's equations, requiring a material constitutive law relating $\mathbf{B}$ and $\mathbf{H}$. The spatial and temporal dependence of mechanical quantities can be described by Newton's laws, requiring a material constitutive law relating $\mathbf{S}$ and $\mathbf{T}$. For magnetostrictive materials, $\mathbf{B}$ and $\mathbf{S}$ are each functions of both $\mathbf{H}$ and $\mathbf{T}$; the functional relationship is generally nonlinear. Descriptions of magnetostriction in a variety of materials are given in the book by Engdahl [36] and O'Handley's book provides a detailed discussion on the energy derivations for magnetomechanical coupling [75].

Passive, ferromagnetic materials always have a nonlinear $\mathbf{B} - \mathbf{H}$ relationship. Although the portion of $\mathbf{B}$ from the permeability of free space is linear, $\mu_0 \mathbf{H}$, the magnetization due to ferromagnetic domains $\mathbf{M}$ depends nonlinearly on $\mathbf{H}$. Chief nonlinear characteristics are saturation, occurring when all of the magnetic moments have

aligned with the field, and hysteresis. Additionally, the behavior may be anisotropic or direction dependent. Passive materials used in magnetostrictive devices are linear elastic, obeying Hooke's law $\mathbf{T} = \mathbf{cS}$.

Since the $\mathbf{B}-\mathbf{H}$ relationship is nonlinear, the nonlinearity of the $\mathbf{B}-\mathbf{T}$ behavior in magnetostrictive materials is not surprising. With regards to stress application, the magnetization also saturates at high stresses, is anisotropic and history dependent. Stress, like magnetic field, causes domain rotation and domain wall motion. Experiments have shown that the $\mathbf{S}-\mathbf{H}$ behavior is also nonlinear and that the portion of $\mathbf{S}$ due to magnetic field is an even function of $\mathbf{H}$. The reason for this is clear when the origin of magnetostriction is explained.

The ions in magnetostrictive materials have anisotropic charge clouds. As a magnetic moment rotates, spin-orbit coupling causes a rotation of the charge cloud which in turn results in a lattice strain from the electrical attraction-repulsion between neighboring ions. The strain associated with moment rotation induced by a magnetic field is Joule magnetostriction. Conversely, if the lattice is stressed then the clouds will rotate and cause a rotation of magnetic moments. This stress-induced magnetization is the inverse or Villari effect.

Isotropic magnetostriction is a simple case which illustrates the nature of the nonlinearity associated with magnetostriction. Consider the four states depicted in Figure 2.6. The direction of the magnetic moment vector is indicated with arrows and their direction is attached to the long axis of the ellipse representing the anisotropy of the electron cloud. In state (1) no field or stress is applied and moments or equivalently, domains are randomly oriented. In states (2) and (3) a magnetic field causes alignment of the moment vectors. For both positive and negative fields, positive

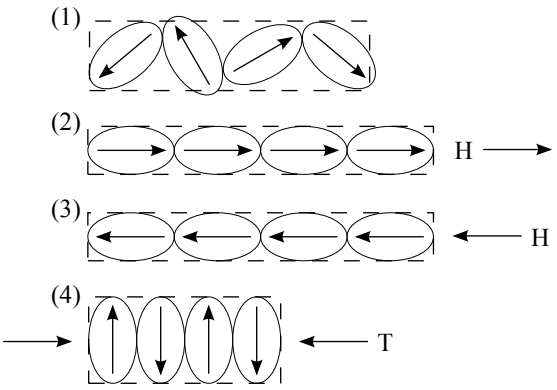

Figure 2.6: Cartoon depiction of magnetomechanical coupling.

magnetostriction occurs. Applying a compressive stress in state (4) causes rotation perpendicular to the stress. This eliminates the bulk magnetization in the horizontal direction. Since the stress causes no preference for the up or the down orientation, there is no net magnetization in the vertical direction either. The magnetomechanical process is volume conserving. Positive magnetostriction in the horizontal direction results in negative magnetostriction in the vertical direction and visa versa.

2.4.1 Magnetomechanical coupling of cubic anisotropy

Since Galfenol (unannealed) has cubic symmetry, special attention is given here to magnetomechanical coupling in cubic materials. The magnetomechanical coupling energy depends on the bond $\mathbf{R} = R\mathbf{r}$, where R is the bond length and $\mathbf{r}$ the direction between neighboring ions, and the direction $\mathbf{m}$ of the atomic magnetic moment. For simplicity, consider a bond in the 1 Cartesian direction with an initial bond $\mathbf{R}_0 = R_0[1, 0, 0]$. A lattice strain $\mathbf{S}$, using compact vector notation for infinitesimal strains, changes the bond to $\mathbf{R} = [R_0(1 + S_1), 1/2S_4, 1/2S_6]$. The energy of the initial bond is expressed by a series expansion with cubic symmetry on the Legendre polynomial

basis,

$$\begin{aligned} u_0 &= g(R_0) + l(R_0)\left[(\mathbf{r}_0 \cdot \mathbf{m})^2 - 1/3\right] ... \\ &= g(R_0) + l(R_0)\left(m_1^2 - 1/3\right) + ... \end{aligned} \tag{2.75}$$

Expanding $g(R)$ and $l(R)$ about R_0, the energy after the strain is

$$\begin{aligned} u &= g(R_0) + \frac{dg}{dR}(R_0)S_1 + \left(l(R_0) + \frac{dl}{dR}(R_0)S_1\right)\left[(\mathbf{r}\cdot\mathbf{m})^2 - 1/3\right] ... \\ &= g(R_0) + \frac{dg}{dR}(R_0)S_1 + \left(l(R_0) + \frac{dl}{dR}(R_0)S_1\right) \\ &\quad \times \left[(m_1 + m_2S_4 + m_3S_6)^2 - 1/3\right] + ... \end{aligned} \tag{2.76}$$

The magnetomechanical coupling energy between the strain and magnetic moment direction for a bond in the 1 direction is defined as

$$\begin{aligned} u_C :=& u - u_0 = \frac{dg}{dR}(R_0)S_1 + \frac{dl}{dR}(R_0)S_1(m_1^2 - 1/3) \\ &+ l(R_0)\left(m_1m_2S_4 + m_1m_3S_6\right) + ... + O(S_i^2). \end{aligned} \tag{2.77}$$

After summing this expression and similar expressions for the strain of bonds in the 2 and 3 directions, the magnetomechanical coupling energy for a cubic lattice is

$$\begin{aligned} U_C =& B_1\left[(m_1^2 - 1/3)S_1 + (m_2^2 - 1/3)S_2 + (m_3^2 - 1/3)S_3\right] \\ &+ B_2(m_1m_2S_4 + m_2m_3S_5 + m_1m_3S_6). \end{aligned} \tag{2.78}$$

The parameters B_1 and B_2 are the magneto-elastic coupling coefficients. The total energy from strain also includes the purely elastic energy associated with the lattice stiffness

$$U_E = \frac{1}{2}\mathbf{S}\cdot\mathbf{cS}. \tag{2.79}$$

Minimization of $U_C + U_E$ yields the total equilibrium strain. Since the total energy is a superposition of the coupling energy and the purely elastic energy, the total strain is the superposition of the elastic strain due to stress and the strain due to moment rotation or the magnetostriction,

$$\mathbf{S} = \mathbf{S}_m + \mathbf{c}^{-1}\mathbf{T}, \tag{2.80}$$

where

$$\mathbf{S}_m = \begin{bmatrix} (3/2)\lambda_{100}(m_1^2 - 1/3) \\ (3/2)\lambda_{100}(m_2^2 - 1/3) \\ (3/2)\lambda_{100}(m_3^2 - 1/3) \\ 3\lambda_{111} m_1 m_2 \\ 3\lambda_{111} m_2 m_3 \\ 3\lambda_{111} m_3 m_1 \end{bmatrix}, \tag{2.81}$$

with magnetostriction coefficients

$$\lambda_{100} = -\frac{2}{3}\frac{B_1}{c_{11} - c_{12}}, \tag{2.82}$$

$$\lambda_{111} = -\frac{1}{3}\frac{B_2}{c_{44}}. \tag{2.83}$$

Inclusion of the 1/3 term is not strictly necessary but simply defines the strain reference state. By including the factor, the magnetostriction of a moment oriented in any of the $\langle 100 \rangle$ directions is λ_{100} and the magnetostriction of a moment oriented in any of the $\langle 111 \rangle$ directions is λ_{111}. Additionally, the bulk magnetostriction of a collection of randomly oriented moments is zero and the total change in strain for full 90 degree moment rotation is $(3/2)\lambda_{100}$.

2.5 Concluding remarks

In this chapter, the continuum quantities of interest in devices employing magnetostrictive materials have been discussed, including the field equations governing their spatial and temporal dependencies. The quantities of interest in the electromagnetic domain are magnetic field $\mathbf{H}$ and flux density $\mathbf{B}$ as well as current density $\mathbf{J}$ and vector magnetic potential $\mathbf{A}$, kinematically related to $\mathbf{B}$. The quantities of interest in the mechanical domain are stress $\mathbf{T}$ and strain $\mathbf{S}$ as well surface traction $\mathbf{t}$ and displacement $\mathbf{u}$, kinematically related to $\mathbf{S}$. It was shown that constitutive relationships are needed between $\mathbf{B}$ and $\mathbf{H}$ and $\mathbf{S}$ and $\mathbf{T}$ in order to solve the field equations.

Chapters 3 and 4 are devoted to modeling and characterization of Galfenol constitutive behavior and Chapter 5 to transducer applications, including a finite element solution of the field equations.

CHAPTER 3

Constitutive modeling: Part I

3.1 Preamble

Magnetostrictive materials and devices can be studied at different length scales, from the atomic and micro-scales involving individual atomic moments and magnetic domain configurations, to the macro-scale. At the macro-scale, bulk magnetization and strain are of interest as well as the interaction between magnetostrictive materials and the surrounding media employed in transducers. This chapter presents initial work in the modeling and characterization of the magnetization/strain versus magnetic field/stress constitutive behavior exhibited by Galfenol alloys. The work relies on a set of magnetization and strain measurements acquired while applying magnetic field at constant stress. Two modeling approaches are presented; both employ statistical principles to relate the micro-scale with the macro-scale but they provide different interpretations of hysteresis.

Section 3.2 details a 1-D model employing Boltzmann statistics [38]. Bulk behavior is calculated from the expected value of the orientation of a continuum of magnetic moments. A triple well energy potential for the magnetic moments is employed; the distribution of the moments within an energy well is given by Boltzmann's equation.

Boltzmann's equation is again used to quantify the rate at which perturbations from thermal energy cause moments to jump between wells. The rate equations are assembled into a state-space model where the states are the volume fractions of moments in each of the energy wells and the output is the bulk magnetization and strain, given by the sum of the contributions of each state. Hysteresis is thereby interpreted as the time-delay in moment jumping as stress and field change the energy landscape. This interpretation of hysteresis is therefore rate-dependent. The state-space form of this model is particularly advantageous for device design and control because it is readily integrated with transducer models and because the stability of state-space systems is well understood.

Section 3.3 is an attempt to extend the energy and statistical principles in Section 3.2 to 3-D while providing a rate-independent interpretation of hysteresis. A key simplification is made to enable 3-D application in an efficient manner. Rather than consider a continuum of magnetic moments, a finite number of orientations is considered. Furthermore, it is assumed that like-oriented moments are assembled in groups and act as magnetization particles. These particles rotate with stress and field application, are non-interacting, and approximate domains. The bulk anhysteretic behavior is calculated by assuming a Boltzmann distribution of the particle orientations. In this section, hysteresis loss is interpreted as the energy loss occurring when domain walls pass through material defects. Since domain wall motion is a mechanism whereby the volume fractions of differently oriented magnetic moments change, the effect of the loss can be modeled by a differential equation for each of the volume fractions, driven by the anhysteretic value.

During the peer review of the work in Section 3.2 prior to its publication [40], a question was raised regarding the scaling parameter used in the Boltzmann relation. In the pre-publication form of [38], the scaling parameter was interpreted as thermal energy density $k_B\theta/\vartheta$, where k_B is Boltzmann's constant, θ is temperature, and ϑ is volume. A reviewer objected to this for two reasons regarding the interpretation of ϑ. If ϑ is interpreted as the volume of a magnetic moment, then the Boltzmann relation is the exponential of ratio of the energy density of a single moment with its thermal energy density. The reviewer objected to this because the energy density used in the model does not include exchange energy, a chief competitor with thermal energy. The reviewer also objected to the value of ϑ used in the model simulations compared with experiments because the volume was much larger than the volume of a moment. The reviewer's conclusion was that the volume was artificially scaled because the exchange energy was not included. This interpretation of the scaling parameter was therefore withdrawn from the paper and replaced with an empirical parameter Ω.

The following derivation is meant to provide an explanation for the large value of ϑ by deriving the Boltzmann distribution from entropy principles. It provides a more precise definition of ϑ without any artificial scaling. Following the derivation, the two modeling approaches described above are presented.

Entropy formulation for magnetic domain scale particles

Consider a collection of N magnetization particles; as described earlier, the particles approximate domains and consist of like-oriented moments. Furthermore, the orientation of one particle does not affect the orientation of another. The particles have r possible orientations of free energy density G_k and occupy volume V. The number of particles in the k^{th} orientation is N_k. The entropy of a collection of N

particles where each particle has r possible states is proportional to the number of ways the collection can be arranged to produce the same energy [45]

$$\begin{aligned}\bar{\eta} &= k_B \ln\left(\frac{N!}{N_1!N_2!N_3!...!N_r!}\right), \\ &= k_B \left(\ln N! - \ln N_1! - \ln N_2! - ...\right),\end{aligned} \tag{3.1}$$

where Boltzmann's constant k_B is the proportionality constant. Using Stirling's approximation $\ln x! \approx x \ln x - x$

$$\begin{aligned}\bar{\eta} &\approx k_B \left(N \ln N - N - N_1 \ln N_1 + N_1 - N_2 \ln N_2 + N_2 + ...\right), \\ &= k_B \left(N \ln N - N_1 \ln N_1 - N_2 \ln N_2 - ...\right), \\ &= k_B \left[N \ln N - N_1 \ln\left(\frac{N_1}{N}N\right) - N_2 \ln\left(\frac{N_2}{N}N\right) - ...\right], \\ &= k_B \left[N \ln N - N_1 \left(\ln\frac{N_1}{N} + \ln N\right) - N_2 \left(\ln\frac{N_2}{N} + \ln N\right) - ...\right], \\ &= k_B \left[N \ln N - (N_1 + N_2 + ...) \ln N - N_1 \ln\frac{N_1}{N} - N_2 \ln\frac{N_2}{N} - ...\right], \\ &= k_B \left(-N_1 \ln\frac{N_1}{N} - N_2 \ln\frac{N_2}{N} - ...\right), \\ &= k_B N \left(-\frac{N_1}{N}\ln\frac{N_1}{N} - \frac{N_2}{N}\ln\frac{N_2}{N} - ...\right).\end{aligned} \tag{3.2}$$

The volume fraction of particles in orientation k is $\xi_k = N_k/N$ and the entropy density is then

$$\bar{\eta} = \frac{k_B N}{V} \sum_{k=1}^{r} -\xi_k \ln \xi_k. \tag{3.3}$$

The parameter ϑ can now be precisely defined from the particle density, $1/\vartheta = N/V$; it is the average volume of a magnetization particle. With this definition, the entropy density is

$$\eta = \frac{k_B}{\vartheta} \sum_{k=1}^{r} -\xi_k \ln \xi_k. \tag{3.4}$$

The total energy density of a collection of particles at temperature θ is

$$G = -\theta\eta + \sum_{k=1}^{r} G_k, \tag{3.5}$$

and substitution from (3.4) gives

$$G = \frac{k_B\theta}{\vartheta}\sum_{k=1}^{r}\xi_k \ln \xi_k + \sum_{k=1}^{r} G_k. \tag{3.6}$$

The volume fractions are internal variables and can be found through energy minimization $\partial G/\partial \xi_k = 0$. The result is the Boltzmann probability function

$$\xi_k = \frac{e^{-G_k/(k_B\theta/\vartheta)}}{\sum_{k=1}^{r} e^{-G_k/(k_B\theta/\vartheta)}}. \tag{3.7}$$

This same function is used in Section 3.3 but with the thermal energy density $k_B\theta/\vartheta$ replaced with an empirical parameter Ω. Typical values for the parameter Ω which result in good agreement with bulk magnetization measurements are on the order of hundreds of J/m^3. This supports using $k_B\theta/\vartheta$ in place of Ω since it gives a volume consistent with the definition of ϑ. Using a thermal energy density $k_B\theta/\vartheta$ on the order of hundreds of J/m^3, the volume of magnetization particles would then have a length on the order of hundreds of nanometers at room temperature. This length is consistent with the physical description given for the magnetization particles. It is larger than the length scale of atomic moments and smaller than the length scale of magnetic domains. Experiments have shown that domain volume fractions change in discrete jumps as groups of moments having a volume smaller than a domain yet larger than a magnetic moment flip from one orientation to another. These jumps actually cause acoustic signals called Barkausen noise (see page 302 of [28].)

3.2 State-space constitutive model for magnetization and magnetostriction of Galfenol alloys

Previous models for Galfenol [86, 8] have followed Armstrong's approach [6] of using a single energy-weighted average of the Gibbs free energy for the entire material to calculate the distribution of moments. The weighting function tends to

smooth the sharp magnetization and magnetostriction transitions obtained by direct minimization of the Gibbs free energy, thus providing a more accurate description of physical measurements. However, the weighting function depends on a non-physical parameter. Because the moment volume fractions are not tracked, this model cannot characterize the hysteresis due to anisotropy or rate dependent thermal effects, which occurs because of the history dependence of the moment volume fractions in each Gibbs energy well.

In this work we present a macroscopic constitutive model that accurately quantifies hysteresis, stress and annealing-induced anisotropies, and thermal relaxation effects present in the magnetization and magnetostriction of general magnetostrictive materials, with especial consideration to Galfenol's specific properties. Our approach consists of finding a local magnetization kernel through minimization of the Gibbs free energy of a single magnetic moment and then applying Boltzmann statistics to calculate the evolution of moment volume fractions in the bulk material. We formulate the model in state-space form, which greatly simplifies model implementation for large-signal (i.e., nonlinear) device design and control. The model requires a small number of parameters which can be correlated with physical properties of the data.

In our approach, thermal energy creates a Boltzmann distribution of moments in each of the Gibbs energy wells and causes moments to jump between wells. The bulk magnetization and magnetostriction are calculated by tracking the volume fraction of moments in each well and summing their expected contribution to the bulk magnetization or magnetostriction. The result is a linear time-variant equation which is expressed in state-space form. The modeling of a nonlinear time-invariant system as

a linear time-variant system is advantageous because the stability properties of such systems are well understood (see, for example, [3]).

3.2.1 Model development

Energy formulations

The Helmholtz free energy ψ is given by the Legendre transformation of the internal energy U, $\psi = U - \theta\eta$, where θ is temperature and η is entropy. The internal energy is comprised of magnetocrystalline anisotropy energy U_a and stress-induced anisotropy energy U_T.

The magnetocrystalline anisotropy energy depends on the orientation $\hat{\mathbf{m}} = [\hat{m}_x, \hat{m}_y, \hat{m}_z]$ of the magnetization. Stress-annealed Galfenol has tetragonal crystal symmetry [86] for which U_a has been given in [63],

$$\begin{aligned} U_a(\hat{\mathbf{m}}) = K_2\left(\hat{m}_z^2 - \frac{1}{3}\right) + K_4\left(\hat{m}_x^4 + \hat{m}_y^4 + \hat{m}_z^4 - \frac{3}{5}\right) \\ + K_4'\left(\hat{m}_z^4 - \frac{6}{7}\hat{m}_z^2 + \frac{3}{35}\right). \end{aligned} \tag{3.8}$$

The x, y, and z spatial directions are assumed to be aligned with the [100], [010], and [001] crystal directions. The constant K_4 is the fourth order cubic anisotropy constant and the constants K_2 and K_4' are the second-order and fourth-order uniaxial anisotropy constants which favor or penalize the z direction depending on their sign. Recognizing that $\hat{m}_x^2 + \hat{m}_y^2 + \hat{m}_z^2 = 1$, K_4 can be shown to be related to K_1 in the traditional cubic formulation (used, for example, in [6])

$$E = K_0 + K_1(\hat{m}_x^2\hat{m}_y^2 + \hat{m}_y^2\hat{m}_z^2 + \hat{m}_z^2\hat{m}_x^2) + \cdots \tag{3.9}$$

by $2K_4 = -K_1$. Rafique et al. [83] measured K_1 for single-crystal Galfenol alloys with 5-20 at.% Ga. We use a K_4 value that is about 40% lower than the corresponding

K_4 value obtained from the K_1 coefficients presented in [83]. The difference is due to our samples being highly textured polycrystals rather than single crystals.

The stress anisotropy, which is induced by the magneto-elastic coupling energy, depends on the stress tensor T_{ij} in a manner dictated by the crystal symmetry. The derivation of the stress anisotropy from the magneto-elastic coupling energy for materials exhibiting cubic symmetry in the magnetostriction has been presented by Kittel [61]. The stress contribution to the anisotropy is

$$\begin{aligned} U_T(\hat{\mathbf{m}}, T_{ij}) = &-(3/2)\lambda_{001}\left(\hat{m}_x^2 T_{xx} + \hat{m}_y^2 T_{yy} + \hat{m}_z^2 T_{zz}\right) \\ &- 3\lambda_{111} T\left(\hat{m}_x \hat{m}_y T_{xy} + \hat{m}_y \hat{m}_z T_{yz} + \hat{m}_z \hat{m}_x T_{zx}\right) \end{aligned} \tag{3.10}$$

where λ_{001} and λ_{111} are magnetostriction along the [001] and [111] directions, respectively.

By considering only isothermal processes and incorporating irreversibilities into the moment rotations (see Section 3.2.1) rather than through a direct entropy formulation, the Helmholtz free energy reduces to the internal energy $\psi = U_a(\hat{\mathbf{m}}) + U_T(\hat{\mathbf{m}}, T_{ij})$.

Figure 3.1 shows the effect of stress-annealing or compressive stresses along the z-axis on the Helmholtz free energy. The z-direction becomes a higher energy direction, which has two effects on the magnetization due to magnetic fields applied in this direction. First, the hysteresis and remanence magnetization decrease because there is no longer a deep energy well to trap magnetic moments. Second, higher fields are required to saturate the material. The depth of the wells on the z-axis is determined by the magnitude and sign of K_2 and K_4' relative to K_4. In the case when K_2 and K_4' are zero as in Figure 3.1(a), relation (3.8) is identical to (3.9) up to the K_1 term and the symmetry is cubic.

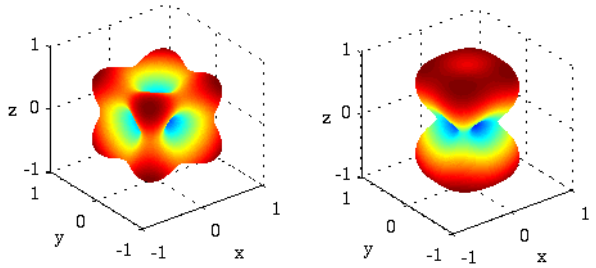

(a) (b)

Figure 3.1: Comparison of (a) unannealed and (b) annealed Helmholtz free energies with no applied stress. The energy has been normalized and is proportional to the distance from the origin and the color.

The Gibbs free energy of a single magnetic moment is obtained through the Legendre transformation $G = \psi - \mu_o M_s \hat{\mathbf{m}} \cdot \mathbf{H}$, where M_s is the saturation magnetization and $\mathbf{H}$ is an applied magnetic field. In the common case in which the applied magnetic field and stress are oriented along the z-axis, the Gibbs free energy has the form

$$\begin{aligned} G = {} & K_4 \left(\hat{m}_x^4 + \hat{m}_y^4 + \hat{m}_z^4\right) + K_4' \hat{m}_z^4 \\ & + \left(K_2 - \frac{6}{7} K_4' - \frac{3}{2} \lambda_{001} T\right) \hat{m}_z^2 - \mu_0 M_s H \hat{m}_z, \end{aligned} \tag{3.11}$$

with H the magnetic field and T the stress along the z-axis. Constant terms have been omitted because it is the change in the Gibbs energy that determines the moment orientation. The Gibbs energy (3.11) is expressed more efficiently in spherical coordinates with the orientation of the magnetization vector defined by the angle ϕ it makes with the z-axis and the angle α that its projection in the x-y plane makes with the x-axis,

$$\begin{aligned} G = {} & K_4 \left(\sin^4\phi \left(\sin^4\alpha + \cos^4\alpha\right) + \cos^4\phi\right) + K_4' \cos^4\phi \\ & + \left(K_2 - \frac{6}{7} K_4' - \frac{3}{2} \lambda_{001} T\right) \cos^2\phi - \mu_0 M_s H \cos\phi. \end{aligned} \tag{3.12}$$

When thermal energy and material defects are negligible, all of the magnetic moments will be oriented in the locally minimum directions in each of the energy wells. The bulk magnetization is the vector sum of the magnetization due to each magnetic moment. Therefore, to determine the bulk magnetization one requires an equation for the trajectory of the energy wells produced by applied magnetic fields and the volume fraction of moments in each well. The symmetry in the 3-D Gibbs energy implies that the moments in each of the four energy wells in the basal plane follow the same ϕ path when an applied magnetic field in the z-direction induces rotation of moments into the field direction. It is sufficient then to model the trajectory of just one of these wells because the contribution to the magnetization in the z-direction of moments lying in any of the four wells will be the same (Figure 3.2(a, c, e)). Choosing the energy well in the x-direction ($\alpha = 0$) to be tracked and using only cos functions, (3.12) becomes

$$G = (2K_4 + K_4')\cos^4\phi + \left(K_2 - \frac{6}{7}K_4' - 2K_4 - \frac{3}{2}\lambda_{001}T\right) \times \cos^2\phi - \mu_0 M_s H \cos\phi. \tag{3.13}$$

This reduced-dimension energy potential is shown in Figures 3.2(b, d, f) beside the 3-D energy potential (3.11). Minimization of (3.13) yields the ϕ orientation of the energy wells. Since K_4 and K_4' always contribute together and in nearly the same proportion, we neglect K_4' as was done in the anhysteretic model of Restorff et al. [86].

Gibbs energy (3.13) was derived for single crystals under uniaxial compression. However, it is also appropriate for highly textured polycrystals having negligible grain misalignment. Consider for example a grain with a five degree misalignment of the [001] direction with the axis of a rod subjected to a compressive stress T along the axis (z-direction). The stress state in the rod reference frame would be

$[T_x, T_y, T_z, T_{xy}, T_{yz}, T_{zx}] = T[0, 0, 1, 0, 0, 0]$ while the stress state in the grain reference frame would be $T[0.001523, 0, 0.999999, 0, 0, 0.001523]$ which is approximately uniaxial. To accommodate lower grade polycrystals having appreciable grain misalignment, the tensorial stress-induced anisotropy energy (3.10) would need to be used along with a homogenization technique like that of Appino, Valsania, and Basso [4] to characterize the distribution of grain orientations.

Local magnetization

The orientation of a single magnetic moment is determined by two conditions, $\partial G/\partial\phi = 0$ and $\partial^2 G/\partial\phi^2 > 0$. Application of the first condition to (3.13), followed by factorization gives

$$\begin{aligned} 8K_4\cos^3\phi + 2\left(K_2 - 2K_4 - \frac{3}{2}\lambda_{001}T\right)\cos\phi \\ - \mu_0 M_s H = 0, \end{aligned} \tag{3.14}$$

$$\sin\phi = 0. \tag{3.15}$$

Relation (3.15) coupled with the second condition simply identifies the easy axes in the positive and negative z-directions and their intervals of existence. The positive z-direction is a minimum energy direction on the interval $[2(2K_4+K_2-3/2\lambda_{001}T)/\mu_0 M_s, +\infty)$ and the negative z-direction is a minimum on the interval $(-\infty, -2(2K_4 + K_2 - 3/2\lambda_{001}T)/\mu_0 M_s]$. Magnetic fields outside of the first interval will cause the easy axis in the positive z-direction to become hard and magnetic fields outside of the second interval will cause the easy axis in the negative z-direction to become hard.

Relation (3.14) is a cubic equation in $\cos\phi$ which can be solved analytically with Cardano's method. The three solutions give the ϕ location of the two energy maxima and the energy minimum in Figure 3.2(a). The discriminant in Cardano's method

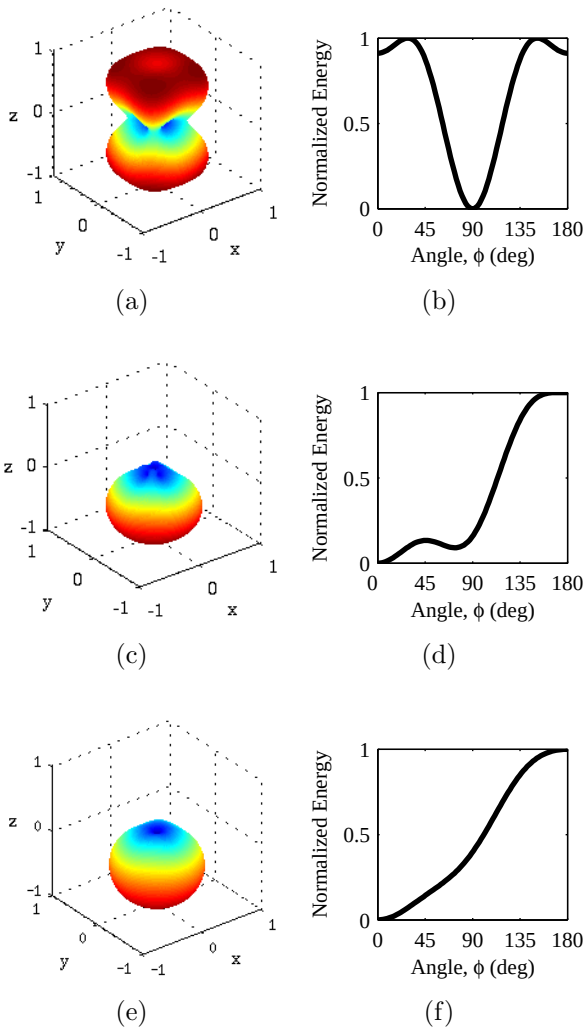

Figure 3.2: Left column: 3-D Gibbs free energy given by (3.11). Right column: Reduced 2-D Gibbs free energy given by (3.13). The rows represent low, medium, and high magnetic fields (top to bottom).

can be used to determine the interval of existence of the energy minimum; this yields a simpler solution than the condition on the second derivative of the Gibbs energy. Setting the discriminant equal to zero yields the interval of existence

$$|H| \leq -16\frac{K_4}{\mu_0 M_s}\left(\frac{2K_4 - K_2 + \frac{3}{2}\lambda_{001}T}{12K_4}\right)^{3/2}. \tag{3.16}$$

The hysteretic, local magnetization in the z-direction (Figure 3.3) is constructed from the relation $\bar{M} = M_s \cos\phi$, in which possible values of ϕ are the solutions to (3.14) and (3.15) with their respective magnetic field intervals of existence. The result is a triple valued hysteron in which the cubic branch that passes through the origin accounts for the low hysteresis and characteristic "S" shape of the $M - H$ major loop of bulk Galfenol. The shallow slope and finite interval of existence of the cubic branch is a manifestation of the rotation of magnetic moments away from the four energy wells in the xy-plane into the direction of the applied magnetic field and the eventual disappearance of these wells.

Local anhysteretic magnetization

At low magnetic field levels and in cases when a compressive stress is applied or stress-annealed Galfenol is used, the energy wells that give rise to the cubic branch of the kernel are much deeper than the wells that give rise to the saturation solutions. As a result, at low magnetic fields most of the magnetic moments will reside in these energy wells and the bulk magnetization will follow the cubic branch of the kernel. The slope of the cubic branch at zero field can be obtained through a linear approximation to (3.14),

$$\bar{M} = \frac{(\mu_0 M_s)^2}{2\left(K_2 - 2K_4 - \frac{3}{2}\lambda_{001}T\right)}H, \tag{3.17}$$

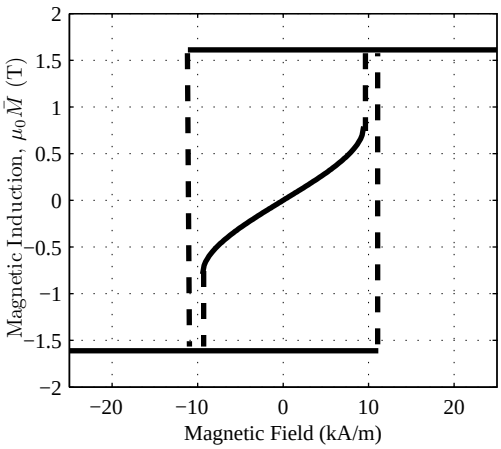

Figure 3.3: Local magnetization hysteron obtained from minimization of the Gibbs free energy.

$$\frac{d\bar{M}}{dH}(H=0) = \frac{(\mu_0 M_s)^2}{2\left(K_2 - 2K_4 - \frac{3}{2}\lambda_{001}T\right)}. \tag{3.18}$$

Under the assumption that the bulk magnetization follows the cubic branch closely at low fields, (3.18) provides a useful measure of the anisotropy since $d\bar{M}/dH(H=0)$, λ_{001}, and $\mu_o M_s$ are all easily measured. This assumption is accurate for sufficiently high compressive stress.

A second measure of the anisotropy is necessary since there are two anisotropy coefficients. As the applied magnetic field is increased or decreased from zero, it reaches a level where the energy well of the saturation solution in the direction of the applied field becomes deeper than the energy wells of the cubic branch. At this point, rapid jumping of magnetic moments occurs from the energy wells of the cubic branch to the energy well of the saturation solution. This situation is evident in the burst region of the magnetization curve. A close approximation of the field level that will initiate the burst region can be found analytically by equating the Gibbs

energy (3.13) evaluated on the saturation solution with the Gibbs energy evaluated on the linear approximation of the cubic branch (3.17). This yields

$$H_B = \frac{2(2K_4 - K_2 + 3/2\lambda_{001}T)}{\mu_0 M_s} \cdot \left(\sqrt{\frac{K_2 - 3/2\lambda_{001}T}{2K_4 - K_2 + 3/2\lambda_{001}T}} - 1 - 1 \right). \tag{3.19}$$

Since the transition into the burst region of the measured magnetization curve is smooth, it is not possible to measure H_B exactly. However, a first approximation of the anisotropy constants can be obtained by assuming that H_B is the start of the linear portion of the burst region (which is observable in data, see Figure 3.4) and then using relations (3.18) and (3.19). This point is more clearly identifiable when either a moderate compressive stress is applied or the material has been stress-annealed.

The anhysteretic curve is generated by forcing all of the magnetic moments to follow the cubic branch of the kernel until the saturation branches become the global minima at fields above H_B or below $-H_B$ (Figure 3.4). This anhysteretic curve does not closely follow actual magnetization curves due to the effects of thermal energy. However, relations (3.18) and (3.19) do provide an approximate measure of the anisotropy coefficients without the need of a least-squares fitting procedure to a full model. Furthermore, these relations could be used in transducer design to select the mechanical pre-stress needed to achieve a prescribed magnetization, and hence magnetostriction, response.

The magnetization kernel also provides insight into the magnetization process. Since the energy wells of the cubic branch shrink continuously with increasing fields until they disappear, it is expected that by the time they disappear, nearly all of the moments have jumped to the saturation branch. Thus, the end point of the

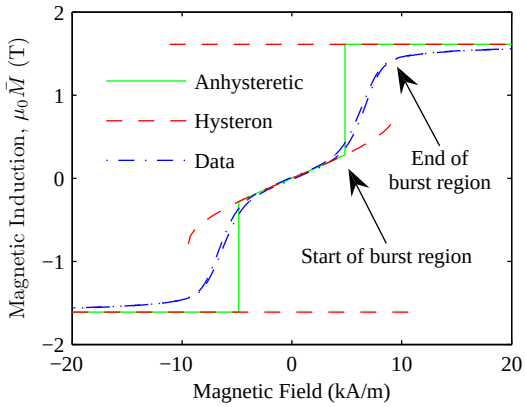

Figure 3.4: Anhysteretic magnetization calculated from the measured magnetization curve of $Fe_{18.4}Ga_{81.6}$. The following values were observed from the data using (3.18) and (3.19): $K_4 = -8.0\,\mathrm{kJ/m^3}$, $K_2 = -0.10\,\mathrm{kJ/m^3}$, $\mu_o M_s = 1.61\,\mathrm{T}$ and $(3/2)\lambda_{001} = 260\,\mu\mathrm{strain}$.

cubic branch can be interpreted as the end of the burst region. Figure 3.4 shows the theoretical anhysteretic curve and kernel along with Galfenol data. The material is unannealed $Fe_{81.6}Ga_{18.4}$ subjected to a constant compressive stress of 27.6 MPa. The anisotropy constants were approximated using (3.18) and (3.19).

Thermal energy

As proposed by Néel [72], thermal energy causes precession of magnetic moments about local energy minima and jumping between energy wells. Following the approach of Smith et al. [92], we assume that the magnetic moments follow a Boltzmann distribution within each energy well and that Boltzmann statistics quantify the likelihood that moments overcome the barrier between adjacent wells. Since jumping between the four energy wells in the xy-plane and precession in the θ coordinate have little

effect on the magnetization or strain in the z-direction, we neglect these effects and continue using the reduced-dimension Gibbs energy (3.13).

The expected value of magnetization in the z-direction of moments residing in each of the energy wells can be calculated from the assumed Boltzmann distribution (with $k\theta/V$ the ratio of Boltzmann constant, temperature, and effective moment volume) [92],

$$\begin{aligned}
\langle \bar{M} \rangle_+ &= \frac{\int_{M_0}^{1} \mu_0 M_s \bar{M}_r e^{-G(\bar{M}_r,T,H)V/k\theta} d\bar{M}_r}{\int_{M_0}^{1} e^{-G(\bar{M}_r,T,H)V/k\theta} d\bar{M}_r}, \\
\langle \bar{M} \rangle_c &= \frac{\int_{-M_0}^{M_0} \mu_0 M_s \bar{M}_r e^{-G(\bar{M}_r,T,H)V/k\theta} d\bar{M}_r}{\int_{-M_0}^{M_0} e^{-G(\bar{M}_r,T,H)V/k\theta} d\bar{M}_r}, \\
\langle \bar{M} \rangle_- &= \frac{\int_{-1}^{-M_0} \mu_0 M_s \bar{M}_r e^{-G(\bar{M}_r,T,H)V/k\theta} d\bar{M}_r}{\int_{-1}^{-M_0} e^{-G(\bar{M}_r,T,H)V/k\theta} d\bar{M}_r}.
\end{aligned} \tag{3.20}$$

Here, $\langle \bar{M} \rangle_+$, $\langle \bar{M} \rangle_c$ and $\langle \bar{M} \rangle_-$ are the expected values of magnetization of moments residing in the energy wells associated with the positive saturation branch, the cubic branch, and the negative saturation branch of the kernel, respectively. The integration limit $M_0 = \cos\phi_0$ is the location of the energy hump that separates the energy wells and $\bar{M}_r = \cos\phi$ is the relative magnetization in the z-direction (Figure 3.5).

To calculate the bulk magnetization, both the volume fraction of moments residing in each energy well and the expected values of magnetization for each energy well are needed. This requires knowledge of the initial distribution and the rates at which moments jump between energy wells. When a magnetic moment is excited to the inflection point in the Helmholtz free energy, it has enough energy to jump to the adjacent energy well [28]. The probabilities $p_{i,j}$ of a magnetic moment jumping from

an initial energy well i ($i = +, c, -$) to a destination well j ($j = +, c, -$) are [92]

$$\begin{aligned}
p_{+,c} &= \frac{1}{\tau}\frac{\int_{M_{I,1}-\epsilon}^{M_{I,1}} e^{-G(\bar{M}_r,T,H)V/k\theta} d\bar{M}_r}{\int_{M_{I,1}-\epsilon}^{1} e^{-G(\bar{M}_r,T,H)V/k\theta} d\bar{M}_r}, \\
p_{c,+} &= \frac{1}{\tau}\frac{\int_{M_{I,2}}^{M_{I,2}+\epsilon} e^{-G(\bar{M}_r,T,H)V/k\theta} d\bar{M}_r}{\int_{0}^{M_{I,2}+\epsilon} e^{-G(\bar{M}_r,T,H)V/k\theta} d\bar{M}_r}, \\
p_{c,-} &= \frac{1}{\tau}\frac{\int_{-M_{I,2}-\epsilon}^{-M_{I,2}} e^{-G(\bar{M}_r,T,H)V/k\theta} d\bar{M}_r}{\int_{M_{I,2}}^{0} e^{-G(\bar{M}_r,T,H)V/k\theta} d\bar{M}_r}, \\
p_{-,c} &= \frac{1}{\tau}\frac{\int_{-M_{I,1}}^{-M_{I,1}+\epsilon} e^{-G(\bar{M}_r,T,H)V/k\theta} d\bar{M}_r}{\int_{-1}^{-M_{I,1}+\epsilon} e^{-G(\bar{M}_r,T,H)V/k\theta} d\bar{M}_r}.
\end{aligned} \tag{3.21}$$

The proportionality constant $1/\tau$ is the frequency at which moments attempt to jump, with τ the thermal relaxation time constant. The integral bounds $M_{I,1}$ and $M_{I,2}$ are the inflection points on either side of the energy humps in the Helmholtz free energy (Figure 3.5) which may be found as the positive roots of the second derivative of the Gibbs energy (3.13) under zero field. The parameter ϵ is the width of a small interval of relative magnetization which includes the inflection point in the Helmholtz energy. Because ϵ has to be small compared to the width of the energy wells, the integrals in the numerators of (3.21) can be evaluated using right endpoint numerical integration,

$$\int_{M_{I,1}-\epsilon}^{M_{I,1}} e^{-G(\bar{M}_r,T,H)V/k\theta} d\bar{M}_r \approx \epsilon\, e^{-G(M_{I,1},T,H)V/k\theta}. \tag{3.22}$$

This approximation allows us to define a time constant ratio, $\bar{\tau}_i = \tau/\epsilon_i$, $i = 1, 2$, in which index i is 1 for the positive and negative energy wells and 2 for the cubic energy well. The unit of measure for $\bar{\tau}_i$ is seconds because ϵ_i is unit-less. The time constant ratio is treated as a parameter to be identified from experimental data. Assuming a typical time constant $\tau = 1 \times 10^{-9}$ seconds, the integration intervals are calculated to vary between 5.3×10^{-9} and 2.5×10^{-10} depending on stress, annealing, and which energy well is considered (Tables 3.2 and 3.3). These values are sufficiently small

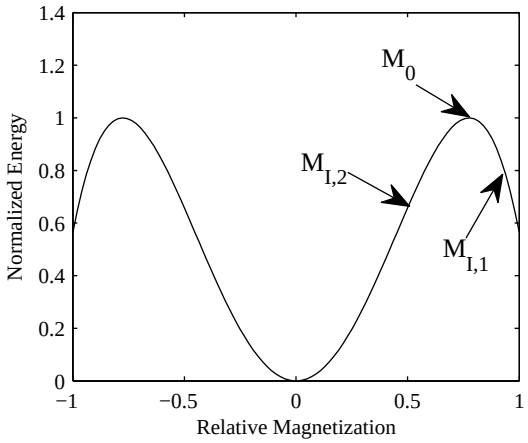

Figure 3.5: Two-dimensional representation of the Helmholtz free energy.

relative to the width of the positive, negative, and cubic energy wells, which have the relative magnetization values of 0.3172 $(1 - M_0)$, 0.3172 $(-M_0 + 1)$, and 1.3656 $(2 \cdot M_0)$, respectively.

With the jumping probabilities (3.21), the evolution of the moment volume fraction in each energy well, X_i $(i = +, c, -)$, can be expressed as

$$\begin{aligned} \dot{X}_+ &= -p_{+,c}X_+ + p_{c,+}X_c, \\ \dot{X}_c &= p_{+,c}X_+ - (p_{c,+} + p_{c,-})X_c + p_{-,c}X_-, \\ \dot{X}_- &= p_{c,-}X_c - p_{-,c}X_-. \end{aligned} \tag{3.23}$$

Implicit in model equations (3.20)-(3.23) is the assumption that the rate at which thermal equilibrium is achieved within each energy well is much faster than the rate at which moments jump between wells. This justifies the local use of the Boltzmann probability in (3.20)-(3.21) which is derived assuming thermal equilibrium (see pp. 104-108 of [90] for details). Analogous kinetic models have been used to characterize the quasi-static behavior of piezoelectric and shape-memory materials [95, 89]. The

bulk magnetization can now be obtained by integrating (3.23) and summing the products of the volume fractions and their respective expected value of magnetization,

$$M = \langle \hat{M} \rangle_{+} X_{+} + \langle \hat{M} \rangle_{c} X_{c} + \langle \hat{M} \rangle_{-} X_{-}. \tag{3.24}$$

Equations (3.23) and (3.24) can be assembled in state-space form to yield a linear, time-variant system of the form

$$\begin{aligned} \dot{\mathbf{X}} &= \mathbf{A}(t)\mathbf{X}, \\ M &= \mathbf{C}_M(t)\mathbf{X}, \end{aligned} \tag{3.25}$$

where $\mathbf{X}$ is the vector of volume fractions, $\mathbf{A}(t)$ is the matrix of field dependent jumping probabilities, and $\mathbf{C}_M(t)$ is the vector of field dependent expected values of magnetization. System (3.25) depends only on the input magnetic field, applied stress, and the six material constants in Table 3.1.

The thermal quantity $k\theta/V$ is interpreted as the thermal energy per volume, where the volume is that of a single rotational element. This volume changes with field and varies throughout the material because three distinct rotations take place: coherent rotation of moments (domain rotation), incoherent rotation of moments within domains (moment precession), and rotation of single moments at domain walls (domain wall motion). Domain rotation occurs in the high permeability burst region, moment precession at all field levels, and domain wall motion mainly in the low field region [49]. To preserve the low order of the model we do not attempt to characterize the domain configuration and hence use a constant volume which is determined through a least squares fit to the data ($V = 8.09 \times 10^{-24}$ m^3, or the volume of a sphere with radius 12 nm).

While the hysteron described by relations (3.14) and (3.15) and shown in Figure 3.3 does not appear explicitly in the model (3.25), the model converges to the hysteron

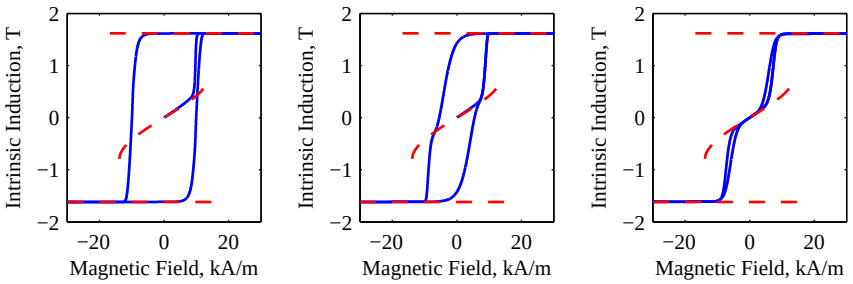

Figure 3.6: Bulk magnetization model (3.25) calculated for the cases: (a) low thermal energy, (b) medium thermal energy, and (c) high thermal energy compared to the local hysteron described by relations (3.14) and (3.15).

as the thermal energy decreases, i.e., as the quantity $k\theta/V$ decreases. This was shown in [92] for a double well potential and is illustrated in Figure 3.6 for the triple well potential (3.13).

Table 3.1: Model Parameters

K_4	Anisotropy coefficient
K_2	Anisotropy coefficient
$3/2\lambda_{001}$	Saturation magnetostriction
$\mu_0 M_s$	Saturation magnetic flux density (intrinsic)
$k\theta/V$	Boltzmann constant, temperature, effective volume
$\bar{\tau}_1$	Time constant ratio for the positive and negative wells
$\bar{\tau}_2$	Time constant ratio for the cubic well

Magnetostriction model

Kellogg et al. [57] experimentally quantified the nonlinear relationship between the magnetostriction and the square of the magnetization, concluding that the magnetization process does not occur solely from 90° moment rotation. Since this agrees with the magnetization model developed in Section 3.2.1, we follow the same approach for the magnetostriction model. Probabilities (3.21) remain unchanged. We simply need to calculate the expected value of the strain contribution of moments residing in each energy well and sum their product with the volume fractions calculated from integration of (3.23). With cubic crystal symmetry the relationship between the magnetization and magnetostriction under axially applied stresses and negligible thermal activation is $\bar{S} = (3/2)lambda_{001}\cos^2\phi$ [61]. The effect of thermal energy is quantified as in Section 3.2.1 by classical Boltzmann statistics. The expected values of the magnetostriction thus are

$$\begin{aligned}
\langle \bar{S} \rangle_+ &= \frac{\int_{M_0}^{1} \frac{3}{2}\lambda_{001}\bar{M}_r^2 e^{-G(\bar{M}_r,T,H)V/k\theta} d\bar{M}_r}{\int_{M_0}^{1} e^{-G(\bar{M}_r,T,H)V/k\theta} d\bar{M}_r}, \\
\langle \bar{S} \rangle_c &= \frac{\int_{-M_0}^{M_0} \frac{3}{2}\lambda_{001}\bar{M}_r^2 e^{-G(\bar{M}_r,T,H)V/k\theta} d\bar{M}_r}{\int_{-M_o}^{M_o} e^{-G(\bar{M}_r,T,H)V/k\theta} d\bar{M}_r}, \\
\langle \bar{S} \rangle_- &= \frac{\int_{-1}^{-M_0} \frac{3}{2}\lambda_{001}\bar{M}_r^2 e^{-G(\bar{M}_r,T,H)V/k\theta} d\bar{M}_r}{\int_{-1}^{-M_0} e^{-G(\bar{M}_r,T,H)V/k\theta} d\bar{M}_r}.
\end{aligned} \tag{3.26}$$

These are assembled into the output vector $\mathbf{C_S}(t)$ to yield a state-space magnetostriction model of the same form as (3.25),

$$\begin{aligned}
\dot{\mathbf{X}} &= \mathbf{A}(t)\mathbf{X}, \\
S &= \mathbf{C}_S(t)\mathbf{X}.
\end{aligned} \tag{3.27}$$

This system also depends only on the input field, applied bias stress, and the material parameters in Table 3.1.

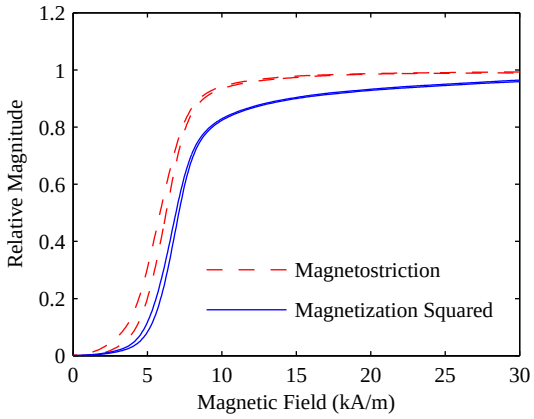

Figure 3.7: High field measurement of $Fe_{81.6}Ga_{18.4}$ with 27.6 MPa pre-load.

Bulk anhysteretic model

The anhysteretic magnetization and magnetostriction are given by the steady-state solution to systems (3.25) and (3.27),

$$M_{an} = \mathbf{C}_M \mathbf{X}_{ss},$$

$$S_{an} = \mathbf{C}_S \mathbf{X}_{ss}.$$

The components of the steady state vector $\mathbf{X}_{ss}$ are calculated from $\mathbf{A}(t)\mathbf{X} = \mathbf{0}$ and the conservation relation $X_+ + X_c + X_- = 1$,

$$\begin{aligned}
X_{+,ss} &= \frac{p_{c,+}\left(p_{-,c} + p_{c,-}\right) - p_{c,+}p_{c,-}}{\left(p_{+,c} + p_{c,+}\right)\left(p_{-,c} + p_{c,-}\right) - p_{c,+}p_{c,-}}, \\
X_{-,ss} &= \frac{p_{c,-}\left(p_{+,c} + p_{c,+}\right) - p_{c,+}p_{c,-}}{\left(p_{+,c} + p_{c,+}\right)\left(p_{-,c} + p_{c,-}\right) - p_{c,+}p_{c,-}}, \\
X_{c,ss} &= 1 - X_{+,ss} - X_{-,ss}.
\end{aligned}$$

The steady-state anhysteretic model may be used to quantify the magnetostriction and magnetization of materials with small τ and in cases when the input magnetic field varies slowly. Figure 3.8 illustrates the convergence of the hysteretic model to

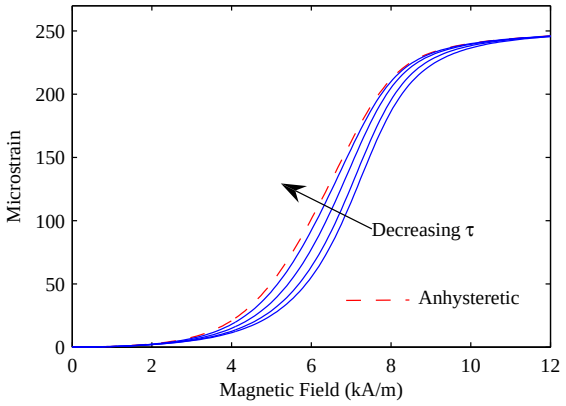

(a)

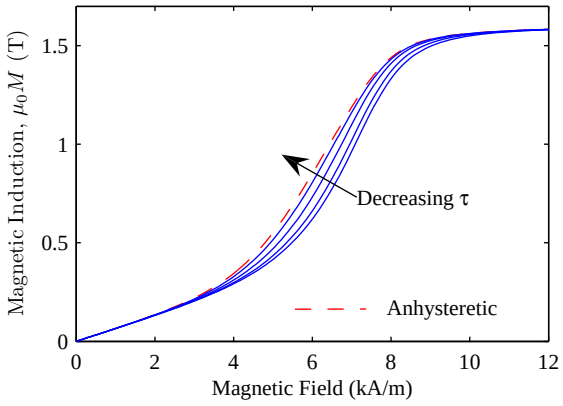

(b)

Figure 3.8: (a) Magnetostriction model and (b) magnetization model for decreasing time constant τ including the anhysteretic steady-state model.

the anhysteretic model as τ is decreased. As τ is decreased, the delay decreases and so does the hysteresis.

High stress or stress annealing

When the pre-stress or the uniaxial anisotropy constant K_2 exceed a critical value, the Helmholtz energy becomes a single-well potential. In this case all of the moments

reside in the same well and there is no hysteresis due to anisotropy. This situation occurs when the unstable equilibrium M_0 of the Helmholtz free energy (see Figure 3.5) is greater than unity. The level of stress or uniaxial anisotropy that produces $M_0 = 1$ can be found by expressing M_0 explicitly from $d\psi/d\phi = 0$, setting it equal to unity, and solving for T or K_2. This gives

$$T = \frac{2}{3\lambda_{001}} 2K_4 + K_2,$$

$$K_2 = \frac{3}{2}\lambda_{001} T - 2K_4.$$

With a single-well Helmholtz potential there are no moment jumping effects due to thermal energy. However, thermal energy does create a Boltzmann distribution of moments within the well. Thus, for a single-well potential, the magnetization and magnetostriction can be modeled as

$$M = \frac{\int_{-1}^{1} \mu_0 M_s \bar{M}_r e^{-G(\bar{M}_r,T,H)V/k\theta} d\bar{M}_r}{\int_{-1}^{1} e^{-G(\bar{M}_r,T,H)V/k\theta} d\bar{M}_r}, \tag{3.28}$$

$$S = \frac{\int_{-1}^{1} \frac{3}{2}\lambda_{001} \bar{M}_r^2 e^{-G(\bar{M}_r,T,H)V/k\theta} d\bar{M}_r}{\int_{-1}^{1} e^{-G(\bar{M}_r,T,H)V/k\theta} d\bar{M}_r}. \tag{3.29}$$

3.2.2 Comparison with experimental data

The model is compared to major loop measurements of both unannealed and annealed $Fe_{81.6}Ga_{18.4}$. The samples are research-grade highly textured polycrystals from Etrema Products Inc. which have a large fraction of the crystallites with the [001] direction oriented within five degrees of the rod axis. Galfenol manufactured in this fashion exhibits cubic anisotropy when unannealed and tetragonal anisotropy when annealed [86]. The measurements were performed in a closed magnetic circuit with ramp current inputs to a solenoid that take 40 seconds to go from the positive

saturation to negative saturation. Because of the nonlinear nature of the magnetic circuit, the applied magnetic field was not a perfect ramp. However, perfect ramp inputs were used in the model. Because the tests were quasi-static, the shape of the major loop is not affected by the shape of the input field provided it is monotonic as it increases to positive saturation and monotonic as it decreases to negative saturation.

To evaluate the accuracy of the model and its sensitivity to operating conditions, we optimized the model parameters with a least-squares algorithm for four different cases, each with a different level of compressive stress (Tables 3.2 and 3.3) for both unannealed and annealed material. The parameters $\mu_0 M_s$ and $3/2\lambda_{001}$ were measured directly as 1.62 T and 260 μstrain, respectively. Initial values for the anisotropy constants were estimated from the M-H curve as described in Section 3.2.1. For the magnetostriction measurements, the zero-field magnetostriction is defined as zero for each curve. Zero magnetostriction for model equation (3.27) is the 90^o moment orientation which is only achieved at high stress levels. Hence, to compare the model to measurements, the zero-field magnetostriction must be subtracted from the model.

The objective function of the optimization algorithm was the sum of the square of the errors in the magnetostriction at each data point. The magnetostriction was used partly because of the difference in the magnetostriction and magnetization-squared behavior shown in Figure 3.7 and because the magnetostriction is of greater interest for transducer design. If the magnetostriction were due solely to domain rotation and domain rotation were the only magnetization process, the magnetostriction vs. field and magnetization-squared vs. field would be nearly identical when plotted as a relative magnitude. Since they are not, there are unmodeled effects present such as domain wall motion and material defects.

Table 3.2: Parameter optimization for unannealed $Fe_{81.6}Ga_{18.4}$ at four stress levels

Case	**1**	**2**	**3**	**4**
T MPa	**−1.38**	**−13.9**	**−27.6**	**−41.4**
K_4 kJ/m^3	−6.44	−6.64	−6.89	−9.37
K_2 kJ/m^3	−1.23	−0.455	0.182	−0.173
$k\theta/V$ kJ/m^3	0.552	0.519	0.404	0.458
$\bar{\tau}_1$ sec	0.918	1.69	1.90	1.53
$\bar{\tau}_2$ sec	0.190	0.349	0.392	0.317
Maximum % error	1.2	1.2	0.70	0.96

Table 3.3: Parameter optimization for annealed $Fe_{81.6}Ga_{18.4}$ at four stress levels

Case	**1**	**2**	**3**	**4**
T MPa	**−1.38**	**−13.9**	**−27.6**	**−41.4**
K_4 kJ/m^3	−8.29	−10.0	−1.26	−9.07
K_2 kJ/m^3	15.6	15.6	15.8	13.8
$k\theta/V$ kJ/m^3	0.878	0.994	1.09	0.956
$\bar{\tau}_1$ sec	4.07	4.35	3.95	NA
$\bar{\tau}_2$ sec	0.841	0.898	0.815	NA
Maximum % error	0.64	0.85	0.85	1.7

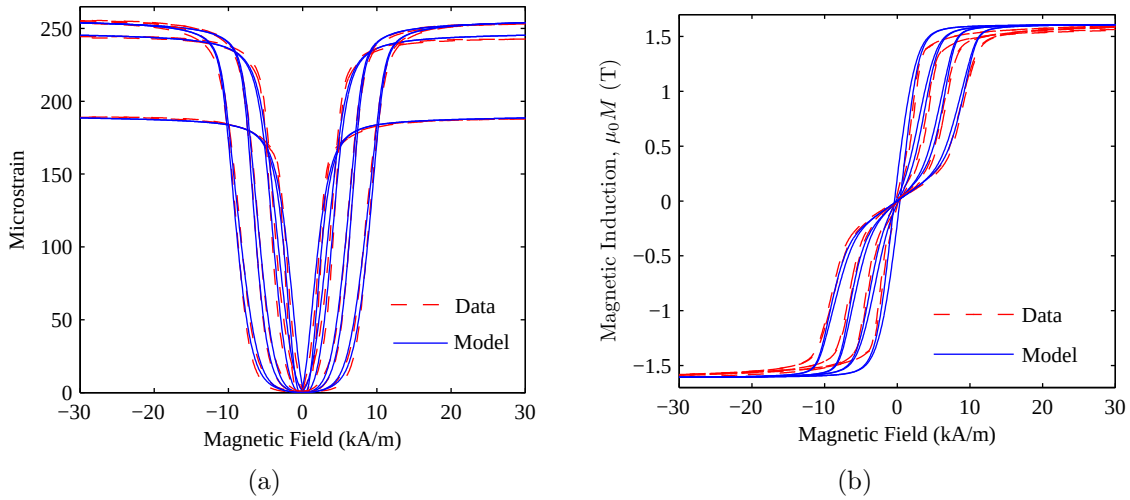

(a) (b)

Figure 3.9: Comparison of model with experimental data of unannealed $Fe_{81.6}Ga_{18.4}$ with stresses of $-1.38, -13.9, -27.6$, and -41.4 MPa. Each model curve was generated with parameters obtained through minimization of the error with the respective curve.

Because of our choice of objective function, the error in the magnetostriction (Figure 3.9(a)) is smaller than the error in the magnetization (Figure 3.9(b)). Tables 3.2 and 3.3 show the parameters optimized for each stress case and some amount of variability in the parameters is noted. While clear trends in the parameters with respect to stress are not evident, the errors are larger for the unannealed, low-stress cases 1 and 2. This may be attributed to domain wall motion being a more significant magnetization process when stress is low in unannealed material. Both stress and annealing tend to align magnetic moments perpendicular to the rod; rotation then becomes the dominant process as moments rotate into the direction along the rod in response to an applied field.

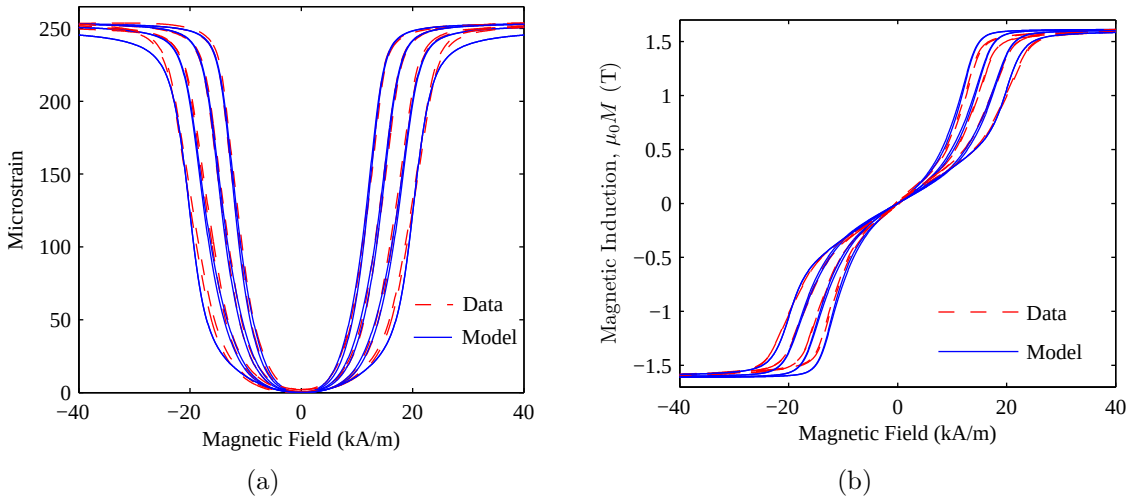

Figure 3.10: Comparison of model with experimental data of annealed $Fe_{81.6}Ga_{18.4}$ with stresses of $-1.38, -13.9, -27.6$, and -41.4 MPa. Each model curve was generated with parameters obtained through minimization of the error with the respective curve.

The model accurately quantifies both the shape and the small amount of hysteresis present in the data. Figure 3.9(a) shows that the thermal energy formulation in Section 3.2.1 describes the ability of a compressive stress to encourage 90° initial moment orientations. The model also describes the decrease in hysteresis to near non-existence due to annealing and applied stress (Figure 3.10). For the fourth stress level (-41.4 MPa), the uniaxial anisotropy and stress were high enough to require use of the constitutive equations for a single-well potential (3.28) and (3.29). Figure 3.11 shows measurements of the annealed material at higher stresses and further illustrates the accuracy of the single-well constitutive model.

The model parameters are related to physical properties of the data. The saturation intrinsic flux density $\mu_0 M_s$ and magnetostriction are simply the intrinsic

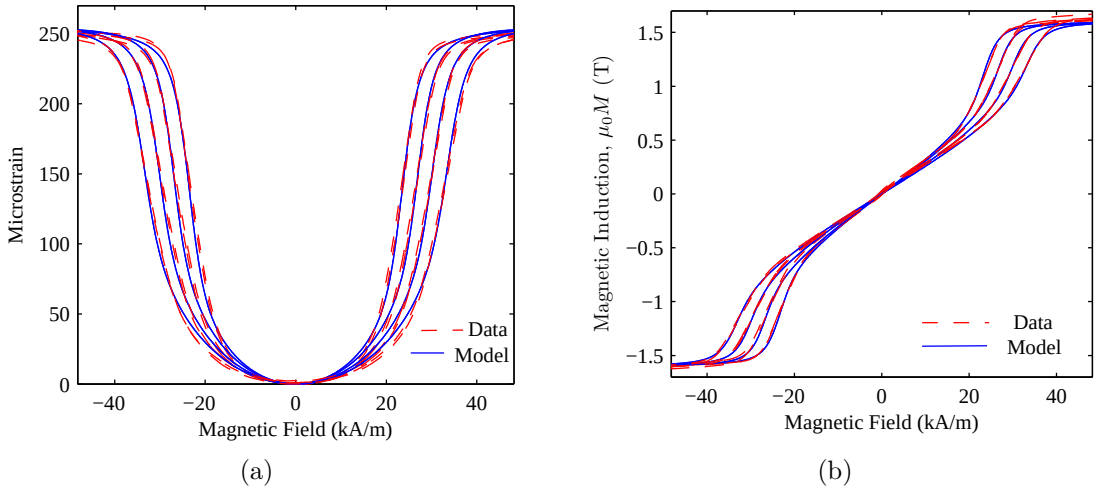

Figure 3.11: Comparison of the single-well model with experimental data of annealed $Fe_{81.6}Ga_{18.4}$ for stresses of $-55.2, -69, -82.7$, and -96.5 MPa. Each model curve was generated with parameters obtained through minimization of the error with the respective curve.

flux density and magnetostriction (when sufficient pre-stress is applied) achieved at high magnetic field. The effect of the anisotropy constants K_2 and K_4 is manifested through relations (3.18) and (3.19) which describe how the low-field slope and the start of the burst region change with stress. This change can be seen in the data (see Figures 3.9(b), 3.10(b), and 3.11(b)) where the low-field slope decreases and the start of the burst region is delayed with increasing stress. The effect of the thermal energy $k_B\theta/V$ is evident in the smooth transitions of the burst region as opposed to sharp jumps as predicted by minimization of the Gibbs energy. Finally, the time constants are related to the amount of hysteresis in the data where less hysteresis implies a smaller time constant.

Figure 3.12 illustrates the performance of the model when the same parameter set is used on the four stress cases; the parameters were optimized for the first and

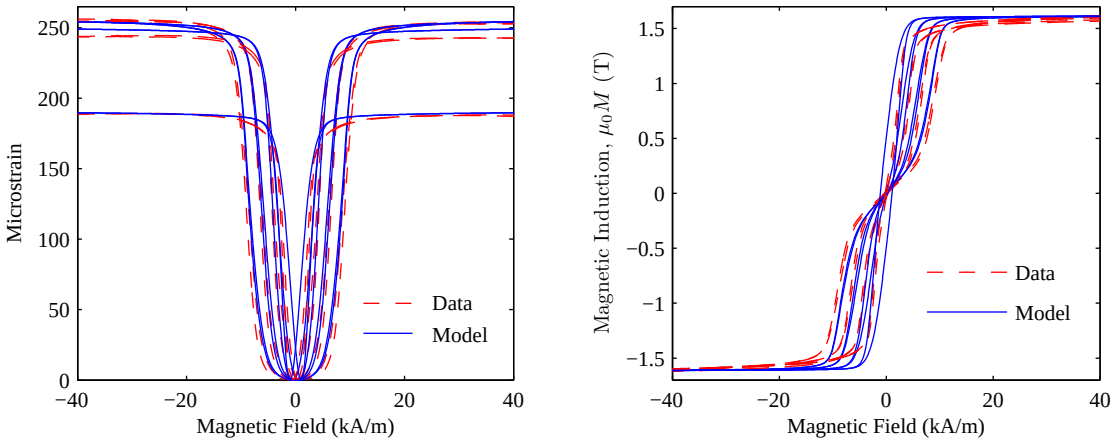

(a) (b)

Figure 3.12: Comparison of model with experimental data of unannealed $Fe_{81.6}Ga_{18.4}$ with stresses of $-1.38, -13.9, -27.6$, and -41.4 MPa. Each model curve was generated with the same set of parameters.

third stress values with the error in the magnetostriction used as the optimization objective function. The maximum percent error was 3.6%, 5.6%, 1.3%, and 1.3% for stress cases 1-4, respectively (compare to Table 3.2.) The error is again larger in cases 1 and 2 where the stress is not large enough to achieve complete alignment of moments perpendicular to the rod axis.

3.2.3 Concluding remarks

A linear, time-variant, state-space constitutive model is presented which quantifies the nonlinear magnetization and magnetostriction of Galfenol alloys. The effects of external magnetic fields, stresses and stress annealing on the magnetization and

magnetostriction of Galfenol are modeled by quantifying the coupling between magnetocrystalline anisotropy, magneto-elastic, Zeeman, and thermal energies. A triple-valued magnetization kernel characterized by a triple-well Gibbs energy potential provides an understanding of both the low permeability and burst regions of the major loop magnetization curve. Boltzmann statistics is used to describe the distribution and rotations of magnetic moments. This provides a physical basis for understanding the key features of the magnetization and magnetostriction loops as well as the ability of a compressive stress to align magnetic moments 90° from the z-axis for maximum magnetostriction. A small amount of hysteresis is naturally present in the model due to anisotropy and which agrees well with experimental measurements. Unaccounted-for effects such as pinning sites are likely to contribute to the magnetic hysteresis as well.

3.3 Efficient model for field-induced magnetization and magnetostriction of Galfenol

Recently, Datta, Atulasimha, and Flatau [31] presented a 3-D, quasi-static transducer model for single-crystal Galfenol in bending which couples Euler-Bernoulli beam theory with the Armstrong model [6] for characterizing magnetomechanical behavior. The 3-D Armstrong model has also been used to model the anhysteretic magnetomechanical behavior of polycrystals [10] and hysteresis of single crystals [7]. The model is a statistical approach in which it is assumed that magnetic moment orientations (ϕ, θ) follow a Boltzmann distribution. Magnetomechanical coupling is incorporated through a stress-induced anisotropy term in the total energy (E) used in the distribution. In the Armstrong model, a bulk quantity is calculated as an energy weighted

integral of the point-wise quantity over all possible domain orientations,

$$\bar{Q} = \frac{\int_0^{\pi} \int_0^{2\pi} Q(\phi,\theta) e^{-E(\phi,\theta)/\Omega} d\theta d\phi}{\int_0^{\pi} \int_0^{2\pi} e^{-E(\phi,\theta)/\Omega} d\theta d\phi}. \tag{3.30}$$

The weighted average (3.30) serves to smooth the sharp transitions obtained by direct minimization of the total energy.

To characterize, design, and control general Galfenol devices with 3-D functionality it is necessary to quantify the effects of domain wall motion, material texture, hysteresis, and transducer geometry. Extending the Armstrong model (3.30) to include these effects comes at great computational expense, hence limiting the utility of the resulting model. For example, to include irreversible domain wall motion Atulasimha, Akrhas, and Flatau [7] approximate the double integral in (3.30) with a summation of ninety-eight point evaluations, which leads to ninety-eight ordinary differential equations to be solved. Armstrong's approach to including irreversible domain wall motion is less computationally intensive as it only considers eight domain orientations corresponding to the eight easy crystal directions or internal energy minima in Terfenol-D [5]. However, the approach is accurate only when the applied field or stress is aligned with an easy crystal axis, since the easy crystal directions do not rotate.

Extending (3.30) to include texture effects (neglecting grain boundary interactions) can be done through a summation of double integrals [10]. To solve the boundary-value problem of general Galfenol transducers it is necessary to couple Maxwell's equations with momentum conservation equations through a constitutive model relating magnetization and strain to stress and magnetic field. This system of partial differential equations must be discretized for numerical solution and the

constitutive model evaluated at each node. A computationally efficient constitutive model is thus highly desirable.

In this work we present an efficient, 3-D constitutive model describing magnetization and strain as a function of applied magnetic field and stress. Owing to its computational efficiency, the model is ideal for design and control of cubic magnetostrictive devices. The model provides greater accuracy than Armstrong's hysteresis model [5], while avoiding the computational expense of the approach presented by Atulasimha et al. [7] by employing thermodynamic principles. Rather than discretize (3.30) with a large number of fixed orientations, we directly minimize the enthalpy in order to find the stress and magnetic field dependent local minima. Since the empirical smoothing operator (3.30) most heavily weights the enthalpy minima, good accuracy is achieved using only six orientations which rotate with stress and field.

3.3.1 Model development

Ferromagnetic materials are composed of regions of uniform magnetization M_s called domains [61]. In the Stoner-Wohlfarth (S-W) approximation used here and in other magnetomechanical models [54], the material is modeled as a collection of non-interacting, single-domain particles [65]. The internal energy of a particle is due to magnetocrystalline anisotropy which, for body-centered cubic materials such as Galfenol, makes domains align in the $\langle 100 \rangle$ and $\langle 111 \rangle$ directions in the absence of field and stress. Work is required to rotate domains away from these easy directions. Gallium content affects the anisotropy energy and hence which directions are easy. Measurements of Galfenol's anisotropy [83] indicate that for Galfenol having less than 20 at.% Ga, the $\langle 100 \rangle$ directions are easy. As magnetic fields $\mathbf{H}$ and stresses $\mathbf{T}$ are

applied, domains rotate towards the field direction and perpendicular to the principal stress directions. When magnetic domains rotate, the magnetomechanical coupling induces lattice strain and bulk magnetostriction. For a material composed of a collection of S-W particles in thermodynamic equilibrium having r possible orientations, the bulk magnetization $\mathbf{M}$ and strain $\mathbf{S}$ due to magnetostriction are the sum of the magnetization $M_s\hat{\mathbf{m}}^k$ and magnetostriction $\hat{\mathbf{S}}_m^k$ due to each orientation, weighted by the volume fraction $\hat{\xi}^k$ of particles in each orientation

$$\mathbf{M} = M_s \sum_{k=1}^{r} \hat{\xi}^k \hat{\mathbf{m}}^k, \qquad \mathbf{S} = \sum_{k=1}^{r} \hat{\xi}^k \hat{\mathbf{S}}_m^k. \tag{3.31}$$

The equilibrium orientations and magnetostrictions are found from the enthalpy of a single S-W particle and the equilibrium volume fractions are calculated with the empirical smoothing function (3.30).

Equilibrium orientations

The energy formulation here pertains to non-interacting, single-domain particles in accordance with the Stoner-Wohlfarth model for magnetization [65]. The material is assumed to be well below the Curie temperature so that the thermal energy may be neglected. The internal energy of a particle with orientation $\mathbf{m} = [m_1 \quad m_2 \quad m_3]$ is due to the magnetocrystalline anisotropy energy, which can be expressed as a series expansion [61]. After considering the cubic crystal symmetry and neglecting higher order terms, the internal energy with natural dependence on magnetization is

$$U(\mathbf{m}) = K_4 \left(m_1 m_2 + m_2 m_3 + m_3 m_1 \right), \tag{3.32}$$

where K_4 is the fourth-order, cubic anisotropy coefficient. The enthalpy is

$$\mathcal{H}(\mathbf{H}, \mathbf{T}) = U(\mathbf{m}) - \mathbf{S}_m \cdot \mathbf{T} - \mu_0 M_s \mathbf{m} \cdot \mathbf{H}. \tag{3.33}$$

Here, $\mathbf{T}$ is the six-element stress vector in which the first three components the longitudinal stresses and the last three the shear stresses. The magnetostriction $\mathbf{S}_m = \mathbf{S}_m(\mathbf{m})$ has longitudinal components

$$S_{m,i} = \frac{3}{2}\lambda_{100} m_i^2, \quad i = 1, 2, 3 \tag{3.34}$$

and shear components

$$\begin{aligned} S_{m,4} &= 3\lambda_{111} m_1 m_2, \\ S_{m,5} &= 3\lambda_{111} m_2 m_3, \\ S_{m,6} &= 3\lambda_{111} m_3 m_1. \end{aligned} \tag{3.35}$$

These expressions are derived by balancing the elastic and magneto-elastic coupling energies [61].

For $K_4 > 0$, the internal energy has six minima or easy axes ($r = 6$) in the $\langle 100 \rangle$ directions and for $K_4 < 0$, the internal energy has eight minima or easy axes ($r = 8$) in the $\langle 111 \rangle$ directions. Applied magnetic and magnetomechanical work rotates particles away from the easy axes towards the magnetic field direction and perpendicular to the principal stress directions (see Figure 3.13). The equilibrium orientations ($\hat{\mathbf{m}}^k; k = 1, ..., r$), needed for calculation of the bulk magnetization (4.44), are obtained through the conditions $\partial \mathcal{H} / \partial m_i = 0$ constrained to a unit sphere. The equilibrium magnetostrictions ($\hat{\mathbf{S}}_m^k; k = 1, ..., r$), needed for calculation of the bulk strain (4.44) due to magnetostriction, are obtained by evaluating relations (3.34) and (3.35) using the equilibrium orientations, $\hat{\mathbf{S}}_m^k = \mathbf{S}_m(\hat{\mathbf{m}}^k)$.

Numerical calculation of equilibrium orientations

The derivatives of the enthalpy $\partial \mathcal{H} / \partial m_i$ restricted to a unit sphere are nonlinear functions of m_i yielding equations $\partial \mathcal{H} / \partial m_i = 0$ which cannot be solved analytically.

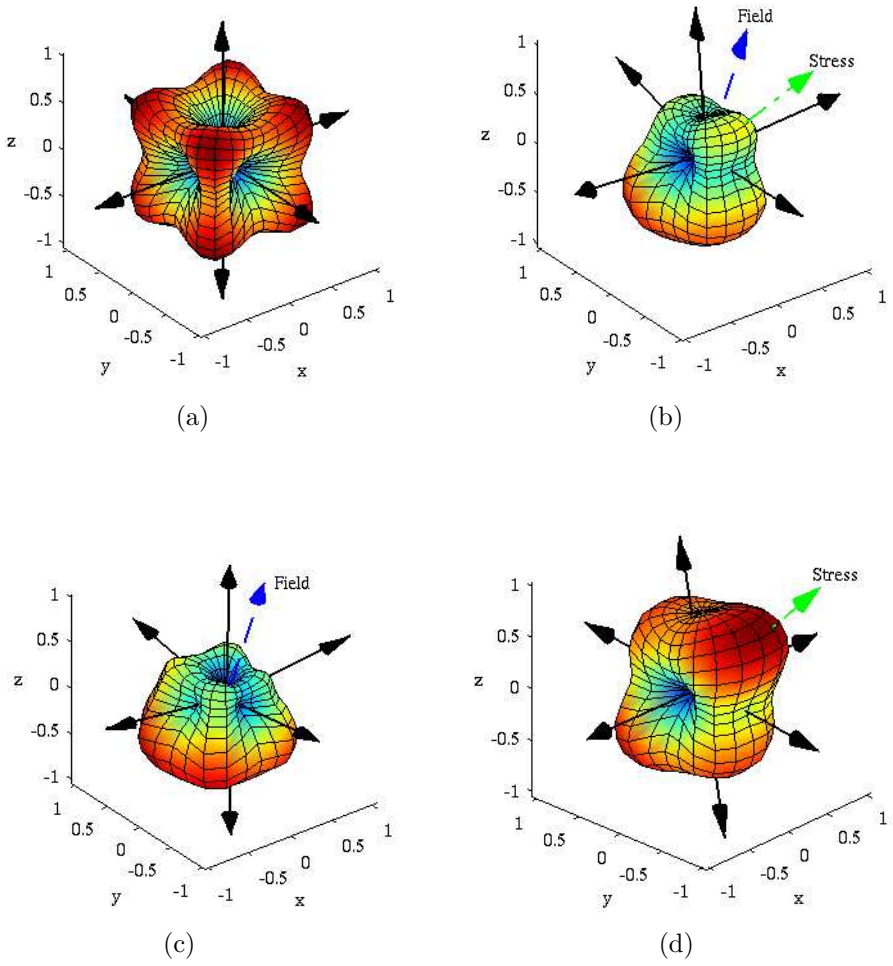

(a) (b) (c) (d)

Figure 3.13: Enthalpy with equilibrium orientations (solid) for (a) no field or stress (b) field (dash) and stress (dash-dot) (c) field only (d) and stress only.

Newton's method may be used for approximating a solution. For example, to calculate

the energy equilibrium near the [001] easy direction (when $K_4 > 0$), the system

$$m_3 = \sqrt{1 - m_1^2 - m_2^2}, \tag{3.36}$$

$$\frac{\partial \mathcal{H}}{\partial m_1} = 0, \tag{3.37}$$

$$\frac{\partial \mathcal{H}}{\partial m_2} = 0, \tag{3.38}$$

is approximately solved by finding the perturbations $\tilde{m}_1$, $\tilde{m}_2$, $\tilde{m}_3$ about the [001] direction from the linearized system

$$m_3 \approx (m_3)_0 + \left(\frac{\partial m_3}{\partial m_1}\right)_0 \tilde{m}_1 + \left(\frac{\partial m_3}{\partial m_2}\right)_0 \tilde{m}_2, \tag{3.39}$$

$$\frac{\partial \mathcal{H}}{\partial m_1} \approx \left(\frac{\partial \mathcal{H}}{\partial m_1}\right)_0 + \left(\frac{\partial^2 \mathcal{H}}{\partial m_1^2}\right)_0 \tilde{m}_1 + \left(\frac{\partial^2 \mathcal{H}}{\partial m_1 m_2}\right)_0 \tilde{m}_2 = 0, \tag{3.40}$$

$$\frac{\partial \mathcal{H}}{\partial m_2} \approx \left(\frac{\partial \mathcal{H}}{\partial m_2}\right)_0 + \left(\frac{\partial^2 \mathcal{H}}{\partial m_1 m_2}\right)_0 \tilde{m}_1 + \left(\frac{\partial^2 \mathcal{H}}{\partial m_2^2}\right)_0 \tilde{m}_2 = 0, \tag{3.41}$$

where the subscript 0 denotes evaluation of the quantity at the linearization point $(m_1)_0$, $(m_2)_0$, $(m_3)_0$ which is initially $(m_1)_0 = (m_2)_0 = 0$, $(m_3)_0 = 1$ for this case. Greater accuracy is achieved by iterating according to Newton's method. Because of the moderate magnetocrystalline anisotropy of Galfenol, the equilibrium direction will remain near the $\langle 100 \rangle$ crystal directions; thus, high accuracy is achieved with few iterations. Figure 3.14 shows the calculated equilibria with no iteration (linear approximation), 1 iteration, and 100 iterations. Excellent accuracy is achieved with only the linear approximation. The error gets larger as the equilibrium gets further away from the easy crystal direction, i.e., at the ends of the magnetization kernel branches. However, the energy also increases, so the global minimum switches before significant error occurs.

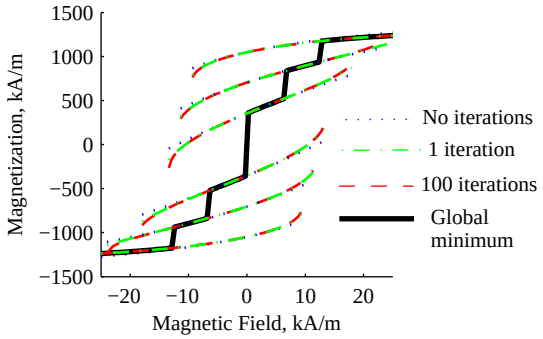

Figure 3.14: Equilibrium domain orientations for field and stress applied in the [132] direction, calculated with 0, 1, and 100 iterations as described in Section 3.3.1.

The volume fractions are calculated as the energy weighted average

$$\hat{\xi}^k = \frac{\exp(-\mathcal{H}^k/\Omega)}{\sum_{j=1}^{r} \exp(-\mathcal{H}^j/\Omega)}, \tag{3.42}$$

where $\mathcal{H}^k$ is the enthalpy of the equilibrium orientation $\mathbf{m}^k$. Substitution of (3.42) into (4.44) gives the bulk magnetization and magnetostriction

$$\mathbf{M} = \frac{\sum_{k=1}^{r} M_s \hat{\mathbf{m}}^k \exp(-\mathcal{H}^k/\Omega)}{\sum_{k=1}^{r} \exp(-\mathcal{H}^k/\Omega)}, \qquad \mathbf{S} = \frac{\sum_{k=1}^{r} \hat{\mathbf{S}}^k \exp(-\mathcal{H}^k/\Omega)}{\sum_{k=1}^{r} \exp(-\mathcal{H}^k\Omega)}. \tag{3.43}$$

The volume fraction ξ^k calculated with (3.42) approaches unity as $\mathcal{H}^k$ becomes much less than all other orientation enthalpies $\mathcal{H}^j$. This property makes (3.43) a good approximation to (3.30) since it considers only orientations which are locally minimum.

Single-crystal, anhysteretic simulation and discussion

Simulations of anhysteretic, single-crystal behavior in the [001] and [011] directions are shown in Figure 3.15 and Figure 3.16, respectively. The ⟨100⟩ directions

are important because Galfenol rods are typically grown with this orientation along the rod axis. The $\langle 110 \rangle$ directions are important because thin films manufactured by electrochemical deposition typically have this orientation [11]. The macroscopic magnetization and magnetostriction were calculated from (3.43) with $r = 6$ which assumes $K_4 > 0$. Because of the crystal symmetry, both application directions have only three distinct contributions to the macroscopic behavior from the six equilibrium domain orientations. For [001] application there are equilibria which remain fixed in the the [001] and $[00\bar{1}]$ directions. They are constant with field because they are parallel with the field. A third contribution comes from domains which are aligned with the [100], $[\bar{1}00]$, [010], and $[0\bar{1}0]$ easy crystal directions in the absence of field and rotate into the direction of the applied field. Application of compressive stress decreases the slope of this contribution and increases its volume fraction. Both of these effects are due to the energy decrease of orientations perpendicular to compressive stress. The volume fraction increase results in a significant increase in macroscopic magnetostriction because more domains go through a full 90^{o} rotation. A kink in the field-magnetization and field-magnetostriction behavior also results as the field eventually pulls all the domains to the [001] direction for positive field and $[00\bar{1}]$ direction for negative field.

The [011] application direction differs from the [001] direction in its saturation behavior and magnetostriction magnitude. The domain orientations which contribute to the positive saturation behavior are the domain families which start in the [010] and [001] easy crystal directions, the easy crystal directions nearest the positive field direction, and rotate into the applied field. The domain orientations which contribute to the negative saturation behavior are the domain families which start in the $[0\bar{1}0]$

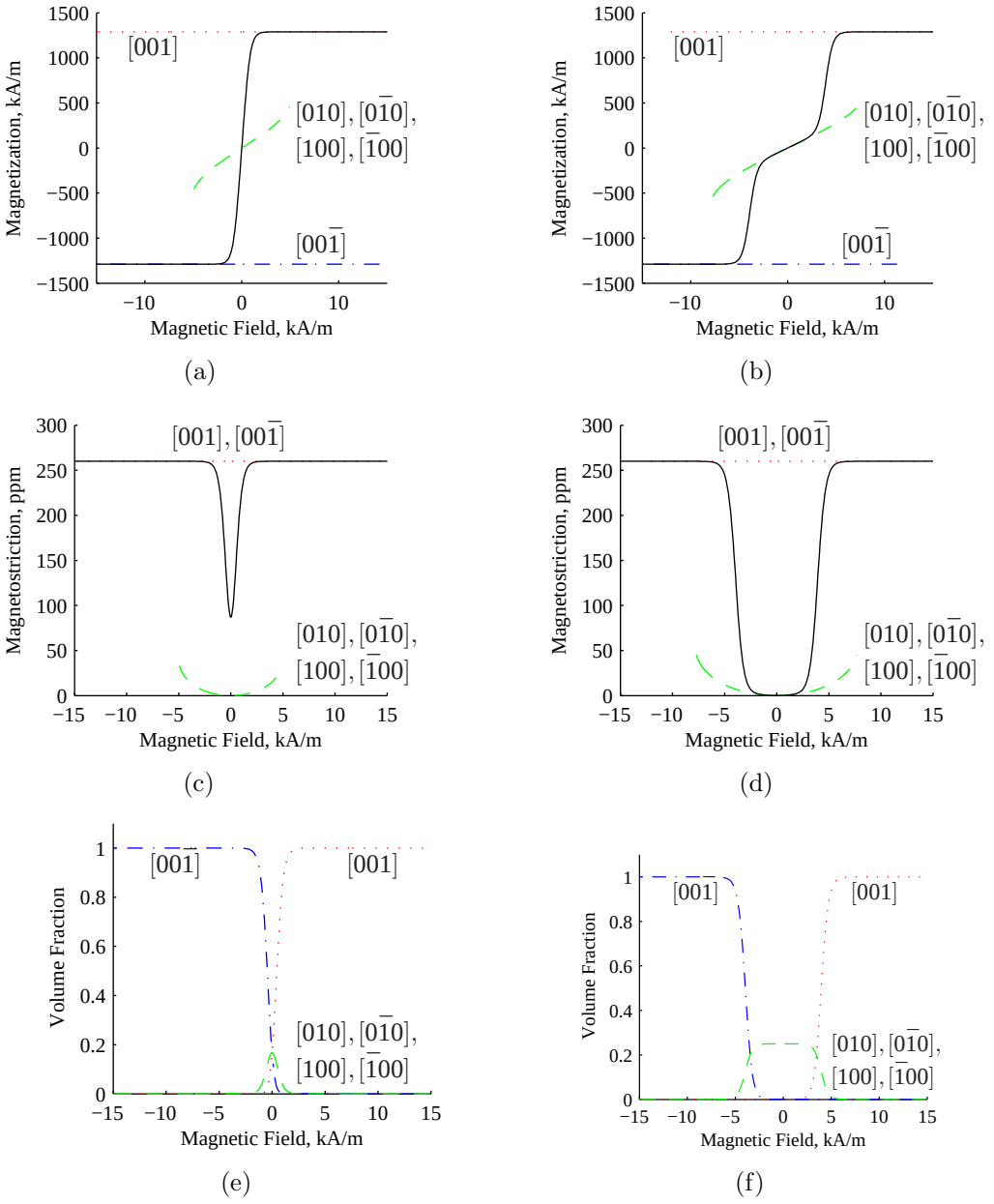

Figure 3.15: Simulation of the (a),(b) magnetization (c),(d) magnetostriction and (e),(f) domain volume fractions for [001] applied field with (a),(c), and (e) no pre-stress and (b), (d), and (f) 30 MPa pre-stress (compression). Solid lines are bulk quantities calculated from (3.43) and dashed/dotted lines correspond to local equilibria calculated as described in Section 3.3.1 and by (3.42).

and $[00\bar{1}]$ easy crystal directions, the easy crystal directions nearest the negative field direction, and rotate into the applied field direction. Because of this rotation, saturation is gradual rather than abrupt as in the [001] application. Furthermore, the magnetostriction decreases at high fields as the domains rotate away from the easy crystal directions because the material anisotropy is such that the magnetostriction is maximum in the $\langle 100 \rangle$ directions and minimum in the $\langle 111 \rangle$ directions. A third contribution to the macroscopic magnetization and magnetostriction comes from domains which start in the [100] and $[\bar{1}00]$ directions and rotate into the direction of the applied field direction. Here also compressive stress decreases the slope of the contribution and increases its volume fraction resulting in an increase in the total magnetostriction.

Hysteresis

Armstrong [5] modeled hysteresis due to irreversible domain wall motion by including pinning energy in the evolution of the domain family volume fractions. We take a similar approach,

$$\frac{d\hat{\xi}}{dH} = \frac{\hat{\xi}_{\text{an}} - \hat{\xi}}{K}, \tag{3.44}$$

where K is proportional to the pinning site energy, $\hat{\xi}_{an}$ is the anhysteretic volume fraction given by (3.42), and H is the magnitude of the applied field. This implementation differs from that of Armstrong in that the domains are allowed to rotate in order to minimize the enthalpy whereas Armstrong only considered the 8 fixed $\langle 111 \rangle$ orientations which correspond to the easy crystal axes or internal energy minima in Terfenol-D. Neglecting domain rotation limits the accuracy of the model, especially when operated in directions away from the easy axes. Atulasimha, Akhras

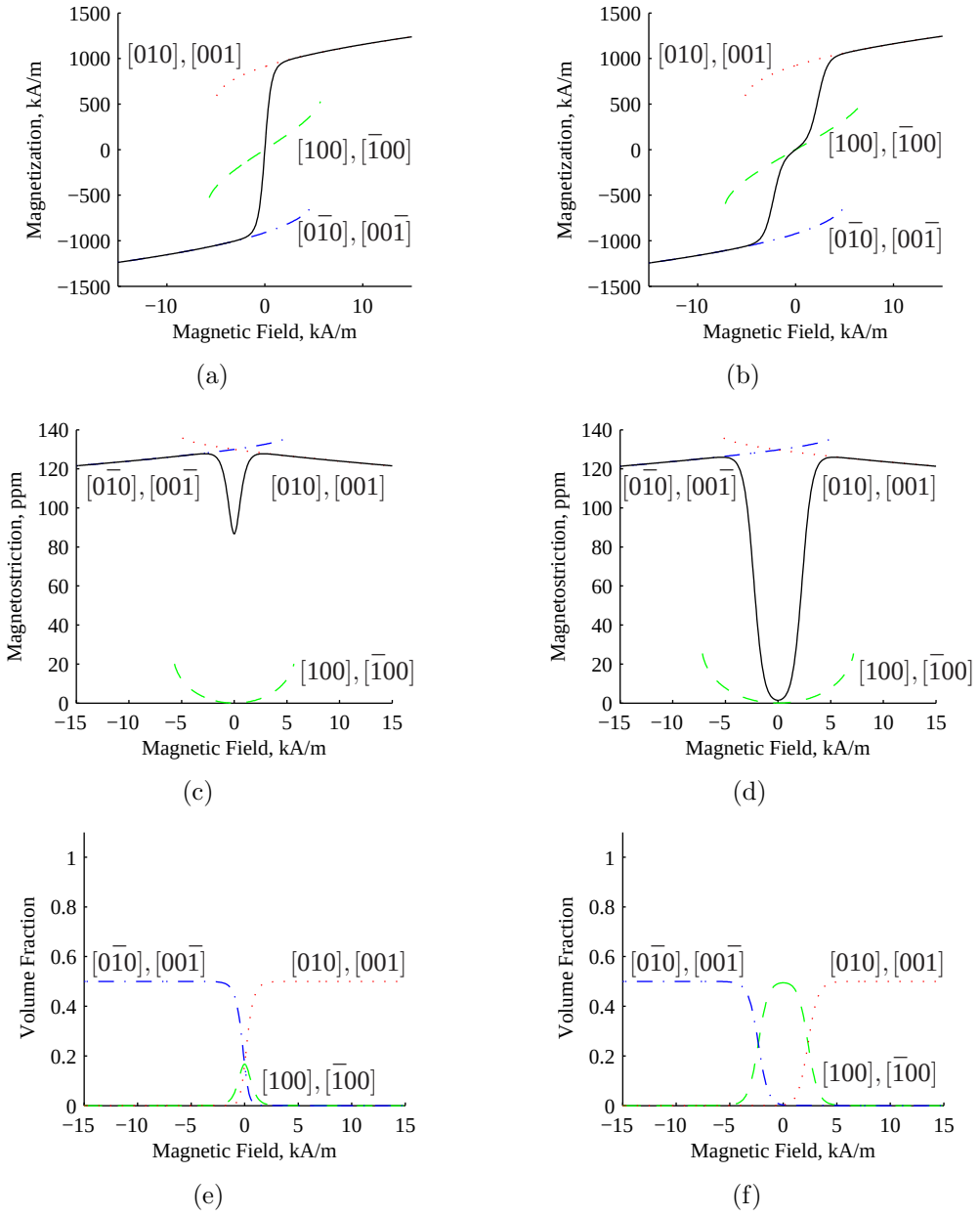

Figure 3.16: Simulation of the (a),(b) magnetization (c),(d) magnetostriction and (e),(f) domain volume fractions for [011] applied field with (a),(c), and (e) no pre-stress and (b), (d), and (f) 30 MPa pre-stress (compression). Solid lines are bulk quantities calculated from (3.43) and dashed/dotted lines correspond to local equilibria calculated as described in Section 3.3.1 and by (3.42).

and Flatau [7] improved the accuracy by considering ninety-eight fixed orientations. Allowing domains to rotate in order to minimize enthalpy is thermodynamically consistent and reduces the number of domain orientations to be tracked to six while preserving accuracy.

This order of magnitude decrease in the number of volume fractions needed for good accuracy is especially important for real-time, model-based controllers and when extending the model to include additional effects such as material geometry and texture. Inclusion of geometry effects necessitates numerical solution of Maxwell's equations, requiring evaluation of the model at many spatial locations. Material texture or polycrystallinity, discussed in the next section, can be included through stochastic homogenization which requires many evaluations of the model at each field and stress value.

Polycrystallinity

Polycrystallinity is incorporated by considering the material to be composed of regions of uniform crystal lattice having a statistically distributed orientation with respect to the coordinate frame of the applied field and stress. Interactions at the grain boundaries are neglected. This approach is similar to that of Appino, Valsania, and Basso [4] which considers in-plane domain rotations in polycrystalline materials with uniaxial anisotropy. For 3D rotations with cubic anisotropy, the bulk magnetization takes the form

$$\mathbf{M}_{poly} = \int_0^{\pi/2} \int_0^{\pi/2} \mathbf{M}(\mathbf{H}, \mathbf{T}, \phi_0, \theta_0) \nu(\phi_0, \theta_0) d\phi_0 d\theta_0, \tag{3.45}$$

where (ϕ_0, θ_0) is the lattice shift, in spherical coordinates, of the crystal lattice with respect to the field and stress directions. The grain orientation distribution ν depends on the material texture, which influences the bulk magnetostriction [57]. This approach differs from that of Atulasimha, Flatau and Summers [10] in that it considers a continuum of orientations rather than a finite sample and can describe various textures through the density ν. Consider for example cylindrical rods grown by the techniques described by Summers, Lograsso, Snodgrass, and Slaughter [97]. Orientation imaging microscopy shows a high degree of grain alignment with grains narrowly distributed about the rod axis. This motivates the use of a normal distribution

$$\nu(\phi_0, \theta_0) = \frac{e^{-\phi_0^2/2\sigma^2}}{\sigma\sqrt{2\pi}} \frac{e^{-\theta_0^2/2\sigma^2}}{\sigma\sqrt{2\pi}}, \tag{3.46}$$

where σ is the standard deviation of the grain misalignment angle. Since the $\langle 100 \rangle$ direction has the largest magnetostriction, any off-axis grains tend to decrease the bulk magnetostriction [97], hence as the distribution broadens (increasing σ), the maximum magnetostriction decreases (see Figure 3.17.) The degree of grain alignment also affects the kinked shape which arises due to the magnetic and stress anisotropy. Increasing grain misalignment tends to decrease the effect of kinking due to anisotropy (see Figure 3.17.)

3.3.2 Experimental validation

The model given by (3.43), (3.44), and (3.45) is validated by comparing simulations to measurements of field-induced magnetization and strain at five levels of constant compressive stress. The integral (3.45) is computed numerically with Gauss-Quadrature integration and the distribution (3.46) is used. The material sample used is research grade $Fe_{81.6}Ga_{18.4}$ from Etrema Products Inc., produced by the Free Stand

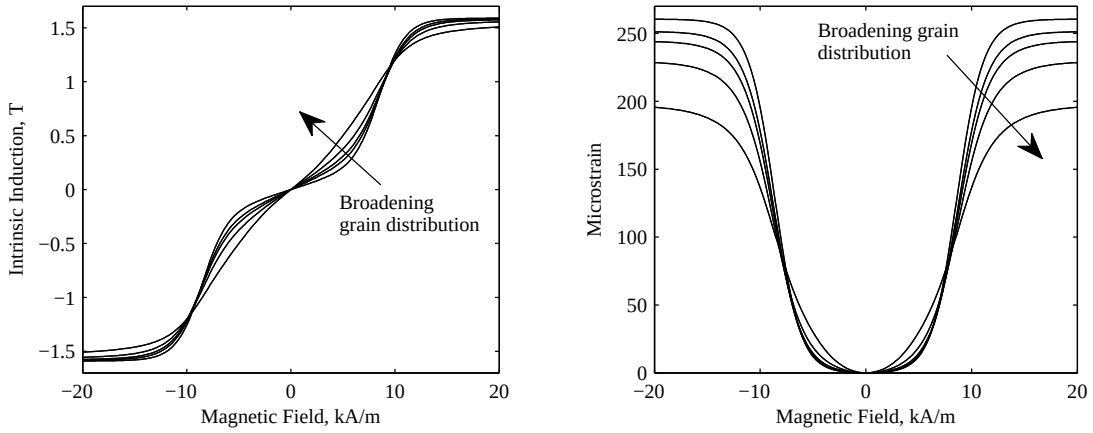

Figure 3.17: Inverse effect simulation using (3.45) and (3.46) with increasing grain misalignment.

Zone Melt method which results in a polycrystalline rod with a large percentage of the grains having the [100] direction oriented along the axis of the rod, consistent with (3.46). Magnetic field and induction are measured along the rod axis. The model parameters are determined through a least-squares algorithm with initial values in the parameter optimization algorithm chosen to be consistent with the literature. The optimized parameters are $K = 300$ A/m, $\sigma = 7.10$ deg, $M_s = 1.26 \times 10^{-3}$ kA/m, $K_4 = 36.0$ kJ/m^3, $\lambda_{100} = 174\ \mu\epsilon$, $\lambda_{111} = -13.3\ \mu\epsilon$, and $\Omega = 1.6$ kJ/m^3. The accuracy of the model is illustrated by the fact that a single set of model parameters is used to accurately describe data sets at five different compressive stresses (see Figure 3.18.)

3.3.3 Concluding remarks

A low-order, 3-D constitutive model relating magnetization and strain to magnetic field and stress has been developed by utilizing thermodynamic principles with an

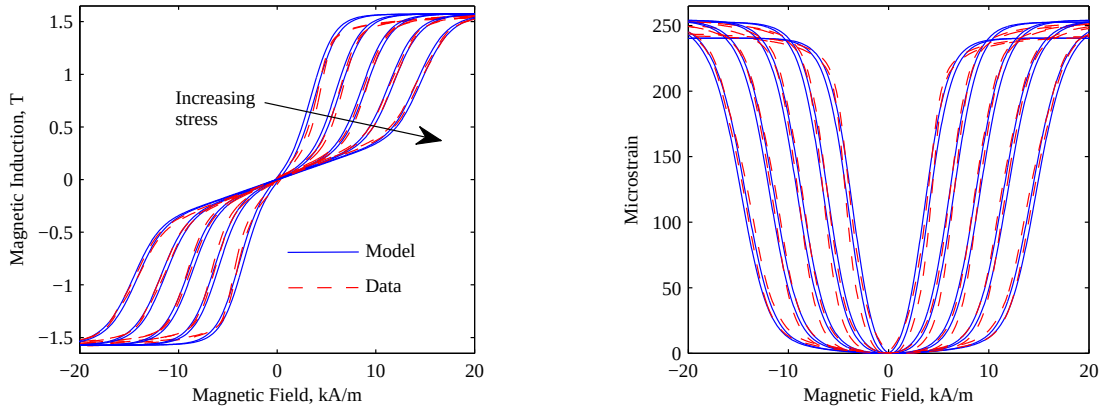

Figure 3.18: Comparison of Galfenol inverse effect data with the hysteretic, polycrystalline model at stress levels of −13.8, −27.6, −41.4, −55.2, −69 MPa.

empirical smoothing operator. By directly minimizing the enthalpy to find the most likely domain orientations, smooth constitutive behavior is achieved with a summation of only six terms. As a result, the framework is extended to include irreversible domain wall motion and material texture without making it too cumbersome for use in distributed parameter, general transducer models which are often solved with the finite-element method, requiring evaluation of the material constitutive model at each node. Comparison of the model to experiments has shown it to accurately model field induced-magnetization and strain at constant stress. The efficiency and accuracy of the model make it ideal for lumped parameter transducer models which may be used for model-based, real-time control of magnetostrictive devices. While accurate, low-order transducer models have been developed for magnetostrictive devices operated in 1-D modes, the framework developed here can be used for characterization, design, and control of Galfenol devices capable of 3-D magnetic field and stress loading.

CHAPTER 4

Constitutive modeling: Part II

4.1 Preamble

This chapter presents a refinement of concepts from Chapter 3 and introduces additional modeling approaches in order to describe features observed in a new set of Galfenol magnetization and strain measurements which include stress application at constant magnetic field. The contributions of the chapter include measurements that characterize the nonlinearity in Galfenol constitutive behavior as well as a 2-tiered modeling approach, a comprehensive framework for material characterization and for inclusion of Galfenol constitutive behavior in device-level models. The first tier of the modeling framework seeks to describe the finer details regarding Galfenol constitutive behavior and is based on stochastic homogenization of energy functions formulated at the domain level. The second tier provides an efficient yet accurate model [39] based on discrete energy averaging and is intended for use in the device-level modeling carried out in Chapter 5.

Section 4.2 reports a novel set of Galfenol measurements aimed at characterizing the nature of the hysteresis loss in Galfenol alloys for both magnetic field and stress loading. The measurements demonstrate that while the magnetization and strain

processes are thermodynamically irreversible, evidenced by hysteresis, these processes are kinematically reversible in that cyclic processes overlap. The data further shows that the magnetomechanical coupling exhibits an additional sense of reversibility, defined by the ability to generate the same magnetization trajectories from both applied stress at constant field and applied field at constant stress. The remainder of the section is devoted to the development a new homogenized energy model, capable of describing the features of Galfenol constitutive behavior that were brought to light in the measurements.

Section 4.3 is a refinement of the efficient modeling framework in Section 3.3. It again employs concepts from Boltzmann statistics, using an energy-weighted average of a discrete number of domain orientations to relate micro-scale behavior to macro-scale behavior. Two refinements are made: (1) an alternate energy formulation for the magnetization particles representing domains is used and (2) the hysteresis model is extended for 3-D magnetic field and stress loading and to include reversible domain processes. The first refinement results in the ability to apply a single energy formulation to materials of any anisotropy symmetry. The parameters in the energies are readily found from features of the macroscopic measurements. The significance of the second refinement is that the model can now be used at the transducer-level for 3-D, nonlinear, and hysteretic behavior under combined magnetic field and stress loading.

Both models in this tiered framework, the homogenized energy model and the discrete energy-averaged model, make use of energy terms defined at the magnetic domain scale. The difference lies in how the macro-scale behavior is determined from the domain scale. For the homogenized energy model, stochastic homogenization

requiring quadruple integration bridges the two scales. The process tracks the orientation of a large number of magnetization particles and can describe the details of hysteretic changes in the domain volume fractions. While the model is certainly a computational improvement over related models which require sextuple integration, the discrete energy-averaged model utilizes a simple six-term summation and is shown to be 100 times faster than previous models. It does not describe the details of the domain volume fraction changes but provides an accurate description of the magnetization/strain versus stress/field relationship in an efficient manner.

4.2 Measurement and modeling of magnetic hysteresis under field and stress in iron-gallium alloys

While linear characterization of Galfenol has been performed [57, 112], a nonlinear description of the coupled magnetomechanical behavior including hysteresis has not been done. In this work, magnetization measurements of production and research grade Galfenol from Etrema Products, Inc. are presented. The grades of Galfenol differ in crystal growth rate. Experiments include applied magnetic field at constant stress, applied stress at constant field, and alternately applied field and stress. The measurements show a remarkable degree of kinematic reversibility in the magnetomechanical coupling, even in the production grade sample. This is in contrast with the magnetomechanical coupling in steel which has been shown to exhibit stress and field induced magnetization that is both thermodynamically and kinematically irreversible [26, 81]. The kinematic reversibility in Galfenol is demonstrated by comparing a single stress-induced magnetization curve at constant magnetic field with a series of field-induced magnetization curves at constant stress. Minor loop measurements consisting of decreasing the field from a bias point, decreasing stress

from a bias point, returning the field, and returning the stress show accommodation is insignificant in Galfenol. These measurements indicate that magnetic hysteresis for both applied field at constant stress and applied stress at constant field results from the same physical mechanism.

A new modeling framework is needed for magnetostrictive materials like Galfenol which respond in a nonlinear, anisotropic, and hysteretic manner to applied field and stress yet are kinematically reversible. While many models have been developed for ferromagnetic hysteresis and magnetomechanical coupling, a vector hysteresis model for anisotropic, magnetostrictive materials applicable for both field and stress loading is not available. Common approaches for modeling hysteretic materials include the differential equation-based approaches, derived from energy principles like the Jiles-Atherton model [49, 52] and empirical approaches like the Preisach model [82]. Scalar in its classical form, the Jiles-Atherton model has been generalized as a vector, anisotropic model as well as a scalar magnetomechanical model [14, 54]. The magnetomechanical model is for kinematically irreversible behavior which has been reported for nickel, mild steel, and silicon iron [26, 81]. The Preisach model is also scalar in its classical form and has likewise been generalized for isotropic vector simulations [1, 2, 68], anisotropic vector simulations [104] and scalar stress-induced magnetization [13, 15]. The Preisach model has also been used to calculate magnetostriction [35, 84]. Recent work has combined aspects of the differential equations approach and the Preisach approach resulting in a model that benefits from the computational simplicity of the former and physically accurate hysteresis properties of the latter [77]. An alternative to these classical approaches is an energy weighting approach for magnetostrictive materials consisting of an anhysteretic vector model for both field and

stress application with a scalar hysteresis mechanism [6, 5, 7, 40]. The hysteresis mechanism uses concepts from Jiles-Atherton model and hence inherits minor loop properties which do not agree with measurements.

Preisach-like models based on energy principles have been developed by replacing the simple Preisach relay which takes values of ± 1 with multi-state relays with states calculated from energy principles. In a class of vector models the states represent Stoner-Wohlfarth particle orientations which have anisotropic dependence on magnetic field [76, 4]. A homogenized energy framework applicable to ferroic materials utilizes a relay derived from the balance of exchange and thermal energies of magnetic moments and models scalar magnetic hysteresis for both field and stress application [91, 92]. This framework has been extended in an anisotropic 2-D vector implementation for electrostrictive materials [74]. In general, energy based models which utilize a Preisach-like switching mechanism provide physical insight from physics based relays and exhibit hysteresis properties which agree with measurements.

In this work, a formal thermodynamic development is undertaken to construct a relay or hysteron which is applicable to magnetostrictive materials of arbitrary anisotropy. The hysteron depends on the 3-D field and stress and includes a small number of parameters, each with a clear physical interpretation. The number of hysteron states is dictated by material symmetry and anisotropy with one state for each easy axis. The criterion for switching follows from the second-law of thermodynamics and results in a unified hysteresis model which has the same properties as observed in the measurements. Following the approach of Smith et al. [91, 92], a statistically distributed interaction field is superimposed on the applied field. Rather than employ a 3-D, statistically distributed coercive field, a scalar coercive energy is used

in the homogenization scheme resulting in fewer computations. This model enables accurate description of the measurements and provides a framework for understanding hysteresis in ferromagnetic materials which exhibit kinematically reversible and hysteretic magnetomechanical coupling.

4.2.1 Measurements

Measurements include magnetization and strain of $\langle 100 \rangle$ oriented, production and research grade Galfenol samples from Etrema Products, Inc. in cylindrical rod form with dimensions of 0.25×1 inches. In the measurement system, stress is applied with an MTS 858 tabletop system, capable of applying compressive loads only, by loading the sample between parallel plates. Magnetic field is applied with a drive coil situated with the Galfenol sample in a steel canister providing a flux return path. Since the permeability of Galfenol is similar to that of the steel return path, it is necessary to use a feedback controller for the magnetic field. The changing permeability of Galfenol results in a nonlinear relationship between the voltage applied to the drive coil and the magnetic field in the Galfenol sample. Drive coil voltage is supplied by a Test Star II MTS controller. The level of voltage required to achieve a desired reference field is found by measuring the field with a Lakeshore 421 gauss meter and implementing a PI controller with an NI SCB-69 DAQ acquisition board. Magnetic flux density is measured with a Walker Scientific MF-30 fluxmeter and pick-up coil. Magnetization is calculated by subtracting the field measurements from flux density measurements. A cartoon depiction of the measurement setup is shown in Figure 4.1.

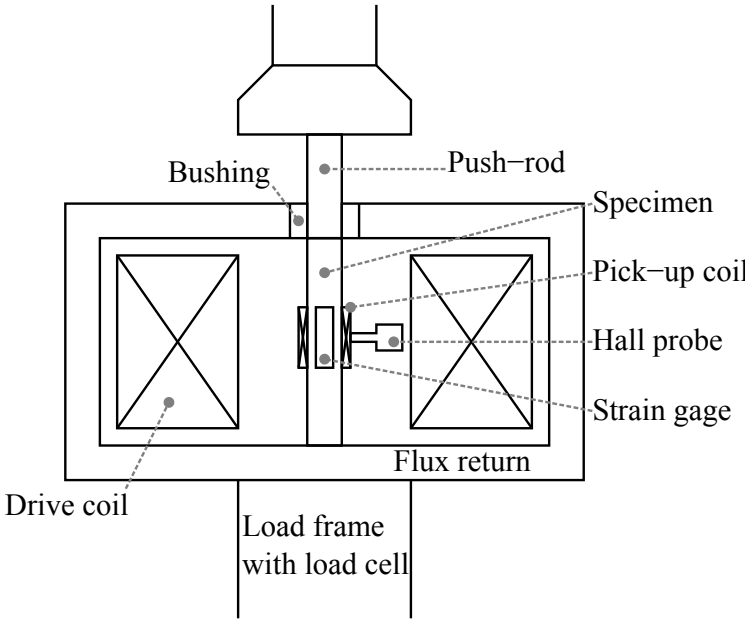

Figure 4.1: Experimental setup for measuring magnetization and strain of Galfenol under magnetic field and stress.

Production Grade 18.4 at. % Ga

Major magnetization loops for applied magnetic field at constant stress and applied stress at constant field are shown in Figure 4.2. Magnetization versus field measurements have two regions of noticeable hysteresis, one at low fields and another at higher fields. Consider for example the curve obtained under 79 MPa compressive stress. There is a hysteretic region below 1 kA/m and another between 7-12 kA/m. The higher field region moves higher with increasing stress. The magnetization versus stress, at low stresses, depends strongly on the field history. The curves in Figure 4.3(a) are measured after applying a positive saturating field and subsequently lowering the field to the bias point while the curves in Figure 4.3(b) are measured after applying a negative saturating field and subsequently bringing the field to the

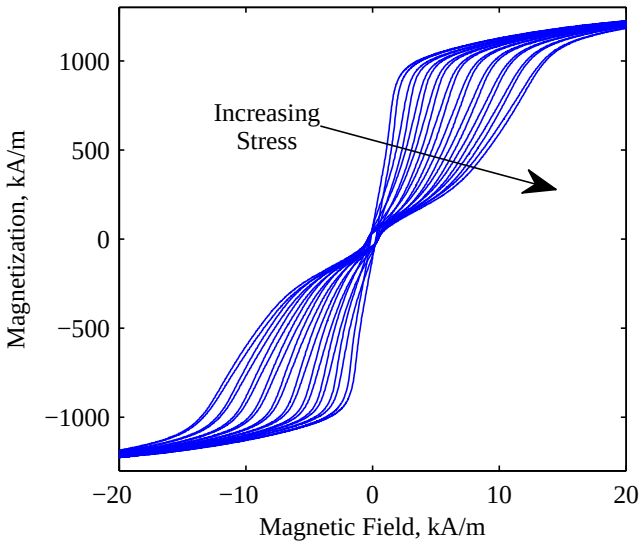

(a)

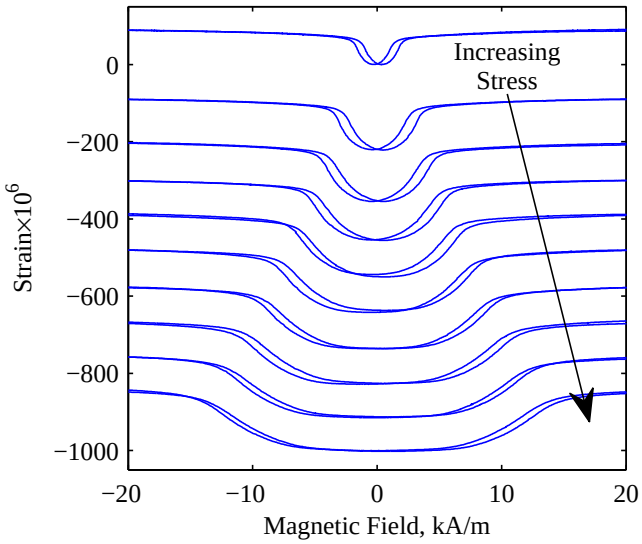

(b)

Figure 4.2: Magnetization and strain measurements of production grade $Fe_{81.6}Ga_{18.4}$ with constant stress levels of 0, −11, −19, −26, −35, −44, −52, −61, −70, −79 MPa.

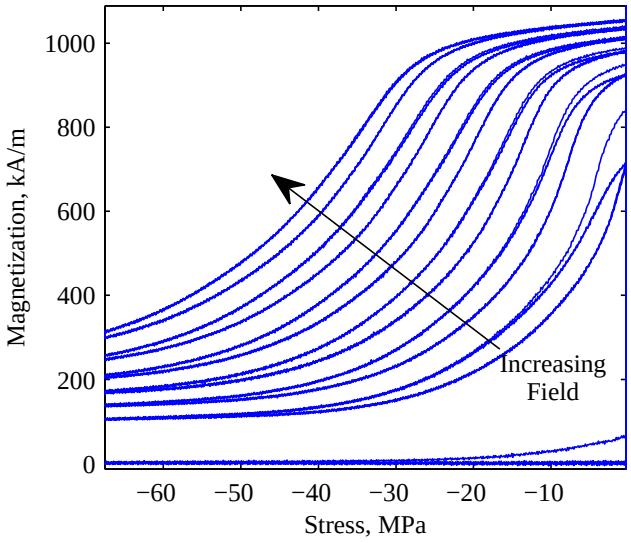

(a)

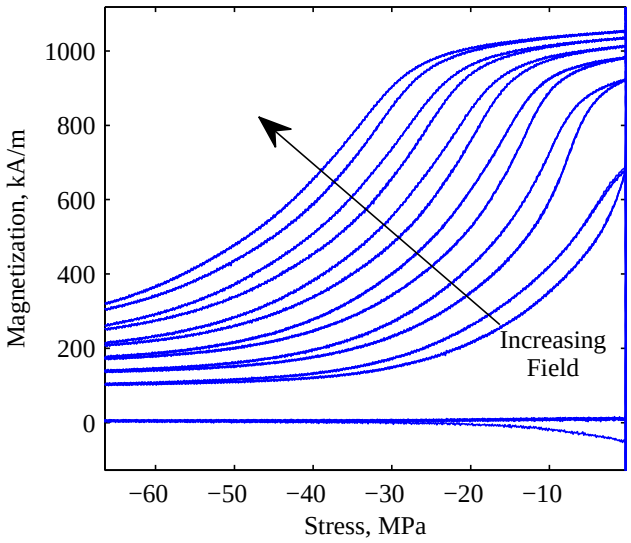

(b)

Figure 4.3: Magnetization and strain measurements of production grade $Fe_{81.6}Ga_{18.4}$ with constant field levels of 0, 1.6, 2.4, 3.3, 4.0, 4.8, 5.6 kA/m.

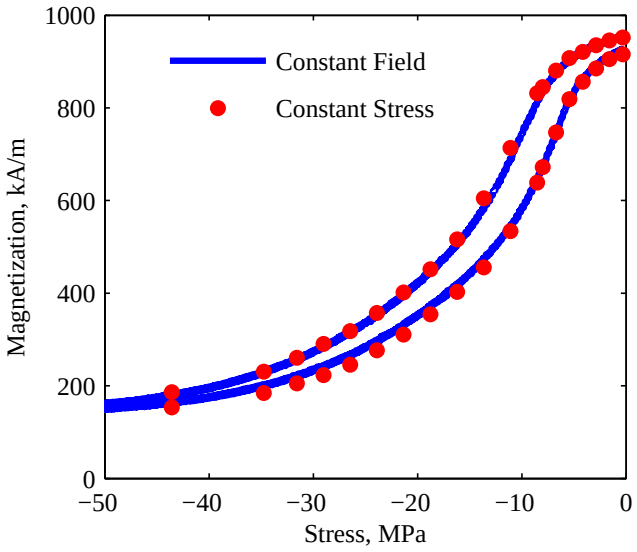

(a)

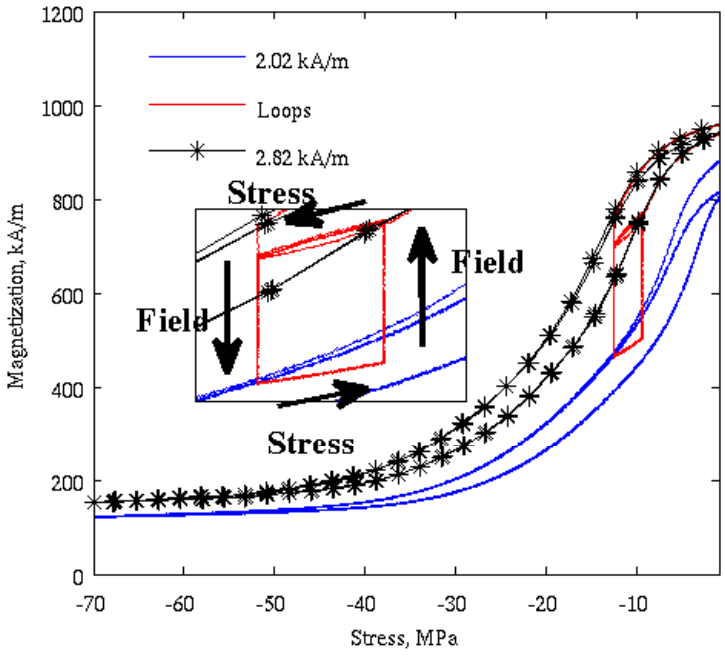

(b)

Figure 4.4: (a) Comparison of production grade Fe-Ga magnetization versus stress at 2.8 kA/m field obtained from sensing and actuation measurements and (b) minor loops from alternately varying the field between 2 and 2.8 kA/m and the stress between 9.4 and 12.6 MPa compression, with the cycle repeated three times.

bias point. In the latter, multiple loops overlap while in the former, the first loop does not close. An exception is the case where there is zero bias field after having negatively saturated the material. In this case the negative remanence resulting from bringing the field from negative saturation to zero, is wiped out by a single cycle of stress. Further cycles of the stress do not result in any magnetization change. Reported measurements of steel have a very different response, exhibiting significant accommodation with each stress cycle and a gradual convergence to a limiting loop.

Measurements shown in Figure 4.4 show a remarkable degree of reversibility in the magnetomechanical coupling of Galfenol. In 4.4(a) a magnetization versus stress curve at constant field is obtained from direct measurement and compared to magnetization versus stress points obtained from multiple sets of magnetization versus field measurements at different bias stress levels. The points are obtained from the upper and lower branches of the magnetization versus field hysteresis curves at the bias field level. These points are then plotted versus the respective bias stresses at which the magnetization versus field curves are measured. The overlap of the curve measured directly while applying stress and the points obtained from magnetization versus field curves at constant stress suggests that the magnetomechanical coupling is reversible and that magnetic hysteresis from applied field and applied stress results from the same physical mechanism.

Figure 4.4(b) shows measurements from alternately applied field and stress along with two magnetization versus stress curves at constant field. The two magnetization versus stress curves are obtained by first positively saturating the material and then lowering the field to the bias point. A stress is then cycled three times to -70 MPa. As before, the first loop is not closed. The curve from alternate stress and field

application is initialized in the same manner by saturating positive and lowering the field to the first bias field of 2.8 kA/m. Thus as stress is applied it follows the magnetization versus stress curve with the higher bias field. At 12.6 MPa compression the stress is held constant and the field is lowered to 2 kA/m from its previous value of 2.8 kA/m. This moves the magnetization from the upper branch of the magnetization versus stress curve at the higher bias field to the upper branch of the magnetization versus stress curve at the lower bias. Here the field is again held constant and the stress is relaxed to 9.4 kA/m resulting in a shift of the magnetization towards the lower branch of the major magnetization versus stress loop. The stress is again held constant and the field is returned to 2.8 kA/m bringing the magnetization to the lower branch of the magnetization versus stress curve obtained with a 2.8 kA/m bias field. The stress is then returned to 12.6 MPa at constant field, moving the magnetization towards the upper branch of the magnetization versus stress major loop. This stress and field cycle is repeated three times before returning the stress to zero. These minor loops obtained by alternately applying field and stress about a bias point lack any noticeable accommodation. This again is in contrast with measurements of steel which exhibit large changes in the shape of magnetization loops obtained from cycling the stress and field [26, 81].

Research Grade 18.5 at. % Ga

Major magnetization loops of research grade material have similarities with the production grade material. Specifically, the field location of the burst region is moved to higher fields with increasing bias stress (see Figure 4.5(a).) The loops however do not have a noticeable hysteretic region at low fields as do the production grade magnetization loops. Additionally, the differential susceptibility is higher in the hysteretic

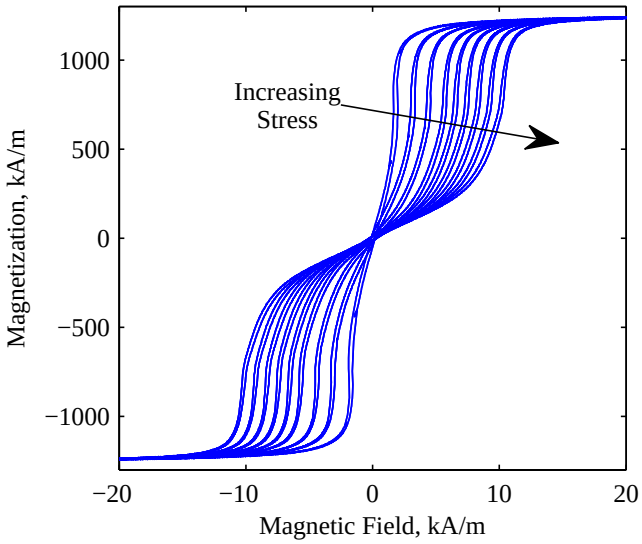

(a)

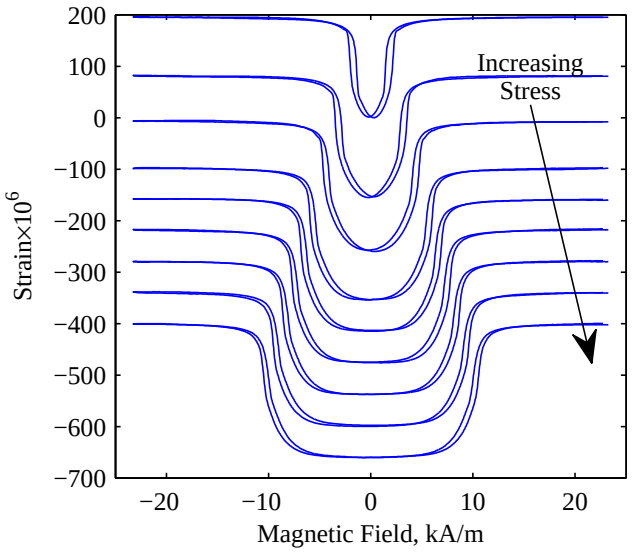

(b)

Figure 4.5: Magnetization and strain measurements of research grade $Fe_{81.5}Ga_{18.5}$ with constant stress levels of 0, −9, −16, −23, −28, −32, −37, −42, −46 MPa.

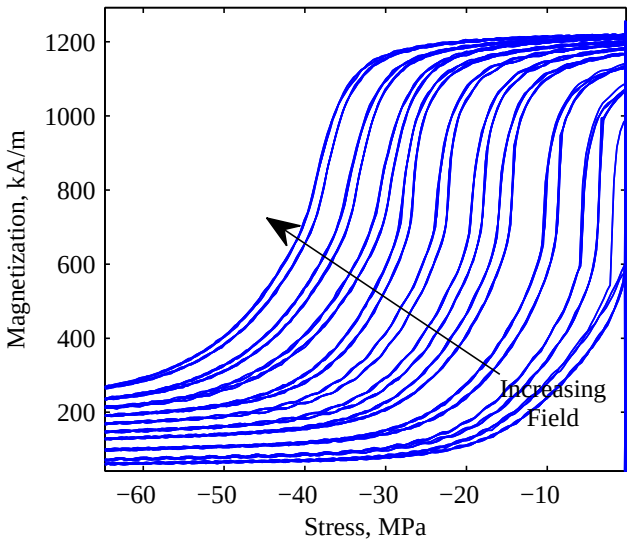

(a)

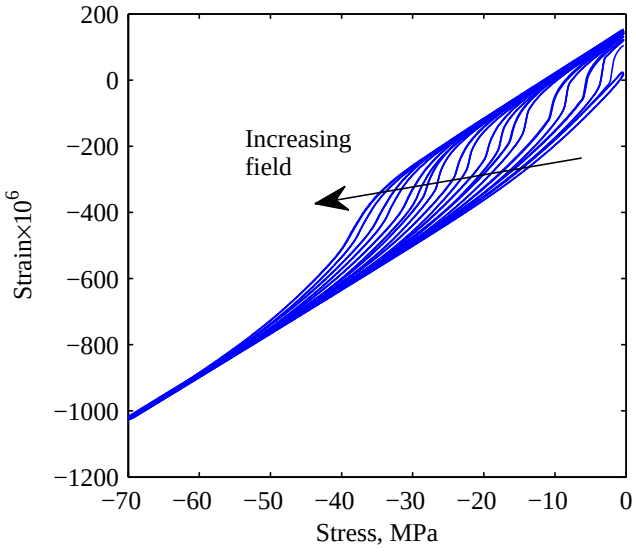

(b)

Figure 4.6: Magnetization and strain measurements of research grade $Fe_{81.5}Ga_{18.5}$ with constant field levels of 1.9, 4.2, 2.4, 3.2, 4.8, 5.6, 6.5, 7.3, 8.1, 8.9 kA/m.

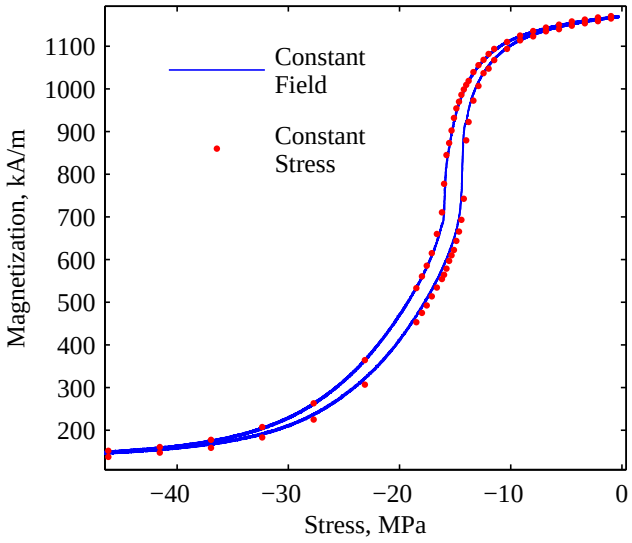

(a)

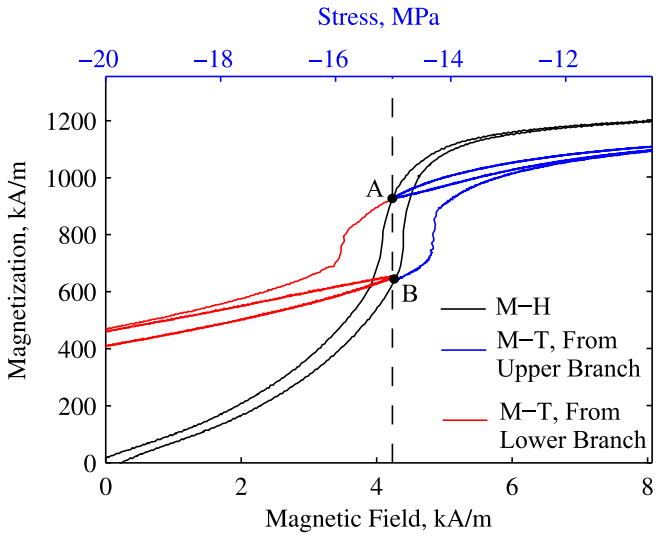

(b)

Figure 4.7: (a) Comparison of research grade $Fe_{81.5}Ga_{18.5}$ magnetization versus stress at 4.2 kA/m field obtained from sensing and actuation measurements and (b) magnetization excursions from the upper and lower hysteresis branches about a bias of 15 MPa and 4.2 kA/m, cycled three times.

burst regions. The magnetization versus stress loops (see Figure 4.6(a)) are similar to the production grade measurements where the first cycle is not closed and subsequent cycles overlap. They differ in the high slope regions, having much sharper transitions. The magnetomechanical coupling in the research grade material is shown to be reversible by comparing the magnetization versus stress measured at constant field and the magnetization versus stress measured at constant stress in the same manner as was done with the production grade material (see Figure 4.7(a).)

The coupled nature of the hysteresis mechanism observed in the magnetization from both applied field and applied stress is emphasized in Figure 4.7(b). Starting from a field of 4.2 kA/m and compressive stress of 15 MPa, if the magnetization starts at point A on the upper branch of the major magnetization versus field loop, increasing the stress and returning to 15 MPa pushes the magnetization to point B on the lower branch of the major loop in a single cycle. Further cycles always return to point B on the lower branch and overlap. Starting at point B on the lower branch of the hysteresis loop, when the stress is lowered to zero and brought back to 15 MPa, the magnetization is pushed to point A on the upper branch of the major loop. Further cycles always return to the upper branch of the major loop and overlap. These results show that the width of the hysteresis loops for applied stress and applied field are constrained in that knowledge of one determines the other.

4.2.2 Model Development

A constitutive model relating magnetization and strain to magnetic field and stress will be developed from thermodynamic principles with stochastic homogenization. A hysteron for single crystalline material devoid of imperfections is first derived from

thermodynamic principles. Stochastic homogenization is then employed to incorporate the smoothing effect of material inhomogeneities.

The first law of thermodynamics states that the rate of change of the internal energy U is equal to the rate of change of the applied work plus generated heat, less the heat leaving. For a thermomagnetomechanical material with stress $\mathbf{T}$ and strain $\mathbf{S}$ (using vector notation), magnetic field $\mathbf{H}$, magnetization $\mathbf{M}$, heat generation Q and heat flux $\mathbf{q}$, this is expressed by

$$\dot{U} = \mathbf{T} \cdot \dot{\mathbf{S}} + \mu_0 \mathbf{H} \cdot \dot{\mathbf{M}} + Q - \nabla \cdot \mathbf{q}. \tag{4.1}$$

The second law of thermodynamics states that thermal processes result in entropy η increase. At temperature θ this can be expressed through the Clausius-Duhem inequality

$$\dot{\eta} \geq \frac{Q}{\theta} - \nabla \cdot \left(\frac{\mathbf{q}}{\theta} \right). \tag{4.2}$$

Eliminating the heat generation by combining the first and second laws gives

$$\theta \dot{\eta} - \dot{U} + \mathbf{T} \cdot \dot{\mathbf{S}} + \mu_0 \mathbf{H} \cdot \dot{\mathbf{M}} - \frac{1}{\theta} \mathbf{q} \cdot \nabla \theta \geq 0. \tag{4.3}$$

The dependencies are

$$U = U(\mathbf{S}, \mathbf{M}, \eta), \tag{4.4}$$

$$\mathbf{T} = \mathbf{T}(\mathbf{S}, \mathbf{M}, \eta), \tag{4.5}$$

$$\mathbf{H} = \mathbf{H}(\mathbf{S}, \mathbf{M}, \eta). \tag{4.6}$$

In practice it is easier measure magnetization and strain as a function of field, stress, and temperature. Furthermore, the magnetization can be interpreted as being a function of internal variables representing r possible domain orientations $\mathbf{m}^k$ each of

which occurs with volume fraction of material ξ^k. The internal variables will provide a mechanism for energy dissipation leading to a unified hysteresis mechanism for both applied field and stress. The dependencies are switched through the Legendre transformation

$$G(\mathbf{H}, \mathbf{T}, \theta) = U(\mathbf{M}, \mathbf{S}, \eta) - \eta\theta - \mathbf{S} \cdot \mathbf{T} - \mu_0 \mathbf{M} \cdot \mathbf{H}. \tag{4.7}$$

Since magnetization is also dependent on the internal variables $\mathbf{m}^k$ and ξ^k, the dependencies after transformation are

$$\mathbf{M} = \mathbf{M}(\mathbf{H}, \mathbf{T}, \theta, \mathbf{m}^k, \xi^k), \tag{4.8}$$

$$\mathbf{S} = \mathbf{S}(\mathbf{H}, \mathbf{T}, \theta, \mathbf{m}^k, \xi^k), \tag{4.9}$$

$$\eta = \eta(\mathbf{H}, \mathbf{T}, \theta, \mathbf{m}^k, \xi^k). \tag{4.10}$$

The time rate of change of the free energy G is then

$$\dot{G} = \frac{\partial G}{\partial \mathbf{H}} \cdot \dot{\mathbf{H}} + \frac{\partial G}{\partial \mathbf{T}} \cdot \dot{\mathbf{T}} + \frac{\partial G}{\partial \theta}\dot{\theta} + \sum_{k=1}^{r} \left[\frac{\partial G}{\partial \mathbf{m}^k} \cdot \dot{\mathbf{m}}^k + \frac{\partial G}{\partial \xi^k}\dot{\xi}^k \right]. \tag{4.11}$$

From (4.7), the time rate of change of the internal energy is

$$\dot{U} = \dot{G} + \eta\dot{\theta} + \theta\dot{\eta} + \mathbf{S} \cdot \dot{\mathbf{T}} + \mathbf{T} \cdot \dot{\mathbf{S}} + \mu_0 \mathbf{H} \cdot \dot{\mathbf{M}} + \mu_0 \mathbf{M} \cdot \dot{\mathbf{H}}. \tag{4.12}$$

Substitution of (4.12) and (4.11) into (4.3) gives the following restriction on thermodynamic processes resulting from changes in the independent and internal variables,

$$\begin{aligned} -\left(\eta + \frac{\partial G}{\partial \theta}\right)\dot{\theta} - \left(\mu_0 \mathbf{M} + \frac{\partial G}{\partial \mathbf{H}}\right)\dot{\mathbf{H}} - \left(\mathbf{S} + \frac{\partial G}{\partial \mathbf{T}}\right)\dot{\mathbf{T}} \\ + \sum_{k=1}^{r} \left[\frac{\partial G}{\partial \mathbf{m}^k} \cdot \dot{\mathbf{m}}^k + \frac{\partial G}{\partial \xi^k}\dot{\xi}^k \right] - \frac{1}{\theta}\mathbf{q} \cdot \nabla\theta \geq 0. \end{aligned} \tag{4.13}$$

For thermo-magnetomechanical materials that are thermodynamically reversible, the inequality becomes an equality and the constitutive relations can be found from

$$\mu_0 \mathbf{M} = -\frac{\partial G}{\partial \mathbf{H}}, \tag{4.14}$$

$$\mathbf{S} = -\frac{\partial G}{\partial \mathbf{T}}, \tag{4.15}$$

$$\eta = -\frac{\partial G}{\partial \theta}, \tag{4.16}$$

$$\frac{\partial G}{\partial \xi_k} = 0, \tag{4.17}$$

$$\frac{\partial G}{\partial \mathbf{m}^k} = 0, \tag{4.18}$$

$$\mathbf{q} = -k\nabla\theta. \tag{4.19}$$

Now the following assumptions are made on the processes

- Isothermal
- Negligible temperature gradients
- Reversible domain rotation
- Irreversible domain volume fraction evolution

With these assumptions, the following constitutive relationships are consistent with the first and second laws of thermodynamics

$$\mu_0 \mathbf{M} = -\frac{\partial G}{\partial \mathbf{H}}, \tag{4.20}$$

$$\mathbf{S} = -\frac{\partial G}{\partial \mathbf{T}}, \tag{4.21}$$

$$\frac{\partial G}{\partial \mathbf{m}^k} = 0, \tag{4.22}$$

$$-\frac{\partial G}{\partial \xi_k}\dot{\xi}^k \geq 0. \tag{4.23}$$

For this case, dissipation occurs as domains reconfigure. The free energy and volume fraction evolutions need to be defined. Given the free energy, the magnetization, strain, and possible domain orientations can be calculated from the constitutive relations (4.20)-(5.9). The volume fraction evolution must satisfy the inequality (4.23) in order for the thermo-magnetomechanical process to satisfy the first and second laws of thermodynamics.

Energy formulation

The free energy has terms for magnetic anisotropy G_A, magnetomechanical coupling G_C, Zeeman or field energy G_Z, and elastic strain energy G_E. These energies will be expressed while idealizing the complex domain structure of ferromagnetic materials as a system of non-interacting, single-domain, Stoner-Wohlfarth (S-W) particles. Rather than employ an energy expression which is valid for all domain variants, a local definition is used for each variant which depends only on the easy axis of the variant $\mathbf{c}^k$ and its temperature dependent anisotropy coefficient $K^k(\theta)$,

$$G_A^k = \frac{1}{2} K^k(\theta) |\mathbf{m}^k - \mathbf{c}^k|^2. \tag{4.24}$$

This energy characterizes the torque require to rotate a S-W particle away from its easy axis. For small rotations, the coefficient K^k is the slope of the torque-angle curve. For cubic materials, the $\langle 100 \rangle$ or $\langle 111 \rangle$ directions tend to be easy. Because of crystal symmetry, the anisotropy coefficient in each direction family is the same, thus $K^k = K_{100}$ for all six $\langle 100 \rangle$ directions and $K^k = K_{111}$ for all eight $\langle 111 \rangle$ directions. For negative anisotropy coefficients K^k, the direction $\mathbf{c}^k$ is magnetically hard or an unstable equilibrium. For the isothermal processes considered here the anisotropy coefficients are constant.

The total anisotropy energy is simply the sum of the contribution from each variant,

$$G_A = \sum_{k=1}^{r} G_A^k \xi^k. \tag{4.25}$$

The volume fraction evolution will ensure that using a locally defined anisotropy energy introduces little error into the total anisotropy energy. For magnetically soft materials, as a domain is pulled away from an easy axis, its size is reduced through domain wall motion and the size of domains lying nearer an easy axis is increased. This domain reconfiguration is modeled here through the evolution of the S-W particle volume fractions and as ξ^k decreases, the anisotropy energy contribution from the k^{th} variant is likewise reduced.

The magnetomechanical coupling energy is the sum of the contributions to the mechanical work from the magnetostriction $\boldsymbol{\lambda}^k$ of each particle variant

$$G_C = -\sum_{k=1}^{r} \left(\boldsymbol{\lambda}^k \cdot \mathbf{T}\right) \xi^k, \tag{4.26}$$

and the Zeeman energy is the magnetic work due to each particle variant

$$G_Z = -\sum_{k=1}^{r} \left(\mu_0 M_s(\theta) \mathbf{m} \cdot \mathbf{H}\right) \xi^k, \tag{4.27}$$

where M_s is the magnetization of a S-W particle, constant for isothermal processes. For Galfenol, the magnetostriction of a S-W particle for cubic materials is used [61]

$$\boldsymbol{\lambda}^k = \begin{bmatrix} (3/2)\lambda_{100}(\theta)\left(m_1^k\right)^2 \\ (3/2)\lambda_{100}(\theta)\left(m_2^k\right)^2 \\ (3/2)\lambda_{100}(\theta)\left(m_3^k\right)^2 \\ 3\lambda_{111}(\theta) m_1^k m_2^k \\ 3\lambda_{111}(\theta) m_2^k m_3^k \\ 3\lambda_{111}(\theta) m_3^k m_1^k \end{bmatrix}. \tag{4.28}$$

The spontaneous magnetostrictions in the $\langle 100 \rangle$ and $\langle 111 \rangle$ directions are constant for isothermal processes. The mechanical strain energy density of the material is

$$G_E = -\frac{1}{2}\mathbf{T} \cdot \mathbf{sT}, \tag{4.29}$$

where the 6×6 compliance $\mathbf{s}$ has symmetry consistent with the material crystal structure. Summing the energy terms and weighting with the volume fractions, the free energy of the material is

$$G = \sum_{k=1}^{r} \xi^k G^k + \mathbf{T} \cdot \mathbf{sT}, \tag{4.30}$$

$$G^k = \frac{1}{2}K^k |\mathbf{m}^k - \mathbf{c}^k|^2 - \boldsymbol{\lambda}^k \cdot \mathbf{T} - \mu_0 M_s \mathbf{m}^k \cdot \mathbf{H}. \tag{4.31}$$

From (4.20), the magnetization is

$$\mathbf{M} = -\frac{1}{\mu_0}\frac{\partial G}{\partial \mathbf{H}} = M_s \sum_{k=1}^{r} \xi^k \mathbf{m}^k, \tag{4.32}$$

and from (4.21) the strain is

$$\mathbf{S} = -\frac{\partial G}{\partial \mathbf{T}} = \sum_{k=1}^{r} \xi^k \boldsymbol{\lambda}^k + \mathbf{sT}, \tag{4.33}$$

thus to calculate the magnetization and magnetostriction, the S-W particle orientations and volume fractions need to be known.

Calculation of particle orientations

The magnetic orientations $\mathbf{m}^k$ of the S-W particles are calculated from the minimization (5.9). This minimization is constrained since the vector $\mathbf{m}^k$ is a unit vector. The constraint is $C = |\mathbf{m}^k| - 1 = 0$. The constrained minimization can be cast in the form of an inhomogeneous eigenvalue problem by using Lagrange multipliers, $\partial G^k / \partial \mathbf{m}^k = \gamma \partial C / \partial \mathbf{m}^k$. Gathering terms from (4.50) and expressing the particle free

energy as $G^k = \frac{1}{2}\mathbf{m}^k \cdot \mathbf{K}^k\mathbf{m}^k - \mathbf{m}^k \cdot \mathbf{B}^k$ the eigenvalue problem is

$$\left(\mathbf{K}^k - \gamma\mathbf{I}\right)\mathbf{m}^k = \mathbf{B}^k, \tag{4.34}$$

where the magnetic stiffness matrix $\mathbf{K}^k$ and force vector $\mathbf{B}^k$ are

$$\mathbf{K}^k = \begin{bmatrix} K^k - 3\lambda_{100}T_1 & -3\lambda_{111}T_4 & -3\lambda_{111}T_6 \\ -3\lambda_{111}T_4 & K^k - 3\lambda_{100}T_2 & -3\lambda_{111}T_5 \\ -3\lambda_{111}T_6 & \lambda_{111}T_5 & K^k - 3\lambda_{100}T_3 \end{bmatrix}, \tag{4.35}$$

$$\mathbf{B}^k = \begin{bmatrix} c_1^k K^k + \mu_0 M_s H_1 & c_2^k K^k + \mu_0 M_s H_2 & c_3^k K^k + \mu_0 M_s H_2 \end{bmatrix}^{\mathrm{T}}. \tag{4.36}$$

While the orientation can be easily solved for in terms of γ through diagonalization, determination of γ requires solution of a sixth-order polynomial obtained by substituting the γ dependent orientation into the constraint. It is important to keep the computation expense of the hysteron to a minimum since a large number of hysterons are summed in the stochastic homogenization process. To this end, the constraint is relaxed through linearization about the easy direction $\mathbf{c}^k$. This is accurate because as a field or stress pulls a particle away from the easy direction, at a critical energy level the particle flips to an equilibrium closer to the applied field or perpendicular to the applied principal stresses. This is modeled through an instantaneous change in ξ^k. Hence particles oriented near an easy axis always have large volume fractions as compared to particles which have been rotated far from their easy axis. For the relaxed, linear constraint, the solution to the inhomogeneous eigenvalue problem is

$$\mathbf{m}^k = \left(\mathbf{K}^k\right)^{-1}\left[\mathbf{B}^k + \frac{1 - \mathbf{c}^k \cdot \left(\mathbf{K}^k\right)^{-1}\mathbf{B}^k}{\mathbf{c}^k \cdot \left(\mathbf{K}^k\right)^{-1}\mathbf{c}^k}\mathbf{c}^k\right]. \tag{4.37}$$

The particle orientations (4.54) define the possible states of a 3D, anisotropic, field and stress dependent magnetization and strain hysteron. The magnetization of the hysteron is calculated from (4.32) and the strain from (4.33). An evolution equation

for ξ^k will be defined in the next section. This evolution defines the switches in the hysteron states and is consistent with the second law of thermodynamics.

Evolution of domain volume fractions and hysteron development

The hysteron represents the magnetization and strain at the the domain level and is constructed by tracking a single S-W particle as it switches state from an initial orientation variant $\mathbf{m}^I$ to a final orientation variant $\mathbf{m}^F$. This switching is modeled through changes in ξ^k where prior to switching $\xi^I = 1$ and $\xi^k = 0$ for $k \neq I$ and after switching $\xi^F = 1$ and $\xi^k = 0$ for $\xi_k \neq F$. Switching occurs when the energy difference $G^I - G^F := G^{IF}$ reaches a coercive energy E_c. As the field and stress change, the energy difference with the globally minimum orientation always reaches the coercive energy first, hence the state of the hysteron after switching $\mathbf{m}^F$ is always the globally minimum orientation variant. Since $\xi^k = 1$ for $k = I$ or $k = F$ and all other ξ^k are non-zero, from (4.58) the free energy of the hysteron is

$$G = \xi^I G^I + \xi^F G^F - \mathbf{s} \cdot \mathbf{T}, \tag{4.38}$$

and the thermodynamic condition (4.23) which is the rate of energy dissipation becomes

$$-\frac{\partial G}{\partial \xi^I}\dot{\xi}^I - \frac{\partial G}{\partial \xi^F}\dot{\xi}^F = -G^I\dot{\xi}^I - G^F\dot{\xi}^F \geq 0. \tag{4.39}$$

The criterion for switching from $\mathbf{m}^I$ to $\mathbf{m}^F$ can be expressed mathematically as a dirac-delta function

$$\dot{\xi}^F = \delta(G^{IF} - E_c), \qquad \dot{\xi}^I = -\dot{\xi}^F. \tag{4.40}$$

The energy dissipation becomes

$$\begin{aligned} &- G^I\dot{\xi}^I - G^F\dot{\xi}^F = G^I\dot{\xi}^F - G^F\dot{\xi}^F = G^{If}\dot{\xi}^F \\ &= G^{IF}\delta(G^{IF} - E_c) = \begin{cases} E_c, \ G^{IF} = E_c \\ 0, \ else \end{cases}. \end{aligned} \tag{4.41}$$

Thus there is an instantaneous energy dissipation of E_c when switching occurs. A hysteron for changing field or stress is constructed as follows. For each time step, the orientations $\mathbf{m}^k$ are calculated from (4.54) and the particle energies G^k from (4.50). The initial state $k = I$ must be known. The final state $k = F$ is taken as the globally minimum state. After a step change in the field or stress, the hysteron state either stays as $k = I$ or switches to $k = F$ if the switching criterion is met. The magnetization and strain of the hysteron are then calculated from (4.32) and (4.33), in other words, the magnetization before and after switching is $M_s\mathbf{m}^I$ and $M_s\mathbf{m}^F$ and the magnetostriction before and after switching $\boldsymbol{\lambda}^I$ and $\boldsymbol{\lambda}^F$ where $\boldsymbol{\lambda}^k$ is given by (5.5) for cubic materials.

Reduction of vector hysteron to scalar hysterons

The classical Preisach model is scalar and depends on magnetic field only. The Preisach relay switches between two field independent states, ± 1 representing domains as oriented up and down. Switching occurs at a field value of $H = \pm H_c$ where H_c is the coercive field and the magnetization contribution of the relay is $\pm M_s$. For the hysteron presented here, consider a material with uniaxial anisotropy having easy axes in the $[\pm 100]$ directions. Associated with these two easy axes are two variants of S-W particle orientations, $\mathbf{m}_{[100]}$ and $\mathbf{m}_{[\bar{1}00]}$ having the same anisotropy constant, K_{100}. If the field is applied in the direction $\mathbf{u} = [1\ 0\ 0]$, then the hysteron reduces to the classical Preisach relay. From Equation (4.54), the component of the variant $\mathbf{m}_{[100]}$ is $+1$ in the direction of $\mathbf{u}$, i.e. $\mathbf{u} \cdot \mathbf{m}_{[100]} = 1$ and the component of the variant $\mathbf{m}_{[\bar{1}00]}$ is -1. No rotation of the S-W particles occurs with field application because it is applied along the easy axes. The energies of the two variants are $\mp\mu_0 M_s H - 1/2K$ giving the energy difference between the two variants as $G_{[\bar{1}00]} - G_{[100]} = 2\mu_0 M_s H$.

Therefore the hysteron switches from the $[\bar{1}00]$ direction to the [100] direction at the coercive field $H_c = E_c/(2\mu_0 M_s)$.

Smith's homogenized energy model [92] employs two energy-based hysterons—one for static operation and another which has rate-dependence characterizing the thermal after-effect. The static hysteron differs from the Preisach relay in that up and down states vary linearly with field. This same relay behavior can be achieved with the proposed hysteron here by again considering uniaxial material but applying the field away from the easy axes. Examples are shown in Figure 4.8 with the field applied 0, 30, 60, and 90 degrees from the easy axis in the [100] direction. At an increasing angle the hysteron reflects greater difficulty in magnetizing since the direction is further away from the easy axes. At 90 degrees the two variants have the same orientation and energy and no switching occurs. For an angle θ the slope or relative susceptibility of the up and down states is

$$\chi = \sin^2(\theta)\frac{\mu_0 M_s}{K_{100}}, \tag{4.42}$$

and the remanence is $\pm\cos\theta$. The energy difference is $G_{[\bar{1}00]} - G_{[100]} = 2\cos(\theta)\mu_0 M_s H$ which results in a coercive field for switching from the down to the up state $H_c = E_c/(2\cos(\theta)\mu_0 M_s)$. This anisotropic hysteron illustrates an important difference between Preisach models and homogenized energy models. Both employ an elementary hysteron with statistically distributed parameters, however, the former includes effects from additional physics such as anisotropy or magnetomechanical coupling in the density functions while the latter includes additional physics in the hysteron, which captures the underlying material behavior. Typically this results in simpler density functions, or in the discretized model, fewer weights.

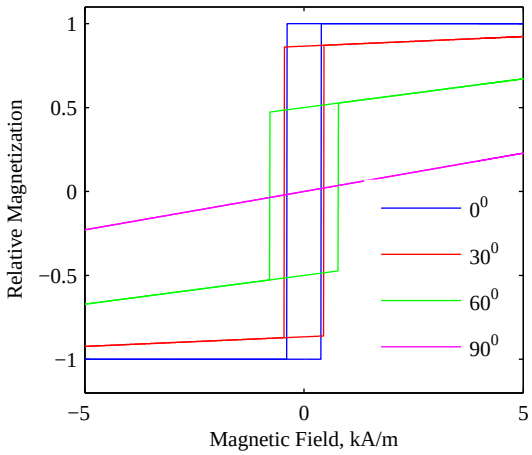

Figure 4.8: Anisotropic hysterons.

Description of measurements with elementary hysteron

The hysteron can describe the underlying shape of the magnetization versus field curves in Figures 4.2(a) and 4.5(a) as well as the magnetization versus stress curves in Figures 4.6(a), 4.3(a) and 4.3(b). Even though the measurements are unidirectional, a vector model is needed for their description because anisotropic, 3-D domain rotation occurs.

For $\langle 100 \rangle$ oriented, research grade material a $\langle 100 \rangle$ orientation is aligned with the rod axis which is the direction of field and stress. The stress dependence of the hysteretic burst regions in Figure 4.5(a) can be understood from the hysterons in Figure 4.9(a). The low-field linear region is due to rotation of $\langle 100 \rangle$ domains perpendicular to the field direction. The hysteron represents this region through the field and stress dependence given by (4.54) of $\mathbf{m}^k$ which have easy axes perpendicular to the field. There are four such $\mathbf{m}^k$ which explains why the hysteron has only three unique states when calculating magnetization and strain in a $\langle 100 \rangle$ direction. The

burst region occurs by domain reconfiguration as the size of domains along the $\langle 100 \rangle$ direction aligned with the field grows at the expense of the perpendicular domains. In the hysteron, the burst region is described by switching from $\mathbf{m}^I$ with easy axes perpendicular to the field to $\mathbf{m}^F$ with the easy axis parallel to the field. The coercive or dissipation energy E_c causes a delay resulting in hysteresis which accounts for the noticeable hysteresis in the burst region and lack thereof in the low-field region where the magnetization process is dominated by domain rotation. With increased stress, the energy of $\mathbf{m}^k$ with easy axes perpendicular to the field is decreased, thus the field location where switching occurs is pushed to higher fields.

The additional hysteretic region at low fields for the production grade, field applied major loops results from misalignment. Two of the $\langle 100 \rangle$ easy directions near the plane perpendicular to the rod axis are closer to the negative rod direction and the other two are closer to the positive rod direction. Thus hysteretic switching occurs between these orientation variants as the field crosses zero (see Figure 4.10(a).) Although this switching results in energy loss, it does not result in a low-field hysteresis region for the magnetostriction (see Figures 4.2 and 4.10) because magnetostriction is a quadratic relation; the variants which are slightly closer to the positive field direction and the variants which are slightly closer to the negative field direction have the same magnetostriction.

The center of the burst region in the magnetization versus field measurements can be calculated analytically from $G^I = G^F$ and the susceptibility in the low field, domain rotation region, can be calculated from (4.54). The anisotropy coefficient K_{100} can be determined directly from the measurements since (4.54) is an analytic function of K_{100} . The particle magnetization M_s and the magnetostriction λ_{100} can

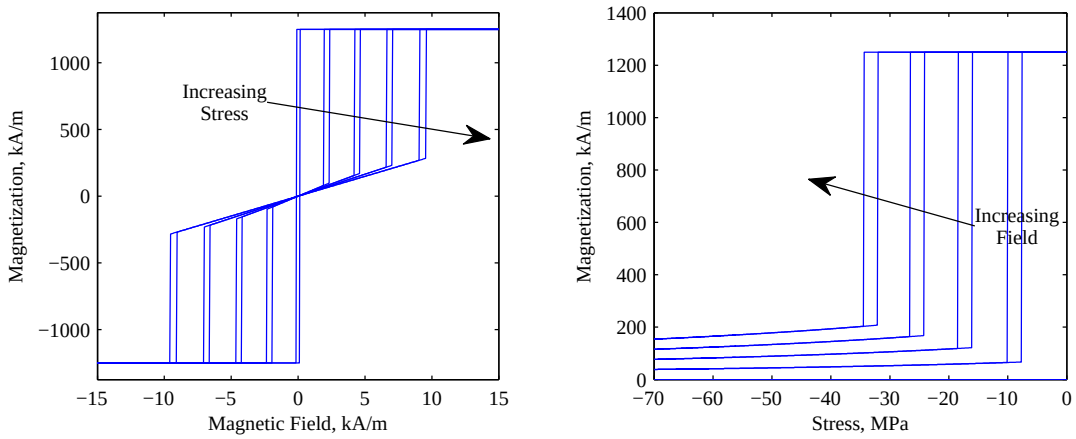

Figure 4.9: Magnetization of a hysteron in the [100] direction for (a) applied field and constant stress and (b) applied stress at constant field.

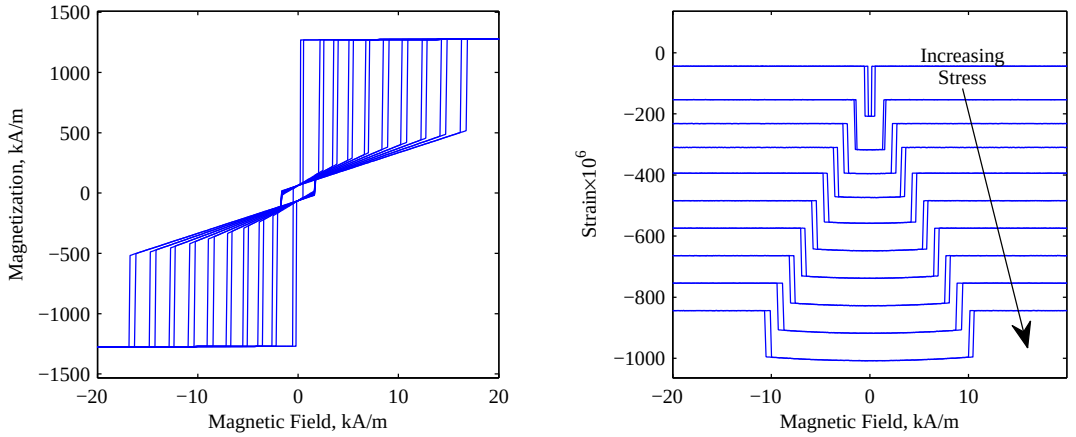

Figure 4.10: Hysteron calculations of (a) magnetization and (b) strain in the near [100] direction for applied field and constant stress.

be directly found from the saturation magnetization and magnetostriction values. The shear magnetostiction coefficient λ_{111} does not affect [100] behavior because no shear stresses are present. The coercive energy can be found from the areas of the hysteretic regions which give the energy loss. The values for the hysteron parameters are in Table 4.1.

Magnetization versus stress loops in Figures 4.6(a), 4.3(a) and 4.3(b) can be understood from the hysterons in Figure 4.9(b). Stress causes domain switching from the bias field direction or high state to the perpendicular plane or low state. At low stresses, when the material has been saturated positively prior to application of the bias field, if the hysteron is double-valued, it will be at the high state. Application of stress switches the hysteron to the low state and upon removal of the stress it remains in the low state. In subsequent loops, the hysteron starts and ends in the low state. This accounts for the observed non-closure of the first loop and closure of all subsequent loops; it is due to the history of the domain configuration. When the material is saturated negatively prior to bias field application, the hysteron starts in the low state and hence the first loop is closed also. A departure from this pattern occurs when the bias field is zero. In this case the hysteron begins negative, described by the $\mathbf{m}^I$ with easy axis oriented in the negative field direction. Applied stress switches the hysteron state to $\mathbf{m}^F$ with easy axis perpendicular to the bias field. Further cycles do not result in magnetization change because there is no field causing a preference for either the positive or negative rod directions. Thus the remanent magnetization of materials with kinematically reversible magnetomechanical coupling can be completely eliminated with a single stress cycle which forces all domains to the perpendicular plane. For sufficiently high bias fields, the hysteron is

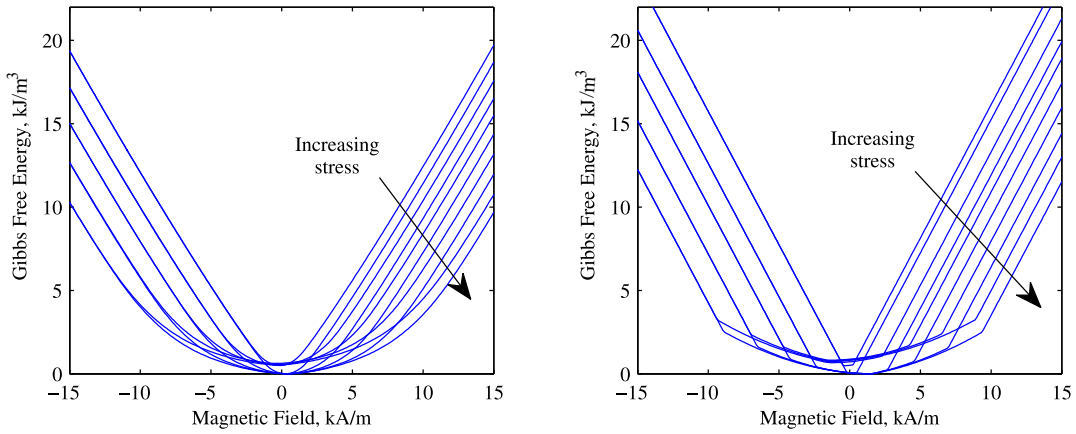

Figure 4.11: Dependence of Gibbs free energy on [100] field and stress for the $Fe_{81.6}Ga_{18.4}$, production grade sample, calculated from (a) the measurements and (b) the model with a single hysteron; bias stresses are 0, -19, -35, -52, and -70 MPa.

not double-valued at zero stress and thus there is no distinction between saturating the material positively or negatively; in both cases, the starting and ending domain configuration is all domains aligned in the bias field direction.

The dependence of the Gibbs free energy on [100] directed field can be calculated from the measurements by numerically integrating (4.20); the free energy calculated from applied field measurements are compared with the free energy of a hysteron in Figures 4.11 and 4.12 for the research and production grade samples, respectively. Just as a single Preisach relay is blocky compared to magnetization-field loops, the energy calculated from a single hysteron has much sharper transitions than the measurements. The energy loss associated with hysteretic domain reconfiguration causes a difference between the beginning and ending energy level which is characterized in the hysteron through the parameter E_c. For a full major loop of the research grade

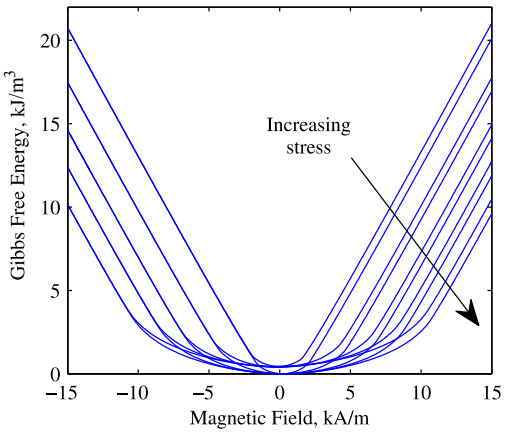

(a)

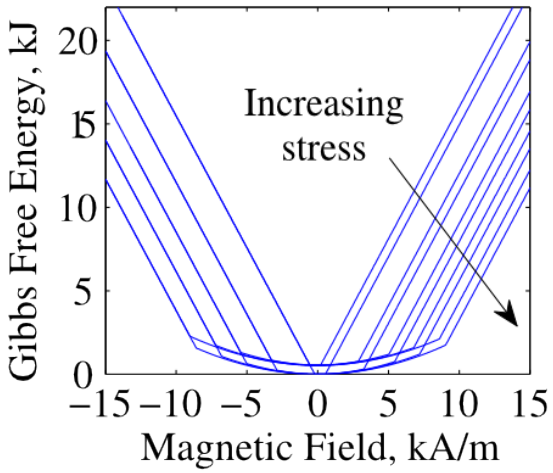

(b)

Figure 4.12: Dependence of Gibbs free energy on [100] field and stress for the $Fe_{81.5}Ga_{18.5}$, research grade sample, calculated from (a) the measurements and (b) the model with a single hysteron; bias stress levels are 0, -16, -28, -37, -46 MPa.

material, the hysteron switches four times and for the production grade material six switches occur, i.e. two switches occur for each hysteresis region—one on the up-side and one on the down-side. The five energy versus field curves for the research grade sample (calculated at different bias stresses) have nearly the same energy loss with an average of 873 J/m^3 which gives a value of 218 J/m^3 for E_c (a fourth of the loop energy loss.) The five energy versus field curves for the production grade sample have an average energy loss of 1.149 kJ/m^3 giving a value of 192 J/m^3 for E_c (a sixth of the loop energy loss.) Though the estimation of E_c is less for the production grade sample, the total energy loss is greater since more switching occurs owing to the low field hysteresis region. Despite this, the comparison is still unexpected and may result from describing the data with a single hysteron. In the next section, stochastic homogenization will be employed where statistical variation in E_c and the magnetic field are considered. Then, a collection of hysterons is considered and the energy loss in a major loop is the average value of the product of the number of switches occurring in a hysteron and E_c.

The dependence of the Gibbs free energy on [100] directed stress can be calculated from the measurements by numerically integrating (4.21). A comparison between the measurements and the free energy of a single hysteron is shown in Figure 4.13 at four different bias fields. Stress-strain data for the production grade sample is not available. For the research grade sample, three stress cycles were performed starting at zero stress at each bias field level. Energy is lost for each cycle resulting in a downward shift of the energy of an amount $2E_c$ since two switches occur—the up and the down switches between the directions parallel to the field and near perpendicular to the field. The average loss per cycle for the four measurements is 659 J/m^3 which is less

Table 4.1: Hysteron parameters for production grade $Fe_{81.4}Ga_{18.6}$ and research grade $Fe_{81.5}Ga_{18.5}$.

	$\mu_0 M_s$ (T)	K_{100} (kJ/m^3)	E_c (J/m^3)
Research	1.55	35	218
Production	1.6	35	192

	λ_{100} $\times 10^6$	λ_{111} $\times 10^6$	E (GPa)
Research	170	N/A	75
Production	110	3	98

than for applied field major loops. That the loss per loop is less than for the applied field measurements is expected since fewer switches or domain reconfigurations occur, however, according to the model it should be exactly half since half as many switches take place. Since it is not exactly half, this suggests the presence of a small amount of energy loss from purely mechanical hysteresis which is neglected here where the purely mechanical strain is modeled through Hooke's law or a quadratic strain energy density.

Stochastic homogenization

Material inclusions and lattice imperfections cause variations in the local magnetic field and coercive energy [92]. This variation is modeled using a statistically distributed interaction field $\mathbf{H}_I$, superimposed on the macroscopic applied field $\mathbf{H}$. The macroscopic magnetization and strain can be calculated through stochastic homogenization of the interaction field and coercive energy,

$$\begin{aligned} \bar{\mathbf{M}}(\mathbf{H},\mathbf{T}) &= \int_0^\infty \int_{-\infty}^\infty \mathbf{M}(\mathbf{H}+\mathbf{H}_I,\mathbf{T},E_c)\nu(\mathbf{H}_I,E_c)d\mathbf{H}_I dE_c, \\ \bar{\mathbf{S}}(\mathbf{H},\mathbf{T}) &= \int_0^\infty \int_{-\infty}^\infty \mathbf{S}(\mathbf{H}+\mathbf{H}_I,\mathbf{T},E_c)\nu(\mathbf{H}_I,E_c)d\mathbf{H}_I dE_c. \end{aligned} \tag{4.43}$$

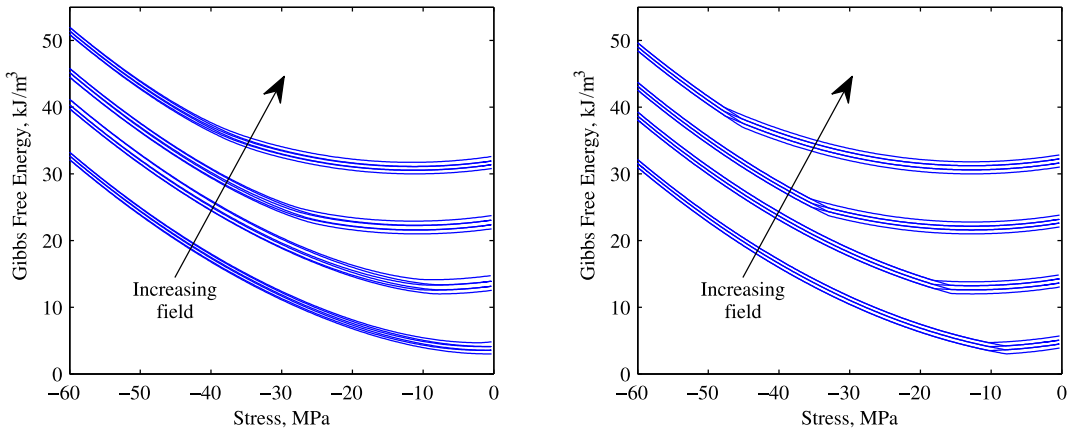

Figure 4.13: Dependence of Gibbs free energy on [100] field and stress for the $Fe_{81.5}Ga_{18.5}$, research grade sample, calculated from (a) the measurements and (b) the model with a single hysteron; bias field levels are 1.9, 3.2, 6.5, 8.9 kA/m.

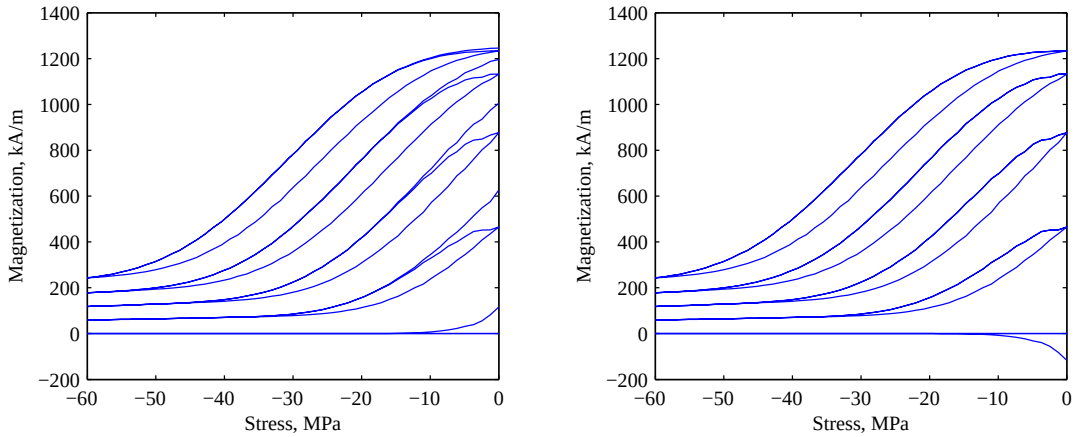

Figure 4.14: Simulated magnetization versus stress loops with bias field applied (a) after positive saturation and (b) after negative saturation.

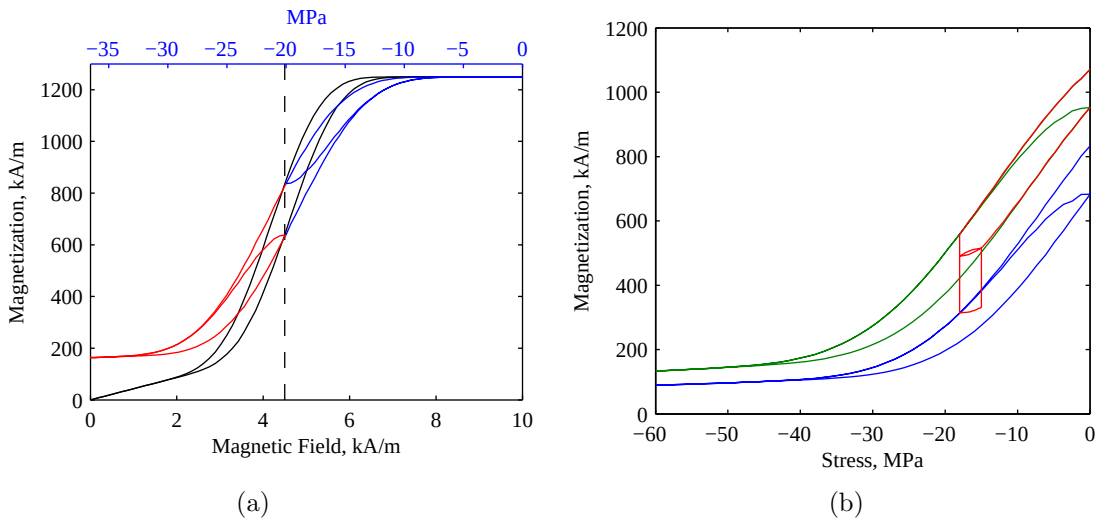

Figure 4.15: (a) magnetization excursions from the upper and lower hysteresis branches about a bias, cycled three times and (b) minor loops from alternately varying the field and stress about a bias point, cycled times.

The homogenization procedure (4.43) is similar to the homogenized energy model of Smith et al. [92] when thermal activation is neglected. Different energy potentials are used for the hysterons and the energy formulation here is done in 3-D. Additionally, a coercive energy consistent with the second law of thermodynamics was defined rather than a coercive field. This homogenization procedure has a distinct computational advantage over the vector implementation of Preisach models. Vector Preisach models for 3-D magnetization-field behavior use six statistically distributed parameters, two for each dimension which dictate when switching occurs from up to down and visa versa. The model proposed here includes four statistically distributed parameters meaning that the model implementation requires quadruple integration rather than the sextuple integration required for vector models using the classical Preisach model.

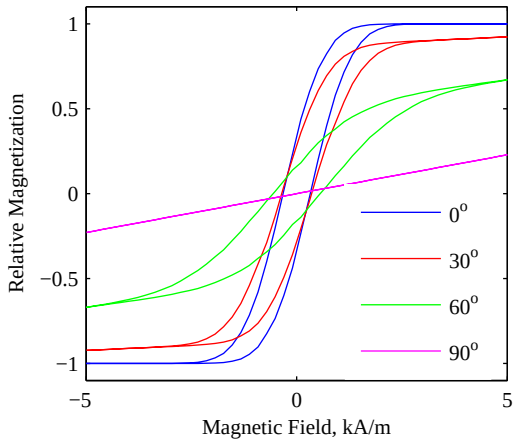

Figure 4.16: Stochastic homogenization of anisotropic, vector magnetization model.

The procedure here offers the additional advantage of simpler density functions since the effects of anisotropy and stress are incorporated in the hysteron behavior rather than the densities. Consider again the case of uniaxial anisotropy for which the hysterons are shown in Figure 4.8. Since the physical information regarding anisotropy is embedded in the hysteron, a simple Gaussian distribution of each component of the interaction field can be used. Figure 4.16 shows the homogenized model with a Gaussian distribution; the behavior is anisotropic even though all three components of the interaction field have the same standard deviation. An exponential distribution was used for the coercive energy.

The model is implemented by splitting the integrals into intervals and using 4-point Gauss quadrature integration for each interval. Magnetization and strain are thus calculated as the weighted sum of hysterons each with a different interaction field and coercive energy. The weights are the discrete form of the probability density function and are determined from least-squares optimization minimizing the error

between simulation and measurement. Figures 4.14(b) and 4.14(a) show simulations of magnetization versus stress loops for the conditions where the material is saturated positively prior to bias field application and negatively prior to bias field application. For the positive saturation case, the first loop is open and subsequent loops are closed. For the negative saturation case, all loops are closed except for the zero field bias case where stress removes the remanent magnetization.

Since the hysterons are stress and field dependent with a delay characterized by a single parameter, the coercive energy, the widths of the hysteretic regions in the magnetization versus field and magnetization versus stress curves are coupled. This is demonstrated in Figure 4.15(a); when applying a stress about a field and stress bias point starting from the top branch of a major magnetization versus field loop, the magnetization is pushed to the lower branch. Subsequent excursions from a cyclic stress always return to the lower branch. Starting from the lower branch, decreasing the stress followed by returning to the bias stress pushes the magnetization to the upper branch. Further stress cycles always return to the upper branch. This agrees with measurements in Figure 4.7(a). Biased minor loops obtained from alternately varying the field and stress give shapes similar to experiment and repeated loops do not exhibit accommodation (see Figures 4.15(b) and 4.4(b).)

4.2.3 Comparison with experiments

Here, the homogenized energy model is compared with research grade measurements. The hysteron parameters in Table 4.1 are used. The discretized probability

density in the homogenized energy model (4.43) are found through least-squares optimization to a single $\mathbf{M} - \mathbf{H}$ curve, measured with a -23 MPa bias stress. The procedure for identifying a general density, described in [93], is used. The integrals are performed over small segments using Gauss-quadrature. The bounds of the integrals for the interaction field are the fields required for positive and negative saturation, ± 10 kA/m. The bound for the coercive energy was chosen as 600, over twice the value used for a single hysteron in Section 4.2.2. This bound was chosen so that the value of $\nu(\mathbf{H}_I, E_c)$ is approximately zero at the bounds. This condition is necessary to ensure that the error introduced by using finite integral bounds is minimal. The Gauss quadrature rules give the hysteron evaluation points $(H_I)_{1,i}$, $(H_I)_{2,j}$, $(H_I)_{3,k}$, $E_{c,l}$ and weights w_{ijkl}. The hysteron values are then calculated at each of the Gauss points $\mathbf{M}(\mathbf{H} + \mathbf{H}_I, \mathbf{T}, E_c)_{ijkl}$. The values of the density at each Gauss point, ν_{ijkl} are found through the least-squares optimization routine lsqnonlin in Matlab. The objective function for the routine is the error between the model and the measurements. The model value of magnetization for each applied field and stress value are calculated with the summation over the four indices, $\mathbf{M}(\mathbf{H} + \mathbf{H}_I, \mathbf{T}, E_c)_{ijkl}(\nu w)_{ijkl}$, which approximates the fourth-order integration. The strain is calculated similarly, but not used in the optimization scheme. To illustrate the accuracy of the model, the density is first found from optimizing for the error between the model and the measured magnetization values for applied field at a constant stress of -23 MP. A comparison with the model is then made between the measured strain of this same experiment along with the magnetization and strain of a separate experiment of applied stress at a constant magnetic field of 4.8 kA/m. The result is displayed in Figure 4.17. The density is only optimized for the measurements in Figure 4.17(a), yet there is

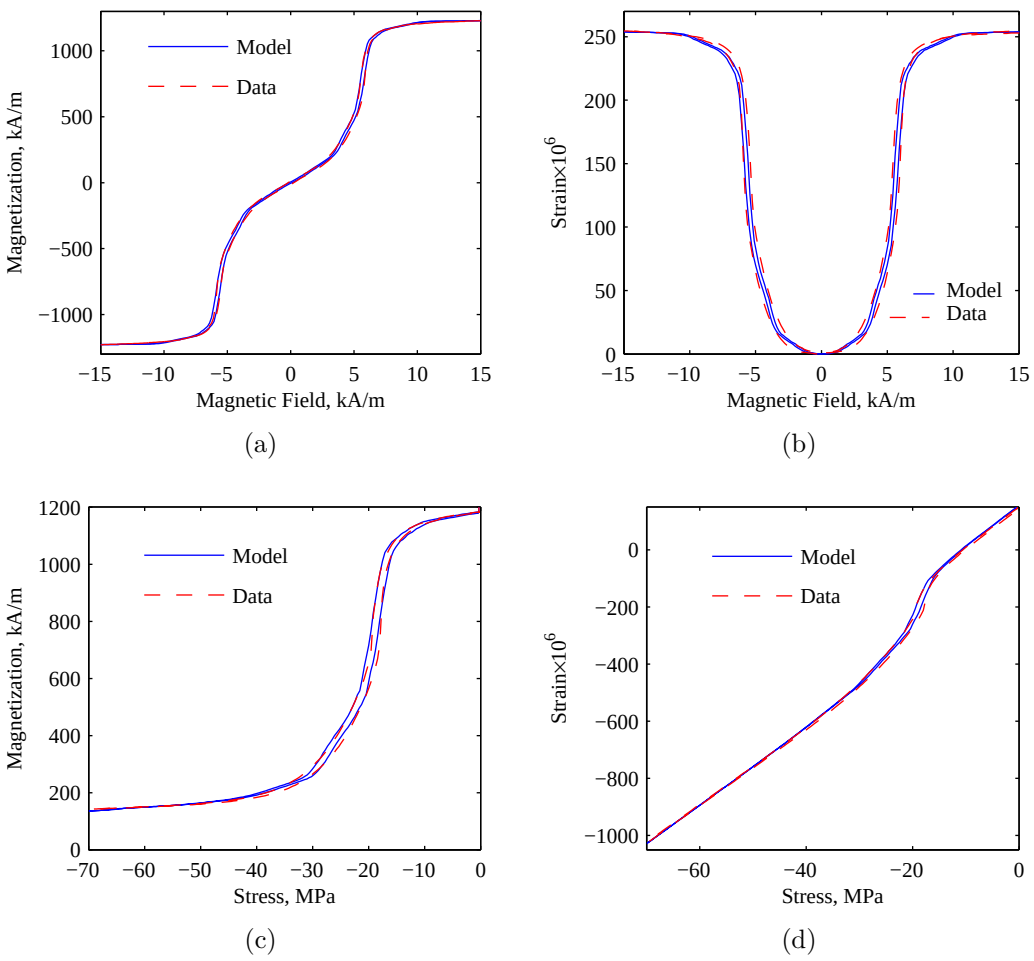

Figure 4.17: Model and measured magnetization and strain from (a),(b) applied field at a bias stress of -23 MPa and (c),(d) applied stress at a bias field of 4.8 kA/m.

excellent agreement between the model and the measurements in Figures 4.17(b)-(c). This confirms that the hysteron describes the underlying physical behavior since from figure to figure, the density remains the same and only the hysteron changes.

4.2.4 Concluding remarks

Measurements were presented to characterize the coupled nonlinear and hysteretic magnetization and strain of production and research grade Galfenol due to applied stress and field. It was shown that hysteresis for both applied quantities can be attributed to the same physical mechanism and that major magnetization versus stress loops in compression depend heavily on magnetic history at low stress levels. Remarkable reversibility in the magnetomechanical coupling was demonstrated by generating the same magnetization versus stress hysteresis loop both from a series of constant stress experiments and from a single constant field experiment. Cyclic application of alternately applied field and stress did not result in any noticeable accommodation, i.e., Galfenol constitutive behavior kinematically reversible.

A thermodynamic framework, satisfying the first and second laws, was developed to describe the observed nonlinear and hysteretic behavior. Like the measurements, magnetization and strain calculations from the model are thermodynamically irreversible, kinematically reversible, and demonstrate reversible magnetomechanical coupling. Hysteresis was attributed to energy loss during the process whereby the volume fractions of differently oriented domains change. This process was modeled by tracking the orientation of a number of elementary hysterons whose states represent the energetically possible domain orientations. The hysteron is 3-D, anisotropic, and both stress and field dependent. The model thereby does not depend on complex density functions to describe these effects, as do models based on the classical Preisach model. An additional advantage over Preisach models is that hysteron switching is characterized by a coercive energy rather than a 3-D coercive field. As a result, the

integration order is four rather than six. The model provides a physical and accurate description of 3-D magnetic and strain hysteresis for anisotropic magnetostrictive materials.

4.3 Efficient magnetic hysteresis model for field and stress application in magnetostrictive Galfenol

Recent models for the 3-D magnetomechanical response have relied on Boltzmann principles [6, 5, 7, 38, 40]. In the work of Armstrong [6], any bulk quantity related to magnetic moment orientation, such as magnetization or magnetostriction, is the expected value of a large collection of magnetic moments. The probability density function is the Boltzmann distribution in which all possible moment orientations are considered and minimum energy orientations are the most likely. While this model was formulated to describe anhysteretic Terfenol-D measurements, extensions include hysteresis in the presence of changing magnetic fields [5]. The hysteresis extension of the model suffers from poor accuracy due to the choice of moment orientations included in the summation for the expected value calculations—only moments attaining a local internal energy minimum are included (eight for Terfenol-D and six for Galfenol.) The work of Atulasimha, Akhras, and Flatau [7] improves the accuracy of the hysteresis model by including ninety-eight distributed orientations. The number of moments and their directions was chosen for $\langle 110 \rangle$-oriented material and may be different for other orientations. To improve the computational efficiency while preserving accuracy, Evans and Dapino [40] again restrict the number of possible orientations but use the local minima of the free-energy, which includes magnetic and magnetomechanical work terms. This approach is both efficient and accurate for device characterization, design, and control.

The previous energy-weighted models have three critical limitations. The first is that the form of the magnetocrystalline anisotropy energy, which determines the orientations preferred by magnetic moments, is material specific. Current material processes for Galfenol are capable of significantly changing the magnetocrystalline anisotropy energy [86], hence determining the appropriate form of the anisotropy energy is challenging and difficult to generalize. The second limitation of previous models is the absence of a mechanism for magnetic hysteresis under stress application. The third limitation is that minor loops from field application have negative susceptibility at the field reversal points, which is inconsistent with data. These limitations are addressed in this work.

First, a general formulation for magnetocrystalline anisotropy energy is developed. Rather than seek to define a global energy which includes the local energy minima or preferred orientations, we define the energy locally about the known preferred orientations. Second, the magnetic hysteresis model is extended to account for hysteresis during both magnetic field and stress trajectories. A single parameter characterizes the hysteresis delay for both field and stress application. Third, the effect of reversible changes in domain walls from wall bowing is included, while restricting the effect of irreversible processes so as to exclude the unphysical behavior of negative susceptibility.

4.3.1 Model development and experiments

Ferromagnetic materials are composed of regions of uniform magnetization M_s called domains [61]. In the Stoner-Wohlfarth (S-W) approximation used here and in other magnetomechanical models [54], the material is modeled as a collection of

non-interacting, single-domain particles [65]. The internal energy of a particle is due to magnetocrystalline anisotropy which gives domains preferred or easy directions. Work is required to rotate domains away from these easy directions. As magnetic fields $\mathbf{H}$ and stresses $\mathbf{T}$ are applied, domains rotate towards the field direction and perpendicular to the principal stress directions. When magnetic domains rotate, the magnetomechanical coupling induces lattice strain and bulk magnetostriction. For a material composed of a collection of S-W particles in thermodynamic equilibrium having r possible orientations, the bulk magnetization $\mathbf{M}$ and magnetostriction $\mathbf{S}_m$ are the sum of the magnetization $M_s\mathbf{m}^k$ and magnetostriction $\mathbf{S}_m^k$ due to each orientation, weighted by the volume fraction ξ^k of particles in each orientation

$$\mathbf{M} = M_s \sum_{k=1}^{r} \xi^k \mathbf{m}^k, \qquad \mathbf{S}_m = \sum_{k=1}^{r} \xi^k \mathbf{S}_m^k. \tag{4.44}$$

The total strain is the sum of the magnetostriction and the purely mechanical strain $\mathbf{sT}$, where $\mathbf{s}$ is compliance. The anhysteretic values of the volume fractions are calculated using an energy-weighted average,

$$\xi_{an}^k = \frac{\exp\left(-G^k/\Omega\right)}{\sum_{k=1}^{r} \exp\left(-G^k/\Omega\right)}. \tag{4.45}$$

The energy G^k is the part of the free energy related to orientation $\mathbf{m}^k$ and the parameter Ω is the Armstrong smoothing factor. A Boltzmann-type, energy-weighting expression was first proposed for use in magnetostrictive materials by Armstrong [6, 5] and applied to Galfenol by Atulasimha, Flatau, and Summers [10]. The cited works use a large number r of fixed $\mathbf{m}^k$. Evans and Dapino reduced r while maintaining accuracy by utilizing only $\mathbf{m}^k$ which attain a local energy minimum [40].

New energy formulation

The free-energy of a magnetostrictive material has terms for magnetic anisotropy, magnetomechanical coupling, and Zeeman or field energy. These energies are formulated by idealizing the complex domain structure of ferromagnetic materials as a system of non-interacting, single-domain, Stoner-Wohlfarth (S-W) particles. The system of S-W particles is composed of r distinct groups or variants which rotate about an energetically favorable or easy direction which for the k^{th} variant is $\mathbf{c}^k$. The variants are distinguished by their easy directions. The free energy is formulated separately for each of the variants whereas in previous work (Atulasimha, Akrhas, and Flatau [7], and Evans and Dapino [40]) a single energy expression is used for any S-W particle orientation. The benefit of this approach is that the anisotropy energy depends explicitly on the easy direction. We can thus describe arbitrary anisotropy symmetries, needing only a knowledge of the easy directions.

The anisotropy energy of the k^{th} variant, G_A^k, is the work required to rotate a S-W particle away from $\mathbf{c}^k$. This is analogous to mechanical systems where work is required to displace a spring from equilibrium. This can be expressed as

$$G_A^k = \frac{1}{2} K^k |\mathbf{m}^k - \mathbf{c}^k|^2. \tag{4.46}$$

For materials with a cubic lattice, the $\langle 100 \rangle$ or $\langle 111 \rangle$ directions tend to be easy. The anisotropy coefficient in each direction family is the same, thus $K^k = K_{100}$ for all six $\langle 100 \rangle$ directions and $K^k = K_{111}$ for all eight $\langle 111 \rangle$ directions. For negative anisotropy coefficients K^k, the direction $\mathbf{c}^k$ is magnetically hard or an unstable equilibrium. Galfenol can thus have six, eight, or fourteen easy directions, which dictates the number of variants r. While unannealed Galfenol is generally cubic and thus has

either one or two distinct K^k coefficients, stress annealing or residual stresses from the crystal growth process can cause a change in symmetry resulting in distinct values for K^k within the orientation families $\langle 100 \rangle$ and $\langle 111 \rangle$.

The magnetomechanical coupling energy G_C^k of a single S-W particle with magnetization M_s is the strain energy density resulting from the magnetostriction of the particle,

$$G_C^k = -\mathbf{S}_m^k \cdot \mathbf{T}, \tag{4.47}$$

and the Zeeman energy is

$$G_Z^k = -\mu_0 M_s \mathbf{m} \cdot \mathbf{H}. \tag{4.48}$$

Kittel [61] provides expressions for the magnetostriction of a S-W particle with cubic symmetry,

$$\mathbf{S}_m^k = \begin{bmatrix} (3/2)\lambda_{100}\left(m_1^k\right)^2 \\ (3/2)\lambda_{100}\left(m_2^k\right)^2 \\ (3/2)\lambda_{100}\left(m_3^k\right)^2 \\ 3\lambda_{111} m_1^k m_2^k \\ 3\lambda_{111} m_2^k m_3^k \\ 3\lambda_{111} m_3^k m_1^k \end{bmatrix}. \tag{4.49}$$

The total free-energy for each particle variant therefore is

$$G^k = K^k |\mathbf{m}^k - \mathbf{c}^k|^2 - \mathbf{S}_m^k \cdot \mathbf{T} - \mu_0 M_s \mathbf{m}^k \cdot \mathbf{H}, \tag{4.50}$$

which is minimized to calculate the particle orientation.

Calculation of particle orientations

The magnetic orientations $\mathbf{m}^k$ of the S-W particles are calculated from minimization of (4.50) with constraint $C = |\mathbf{m}^k| - 1 = 0$ (since $\mathbf{m}^k$ is a unit vector). The constrained minimization can be formulated as an inhomogeneous eigenvalue problem through the use of Lagrange multipliers. Gathering terms from (4.50) and expressing

the particle free energy as $G^k = \frac{1}{2}\mathbf{m}^k \cdot \mathbf{K}^k \mathbf{m}^k - \mathbf{m}^k \cdot \mathbf{B}^k$, one can write the eigenvalue problem as

$$\left(\mathbf{K}^k - \gamma \mathbf{I}\right) \mathbf{m}^k = \mathbf{B}^k, \tag{4.51}$$

where the magnetic stiffness matrix $\mathbf{K}^k$ and force vector $\mathbf{B}^k$ are

$$\mathbf{K}^k = \begin{bmatrix} K^k - 3\lambda_{100}T_1 & -3\lambda_{111}T_4 & -3\lambda_{111}T_6 \\ -3\lambda_{111}T_4 & K^k - 3\lambda_{100}T_2 & -3\lambda_{111}T_5 \\ -3\lambda_{111}T_6 & -3\lambda_{111}T_5 & K^k - 3\lambda_{100}T_3 \end{bmatrix}, \tag{4.52}$$

$$\mathbf{B}^k = \begin{bmatrix} c_1^k K^k + \mu_0 M_s H_1 & c_2^k K^k + \mu_0 M_s H_2 & c_3^k K^k + \mu_0 M_s H_2 \end{bmatrix}^{\mathrm{T}}. \tag{4.53}$$

While the orientations can be easily solved for in terms of γ, determination of γ requires solution of a sixth-order polynomial obtained by substitution of each γ-dependent orientation into the constraint. The constraint is relaxed through linearization about the easy direction $\mathbf{c}^k$. This has little effect on the calculated bulk magnetization and magnetostriction, since the energy weighting operation (4.44) ensures that particles which have rotated far from the easy axis are less likely or have smaller volume fractions than those particles which have not rotated far. In other words, the orientations which have easy axis near the field direction and perpendicular to the stress direction are most favorable. For the linearized constraint, the solution to the inhomogeneous eigenvalue problem is

$$\mathbf{m}^k = \left(\mathbf{K}^k\right)^{-1} \left[\mathbf{B}^k + \frac{1 - \mathbf{c}^k \cdot \left(\mathbf{K}^k\right)^{-1} \mathbf{B}^k}{\mathbf{c}^k \cdot \left(\mathbf{K}^k\right)^{-1} \mathbf{c}^k} \mathbf{c}^k\right]. \tag{4.54}$$

The particle orientations (4.54) define the orientations to be included in the energy averaging (4.44), thus in the present formulation r depends on the number of easy axes. Galfenol has six easy axes in the $\langle 100 \rangle$ directions.

Comparison between Armstrong model for cubic materials and discrete energy-averaged model

The traditional manner of expressing anisotropy energy is to define a global energy expression as a function of S-W particle orientation, which has minima corresponding to the easy axes. The form for cubic materials is [21, 61]

$$G_A = K_4(m_1^2 m_2^2 + m_2^2 m_3^2 + m_3^2 m_1^2). \tag{4.55}$$

The subscript of the anisotropy coefficient refers to the order of the expression which is fourth-order in this case. This energy has extrema in the $\langle 100 \rangle$ and $\langle 111 \rangle$ directions, consistent with Galfenol, and for this reason it has been used in magnetomechanical models for Galfenol [7, 40]. The anisotropy of Galfenol can be changed through stress annealing—application of stress at elevated temperatures. Annealing along a $\langle 100 \rangle$ direction has been shown to result in Galfenol material with tetragonal anisotropy where the four $\langle 100 \rangle$ directions perpendicular to the annealing direction have a lower energy than the remaining two.

The formulation by Trémolet [64] for tetragonal symmetry is

$$\begin{aligned} G_A =& K_2 \left(m_3^2 - \frac{1}{3} \right) + K_4 \left(m_1^4 + m_2^4 + m_3^4 - \frac{3}{5} \right) \\ &+ K_4' \left(m_3^4 - \frac{6}{7} m_3^2 + \frac{3}{35} \right), \end{aligned} \tag{4.56}$$

where the [001] and [00$\bar{1}$] directions have different energies than the remaining four $\langle 100 \rangle$ orientations. The following reduced form for tetragonal symmetry has been used for stress-annealed Galfenol [86, 38],

$$G_A = K_4(m_1^4 + m_2^4 + m_3^4) + K_2 m_3^2. \tag{4.57}$$

While for the global formulations different material symmetries necessitate different forms for G_A, adapting the locally defined expression (4.46) for different material

symmetries requires only an adjustment of the coefficients. Another advantage of the local formulation is the simplicity of the minimization process. Consider for example a cubic material, the globally defined free energy G in this case is

$$G = K_4(m_1^2 m_2^2 + m_2^2 m_3^2 + m_3^2 m_1^2) - \mathbf{S}_m(\mathbf{m}) \cdot \mathbf{T} - \mu_0 M_s \mathbf{m} \cdot \mathbf{H}. \tag{4.58}$$

Depending on the values of the coefficients and the applied stress and field, this expression can have anywhere from one to six minima requiring a robust, nonlinear minimization scheme. The fact that minima can disappear presents a challenge when utilizing (4.44) to calculate the bulk magnetization and magnetostriction with direct energy minimization, since r varies with stress and field. To obviate this issue, previous works [40, 41] considered small particle rotations by performing a second-order expansion of (4.58) about the easy crystal directions. The approach here is to formulate second-order energy expressions directly, for each easy direction.

A comparative study shows that minimum energy orientations using the globally defined energy are similar to the minimum orientations of the locally defined energies. Consider a material with cubic symmetry having $\langle 100 \rangle$ easy directions. For the global energy expression, (4.58) is used, and for the local formulation six expressions are used, one for each of the easy directions. Since the symmetry is cubic, all of the local expressions (4.46) have the same coefficient $K^k = K_{100}$ and differ only in $\mathbf{c}^k$.

When applying field and stress along the [100] direction, energy (4.58) initially has six minimum orientations. Two of the minima are

$$\mathbf{m} = \begin{bmatrix} \pm 1 \\ 0 \\ 0 \end{bmatrix}, \tag{4.59}$$

and the remaining four depend on stress and field, corresponding to the rotation of particles away from the four remaining $\langle 100 \rangle$ directions and towards the applied field.

Stress tends to impede these rotations since it favors perpendicular directions. Evans and Dapino [41] showed that for small rotations these minima have the following component in the [100] direction,

$$m_1 = \frac{\mu_0 M_s}{2K_4 - 3\lambda_{100} T} H. \tag{4.60}$$

The other components are simply zero or ± 1.

The local energies (4.50) result in similar expressions for the six minima. For the energy expressions with $\mathbf{c}^k = [\pm 1\ 0\ 0]$ the minima are

$$\mathbf{m} = \begin{bmatrix} \pm 1 \\ 0 \\ 0 \end{bmatrix}, \tag{4.61}$$

and for the expressions with $\mathbf{c}^k = [0\ \pm 1\ 0]$ and $\mathbf{c}^k = [0\ 0\ \pm 1]$, the component in the [100] direction is

$$m_1 = \frac{\mu_0 M_s}{K_{100} - 3\lambda_{100} T} H, \tag{4.62}$$

and the other components are again zero or ± 1. Since (4.60) and (4.62) describe the same magnetization process, $K_{100} = 2K_4$ should be satisfied.

The Armstrong model uses the global energy expression with fixed orientations whereas the discrete energy-averaged model presented here uses local energy expressions with field and stress dependent orientations. Calculation of bulk behavior using the two approaches yields similar results so long as one recognizes that $K_{100} = 2K_4$. Two cases are considered, [100] field application and [110] field application, both with a bias stress. The bulk magnetization is calculated using (4.45) with various values of smoothing parameter Ω. In the Armstrong model [6], the global energy expression is used and r in (4.45) is a number of fixed particle orientations. In the model presented here, local energy expressions are used and for cubic symmetry, $r = 6$ variants of

orientations which rotate with stress and field, determined from direct minimization of the energy corresponding to each variant. To determine r in the Armstrong formulation, the discrete form (4.45) is found through discretization of the continuous form,

$$\xi(\phi,\theta) = \frac{\exp(-G/\Omega)\sin\phi \; d\phi d\theta}{\int_0^{\pi}\int_0^{2\pi} exp(-G/\Omega)\sin \; \phi d\phi d\theta}, \tag{4.63}$$

where ξ is now interpreted as a probability density and $(\phi,\ \theta)$ represent the particle orientation in spherical coordinates. To numerically integrate, the integration intervals are discretized into N_I segments and over each segment, fourth-order Gauss-quadrature is used. This results in $4N_I$ values each for ϕ and θ and $r = 16N_I^2$ total particle orientations. The required N_I for good accuracy depends on Ω. As Ω approaches zero, $\xi = 1$ for the globally minimum orientation and $\xi = 0$ for all other orientations. In the Armstrong model, if the discretization is too coarse, then it may be that none of the fixed orientations are near the global minimum. In the model presented here, this issue does not arise because the global minimum is simply the minimum of the local minima which are calculated explicitly. Figure 4.18(a) shows $M - H$ curves calculated with the Armstrong model at constant T in which H and T are applied in the $\langle 110 \rangle$ direction and Ω is low. Different values of N_I are used. Curves calculated with $N_I = 20$ ($r = 6400$) and $N_I = 40$ ($r = 25600$) show a small difference, therefore the error in the $N_I = 40$ case is assumed negligible and this curve is taken as the benchmark for error calculations. The relative error was calculated for each of the curves at all field values and is shown in Figure 4.18(b). The maximum error is around 60% for $N_I = 5$ and 10% for $N_I = 20$.

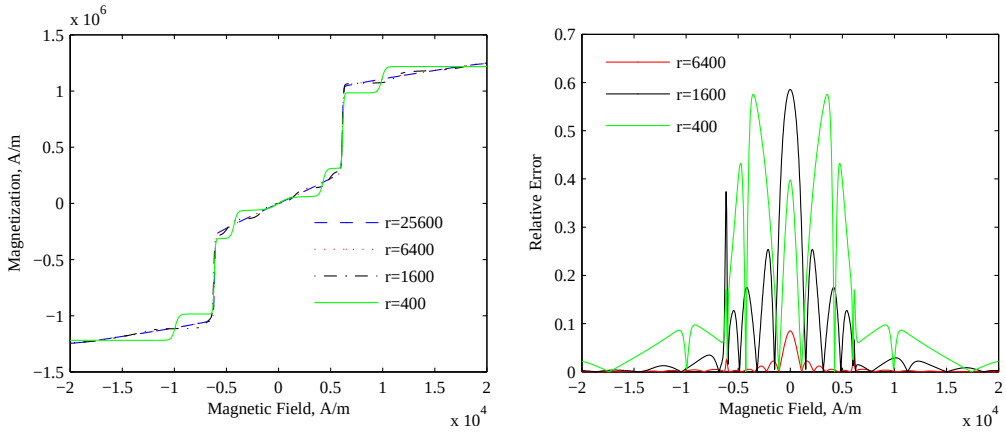

(a) (b)

Figure 4.18: Effect of discretization in the Armstrong model.

Since it has been demonstrated that $r = 25600$ results in good accuracy, this is used for Armstrong model calculations in comparing $M - H$ curves with the anhysteretic discrete energy-averaged model (see Figure 4.19.) The anhysteretic discrete energy-averaged model uses the local energy definition (4.50), S-W particle orientations (4.54) and discrete energy-average (4.45). The model parameters used for the comparison in Figure 4.19 are $\mu_0 M_s = 1.59$ T, $K_{100} = 2K_4 = 17.5$ kJ/m^3, $(3/2)\lambda_{100} = 260 \times 10^{-6}$, and $3\lambda_{111} = -10 \times 10^{-6}$ at various values of Ω (50, 100, 200, 400, and 600 J.) A bias stress of -26 MPa is used for the $\langle 100 \rangle$ calculations and -50 MPa for the $\langle 111 \rangle$ calculations.

Although the difference between the Armstrong model and the model presented here is greater with increasing Ω, both models provide the same trends. When Ω is small, the magnetization is only due to the global minimum orientation. In this case the two models are nearly identical. There is a small difference at high fields (~ 10.5 kA/m) for $\langle 110 \rangle$ application owing to the fact that a linear approximation was used

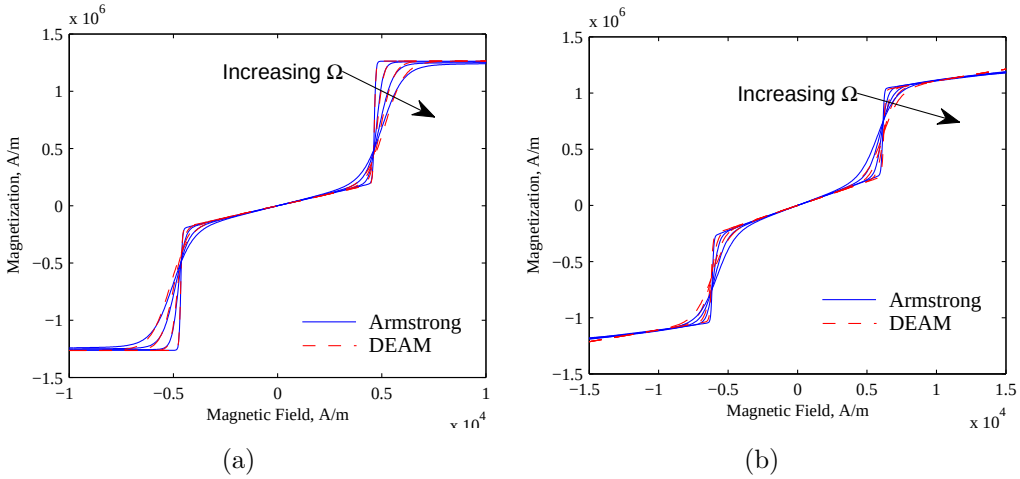

Figure 4.19: Comparison of Armstrong model with the discrete energy-averaged model.

for computing the minimum of the local energy expressions for the discrete energy-averaged model. Though this error is small in all cases, it is greater when field or stress rotates particles to a direction far from the easy axes. In both models, an increasing Ω results in smoother curves. Whereas the curves for small Ω have sharp transitions representing a change in the global minimum from one local minimum to another, for large Ω the volume fractions or probability density are more distributed, meaning that the bulk magnetization has contributions from the global minimum as well as the other local minima in the discrete energy-averaged model, and it has contributions from all the fixed orientations in the Armstrong model. The difference between the two models for higher Ω can be attributed to the presence of orientations that are neither global nor local minima in the Armstrong model, since the orientations used in the summation of the Armstrong model are found from Gauss-quadrature rules without regard to energy.

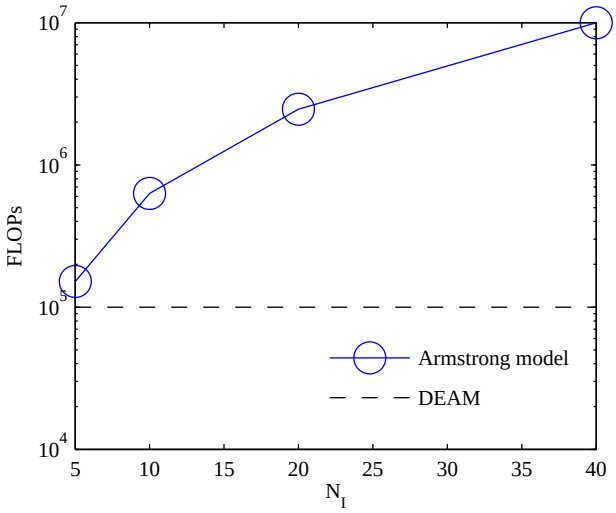

Figure 4.20: FLOPs required for Armstrong model calculation.

In general, the discrete energy-averaged model requires fewer floating-point operations since it utilizes only six particle orientations. Figure 4.20 shows the number of FLOPs required to calculate the magnetization and magnetostriction using $N_I = 5,\ 10,\ 20,\ 40$. The relationship is quadratic since the total number of particle orientations is a function of the square of N_I. For the benchmark $N_I = 40$, the number of flops is 10 MFLOPs. For the discrete energy-averaged model the number of orientations is fixed and the required flops is 0.1 MFLOPs, an improvement of two orders of magnitude. The FLOPs were found by calculating 1000 magnetization and magnetostriction values using a single core of an Intel Core 2 Duo processor running at 1 GHz. The models were implemented in Matlab and timed. The total time was divided by 1000 which was converted to FLOPs using the processor speed and assuming the processor performs 2 FLOPs per clock cycle (measured in Matlab using an algorithm with a known number of FLOPs.)

$\langle 100 \rangle$ Single-crystal $Fe_{79.1}Ga_{20.9}$ measurements and anhysteretic model

Magnetization versus magnetic field measurements at constant stress for [100]-oriented, single-crystal $Fe_{79.1}Ga_{20.9}$ are compared with the anhysteretic discrete energy-averaged model ((4.45), (4.50), and (4.54).) The material was grown with the Bridgman method resulting in a single-crystal rod. Although the material is body-centered cubic, the magnetostriction measurements indicate that the magnetic anisotropy has tetragonal symmetry. Material with cubic symmetry has a maximum magnetostriction of λ_{100} in the [100] direction when no stress is applied and $(3/2)\lambda_{100}$ when sufficient stress is applied to align all domains perpendicular to the field and stress. The measurements in Figure 4.21(b) show that the maximum magnetostriction exhibits little dependence on the bias stress. This suggests that the material has tetragonal symmetry where perpendicular domain orientations are energetically preferred to parallel domain orientations, even when no stress is applied. This could be due to either the crystal growth process or tetragonal material phases. Studies have shown that Fe-Ga alloys have a complicated phase diagram and any given alloy may have multiple phases present [67].

The magnetization data has three linear regions separated by nonlinear transitions (see Figure 4.21(a).) In the model, these regions are described by three variants of S-W particles. The linear region below the approach to magnetic saturation is dominated by rotation of particles away from the [010], [$0\bar{1}0$], [001], [$00\bar{1}$] directions—orientations initially perpendicular to the applied stress and field—and into the field direction. These orientations have anisotropy coefficient $K_\perp$. The component of the orientation in the [100] direction, $m_\perp$ given by (4.62), results in a contribution of $M_\perp = M_s m_\perp(\xi_{010} + \xi_{0\bar{1}0} + \xi_{001} + \xi_{00\bar{1}})$ to the total magnetization. The remaining

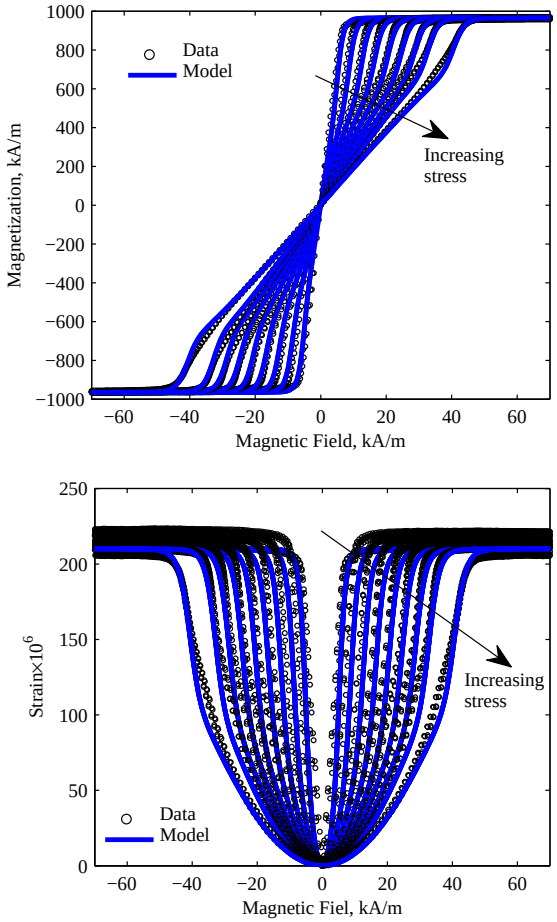

Figure 4.21: Magnetization and magnetostriction of ⟨100⟩ single-crystal $Fe_{79.1}Ga_{20.9}$ at constant stress values of 0.689, 13.8, 27.6, 41.3, 55.1, 68.9, 82.7, 96.4, 123 MPa (compression), compared with anhysteretic model calculations.

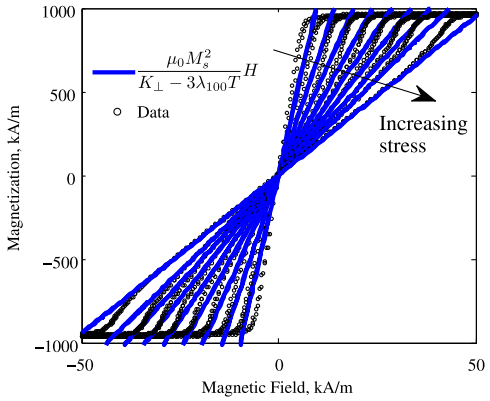

Figure 4.22: Rotation of perpendicular domain orientations compared with data of $\langle 100 \rangle$ single-crystal $Fe_7 9.1 Ga_2 0.9$ at constant stress values of 0.689, 13.8, 27.6, 41.3, 55.1, 68.9, 82.7, 96.4, 123 MPa (compression).

regions are the positive and negative magnetic saturation regions where little magnetization change occurs with varying magnetic fields. These regions are dominated by [100] and $[\bar{1}00]$ particles which are already aligned with the field and stress axis. These particles have anisotropy coefficient $K_\parallel$. The former orientation contributes to positive saturation and the latter to negative saturation. Their contributions to the total magnetization are $M_{[100],[\bar{1}00]} = M_s \xi_{[100]},\ -M_s \xi_{[\bar{1}00]}$.

The volume fractions are determined from the energy-weighted average (4.45). Stresses favor the off-axis or initially-perpendicular variants, each of which have the same energy level, from (4.50)

$$E_\perp = \frac{H^2 (\mu_0 M_s)^2 - 3\lambda_{100} K_\perp T + K_\perp^2}{6\lambda_{100} T - 2K_\perp}. \tag{4.64}$$

Applied magnetic fields favor the parallel orientations which have energies

$$E_{[100],[\bar{1}00]} = \mp H \mu_0 M_s - \frac{3}{2}\lambda_{100} T - \frac{1}{2} K_\parallel. \tag{4.65}$$

With no applied field and stress, $E_\perp$ is much greater than $E_{[100],[\bar{1}00]}$. In the energy weighted average this results in $\xi_{010} + \xi_{0\bar{1}0} + \xi_{001} + \xi_{00\bar{1}} \approx 1$ and the magnetization is simply (4.62); this expression is compared with the data in Figure 4.22. The anisotropy constant $K_\perp$ can thus be calculated directly from the slope of the linear magnetization region. The kink in the magnetization curves or the transition from the linear region to saturation occurs when $E_\perp = E_\parallel$. This gives a measure of the other anisotropy coefficient, $K_\parallel$. Two of the remaining parameters are determined directly from the data; M_s and $(3/2)\lambda_{100}$ are found from the magnetization and magnetostriction at saturation. The smoothing parameter Ω is determined through least-squares optimization and determines the sharpness of the transition to saturation. For $\langle 100 \rangle$ application, the shear magnetostriction coefficient λ_{111} does not enter into the model and hence cannot be determined from the data. The total magnetization as calculated by (4.45) is compared with the data in Figure 4.21. The model parameters are provided in Table 4.2.

Magnetomechanical hysteresis

Hysteresis is included in energy-weighting models [5, 7, 40] through an evolution equation for the volume fractions,

$$d\xi^k = \frac{1}{k_p} \left(\xi^k_{an} - \xi^k \right) |dH|. \tag{4.66}$$

Parameter k_p quantifies pinning site density of the material. Pinning refers to material impurities or defects which impede domain wall motion. This hysteresis model, first proposed by Armstrong [5], employs concepts from the Jiles-Atherton model [51]. In the energy-weighted averaging model framework, domain wall motion is indirectly accounted for through changes in the volume fractions. The energies described in the

previous section pertain to S-W particles which approximately represent domain orientations. The anhysteretic volume fractions ξ_{an}^k are calculated through the averaging function (4.45) which is a function of stress and magnetic field. As stress and magnetic field change, the volume fractions change. Physically, the changes occur through motion of domain walls where the motion grows one set of domain orientations and shrinks another. As the walls pass through defect sites, energy is lost. In the Jiles-Atherton model, which is a domain wall motion model and does not involve volume fractions and domain rotation, this loss is included through a differential equation for magnetization. The energy loss is included in the present framework through the differential equation (4.66) for the volume fractions.

The work of Atulasimha, Akrhas, and Flatau [7] shows that minor loops are closed for the hysteresis model (4.66). Where major loops are complete hysteresis cycles of the magnetization extending from negative saturation to positive saturation, minor loops are small excursions from the major loop due to cyclic field reversal of a magnitude less than that required for saturation. That minor loops are closed in the present framework is an improvement over the Jiles-Atherton hysteresis model where minor loops are not automatically closed. In operating regimes where thermal after-effects are negligible, measured minor loops in ferromagnetic materials are typically closed.

The model represented by (4.66) has three deficiencies: (1) it does not account for hysteresis when stress is varied at constant field, (2) minor loops have an unphysical, negative differential susceptibility at the reversal points, and (3) it is one dimensional. Reported Galfenol measurements indicate that hysteresis is more significant for stress application than for field application [9]. In this work, the reason for the apparently

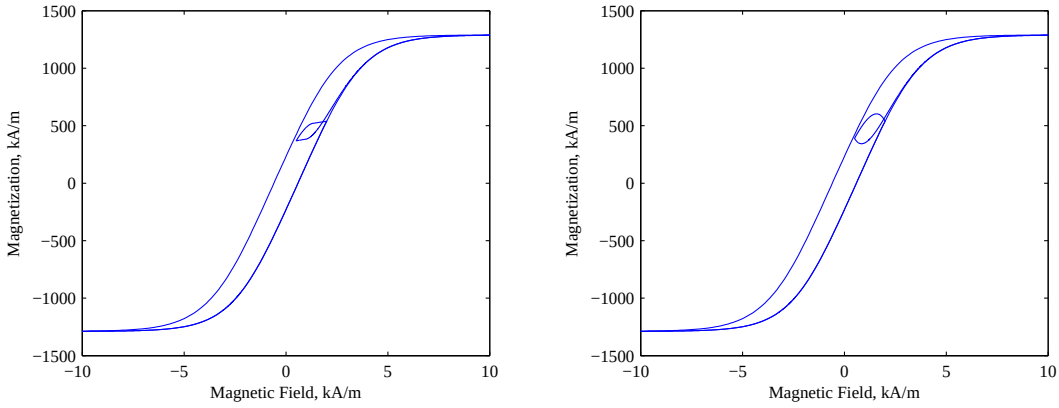

Figure 4.23: Minor loop calculations using (a) the discrete energy-averaged model and (b) the Armstrong model.

wider hysteresis loops for stress application is found to be that for Galfenol the Zeeman energy (4.48) is generally larger than the magnetomechanical coupling energy (4.47).

Since both stress and field change the domain volume fractions through domain wall motion, a single evolution equation should describe the volume fractions in the presence of energy loss from wall pinning for both stress and field application. Additionally, reversible volume fraction changes from domain wall bowing should be accounted for while restricting the irreversible changes predicted by the model which lead to unphysical, negative differential susceptibility. The irreversible changes are described by a modified form of (4.66) which includes stress application and consistent scaling,

$$\begin{aligned} d\xi_{irr}^k =& \frac{\zeta}{k_p}\left(\xi_{an}^k - \xi_{irr}^k\right)\left[\mu_0 M_s(|dH_1| + |dH_2| + |dH_3|) + (3/2)\lambda_{100}(|dT_1| + |dT_2| + |dT_3|)\right. \\ & \left. +3\lambda_{111}(|dT_4| + |dT_5| + |dT_6|)\right]. \end{aligned} \tag{4.67}$$

In this extended evolution equation, 3-D inputs are included and scaled appropriately so that each input has units of energy density, hence, k_p has units of energy density. The value of ζ is zero or one and used to restrict irreversible changes to physically appropriate situations. First the fractional change is calculated with $\zeta = 1$ and if the resulting increment gives a negative susceptibility, then it is changed to zero. This condition was given by Jiles, Thoelke, and Devine [55]. The total volume fraction change is

$$d\xi^k = (1 - c)d\xi^k_{irr} + cd\xi^k_{an}, \tag{4.68}$$

where the parameter c is non-dimensional and has a value between zero and one. For a value of one, volume fraction changes are completely reversible and for a value of zero they are completely irreversible [52]. The magnetic hysteresis model for magnetomechanical materials defined by (4.67) and (4.68) describes magnetic hysteresis for 3-D field and stress inputs. By including reversible magnetization changes and restricting irreversible changes to physically relevant cases, minor loops do not have unphysical negative differential susceptibility as exhibited by the previous model (4.66). Figure 4.23 demonstrates this improvement.

4.3.2 Comparison with experiments

$\langle 100 \rangle$ textured $Fe_{81.5}Ga_{18.5}$ measurements and hysteretic model

Meaurements of $\langle 100 \rangle$ oriented, textured $Fe_{81.5}Ga_{18.5}$ grown with FSZM at Etrema Products Inc. are compared with model calculations. The magnetostriction measurements (see Figure 4.24) indicate a slightly tetragonal magnetic anisotropy but much less so than the higher Ga content sample grown with the Bridgman technique. The ratio of the maximum magnetostriction under zero stress and at 32.3 MPa is 1.34.

Table 4.2: Model parameters.

	$\mu_0 M_s$ (T)	$K_\perp$, $K_\parallel$ (kJ/m^3)	$(3/2)\lambda_{100} \times 10^6$	$3\lambda_{111} \times 10^6$
$\langle 100 \rangle$ $Fe_{81.5}Ga_{18.5}$	1.55	35, 34	255	N/A
$\langle 100 \rangle$ $Fe_{79.1}Ga_{20.9}$	1.21	9.95, 2.0	210	N/A
$\langle 110 \rangle$ $Fe_{81.6}Ga_{18.4}$	1.58	100, 100	290	-40

	Ω (J/m^3)	k_p (J)	c	E (GPa)
$\langle 100 \rangle$ $Fe_{81.5}Ga_{18.5}$	1100	230	0.1	75
$\langle 100 \rangle$ $Fe_{79.1}Ga_{20.9}$	500	N/A	N/A	N/A
$\langle 110 \rangle$ $Fe_{81.6}Ga_{18.4}$	800	300	0.1	150

Increasing the stress beyond 34.3 MPa does not result in high magnetostriction, indicating that the maximum magnetostriction in this case is $(3/2)\lambda_{100}$. The zero stress magnetization versus field curve has a slightly kinked shape. This also suggests that $K_\perp > K_\parallel$ or that the magnetic anisotropy is tetragonal. The anhysteretic model parameters were determined in the same manner as the 20.9% Ga sample. The parameters in the hysteresis model k_p and c determine the width of the hysteresis loops and were found through least-squares optimization.

Figure 4.24 demonstrates the good agreement between model and data. The pinning energy density k_p characterizes the width of the hysteresis loops for both field and stress application. It is the material properties which describe the anhysteretic behavior that account for the apparently wider magnetic hysteresis loops when stress is applied. In the hysteresis model (4.67), it is the ratio of the applied energy to the pinning energy that determines the hysteresis delay. Since Galfenol alloys have high saturation flux density $\mu_0 M_s$ and moderate maximum magnetostriction $(3/2)\lambda_{100}$, the energy from magnetic field application is higher than the energy from stress

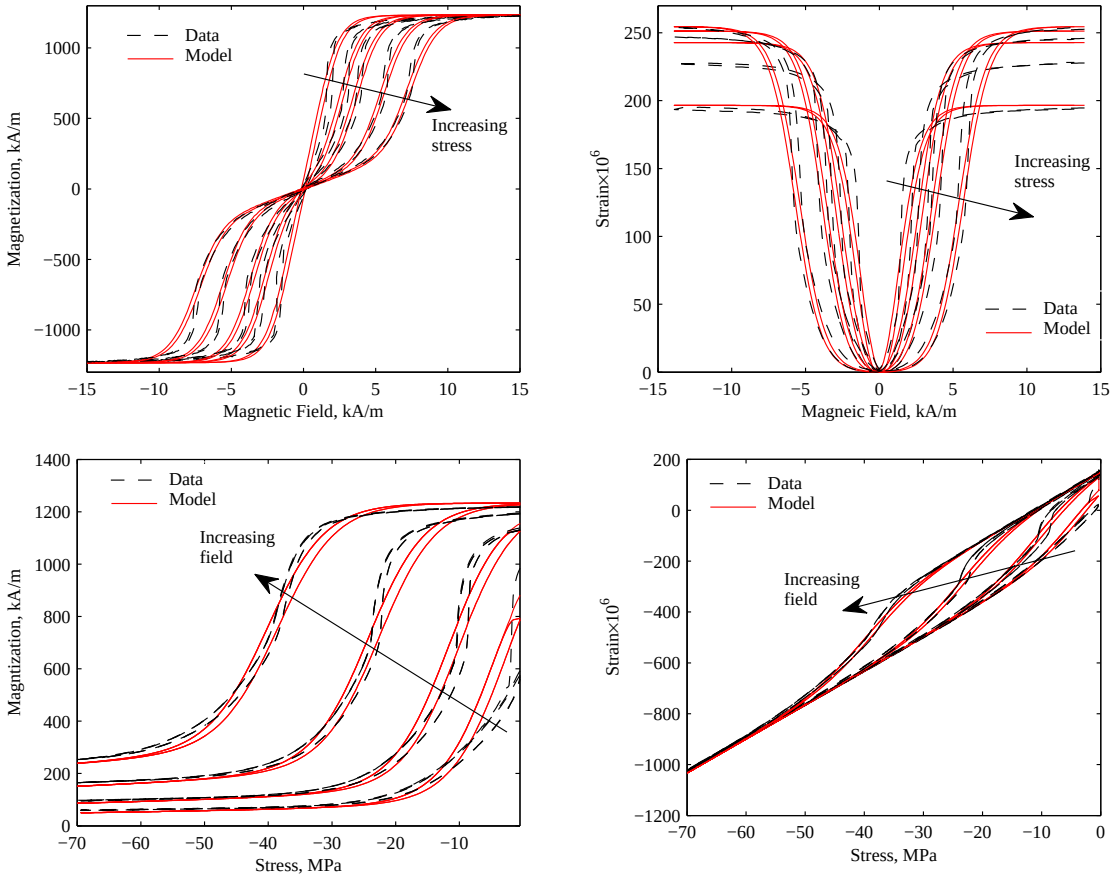

Figure 4.24: Measurement and model calculations for ⟨100⟩ $Fe_{81.5}Ga_{18.5}$ grown with FSZM at constant stress values of 0.32, 8.00, 13.4, 23.1, 32.3 MPa (compression) and constant field values of 1.85, 3.24, 5.65, 8.88 kA/m.

application. It is energetically easier to overcome the pinning energy by applying a magnetic field.

Hysteresis is most significant in the burst regions where volume fraction changes occur and negligible where the magnetization process is dominated by domain rotation. For example, in the magnetization versus magnetic field measurement with the highest bias stress (32.3 MPa), there is little hysteresis in the range $-5 < H < 5$ kA/m, where $\xi_{010} + \xi_{0\bar{1}0} + \xi_{001} + \xi_{00\bar{1}} \approx 1$ and magnetization changes are dominated by rotation of domains away from the four perpendicular $\langle 100 \rangle$ easy directions and towards the magnetic field. Above 5 kA/m, the $\langle 100 \rangle$ easy direction aligned with the field becomes the global minimum which causes a change in the anhysteretic volume fractions (4.45) which drives the first-order hysteresis model (4.67). For field application at constant stress, the first-order equation (4.67) has a pseudo time constant $k_p/\mu_0 M_s$ (the coefficient of the field increment) which determines how the volume fractions approach the anhysteretic volume fractions. Thus smaller k_p and larger $\mu_0 M_s$ reduces the field delay associated with hysteresis. Above 10 kA/m, there is no more change in the anhysteretic volume fractions because $\xi_{[100]} \approx 1$, and as the volume fractions ξ^k_{irr} approach this state, there is no more hysteresis.

Consider now the magnetization versus stress curve at the highest bias field (8.88 kA/m). At zero stress, the bias field is enough to align all domains in the [100] direction since its energy is significantly lower than the four perpendicular directions. As the material is loaded in compression, the perpendicular orientations eventually become globally minimum at around 35 MPa. At this point the anhysteretic volume fractions change, which drives the first-order hysteresis model (4.67). For stress application at constant field, the first-order equation (4.67) has a pseudo time constant

$k_p/(3/2)\lambda_{100}$ which determines the stress delay as the volume fractions approach the anhysteretic values. A smaller k_p again reduces the delay as well as a larger λ_{100}. Above 50 MPa, the volume fractions have reached the anhysteretic fractions which are no longer changing, $\xi_{010} + \xi_{0\bar{1}0} + \xi_{001} + \xi_{00\bar{1}} \approx 1$. At this point the magnetization is dominated by domain rotation as the stress competes with the bias field to more fully align domains in the four perpendicular $\langle 100 \rangle$ crystal directions. This rotation is described by (4.62). The rotation region is linear for applied field because (4.62) is linear in H, however for stress application the rotation region is nonlinear since stress appears in the denominator of (4.62).

The lower bias field cases (1.85 and 3.24 kA/m) have more complex behavior. The first stress cycle is not a closed loop whereas subsequent cycles are closed for both the measurements and the model calculations. This can be understood with the hysteresis model. The first stress cycle has a different initial condition than subsequent cycles. In collecting the measurements, the material is first saturated with a magnetic field at zero stress followed by a reduction in the magnetic field to the bias field value. At saturation, $\xi_{[100]} = \xi_{an,[100]} = 1$ and when the field is decreased to the bias point, $(\xi_{[100]} > \xi_{an,[100]}) < 1$ since there is a delay in the volume fraction change. This is the starting point of the first stress cycle. During the first cycle, the stress (compressive) is increased until $\xi_{[100]} = \xi_{an,[100]} = 0$ or all the domains are in the perpendicular orientations. Upon reduction of the stress to zero, $\xi_{an,[100]}$ increases, but due to the hysteresis delay, $(\xi_{[100]} < \xi_{an,[100]}) < 1$. Hence the final magnetization is less than the initial magnetization for the first stress cycle since the starting and ending values of the volume fractions are different. Additional stress cycles return to the same volume fraction values and hence subsequent loops are closed.

In the strain versus stress curves, the ΔE effect is observed in both the model and the measurements. The linear regions are governed by Hooke's law and are used to determine Young's modulus E, listed in Table 4.2. The steepest part of the active region, where the effective modulus softens significantly, is hysteretic since domain volume fractions change in this region. The hysteresis observed in the strain for both applied field and stress is due to the delay in volume fraction changes of magnetic domains, therefore magnetic hysteresis is responsible for the energy loss in both the magnetization versus field relationship and in the strain versus stress relationship.

$< 110 >$ single crystal $Fe_{79.1}Ga_{20.9}$ measurements and hysteretic model

For [110] application there are three distinct contributions from the six variants. The variants which dominate the positive saturation region have their easy axes closest to the positive field direction, [100] and [010] and rotate until they are aligned parallel to the field (when field is applied at constant stress.) The variants which dominate the negative saturation region have their easy axes closest to the negative field direction $[\bar{1}00]$ and $[0\bar{1}0]$ and rotate until they are aligned parallel to the field. Finally, the variants which dominate the low field region, prior to the burst towards saturation of the magnetization versus field curves, have easy axes perpendicular to the field, [001] and $[00\bar{1}]$. Utilizing (4.54), the component of the orientation in the [110] direction for the variants with easy axes perpendicular to the field and stress is

$$m_{\perp} = \frac{\mu_0 M_s}{K_{\perp} - (3/2)\,(\lambda_{100} + \lambda_{111})\,T} H. \tag{4.69}$$

The energy of these directions is

$$E_{\perp} = \frac{(\sqrt{2}\mu_0 M_s H)^2 - 3K_{\perp}(\lambda_{100} + \lambda_{111})T + 2K_{\perp}^2}{6(\lambda_{111} + \lambda_{100})T - 4K_{\perp}}. \tag{4.70}$$

The component of the orientation in the [110] direction for the variants with easy axes closest to the positive field direction is

$$m_{\|+} = \frac{\mu_0 M_s}{2K_\| - 3\lambda_{100}T} H + \frac{\sqrt{2}}{2}\left(1 + \frac{3\lambda_{111}}{2K_\| - 3\lambda_{100}T}\right). \tag{4.71}$$

The energy of these directions is

$$\begin{aligned} E_{\|+} =& \frac{(\sqrt{2}\mu_0 M_s H)^2 + 6\sqrt{2}((\lambda_{111} - \lambda_{100})HT + (2/3)K_{100}H)\mu_0 M_s}{12\lambda_{100}T - 8K_\|} \\ &+ \frac{9(\lambda_{111}^2 - \lambda_{100}^2)T^2 + 4K_\|^2}{12\lambda_{100}T - 8K_\|}. \end{aligned} \tag{4.72}$$

Finally, the component of the orientation in the [110] direction for the variants with easy axes closest to the negative field direction is

$$m_{\|-} = \frac{\mu_0 M_s}{2K_{100} - 3\lambda_{100}T} H - \frac{\sqrt{2}}{2}\left(1 + \frac{3\lambda_{111}}{2K_\| - 3\lambda_{100}T}\right). \tag{4.73}$$

The energy of these directions is

$$\begin{aligned} E_{\|-} =& \frac{(\sqrt{2}\mu_0 M_s H)^2 - 6\sqrt{2}((\lambda_{111} - \lambda_{100})HT + (2/3)K_\| H)\mu_0 M_s}{12\lambda_{100}T - 8K_\|} \\ &+ \frac{9(\lambda_{111}^2 - \lambda_{100}^2)T^2 + 4K_\|^2}{12\lambda_{100}T - 8K_\|}. \end{aligned} \tag{4.74}$$

Since the S-W orientations are calculated with first-order accuracy, the magnetostriction should also have first-order accuracy. Linearization of the particle magnetostriction (5.5) gives,

$$\mathbf{S}_m \approx \mathbf{S}_{m,0} + \frac{\partial \mathbf{S}_m}{\partial \mathbf{m}} (\mathbf{m} - \mathbf{m}_0). \tag{4.75}$$

For [110] application with high bias-stress, the total magnetostriction (as measured in the [110] direction) at high fields, or above the burst region, is the difference between the magnetostriction of the [100], [010], $[\bar{1}00]$, $[0\bar{1}0]$ easy axis variants and the [001] and $[00\bar{1}]$ easy axis variants. This is because the material starts completely in the

latter variant and after the burst region is completely in the former variant. This gives,

$$S_m = \frac{3\sqrt{2}\mu_0 M_s \lambda_{111}}{4K_\parallel - 6\lambda_{100}T} H + \frac{(18\lambda_{111}^2 - 3\lambda_{100}^2)T + 2\lambda_{100}K_\parallel}{8K_\parallel - 12\lambda_{100}T} + \frac{\lambda_{100}}{2} \tag{4.76}$$

for the total magnetostriction at high fields. The presence of λ_{111} in the coefficient of H explains how it is possible to have negative piezomagnetism at high fields. The sign depends on the sign of λ_{111}. For the measurements shown in Figure 4.25, the slope of the magnetostriction versus magnetic field curve is negative above the burst region. The anhysteretic model properties $K_\perp$, $K_\parallel$, $\mu_0 M_s$, λ_{100} and λ_{111} can all be found by measuring the slopes of the linear regions in the magnetization and magnetostriction versus magnetic field curves and comparing with the analytic expressions (4.69), (4.71), and (4.73). The remaining model parameters are found from least-squares optimization.

The analytic expressions accurately describe the data in the domain rotation regions. There is negligible error in the linear regions below and above the burst regions in the magnetization versus magnetic field curves. Additionally, the correct magnitudes and slopes are predicted by the model for the magnetostriction above and below the burst region, including the negative slope in the magnetostriction at high fields. In both the measured curves and the model curves, the magnetic hysteresis is again more significant for stress application than for magnetic field application. The pseudo time constant for field application is the same as for $\langle 100 \rangle$ application, however for the stress it is

$$\tau = \frac{k_p}{(3/2)\lambda_{100} + 3\lambda_{111}}. \tag{4.77}$$

The negative λ_{111} thus increases the hysteresis delay as compared to $\langle 100 \rangle$ application.

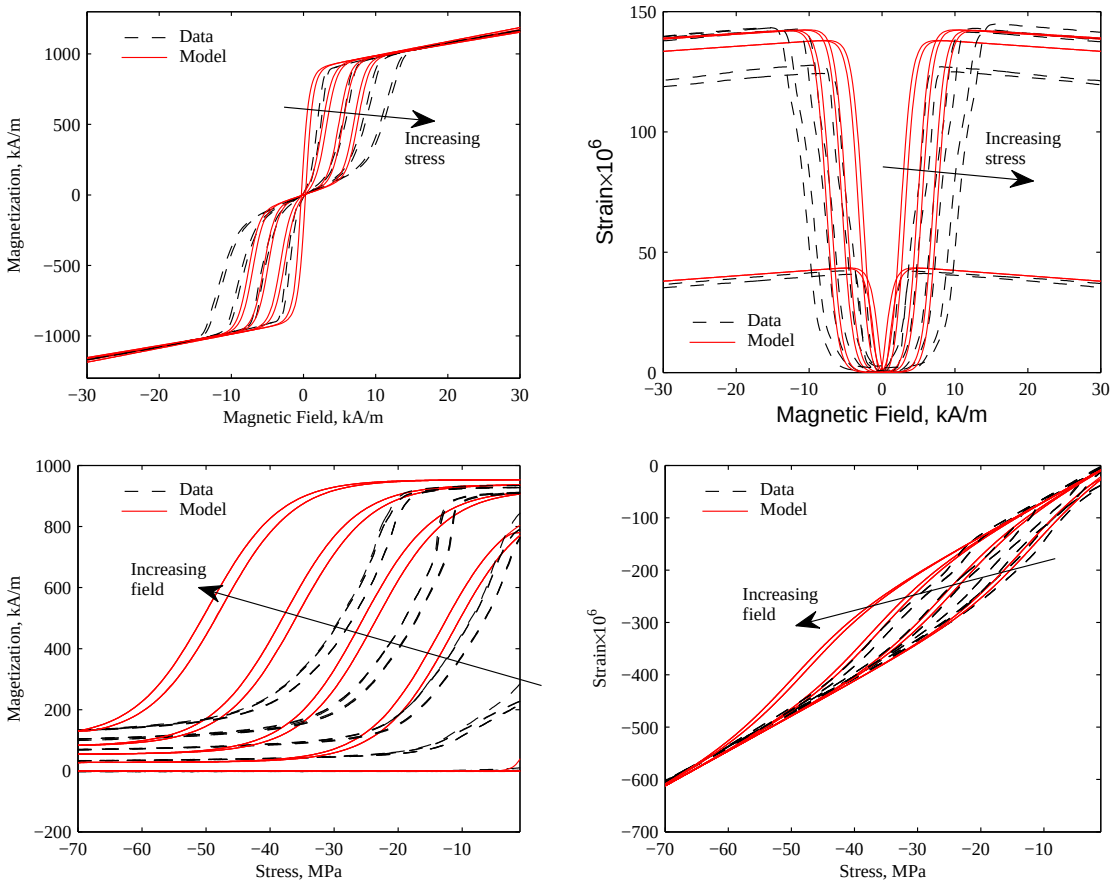

Figure 4.25: Measurement and model calculations for ⟨110⟩ $Fe_{81.6}Ga_{18.4}$ grown with the Bridgman method at constant stress values of 0.644, 22.1, 39.5, 55.3 MPa (compression) and constant field values of 0, 1.61, 3.23, 4.84, 6.46 kA/m.

There is a discrepancy between the model and the experiments regarding the location of the burst region. The predicted field location is lower and the predicted stress location is higher. The location of the burst region caused by volume fraction changes from the perpendicular variant to the variant with easy axes closer to the field direction is governed by $E_{\perp} = E_{\parallel +}$ for positive field application and $E_{\perp} = E_{\parallel -}$ for negative field application. Therefore, the error suggests a missing energy term. However, modification of the energies needs to be done with care since the S-W particle orientations are calculated from the energies and the particle orientations are correctly predicted by the model, as evidenced by the excellent correlation between the model and the measurements in the anhysteretic regions dominated by domain rotation. The details of the burst region are also affected by the energy weighting scheme (4.45). Thus, the discrepancy may be a consequence of unmodeled details in the underlying domain wall motion process which causes the volume fraction changes. The same discrepancy is observed when employing the Armstrong model with the global energy definitions since as was demonstrated earlier, both models predict the same location for the burst region (see Figure 4.19(b).)

4.3.3 Concluding remarks

This work extends the energy-weighted averaging class of magnetomechanical models by developing an efficient implementation for magnetic hysteresis due to both applied field and stress. By using local energy formulations dependent on the magnetic easy axes, the formulation is 100 times faster than previous energy-weighting models and is applicable to materials with any symmetry of magnetocrystalline anisotropy. Since the hysteresis model accounts for magnetic hysteresis for both field and stress

application, it provides a means to understand the history dependence of the magnetization and strain including the apparently larger hysteresis delay for stress application than for field application. Because the model uses analytic expressions for domain rotation, most of the model parameters can be directly determined from features of the measurements. These analytic expressions accurately describe the nonlinear magnetization and strain versus field and stress behavior in regions where domain rotation is the dominant process. In addition to furthering the understanding of Galfenol magnetomechanical behavior, this work provides an efficient modeling framework for Galfenol devices subjected to 3-D magnetic field and stress loading, operated in nonlinear and hysteretic regimes.

CHAPTER 5

Application of Galfenol to force sensing and 3-D dynamic transducer modeling

5.1 Preamble

This chapter addresses Galfenol transducer applications and transducer-level modeling. While Chapters 3 and 4 focus on the nonlinear and hysteretic relationship between magnetization/strain and magnetic field/stress, this chapter focuses on the quantities of interest in motion control transducers: voltage, current, force, and displacement.

The application of Galfenol to force sensing [41], presented in Section 5.2, is motivated by features observed in magnetization measurements of Galfenol, specifically, the presence of linear regions where the slope changes with stress. This effect is described through a simple rotational model using only the saturation magnetization and magnetostriction and the anisotropy constant. A force sensing principle is proposed, along with a Ga content range yielding alloys with properties which best leverage this principle.

The work presented in Section 5.3 seeks to provide a comprehensive framework for the study of magnetostrictive transducers, operated in dynamic and nonlinear regimes

and having any geometry. Throughout the section, the anhysteretic and hysteretic versions of the discrete energy-averaged model, the derivation of which is presented in Section 4.3, are used for Galfenol constitutive behavior. The transducers studied incorporate passive media as well, including the air surrounding the transducer, steel for the flux return path, and copper for a drive solenoid.

5.2 Stress-dependent susceptibility of Galfenol and application to force sensing

Models are used to describe nonlinear behavior in the design and control of magnetostrictive devices [100]. Jiles and Thoelke [54] employed energy minimization to quantify the effect of stress and anisotropy on the magnetization of Terfenol-D. The model incorporates the underlying assumptions present in the Stoner-Wohlfarth (S-W) model and its derivatives. The magnetization is calculated as the sum of the contributions of a set of non-interacting rotational particles or domains where rotation is induced by an applied field or stress. The orientation of the domains is calculated from the minimization of the anisotropy, field and magnetostrictive energies. This model has instantaneous jumps as minima are eliminated and created at certain critical fields and stresses. While the sharp transitions in their approach do not agree with measurements, the model provides an overall description of the magnetization mechanism.

In Armstrong's hysteretic model for magnetostrictive materials [5] magnetization is also attributed to a discrete set of domains, but in this model the domains do not rotate. This assumption can be made when the anisotropy energy is high and the field and stress are applied along one of the preferred crystal directions dictated by the anisotropy energy. Magnetization and magnetostriction changes occur as the

fractional occupancies of the domains in the set change. These changes are calculated from energy principles.

Other models for magnetostrictive materials use statistical mechanics to smooth sharp transitions predicted by direct energy minimization. Smith and Dapino [91] applied stochastic homogenization in conjunction with direct energy minimization to model the effect of stress on magnetization of a variety of ferromagnetic materials. The energy includes thermal, exchange, stress, and magnetic field terms but not anisotropy. Stochastic homogenization smooths the sharp transitions predicted by energy minimization by considering the critical field at which a transition occurs to be a statistically distributed parameter.

Statistical mechanics principles have also been used to characterize the effect of stress-annealing and to model rate-dependent hysteresis in Galfenol [86, 38]. In these models, any domain orientation is possible; the likelihood of a given domain orientation is calculated from the energy of the orientation, which incorporates anisotropy, stress, and magnetic field terms. The energy is not directly minimized but the probability density function causes minimum energy orientations to be more likely. In micromagnetics models, the energy is minimized over a geometry with boundary conditions [116]. While they provide more detailed information such as domain structure they are computationally expensive and better suited for material characterization rather than device design and control.

Chief intent of this study is to derive a simple analytical model for the field and stress dependence of the linear region appearing in magnetization measurements of $\langle 100 \rangle$ oriented Galfenol, obtained from varying the magnetic field at constant stress.

Magnetization changes in this region are attributed to domain rotation and the domain orientation is found from the Gibbs free energy of a S-W particle. Using this simple model it is shown that, because of its lower anisotropy, Galfenol with higher Ga content is ideal for transducers operating on the principle of stress dependent susceptibility from domain rotation. Furthermore, it is shown that although the stress dependence of the susceptibility is nonlinear, a linear force sensor can be constructed using a transformer with a Galfenol element.

5.2.1 Measurements

Magnetization measurements are reported for $\langle 100 \rangle$ oriented, single-crystal $Fe_{79.1}Ga_{20.9}$ and $\langle 100 \rangle$ oriented, textured polycrystal $Fe_{81.6}Ga_{18.4}$. The textured polycrystal sample is near single-crystalline with 95 % of grains having the $\langle 100 \rangle$ axis aligned within 5 degrees of the rod axis. Prior to magnetic field application, a constant bias stress is applied with an MTS 858 table top system capable of applying compressive loads only, by loading the sample between two parallel plates. A cyclic magnetic field is then applied using a drive coil situated with the Galfenol sample in a steel canister providing a flux return path. The waveform is triangular with a rate of 1 kA/m per second and magnitude sufficient to saturate the sample. The magnetic field is measured on the surface of the rod halfway along its length with a Lakeshore 421 gauss meter and magnetic flux density is measured with a Walker Scientific MF-30 fluxmeter and pick-up coil. Magnetization is calculated by subtracting the field measurements from flux density measurements. Prior to saturation, linear regions are observed in the magnetization versus field curves of the single crystal sample (see Figure 5.1) where the slope depends on the bias stress. The sample with lower Ga

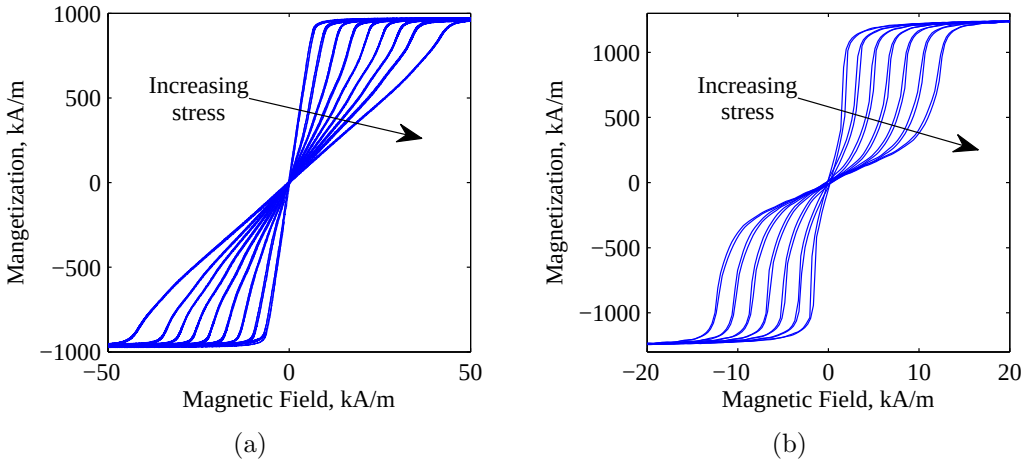

Figure 5.1: Magnetization measurements of (a) $Fe_{79.1}Ga_{20.9}$ at constant compressive stresses of 1.38, 18.8, 27.6, 41.4, 55.2, 68.9, 82.7, 96.5, and 122.7 MPa and (b) $Fe_{81.6}Ga_{18.4}$ at constant compressive stresses of 0.316, 9.17, 18.5, 27.7, 36.9, 46.2, 55.4 MPa.

content also has linear regions but exhibits significant kinking with a nonlinear shape prior to saturation. Section 5.2.3 shows the difference in behavior to be due to a difference in the anisotropy. An analytic expression is derived for the stress dependence of the slope in the linear region. Utilizing this expression, equations for the operation of a linear magneto-elastic force sensor are derived.

5.2.2 Magnetization model

Ferromagnetic materials are composed of regions of uniform magnetization M_s called domains [61]. Magnetization changes occur as domains rotate or as differently orientated domains change size through domain wall motion. In the S-W approximation used here, the material is taken as a collection of non-interacting, single-domain particles [65]. This approximation is accurate when domain rotation is the dominant

magnetization mechanism; domain rotation is modeled as the rotation of S-W particles. The orientation $\mathbf{m}$ of an S-W particle can be calculated from its Gibbs free energy G which has natural dependence on the applied quantities magnetic field $\mathbf{H}$, stress $\mathbf{T}$, and temperature θ as well as the internal state variable $\mathbf{m}$. The Gibbs free energy G is the sum of the anisotropy

$$\begin{aligned} G_{an} = K_4(\theta)(m_1^2 m_2^2 + m_2^2 m_3^2 + m_3^2 m_1^2) \\ + K_6(\theta) m_1^2 m_2^2 m_3^2, \end{aligned} \tag{5.1}$$

Zeeman

$$G_z = -\mu_0 M_s(\theta) \mathbf{m} \cdot \mathbf{H}, \tag{5.2}$$

magnetomechanical coupling

$$G_{coup} = -\boldsymbol{\lambda} \cdot \mathbf{T}, \tag{5.3}$$

and mechanical

$$G_{mech} = -\mathbf{T} \cdot \mathbf{s}\mathbf{T}, \tag{5.4}$$

energies. The anisotropy energy originates from magnetic moments having preferred crystallographic directions, $\langle 100 \rangle$ and $\langle 111 \rangle$ for cubic materials. Rotation of S-W particles away from these easy directions requires energy from field, stress, or temperature application. The energy from the field is expressed as the Zeeman energy. Stress contributes energy through the magnetomechanical coupling energy or the strain energy density from magnetostriction as well as through the purely mechanical energy due to the material compliance $\mathbf{s}$, which for Galfenol has cubic symmetry. In (5.3) and (5.4) the stress and magnetostriction are treated as vectors where the first three components are longitudinal and the last three shear components. The

magnetostriction depends on the S-W particle orientation [61]

$$\lambda_i = \frac{3}{2}\lambda_{100}(\theta)m_i^2,\ i = 1, 2, 3 \tag{5.5}$$

$$\lambda_4 = 3\lambda_{111}(\theta)m_1 m_2, \tag{5.6}$$

$$\lambda_5 = 3\lambda_{111}(\theta)m_2 m_3, \tag{5.7}$$

$$\lambda_6 = 3\lambda_{111}(\theta)m_3 m_1. \tag{5.8}$$

The effect of temperature is accounted for through the temperature dependence of the anisotropy coefficients K_4 and K_6, domain magnetization M_s, and magnetostriction coefficients λ_{100} and λ_{111}. For the isothermal processes considered here, these coefficients are constant.

The particle orientation, magnetization $\mathbf{M}$, and strain $\mathbf{S}$ are calculated from the constitutive relations

$$\frac{\partial G}{\partial \mathbf{m}} = 0, \tag{5.9}$$

$$\mathbf{M} = -\frac{1}{\mu_0}\frac{\partial G}{\partial \mathbf{H}} = M_s\mathbf{m}, \tag{5.10}$$

$$\mathbf{S} = -\frac{\partial G}{\partial \mathbf{T}} = \boldsymbol{\lambda} + \mathbf{s}\mathbf{T}. \tag{5.11}$$

The minimization (5.9) is constrained since $|\mathbf{m}| = 1$. Analytic solution is not possible because G is a sixth-order function of the particle orientation. There are fourteen possible solutions which correspond to rotation about the six $\langle 100 \rangle$ and eight $\langle 111 \rangle$ easy directions in response to applied field or stress. Thoelke and Jiles [101] formulated the energy in spherical coordinates and solved for the local minima with iteration. Here the problem is approximately solved in rectangular coordinates, yielding analytic expressions for particle orientation.

First, the constraint is substituted into the Gibbs energy. For example, to find the minimum orientation which lies near the [100] direction, the relation $m_1 =$

$\sqrt{1-m_2^2-m_3^2}$ is substituted into the energy so that when $m_2 = m_3 = 0$, the remaining component is the one associated with $m_1 = 1$. Similarly, to find the local minimum near the $[\bar{1}00]$ direction, the relation $m_1 = -\sqrt{1-m_2^2-m_3^2}$ is used so that when $m_2 = m_3 = 0$, the remaining component is the one associated with $m_1 = -1$. After this substitution, the two nonlinear equations $\partial G/\partial m_i = 0$ are linearized about the easy direction that was used in the substitution of the constraint. Linearization of $\partial G/\partial m_i = 0$ about the easy crystal directions is accurate because S-W particles are always oriented near an easy crystal direction. If the stress or field rotates a particle far from a particular easy direction it will flip to one of the other thirteen energy equilibria which is closer to an easy direction.

A typical device having a magnetostrictive material consists of a rod in compression with an applied stress sufficiently large to align domains perpendicular to the rod axis. An applied magnetic field causes magnetization change and magnetostriction as domains rotate into the applied field direction. At certain critical fields, domains will flip from the current equilibrium to an equilibrium closer to the field direction; in addition, the size of domains in lower energy equilibria will grow at the expensive of higher energy domains through domain wall motion. For [100] oriented material (see Figure 5.2,) compressive stress at zero field lowers the energy of the four basal plane directions [010], $[0\bar{1}0]$, [001], and $[00\bar{1}]$. A sufficient compressive stress will cause all domains to lie in these directions. Applied field rotates these domains into the field direction along the rod. Eventually domain wall motion and domain flipping occurs as the material saturates with all domains oriented in the [100] direction for positive fields and $[\bar{1}00]$ for negative fields.

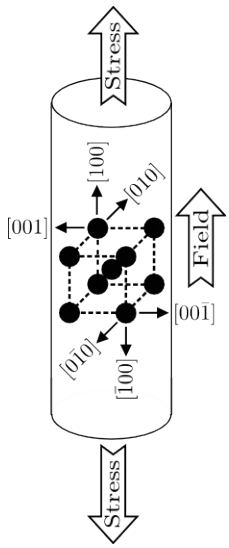

Figure 5.2: [100] oriented material where arrows for the field and stress indicate the positive direction which for the stress indicates a tensile load.

The S-W approximation is accurate when the magnetization process is dominated by domain rotation. This occurs below saturation when sufficient compressive stress has been applied to align all domain in the basal plane. In this case, magnetic field causes magnetization change as domains rotate towards the field. This is calculated with the approximation described previously, linearizing about any of the [010], [0$\bar{1}$0], [001], or [00$\bar{1}$] basal plane directions. Substitution of $m_3 = \sqrt{1 - m_1^2 - m_2^2}$ into G with $H_1 = H$, $T_1 = T$ and all other inputs zero results in the following after differentiation

$$\frac{\partial G}{\partial m_1} = 2K_4(m_1 - 2m_1^3 - m_1 m_2^2) - 3\lambda_{100} T m_1 - \mu_0 M_s H, \tag{5.12}$$

$$\frac{\partial G}{\partial m_2} = 2K_4(m_2 - 2m_2^3 - m_2 m_1^2), \tag{5.13}$$

$$\frac{\partial^2 G}{\partial m_1^2} = 2K_4(1 - 6m_1^2 - m_2^2) - 3\lambda_{100}T, \tag{5.14}$$

$$\frac{\partial^2 G}{\partial m_1 \partial m_2} = -4K_4 m_1 m_2, \tag{5.15}$$

$$\frac{\partial^2 G}{\partial m_2^2} = 2K_4(1 - 6m_2^2 - m_1^2.) \tag{5.16}$$

The linear approximation of (5.12) and (5.13) about $m_1 = m_2 = 0$, the [100] direction, is formulated by

$$\frac{\partial G}{\partial m_1} \approx \left(\frac{\partial G}{\partial m_1}\right)_0 + \left(\frac{\partial^2 G}{\partial m_1^2}\right)_0 m_1 + \left(\frac{\partial^2 G}{\partial m_1 \partial m_2}\right)_0 m_2, \tag{5.17}$$

$$\frac{\partial G}{\partial m_2} \approx \left(\frac{\partial G}{\partial m_2}\right)_0 + \left(\frac{\partial^2 G}{\partial m_2 m_1}\right)_0 m_1 + \left(\frac{\partial^2 G}{\partial m_2^2}\right)_0 m_2. \tag{5.18}$$

Substitution from (5.12)-(5.16), equating to zero, and solving for m_1, the component in the field direction is

$$m_1 = \frac{\mu_0 M_s}{2K_4 - 3\lambda_{100}} H, \tag{5.19}$$

hence, the stress-dependent susceptibility below saturation is

$$\chi(T) = \frac{\mu_0 M_s^2}{2K_4 - 3\lambda_{100}T}. \tag{5.20}$$

5.2.3 Force sensor model

The magnetization calculated using the susceptibility (5.20) is shown with the magnetization measurements in Figure 5.3. The model parameters for the $Fe_{79.1}Ga_{20.9}$ sample are $M_s = 970$ kA/ m, $\lambda_{100} = 138 \times 10^{-6}$, measured directly from the saturation values of the magnetization and magnetostriction of the 122.7 MPa data set, and $K_4 = 4.98$ kJ/m^3, calculated by solving (5.20) for K_4 with the susceptibility and stress values from the 122.7 MPa data set. There is excellent agreement between the model and the measurements except in the lowest stress case (see Figure 5.3(a).) This suggests that 1.38 MPa is not enough stress to fully align domains in the basal

plane and hence the magnetization process is not due to domain rotation alone. Additionally, the full magnetostriction $(3/2)\lambda_{100}$ (measured with a strain gauge) was not achieved for this data set—further evidence that full domain alignment was not achieved.

The model parameters for the $Fe_{81.6}Ga_{18.4}$ sample are $M_s = 1281$ kA/m, $\lambda_{100} = 173 \times 10^{-6}$, measured directly from the saturation values of the magnetization and magnetostriction of the 55.4 MPa data set, and $K_4 = 19.1$ kJ/m^3, calculated by solving (5.20) for K_4 with the susceptibility and stress values from the 55.4 MPa data set. Full magnetostriction was achieved for the 27.7 MPa and higher data sets, these are compared with the rotational model in Figure 5.3(b). These sets follow the model lines at low fields, less than 10 kA/m but diverge rather quickly—giving them a nonlinear shape. The model comparison for each data set is shown in separate plots for the $Fe_{81.6}Ga_{18.4}$ sample (see Figure 5.3(b)) for clarity, since increasing stress causes little change in the susceptibility, whereas the data sets for the $Fe_{79.1}Ga_{20.9}$ sample are easily distinguished in the same plot (see Figure 5.3(a).)

There is variability in the reported values of the fourth-order anisotropy constant K_4. Noting that $K_4 = -2K_{cubic}$ from their paper, Restorff et al. [86] report values of 28.6, 32.0, 45.6 and kJ/m^3 for three different $Fe_{81.6}Ga_{18.4}$ samples. The values are not measured directly but determined from a nonlinear simplex algorithm minimizing the error between an energy averaging model and the data. Rafique et al. [83] report 32.5 kJ/m^3 for a $Fe_{82}Ga_{18}$ sample. Their work uses the classical approach of numerically integrating the magnetic field over magnetization measurements for two different crystal orientations and assuming that all of the field energy goes to changing the internal energy—assumed to be entirely composed of the anisotropy

energy of a rotating S-W particle. If the magnetization measurements are carried out over a range including domain flipping or wall motion, this appears as an apparent scaling of the anisotropy constant since all of the field energy is assumed to go towards overcoming anisotropy energy alone. In our approach, a S-W model is also used, however, it is only applied in the domain rotation region and is measured directly from the slope or susceptibility (after directly measuring the M_s and λ_{100}.) Both cited works show a trend of decreasing anisotropy with increasing Ga content which agrees with our results. Finally, all three approaches actually measure $K_4 + \Delta K_4$ where ΔK_4 is a strain-invariant change in the intrinsic cubic anisotropy due to the magneto-elastic coupling energy [61].

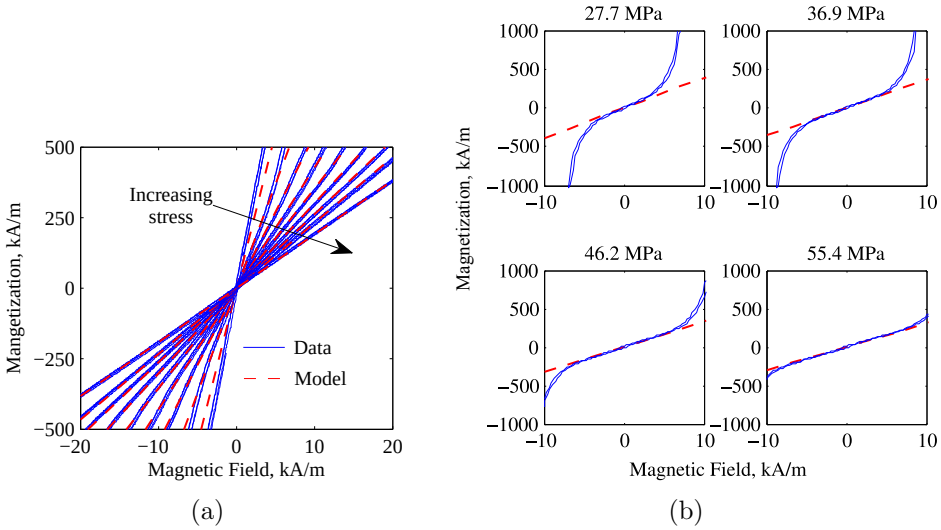

Figure 5.3: Comparison of rotational model with magnetization measurements of (a) $Fe_{79.1}Ga_{20.9}$ and (b) $Fe_{81.6}Ga_{18.4}$.

It is the large difference in anisotropy that results in the different behavior of the differing Ga content samples. Having low anisotropy, the magnetization of the

$Fe_{79.1}Ga_{20.9}$ sample is dominated by domain rotation over a large range of fields and stresses. The magnetomechanical coupling (5.3) dominates the anisotropy energy (5.1) so that domains which rotate from the basal plane with field application have a large contribution to the bulk magnetization. The linear magnetization versus field region arises from this rotation. Eventually the field energy (5.2) dominates, causing a nonlinear approach to saturation as domain flipping and wall motion result in the material being composed entirely of domains oriented in the $\langle 100 \rangle$ direction aligned with the magnetic field. The denominator of (5.20) is dominated by the stress term which causes large changes in the susceptibility as the stress is changed. This effect can be used as the basis of a force sensor.

Whereas the magnetization of the $Fe_{79.1}Ga_{20.9}$ sample was dominated by the rotation of a single set of domains, made energetically favorable by the applied stress, the magnetization of the $Fe_{81.6}Ga_{18.4}$ is due to the simultaneous rotation of domains from the six $\langle 100 \rangle$ and eight $\langle 111 \rangle$ easy axes as well as flipping and wall motion of these domains. The larger anisotropy inhibits domain rotation and the field energy goes to domain flipping and wall motion to change the volume fraction of material having domain orientations close to the field direction. The effect of stress in this case is mostly to shift the field location where flipping and wall motion begins, with little change to the rotations. As an illustration, the slope of the domain rotation region is not changed significantly in Figure 5.3(b) as stress is increased but the width of the field interval where rotation occurs is increased since stress lowers the energy of domains rotating from the basal plane.

To summarize, the $Fe_{79.1}Ga_{20.9}$ sample is dominated by tetragonal anisotropy imparted by the applied stress and the Fe $_{81.6}Ga_{18.4}$ is dominated by the cubic, magnetocrystalline anisotropy. The result is that the $Fe_{79.1}Ga_{20.9}$ magnetization has large intervals of stress and field which can be accurately modeled by a simple stress dependent susceptibility (5.20). The $Fe_{81.6}Ga_{18.4}$ sample magnetization has a kinked shape with limited regions dominated by rotation and would benefit from more complicated models involving statistical distributions of domain orientations [7, 38, 40] or micromagnetics simulations [116].

The $Fe_{79.1}Ga_{20.9}$ sample is better suited for use in Galfenol force sensors. The stress sensitivity of its susceptibility in the rotational region is much higher than in the $Fe_{81.6}Ga_{18.4}$ sample (see Figure 5.4.) The accurate, low-order, expression for the stress dependence of the susceptibility (5.20) enables the design and control of transducers. To ensure that the material is used in the domain rotation region, it can be stress annealed [86]. Magneto-elastic transducers for force sensing and energy harvesting typically rely on the stress dependence of the magnetic susceptibility [29]. Kleinke and Uras [62] proposed a magneto-elastic force sensor using a transformer made from a magnetostrictive material with an excitation coil on one arm and a detection coil on the other (see Figure 5.5.) An amplitude modulated signal results and the stress or force is related to the amplitude ratio between the drive and pickup coils. A key advantage of Galfenol for this application is its combination of high magnetostriction and high yield strength. Furthermore, the relationship between the amplitude ratio and force is linear.

The magnetic field H_e produced by the current of the excitation coil is controlled and the voltage of the detection coil measured. The force is related to the ratio of

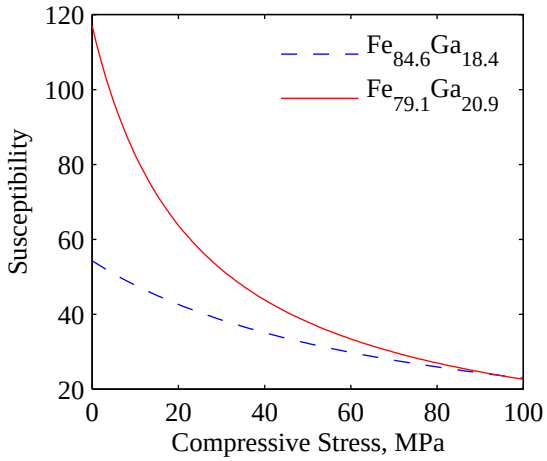

Figure 5.4: The stress dependent susceptibility (5.20) using parameters for the $Fe_{79.1}Ga_{20.9}$ and $Fe_{81.6}Ga_{18.4}$ samples.

the magnetic field and detection voltage. Equations describing the operation of this transducer using Galfenol with cross section area A can be calculated with (5.20) and standard magnetic circuit laws. A bias stress or stress annealing and proper selection of the magnetic field amplitude ensures that the Galfenol is operated in the domain rotation region of its magnetization behavior. The detection voltage due to changing flux ϕ is found from Faraday's law of induction

$$V_d = -N\frac{d\phi}{dt}, \tag{5.21}$$

where the detection coil has N turns of wire. From (5.20) the total magnetic flux is

$$\phi = A\mu_0 \left[1 + \chi(T)\right] H_e \approx A\mu_0\chi(T)H_e. \tag{5.22}$$

The flux due to magnetic field alone can be neglected since $\chi(T) >> 1$. The detection voltage is then

$$V_d = -\mu_0 NA\left[\chi(T)\frac{dH_e}{dt} + \frac{d\chi(T)}{dt}\frac{dT}{dt}H_e\right]. \tag{5.23}$$

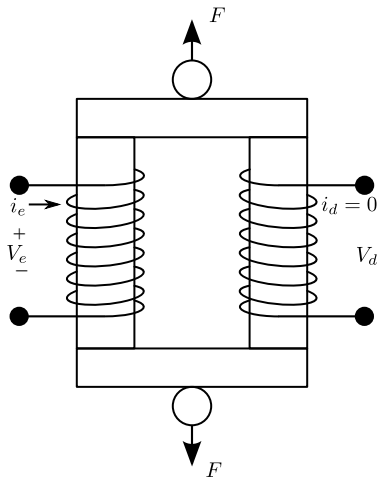

Figure 5.5: Force sensor with magnetostrictive core.

By using an excitation field with a frequency ω_e much greater than the frequency of the force, the second term in the square brackets can be neglected. The amplitude of the detection voltage $\bar{V}_d$ is then related to the magnetic field amplitude $\bar{H}_e$ by

$$\bar{V}_d = \mu_0 N A \omega_e \chi(T) \bar{H}_e. \tag{5.24}$$

The $Fe_{79.1}Ga_{20.9}$ sample has a higher susceptibility which is more sensitive to stress changes (see Figure 5.4,) giving a higher detection voltage. From (5.20), the susceptibility can be increased by decreasing the anisotropy K_4 or increasing the saturation magnetization M_s. The sensitivity to stress changes can be increased by increasing the magnetostriction λ_{100}. Magnetostriction measurements have been reported for Ga concentrations of 0-35 at.% with peaks occurring at 19 and 27 at.% [22]. Anisotropy constants have been separately reported for Ga concentrations of 0-20 at.% [83] and 12.5-22 at.% with a trend of decreasing anisotropy for increasing Ga concentration. The saturation magnetization has also been reported to decrease with Ga concentration but by much lower factors than the anisotropy. Ideally, the anisotropy coefficient

K_4 should be slightly greater than zero. A negative value would result in the need for a higher bias stress to pre-align domains in the basal plane, since in this case the [100] directions are not easy directions. Given the variability and low resolution of reported anisotropy values, it is difficult to accurately select the ideal Ga concentration. However, the trends suggest the optimal value lies between the magnetostriction peak of 19 at.% and the anisotropy sign change value of around 22 at.%.

Using a higher magnetic field frequency and amplitude also gives a higher detection voltage. Substituting from (5.20) and solving for the force $F = 2AT$ gives

$$F = -\frac{2}{3}\frac{N(A\mu_0 M_s)^2\omega_e}{\lambda_{100}}\left(\frac{\bar{H}_e}{\bar{V}_d}\right) + \frac{4AK_4}{3\lambda_{100}}. \tag{5.25}$$

The force is linearly related to the amplitude ratio $\bar{H}_e/\bar{V}_d$ by known material and geometric properties.

Employing the $Fe_{79.1}Ga_{20.9}$ sample, the difference between the maximum expected tensile stress and the bias or internal compressive stress should not exceed 18 MPa. In addition, the excitation field amplitude should be less than 5 kA/m. These limits ensure the accuracy of (5.25) by keeping the magnetization process in the domain rotation region.

5.2.4 Concluding Remarks

Magnetization measurements of $Fe_{79.1}Ga_{20.9}$ and $Fe_{81.6}Ga_{18.4}$ are linear with magnetic field in certain intervals of stress and magnetic field. These regions arise from coherent rotation of domains from the basal plane and occur when a sufficient compressive stress aligns domains in the four easy crystal directions of the basal plane at zero magnetic field. The slope of the linear region is proportional to the field energy and inversely proportional to the anisotropy and magnetomechanical coupling

energies. Energy minimization can be used to interpret the differences in the magnetization processes of the two samples. Magnetization of $Fe_{81.6}Ga_{18.4}$ is more strongly influenced by domain flipping and wall motion due to its higher anisotropy impeding domain rotation. As a result, its magnetization versus field curves at constant stress have a distinctive kinked shape whereas the $Fe_{79.1}Ga_{20.9}$ curves are largely linear until saturation, having lower anisotropy which permits more domain rotation. The susceptibility of the $Fe_{79.1}Ga_{20.9}$ sample is more sensitive to stress in the domain rotation region. The stress dependence of the susceptibility in the linear or domain rotation region of both samples is accurately modeled with a simple expression derived from energy minimization. This expression motivates the use of Galfenol with Ga concentrations having high magnetostriction and saturation magnetization with a small, positive fourth-order anisotropy constant for transducers utilizing stress dependent susceptibility. This expression also shows that despite the nonlinear stress dependence of the susceptibility, a linear force transducer can be constructed with a transformer made from Galfenol.

5.3 Transducer-level modeling with the finite element method

Magnetostrictive transducers operated as actuators have supply voltage applied to a solenoid as input and displacement or force as output. Operated as sensors, the input is force or surface traction and the output is typically the voltage in a pick-up coil, induced by a changing flux density. These input-output relationships depend on the electric flux density $\mathbf{D}$, magnetic flux density $\mathbf{B}$, and strain $\mathbf{S}$ as well as their work conjugates electric field $\mathbf{E}$, magnetic field $\mathbf{H}$, and stress $\mathbf{T}$ which vary in space $\mathbf{x}$ and time t. These are kinematically related to voltage ϕ, vector magnetic potential $\mathbf{A}$,

and displacement **u**—which are often used in the solution process of finite element models.

Transducer-level models are useful for device design and optimization as well as control [78, 71, 78, 96, 100]. Much attention has been given to devices utilizing Terfenol-D loaded unidirectionally. Dapino, Smith, and Flatau [30] modeled 1-D constitutive behavior of Terfenol-D with the Jiles-Atherton model, including an effective field due to prestress. In their transducer-level description, the magnetostriction calculated from the constitutive model is used as input to the wave equation for the structural dynamics of a rod. Huang et al. [46] also used the Jiles-Atherton model for 1-D characterization of a Terfenol-D actuator but included eddy current losses in the energy formulation and used a lumped parameter model for the structural dynamics; the effect of dynamic stress was not included in their constitutive model. Sarawate and Dapino [87] also developed a decoupled model but included time delay from eddy currents through solution of the magnetic field diffusion equation with constant permeability. Engdahl and Bergqvist [37] calculated dynamic losses in a 1-D actuator by fully coupling the magnetic field diffusion equation, the wave equation for structural dynamics, and a lumped parameter model for the magnetic circuit with constitutive behavior obtained from measurement and with constitutive behavior obtained from a Stoner-Wohlfarth hysteresis model. Bottauscio et al. [17] modeled losses from eddy currents using the field diffusion equation along with the Preisach model to calculate the nonlinear permeability and stress-induced flux density changes. All of the works referenced above have as input, externally applied magnetic field.

Some attention has also been given to higher dimension models. Datta et al. [32, 88] used classical laminated plate theory with the Armstrong magnetomechanical

model to characterize laminated sensors and actuators in the absence of current-induced magnetic field. Zhou and Zhou [118] developed a dynamic finite element model for a unimorph actuator with one-way magnetomechanical coupling. The magnetostatic finite element model formulated by Kannan and Dasgupta [56] is 2-D, uses nonlinear constitutive behavior for bi-directional coupling and includes current-induced magnetic fields and electromagnetic body forces. Mudivarthi et al. [70] used a fully-coupled, magnetostatic formulation for stress-induced flux density changes in Galfenol with no current-induced fields. The 3-D model of Kim and Jung [60] employs one-way coupling with force due to magnetostriction driving a coupled fluid-structural model for a sonar transducer. Aparicio and Sosa describe a 3-D [79], fully-coupled finite element model including dynamic effects and give a simple implementation for a magnetostrictive material using a single element.

This work provides a comprehensive framework for design and characterization of 3-D magnetostrictive transducers. The effects of eddy currents, structural dynamics, flux leakage, and nonlinear material behavior are simultaneously included. Complex implementations are considered which include air volumes and current-carrying coils and describe the full input-output relationship between voltage, force, and displacement. Simplified cases which illustrate transducer-level effects are also given. The 3-D formulation is first derived, followed by simplified 1-D and 2-D formulations with example implementations. Finally, a dynamic and 3-D implementation is done to study the efficiency of a Galfenol-based transducer.

5.3.1 3-D Strong form

In the strong form, the spatial and temporal dependence of the electromagnetic work conjugates are described by Maxwell's equations and the inputs of interest in transducers appear either as boundary conditions or source terms. The spatial and temporal dependence of the mechanical work conjugates are described by Newton's laws and the transducer inputs again appear as either boundary conditions or source terms. A description of these equations as well as the relevant kinematic relationships is given in Chapter 2.

5.3.2 3-D Weak form

The weak form is derived here from the method of weighted residuals, using Galerkin's method. Prior to weighting, a few modifications to the local form are made. First, displacement currents are neglected which limits the validity of the resulting equations to quasi-static operation, in the electromagnetic sense. While electromagnetic radiation is neglected, mechanical resonance can still occur, thus the operating regime is still dynamic in the mechanical sense. Second, the current density in (2.7) is defined as the sum of an applied current or source current $\mathbf{J}_s$ and eddy-currents. Finally it is assumed that voltage gradients are negligible, i.e., the only electrical input is that from the source current density.

The magnetic vector potential is used, thus ensuring divergence free magnetic flux density according to (2.5). With the assumptions described above and the definition of the vector potential, the only of Maxwell's equations to be solved is Ampère's

law (2.7) which is reduced to

$$\nabla \times \mathbf{H} = \mathbf{J}_s + \mathbf{J}_E, \tag{5.26}$$

$$\mathbf{J}_E = -\sigma \frac{\partial \mathbf{A}}{\partial t}. \tag{5.27}$$

The weak form is more easily derived using Einstein's indicial notation and defining the permutation tensor

$$\epsilon_{ijk} = \begin{cases} 1, \text{ clockwise sequence (123, 231, 312)} \\ -1, \text{ counter-clockwise sequence (321, 213, 132)} \\ 0, \text{ any two indices equal} \end{cases}. \tag{5.28}$$

Using the permutation tensor, the cross-product is $(\mathbf{a} \times \mathbf{b})_i = \epsilon_{ijk} a_j b_k$ and the curl is $(\nabla \times \mathbf{a})_i = \epsilon_{ijk} \partial a_k / \partial x_j$. Also, switching the order gives $\epsilon_{ijk} a_k b_j = -\epsilon_{ijk} a_j b_k$. In Einstein notation, the equations to be solved are

$$\epsilon_{ijk} \frac{\partial H_k}{\partial x_j} = (J_s)_i - \sigma \frac{\partial A_i}{\partial t}, \tag{5.29}$$

$$\rho_m \frac{\partial^2 u_i}{\partial t^2} + c \frac{\partial u_i}{\partial t} = \frac{\partial T_{ij}}{\partial x_j} + (f_B)_i. \tag{5.30}$$

The flux density is kinematically related to the vector magnetic potential and the strain is kinematically related to the displacement. The magnetic field in (5.29) is related, by a material constitutive law (to be determined), to flux density and strain, if the material is magnetostrictive, or simply to the flux density for both passive materials and free space. The stress in (5.30) is also related to flux density and strain by a material constitutive law for magnetostrictive materials. For passive materials the stress is simply related to the strain. Thus using the kinematic relationships and the material constitutive laws, the two initial boundary value problems (5.29) and (5.30) can be formulated with dependent variables flux density and displacement

and source terms current density and body force. Essential boundary conditions are specified vector potential and displacement. A typical system to be solved is surrounded by an air volume, chosen sufficiently large so as to be able to assume that $A_i = 0$ on the boundary. Upon conversion to weak form, the natural boundary conditions emerge as work terms applied to material boundaries, arising from the tangential component of magnetic fields applied at the boundary and the traction force applied to the boundary.

The weak form is derived from the method of weighted residuals applied to (5.29) and (5.30),

$$\int_{V_B} \epsilon_{ijk} \frac{\partial H_k}{\partial x_j} \psi_i dV + \int_{V_B} \sigma \frac{\partial A_i}{\partial t} \psi_i dV = \int_{V_B} (J_s)_i \psi_i dV, \tag{5.31}$$

$$- \int_{V_u} \frac{\partial T_{ij}}{\partial x_j} \varphi_i dV + \int_{V_u} \rho \frac{\partial^2 u_i}{\partial t^2} \varphi_i dV + \int_{V_u} c \frac{\partial u_i}{\partial t} \varphi_i dV = \int_{V_u} (f_B)_i \varphi_i dV, \tag{5.32}$$

where ψ_i and φ_i are kinematically admissible test functions which are zero where essential boundary conditions exist. The volumes V_B and V_u are the subdomains for which flux density and mechanical displacement are defined, respectively. Consider for example the hypothetical system in Figure 5.6. The displacement volume consists of the magnetostrictive material and the steel flux path, which is deformed by the magnetostrictive material as well as externally applied traction forces. The flux density volume consists of the entire domain since the current-carrying coil results in magnetic fields on the entire domain. The air volume needs to be made sufficiently large to assume magnetic potential on the boundary.

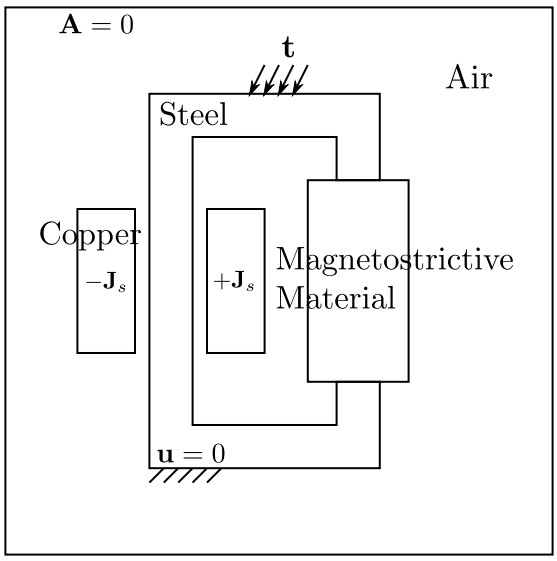

Figure 5.6: Hypothetical system with a magnetostrictive material, flux return path, and drive coil in an air volume.

Integration by parts gives for the first terms in (5.31) and (5.32),

$$\int_{V_B} \epsilon_{ijk} \frac{\partial H_k}{\partial x_j} \psi_i dV = \int_{V_B} \epsilon_{ijk} \frac{\partial (H_k \psi_i)}{\partial x_j} dV - \int_{V_B} \epsilon_{ijk} H_k \frac{\partial \psi_i}{\partial x_j} dV, \tag{5.33}$$

$$- \int_{V_u} \frac{\partial T_{ij}}{\partial x_j} \varphi_i dV = - \int_{V_u} \frac{\partial (T_{ij} \varphi_i)}{\partial x_j} dV + \int_{V_u} T_{ij} \frac{\partial \varphi_i}{\partial x_j} dV. \tag{5.34}$$

Applying the divergence theorem to the first term in each of the above gives,

$$\int_{V_B} \epsilon_{ijk} \frac{\partial (H_k \psi_i)}{\partial x_j} dV = \int_{\partial V_B} \epsilon_{ijk} H_k \psi_i n_j d\partial V, \tag{5.35}$$

$$\int_{V_u} \frac{\partial (T_{ij} \varphi_i)}{\partial x_j} dV = \int_{\partial V_u} T_{ij} \varphi_i n_j d\partial V. \tag{5.36}$$

Substitution of these relations into (5.31) and (5.32) along with $\epsilon_{ijk}H_k\partial\psi_i/\partial x_j = -\epsilon_{ijk}H_i\partial\psi_k/\partial x_j$ and $\epsilon_{ijk}H_k\psi_i n_j = -\epsilon_{ijk}H_j n_k\psi_i$, gives

$$\int_{V_B} H_i\epsilon_{ijk}\frac{\partial\psi_k}{\partial x_j}dV + \int_{V_B}\sigma\frac{\partial A_i}{\partial t}\psi_i dV = \int_{\partial V_B}\epsilon_{ijk}H_j n_k\psi_i d\partial V + \int_{V_B}(J_s)_i\psi_i dV, \tag{5.37}$$

$$\int_{V_u} T_{ij}\frac{\partial\varphi_i}{\partial x_j}dV + \int_{V_u}\rho\frac{\partial^2 u_i}{\partial t^2}\varphi_i dV + \int_{V_u} c\frac{\partial u_i}{\partial t}\varphi_i dV = \int_{\partial V_u} T_{ij}\varphi_i n_j d\partial V + \int_{V_u}(f_B)_i\varphi_i dV. \tag{5.38}$$

In the Galerkin method, the weighting functions have the same basis as the dependent functions which in this case are A_i and u_i. The weighting functions can also be thought of as virtual generalized displacements, $\psi_i = \delta A_i$ and $\varphi_i = \delta u_i$. The weak form, in Einstein notation, is then

$$\begin{aligned}\int_{V_B} H_i\epsilon_{ijk}\frac{\partial\delta A_k}{\partial x_j}dV + \int_{V_B}\sigma\frac{\partial A_i}{\partial t}\delta A_i dV = \\ \int_{\partial V_B}\epsilon_{ijk}H_j n_k\delta A_i d\partial V + \int_{V_B}(J_s)_i\delta A_i dV,\end{aligned} \tag{5.39}$$

$$\begin{aligned}\int_{V_u} T_{ij}\frac{\partial\delta u_i}{\partial x_j}dV + \int_{V_u}\rho\frac{\partial^2 u_i}{\partial t^2}\delta u_i dV + \int_{V_u} c\frac{\partial u_i}{\partial t}\delta u_i dV = \\ \int_{\partial V_u} T_{ij}n_j\delta u_i d\partial V + \int_{V_u}(f_B)_i\delta u_i dV.\end{aligned} \tag{5.40}$$

In matrix notation, the weak form is

$$\begin{aligned}\int_{V_B}\mathbf{H}\cdot(\nabla\times\delta\mathbf{A})\,dV + \int_{V_B}\sigma\frac{\partial\mathbf{A}}{\partial t}\cdot\delta\mathbf{A}\,dV = \\ \int_{\partial V_B}(\mathbf{H}\times\mathbf{n})\cdot\delta\mathbf{A}\,d\partial V + \int_{V_B}\mathbf{J}_s\cdot\delta\mathbf{A}\,dV,\end{aligned} \tag{5.41}$$

$$\begin{aligned}\int_{V_u}\mathbf{T}\cdot\nabla\delta\mathbf{u}\,dV + \int_{V_u}\rho\frac{\partial^2\mathbf{u}}{\partial t^2}\cdot\delta\mathbf{u}\,dV + \int_{V_u} c\frac{\partial\mathbf{u}}{\partial t}\cdot\delta\mathbf{u}\,dV = \\ \int_{\partial V_u}\mathbf{T}\mathbf{n}\cdot\delta\mathbf{u}\,d\partial V + \int_{V_u}\mathbf{f}_B\cdot\delta\mathbf{u}\,dV.\end{aligned} \tag{5.42}$$

The weak form represents a balance of the internal and external virtual work, since the kinematic relationships, $\delta\mathbf{B} = \nabla\times\delta\mathbf{A}$ and $\delta\mathbf{S} = \nabla\delta\mathbf{u}$ appear as work conjugates with $\mathbf{H}$ and $\mathbf{T}$. Additionally, the surface traction at the mechanical boundary is

$\mathbf{t} = \mathbf{Tn}$ and the tangent field at the magnetic boundary is $\mathbf{H}_T = \mathbf{H} \times \mathbf{n}$. Substituting from the kinematic relationships and using the traction and tangential field gives the virtual work

$$\int_{V_B} \mathbf{H} \cdot \delta\mathbf{B} \; dV + \int_{V_B} \sigma \frac{\partial \mathbf{A}}{\partial t} \cdot \delta\mathbf{A} \; dV = \int_{\partial V_B} \mathbf{H}_T \cdot \delta\mathbf{A} \; d\partial V + \int_{V_B} \mathbf{J}_s \cdot \delta\mathbf{A} \; dV, \tag{5.43}$$

$$\int_{V_u} \mathbf{T} \cdot \delta\mathbf{S} \; dV + \int_{V_u} \rho \frac{\partial^2 \mathbf{u}}{\partial t^2} \cdot \delta\mathbf{u} \; dV + \int_{V_u} c \frac{\partial \mathbf{u}}{\partial t} \cdot \delta\mathbf{u} \; dV = \int_{\partial V_u} \mathbf{t} \cdot \delta\mathbf{u} \; d\partial V + \int_{V_u} \mathbf{f}_B \cdot \delta\mathbf{u} \; dV. \tag{5.44}$$

5.3.3 3-D Finite element formulation

In the finite element method, the solution domain is discretized into finite elements and the integrations in the weak form equations (5.41) and (5.42) are performed over elements. The solution variables, vector potential and displacement in the element are interpolated from the nodal values. Therefore, only the interpolation or shape functions are integrated resulting in matrix equations for the nodal values of the solution variables.

The interpolations and integrations, performed over element number e, are done in local or natural coordinates $\boldsymbol{\xi}$ with Jacobian $\boldsymbol{\mathcal{J}}_e$ relating the differential $d\mathbf{x}$ to $d\boldsymbol{\xi}$ so that $d\mathbf{x} = \boldsymbol{\mathcal{J}}_e d\boldsymbol{\xi}$ and $dV = det(\boldsymbol{\mathcal{J}}_e) d\xi_1 d\xi_2 d\xi_3 = J_e \xi_1 d\xi_2 d\xi_3$. For a linearly interpolated geometry, the spatially dependent $\mathbf{A}_e$ and $\mathbf{u}_e$ in an element are interpolated from the nodal values $\mathbf{q}_e^A$ and $\mathbf{q}_e^u$ according to

$$\mathbf{A}_e = \mathbf{N}_A(\boldsymbol{\xi}) \mathbf{q}_e^A, \;\; \mathbf{u}_e = \mathbf{N}_u(\boldsymbol{\xi}) \mathbf{q}_e^u. \tag{5.45}$$

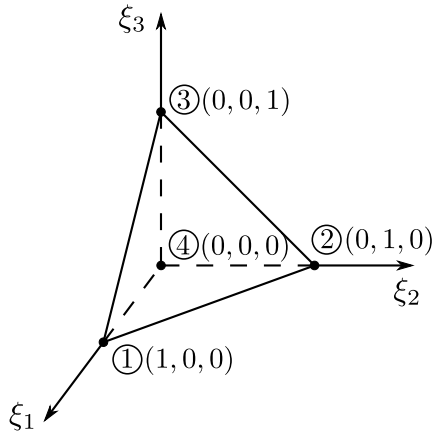

Figure 5.7: 4-node tetrahedral element.

Since the virtual quantities have the same basis in the Galerkin method, the same shape functions are used for the virtual quantities,

$$\delta\mathbf{A}_e = \mathbf{N}^A(\boldsymbol{\xi})\delta\mathbf{q}_e^A,\ \ \delta\mathbf{u}_e = \mathbf{N}^u(\boldsymbol{\xi})\delta\mathbf{q}_e^u. \tag{5.46}$$

As shown above, $\mathbf{A}_e$ and $\mathbf{u}_e$ need not have the same element type or interpolation matrix. The interpolation matrix $\mathbf{N}^A$ has three rows, since $\mathbf{A}$ is a 3-D vector, and for an element having N_n^A nodes (N_n^A depends on the element order) it has N_q^A columns where $N_q^A = 3N_n^A$, since each node has an associated 3-D vector containing the nodal value of $\mathbf{A}_e$. The vector $\mathbf{q}_e^A$ has N_q^A entries which correspond to the three components of $\mathbf{A}_e$ at each node. Since the displacements need not have the same shape functions, $\mathbf{N}^u$ has N_q^u columns which depends on the number of nodes N_n^u. The total degrees of freedom for an element is therefore $N_q = N_q^u + N_q^A$.

Typical choices for the shape functions are linear or quadratic Lagrange shape functions employed over tetrahedral elements. Six-node brick elements may also be used but are more challenging to implement because of a lack of robust meshing

algorithms. If 4-node tetrahedral elements are used for both vector potential and displacement, then $\mathbf{N}^A = \mathbf{N}^q = \mathbf{N}$. A tetrahedral element using linear shape functions has four nodes (see Figure 5.7.) The matrix shape function $\mathbf{N}$ is comprised of the Lagrange shape functions,

$$N_1 = \xi_1, \tag{5.47}$$

$$N_2 = \xi_2, \tag{5.48}$$

$$N_3 = \xi_3, \tag{5.49}$$

$$N_4 = 1 - \xi_1 - \xi_2 - \xi_3. \tag{5.50}$$

Shape functions have the property that at node i, $N_j = 1$ for $j = i$ and $N_j = 0$ for $j \neq i$ and are thus used to interpolate both the geometry and the solution variables. For example, the spatial coordinate x_1 is interpolated from the nodal values $x_{1,n}$ in the following manner,

$$x_1 = N_1 x_{1,1} + N_2 x_{1,2} + N_3 x_{1,3} + N_4 x_{1,4}. \tag{5.51}$$

The vector $\mathbf{q}_e^A$ has twelve entries, the first three are the three components of $\mathbf{A}_e$ at node 1, the second three are the components at node 2 and likewise for the remaining two nodes. It follows that the shape function matrix is,

$$\mathbf{N}(\boldsymbol{\xi}) = \begin{bmatrix} N_1 & 0 & 0 & N_2 & 0 & 0 & N_3 & 0 & 0 & N_4 & 0 & 0 \\ 0 & N_1 & 0 & 0 & N_2 & 0 & 0 & N_3 & 0 & 0 & N_4 & 0 \\ 0 & 0 & N_1 & 0 & 0 & N_2 & 0 & 0 & N_3 & 0 & 0 & N_4 \end{bmatrix}, \tag{5.52}$$

so that when $\boldsymbol{\xi} = (1, 0, 0)$ or at node 1, $\mathbf{A}_e = \mathbf{A}_{e,1}$; the vector potential is simply the value of node 1. Likewise when $\boldsymbol{\xi} = (0, 1, 0)$ or at node 2, $\mathbf{A}_e = \mathbf{A}_{e,2}$; the vector potential is simply the value at node 2 and similarly for the other nodes. Elsewhere in the tetrahedron, the shape functions simply result in a linear interpolation of the

nodal values. For example, if $\boldsymbol{\xi} = (1/2, 1/2, 0)$ which lies midway along the edge connecting nodes 1 and 2, $\mathbf{A}_e = (1/2)(\mathbf{A}_{e,1} + \mathbf{A}_{e,2})$.

In the finite element model, the nodal values of the vector potential and displacement are the unknowns and the nodal values of the virtual vector potential and displacement are arbitrary. To include the finite element discretization in the virtual work equations (5.43) and (5.44), the flux density, magnetic field, strain and stress need to be calculated from the vector potential and displacement,

$$\mathbf{B}_e = \nabla \times \mathbf{A}_e = \nabla \times (\mathbf{N}^A \mathbf{q}_e^A) := \mathbf{C}_e \mathbf{q}_e^A \tag{5.53}$$

$$\mathbf{S}_e = \nabla \mathbf{u}_e = \nabla (\mathbf{N}^u \mathbf{q}_e^u) := \mathbf{G}_e \mathbf{q}_e^u. \tag{5.54}$$

The entries in the matrices $\mathbf{C}_e$ and $\mathbf{G}_e$ contain the derivatives of the local coordinate system $\boldsymbol{\xi}$ with respect to the global coordinate system $\mathbf{x}$ and can be thought of as the discrete form of the curl and gradient operators. For linear elements they do not depend on $\boldsymbol{\xi}$ since the Jacobian $\boldsymbol{\mathcal{J}}$ is a constant matrix containing the side lengths of the tetrahedral element, however for higher order elements including the quadratic element they depend on $\boldsymbol{\xi}$. Making the substitutions and performing the integrals over N^A elements for the magnetic domain and N^u elements for the mechanical domain results in the following summations for the virtual work balance,

$$\sum_{e=1}^{N^A} \left(\int_\Delta \mathbf{H} \cdot \mathbf{C}_e \delta \mathbf{q}_e^A \; J_e d\Delta + \int_\Delta \sigma_e \mathbf{N}^A \frac{\partial \mathbf{q}_e^A}{\partial t} \cdot \mathbf{N}^A \delta \mathbf{q}_e^A \; J_e d\Delta \right) = \sum_{b=1}^{N_S^A} \int_\Delta \mathbf{H}_{T,b} \cdot \mathbf{N}^A \delta \mathbf{q}_b^A \; J_{b,S} d\Delta_S + \sum_{e=1}^{N^A} \int_\Delta \mathbf{J}_{s,e} \cdot \mathbf{N}^A \delta \mathbf{q}_e^A \; J_e d\Delta, \tag{5.55}$$

$$\sum_{e=1}^{N^u}\left(\int_\Delta \mathbf{T}\cdot\mathbf{G}_e\delta\mathbf{q}_e^u\ J_e d\Delta+\int_\Delta \rho_e\mathbf{N}^u\frac{\partial^2\mathbf{q}_e^u}{\partial t^2}\cdot\mathbf{N}^u\delta\mathbf{q}_e^u\ J_e d\Delta+\right.$$
$$\left.\int_\Delta c_e\mathbf{N}^u\frac{\partial\mathbf{q}_e^u}{\partial t}\cdot\mathbf{N}^u\delta\mathbf{q}_e^u\ J_e d\Delta\right)=\sum_{b=1}^{N_S^u}\int_{\Delta_S}\mathbf{t}_b\cdot\mathbf{N}^u\delta\mathbf{q}_b^u\ J_{b,S}d\Delta_S, \tag{5.56}$$

the body force term has been dropped since the effects of gravity and the electromagnetic Lorentz forces are usually negligible in magnetostrictive devices [56]. The subscript b refers to the element number on the boundary; there are N_S^A for the magnetic domain and N_S^u for the mechanical domain which have an applied magnetic field and an applied traction, respectively. The integral $\int_\Delta J_e\ d\Delta$ refers to the integral over the element in natural coordinates and is the volume of the element,

$$\int_\Delta J_e d\Delta := \int_{-1}^{1}\int_{-1}^{1}\int_{-1}^{1} det\left(\frac{\partial\mathbf{x}}{\partial\xi}\right)d\xi_1 d\xi_2 d\xi_3 = V_e, \tag{5.57}$$

and the integral $\int_{\Delta_S} J_{b,S}\ d\Delta_S$ gives the surface area of the element face on the boundary,

$$\int_{\Delta_S} J_{b,S}\ d\Delta_S := \int_{-1}^{1}\int_{-1}^{1} det\begin{bmatrix}\frac{\partial x_i}{\partial\xi_i} & \frac{\partial x_i}{\partial\xi_j}\\ \frac{\partial x_j}{\partial\xi_i} & \frac{\partial x_j}{\partial\xi_j}\end{bmatrix}d\xi_i d\xi_j = A_b. \tag{5.58}$$

Point loads can be included in a very straightforward manner if they are applied at element nodes. For point force $\mathbf{P}_p$ applied at node p, the virtual work is $\mathbf{P}_p\cdot\delta\mathbf{q}_p^u$, so for N_p^u point loads, the following should be added to the right-hand side of the mechanical virtual work balance,

$$\sum_{p=1}^{N_p^u}\mathbf{P}_p\cdot\delta\mathbf{q}_p^u. \tag{5.59}$$

Incorporation of constitutive laws

Galfenol constitutive behavior of magnetic field and stress versus flux density and strain is nonlinear. This nonlinearity is the only such in the finite element model developed in this work. All other materials considered have linear constitutive behavior,

governed mechanically by Hooke's law and magnetically by a constant, isotropic permeability. Geometric nonlinearities are not considered here. It may be necessary to include geometric nonlinearities in order to model manufacturing processes involving plastic strains. In this case, a plastic, nonlinear stress versus strain relationship would be needed as well as the use of finite strains which are nonlinearly related to displacement. The finite element model developed here is applicable to transducers which are operated in the elastic region where the only source of nonlinearity in the stress versus strain relationship is the magnetostriction. In the Newton-Raphson method for solving nonlinear problems, the problem is linearized and solved iteratively for the increments from the initial condition. For small enough increments, the constitutive law for Galfenol and magnetostrictive materials in general is

$$\Delta \mathbf{H} = \boldsymbol{\mu}^{-1} \Delta \mathbf{B} - \mathbf{a} \Delta \mathbf{S}, \tag{5.60}$$

$$\Delta \mathbf{T} = -\mathbf{a}^T \Delta \mathbf{B} + \mathbf{c} \Delta \mathbf{S}. \tag{5.61}$$

The permeability matrix $\boldsymbol{\mu}$ is the permeability at constant $\mathbf{S}$ and the stiffness matrix $\mathbf{c}$ is the stiffness at constant $\mathbf{B}$. For passive materials in the magnetic domain, (5.60) is used with $\mathbf{a} = \mathbf{0}$. For passive materials in the mechanical domain, (5.61) is used with $\mathbf{a} = \mathbf{0}$. The importance of partitioning the total domain to be analyzed into magnetic and mechanical subdomains can be understood from the constitutive law. Consider for example the air volume which does not have an enclosure and is hence free to move. The permeability is simply μ_0 and the stiffness is essentially zero compared to other media in the domain such as copper, steel, and Galfenol. To illustrate, the Galfenol does no work if it deflects while pushing against air. The situation would be different if the air were enclosed in an acoustic chamber. In that case, air pressure would need

to be considered and the air would be characterized by its bulk modulus. Acoustic-structural interactions are not addressed in this work. Integrating the virtual work for both magnetic and mechanical quantities over the entire domain would give the same amount of work as first partitioning and then integrating only over media which have non-zero permeability for the magnetic virtual work and non-zero stiffness for the mechanical virtual work. This is because media with zero permeability introduce no magnetic virtual work, since the magnetic field is zero, and likewise media with zero stiffness introduce no mechanical virtual work. While both approaches lead to the same virtual work, performing the integration and element summation over the entire domain will lead to a singular stiffness matrix in practice, resulting in a non-unique solution.

In the incremental solution, solution starts from an initial state which is known and $\mathbf{q}_e^A$ and $\mathbf{q}_e^u$ are the vector potential and displacement increments. Additionally, the input quantities traction $\mathbf{t}$, surface field $\mathbf{H}_T$ and source current density $\mathbf{J}_s$ are increments. In incremental form, the linear constitutive laws can be used to relate increments of magnetic field and stress to the finite element solution,

$$\mathbf{H}_e = \boldsymbol{\mu}_e^{-1}\mathbf{C}_e\mathbf{q}_e^A - \mathbf{a}_e\mathbf{G}_e\mathbf{q}_e^u, \tag{5.62}$$

$$\mathbf{T}_e = -\mathbf{a}_e^T\mathbf{C}_e\mathbf{q}_e^A + \mathbf{c}_e\mathbf{G}_e\mathbf{q}_e^u. \tag{5.63}$$

These relations can now be substituted into the finite element approximation for the virtual work given by (5.56) and (5.55). This yields matrix equations for increments of the vector potential and displacement nodal values, since they can be pulled from

the integral. To illustrate, the following matrices are defined,

$$\mathbf{k}_e^u = \int_\Delta \mathbf{G}_e^T \mathbf{c}_e \mathbf{G}_e J_e d\Delta, \tag{5.64}$$

$$\mathbf{k}_e^A = \int_\Delta \mathbf{C}_e^T \boldsymbol{\mu}_e^{-1} \mathbf{C}_e J_e d\Delta, \tag{5.65}$$

$$\mathbf{k}_e^{uA} = \int_\Delta \mathbf{C}_e^T \mathbf{a}_e \mathbf{G}_e J_e d\Delta, \tag{5.66}$$

$$\mathbf{d}_e^A = \int_\Delta \left(\mathbf{N}^A\right)^T \sigma_e \mathbf{N}^A J_e d\Delta, \tag{5.67}$$

$$\mathbf{d}_e^u = \int_\Delta \left(\mathbf{N}^u\right)^T c_e \mathbf{N}^u J_e d\Delta, \tag{5.68}$$

$$\mathbf{m}_e = \int_\Delta \left(\mathbf{N}^u\right)^T \rho_e \mathbf{N}^u J_e d\Delta, \tag{5.69}$$

and the following vectors are defined,

$$\mathbf{f}_b^u = \int_{\Delta_S} \left(\mathbf{N}^u\right)^T \mathbf{t}_\mathbf{b} J_{b,S} d\Delta_S, \tag{5.70}$$

$$\mathbf{f}_b^A = \int_{\Delta_S} \left(\mathbf{N}^A\right)^T \mathbf{H}_T J_{b,S} d\Delta_S, \tag{5.71}$$

$$\mathbf{f}_e^J = -\int_\Delta \left(\mathbf{N}^A\right)^T \mathbf{J}_{s,e} J_e d\Delta. \tag{5.72}$$

With these definitions, the finite element approximations for the magnetic and mechanical virtual work balance are

$$\sum_{e=1}^{N^A} \left(\mathbf{d}_e^A \dot{\mathbf{q}}_e^A + \mathbf{k}_e^A \mathbf{q}_e^A - \mathbf{k}_e^{uA} \mathbf{q}_e^u\right) \cdot \delta \mathbf{q}_e^A = \sum_{e=1}^{N_A} \mathbf{f}_e^J \cdot \delta \mathbf{q}_e^A + \sum_{b=1}^{N_S^A} \mathbf{f}_b^A \cdot \delta \mathbf{q}_b^A, \tag{5.73}$$

$$\sum_{e=1}^{N^u} \left(\mathbf{m}_e \ddot{\mathbf{q}}_e^u + \mathbf{d}_e^u \dot{\mathbf{q}}_e^u + \mathbf{k}_e^u \mathbf{q}_e^u - \left(\mathbf{k}_e^{uA}\right)^T \mathbf{q}_e^A\right) \cdot \delta \mathbf{q}_e^u = \sum_{b=1}^{N_S^u} \mathbf{f}_b^u \cdot \delta \mathbf{q}_b^u + \sum_{p=1}^{N_p^u} \mathbf{P}_p \cdot \delta \mathbf{q}_p^u. \tag{5.74}$$

The global assembly process takes into account element connectivity and replaces the summations with matrix operations (see Ch. 3 of [20] or Ch. 12 of [12] for details.) After global assembly, the finite element model is

$$\left(\mathbf{D}^A \dot{\mathbf{Q}}^A + \mathbf{K}^A \mathbf{Q}^A - \mathbf{K}^{uA} \mathbf{Q}^u\right) \cdot \delta \mathbf{Q}^A = \mathbf{F}^A \cdot \delta \mathbf{Q}^A, \tag{5.75}$$

$$\left(\mathbf{M}^u \ddot{\mathbf{Q}}^A + \mathbf{D}^u \dot{\mathbf{Q}}^u + \mathbf{K}^u \mathbf{Q}^u - \mathbf{K}^{uA} \mathbf{Q}^u\right) \cdot \delta \mathbf{Q}^u = \mathbf{F}^u \cdot \delta \mathbf{Q}^u. \tag{5.76}$$

The vector $\mathbf{Q}^A$ contains the nodal values of the vector potential increments. In the meshing scheme and global assembly process, a mapping is created which maps the nodal values of an element $\mathbf{q}_e^A$ to an entry in $\mathbf{Q}^A$. Most nodes are shared between elements and therefore the total degrees of freedom due to vector potential, or the length of the vector $\mathbf{Q}^A$ is less than the product of the number of elements and the degrees of freedom of an element, $N_Q^A < N_e^A N_q^A$. Likewise, the length of the vector of nodal displacement increments is $N_Q^u < N_e^u N_q^u$. A typical model uses thousands of elements to represent the magnetostrictive element which has twelve degrees of freedom for linear, tetrahedral elements. This illustrates the importance of using an efficient constitutive model since it must be separately evaluated for each degree of freedom of which there are tens of thousands.

The final incremental form of the finite-element model for the vector potential and displacement increments results from equating the coefficients of the virtual generalized displacement in (5.75) and (5.76), which can be done because these are arbitrary,

$$\begin{bmatrix} \mathbf{0} & \mathbf{0} \\ \mathbf{0} & \mathbf{M}^u \end{bmatrix} \begin{pmatrix} \ddot{\mathbf{Q}}^A \\ \ddot{\mathbf{Q}}^u \end{pmatrix} + \begin{bmatrix} \mathbf{D}^A & \mathbf{0} \\ \mathbf{0} & \mathbf{D}^u \end{bmatrix} \begin{pmatrix} \dot{\mathbf{Q}}^A \\ \dot{\mathbf{Q}}^u \end{pmatrix} + \begin{bmatrix} \mathbf{K}^A & -\mathbf{K}^{uA} \\ -\left(\mathbf{K}^{uA}\right)^T & \mathbf{K}^u \end{bmatrix} \begin{pmatrix} \mathbf{Q}^A \\ \mathbf{Q}^u \end{pmatrix} = \begin{pmatrix} \mathbf{F}^A \\ \mathbf{F}^u \end{pmatrix}. \quad (5.77)$$

The essential or Dirichlet boundary conditions must be incorporated in order to obtain a unique solution to the finite element model (5.77). The essential boundary conditions are specified displacement and vector potential, mechanically, these remove rigid body modes.

The structure of the finite element model contributes to the understanding of coupled magnetomechanical systems operated under electromagnetically quasi-static conditions. The mass matrix is singular, containing only contributions from the mechanical mass. The absence of entries from the electromagnetic domain is a consequence of neglecting Maxwell's displacement current and prevents the finite element

model from characterizing electromagnetic radiation, which does not occur in the typical operating regime of magnetostrictive devices (<30 MHz.) Sources of damping include the internal material damping (mechanical) which yields $\mathbf{D}^u$ and eddy currents which give rise to $\mathbf{D}^A$. From (5.67), the amount of eddy current damping depends on the conductivity. The magnetic stiffness $\mathbf{K}^A$ depends on permeability and characterizes the ability to magnetically energize the system. The coupling matrix $\mathbf{K}^{ue}$ characterizes the ability to transfer mechanical energy, applied through surface tractions in the mechanical load vector $\mathbf{F}^u$, to magnetic energy and magnetic energy, applied through current in the magnetic load vector $\mathbf{F}^A$, to mechanical energy.

Before presenting 3-D simulations and discussion, the following sections develop 1-D and 2-D implementations in order to better understand magnetostrictive transducer behavior. A dynamic, 1-D implementation elucidates the effect of eddy currents in magnetomechanical systems. A 2-D, magnetostatic implementation is developed to analyze the effect of hysteresis on transducer level behavior. Finally, a dynamic, 2-D implementation for composite beams illustrates structural dynamics which occur due to magnetostriction. The final implementation is done in 3-D for dynamic operating regimes and provides a framework for characterization of magnetostrictive transducer efficiency.

5.3.4 1-D Dynamic implementation with no demagnetizing fields

In this section, the 3-D transducer model is reduced to 1-D for an infinite rod with radius R. The purpose of this is to illustrate the effect of eddy currents on coupled magnetostructural dynamics. The physics which give rise to eddy currents are coupled to the physics which give rise to structural vibrations. Structural vibrations

can result in eddy current losses (or Ohmic heating) which is manifested as a delay in force-displacement loops. Additionally, stress results in a nonlinear distribution of the magnetic field and flux density over the rod cross section. The inputs for this problem are the magnetic field at the surface of the rod, which appears as a boundary condition and a force (or stress) applied uniformly along the rod and appearing as a weak term. The output quantities of interest are the elongation of the rod and the average magnetic flux density over its cross section.

Diffusion equation (strong form)

For an infinite rod of radius R in an infinite solenoid, the flux density occurs only in the direction parallel to the length of the rod and varies only over the radial direction r. Gauss' law is satisfied automatically under these conditions. This is true of any prismatic geometry where the z component varies only over the cross section. If the rod material obeys Ohm's law, Maxwell's equations are reduced to a scalar, parabolic partial differential equation

$$\frac{\partial}{\partial r}\left(r\frac{\partial H}{\partial r}\right) = r\sigma\frac{\partial B}{\partial t}. \tag{5.78}$$

This equation represents the combined physics from the Faraday-Lenz law (2.6) and Ampère's law (2.7). The details of its derivation can be found in the book by Engdahl [36]. The parameter σ is electrical conductivity and r is the distance from the center of the rod in the radial direction. The flux density is generally a nonlinear function of magnetic field and stress and, according to the chain rule, its time rate of change is

$$\begin{aligned}\frac{\partial B}{\partial t} = \frac{\partial}{\partial t}B(H,T) &= \frac{\partial B}{\partial H}\frac{\partial H}{\partial t} + \frac{\partial B}{\partial T}\frac{\partial T}{\partial t},\\ &:= \mu(H,T)\frac{\partial H}{\partial t} + d(H,T)\frac{\partial T}{\partial t}.\end{aligned} \tag{5.79}$$

When applied to (5.78), this yields the initial-boundary value problem

$$\begin{aligned} \frac{\partial}{\partial r}\left(r\frac{\partial H}{\partial r}\right) &= \mu(H,T)(r\sigma)\frac{\partial H}{\partial t} + d(H,T)(r\sigma)\frac{\partial T}{\partial t}, \\ H(r,0) = H_0 \quad \text{and} \quad H(R,t) &= H_R. \end{aligned} \tag{5.80}$$

Additionally, the field and stress magnitudes may be restricted to a linear region of the material response about some field $\bar{H}$, $\bar{T}$ allowing the use of a constant permeability $\bar{\mu}$. The strong form of the model, for constant stress, is then

$$\begin{aligned} \frac{\partial}{\partial r}\left(r\frac{\partial H}{\partial r}\right) &= \bar{\mu}(r\sigma)\frac{\partial H}{\partial t}, \\ H(r,0) = H_0 \quad \text{and} \quad H(R,t) &= H_R. \end{aligned} \tag{5.81}$$

First, analytic solutions for the transient and harmonic response to fields at the surface will be derived and compared with a finite element solution. Subsequently, a nonlinear permeability with stress dependence will be considered in the finite element model in order to describe coupled magnetostructural dynamics.

Analytic harmonic solution

The steady-state solution can be found by assuming the field is harmonic $H(r,t) = h(r)e^{j\omega t}$ [36]; the initial-boundary value problem becomes a boundary value problem and applying the transformation $u = r\sqrt{-i\omega(\bar{\mu}\sigma)} = gr$ to (5.81) yields the zero-order Bessel equation

$$\begin{aligned} u^2\frac{d^2h}{du^2} + u\frac{dh}{du} + u^2h &= 0, \\ h(R) &= H_R, \\ |h(0)| &< \infty, \end{aligned} \tag{5.82}$$

which has solution

$$h(u) = c_1J_0(u) + c_2Y_0(u). \tag{5.83}$$

The second term approaches infinity near zero, so c_2 is zero. The coefficient c_1 can be determined from the boundary condition at R

$$H(gR,0) = c_1 J_0(gR) H_R \rightarrow c_1 = H_R / J_0(gR), \tag{5.84}$$

yielding the field as

$$H(r,t) = H_R \frac{J_0(gr)}{J_0(gR)} e^{j\omega t}. \tag{5.85}$$

For simulation, the input is real, so the real part of the solution is taken.

Analytic transient solution

Applying the method of separation of variables, it is possible to find the transient solution for a rod with an initial field distribution H_0 which is zero at the boundary. The field is first separated into its radial and time dependence $H(r,t) = h(r)g(t)$ which, when substituted into (5.81) yields

$$\begin{aligned} (h'' + \frac{1}{r}h')g &= \bar{\mu}\sigma \dot{g} h, \\ \frac{h'' + \frac{1}{r}h'}{h} &= \bar{\mu}\sigma \frac{\dot{g}}{g} = -\lambda, \end{aligned} \tag{5.86}$$

where prime is spatial derivative and dot is time derivative. According to the method of separation of variables, the ratios must be constant λ, since g and h are independent. Two ordinary differential equations result

$$\begin{aligned} h'' + \frac{1}{r}h' + \lambda h &= 0, \\ h(R) = 0 \quad \text{and} \quad |h(0)| &< \infty, \end{aligned} \tag{5.87}$$

and

$$\begin{aligned} \dot{g} + \lambda \frac{1}{\bar{\mu}\sigma} g &= 0 \\ g(0) &= g_0. \end{aligned} \tag{5.88}$$

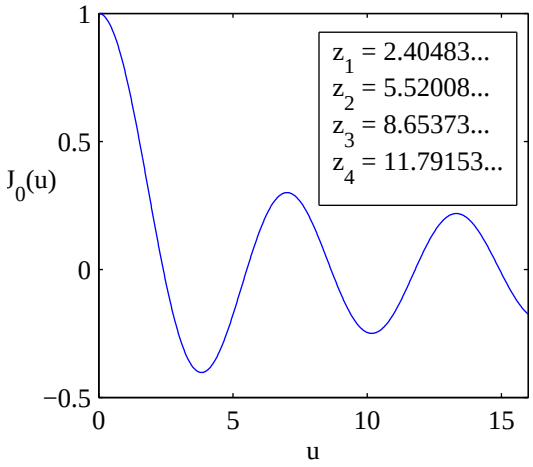

Figure 5.8: Bessel function.

Making the transformation $u = \sqrt{\lambda}r$ and substituting into (5.87) yields Bessel's equation

$$u^2h'' + uh' + u^2h = 0, \tag{5.89}$$

the solution which grows to infinity at zero and is again discarded giving

$$h(r) = c_\lambda J_0(\sqrt{\lambda}r). \tag{5.90}$$

The eigenvalues are determined from the boundary condition $J_0(\sqrt{\lambda}R) = 0$ which yields $\lambda = (z_n/R)^2$, where z_n are the zeros of Bessel's function (see Fig. 5.8) of which there are infinitely many. The solution to (5.88) is $g(t) = g_0 \exp(-\lambda t/(\bar{\mu}\sigma))$ and the solution for the field is an infinite series

$$H(r,t) = \sum_{n=1}^{\infty} a_n J_0(\sqrt{\lambda_n}r) \exp\left(-\lambda_n \frac{1}{\bar{\mu}\sigma} t\right), \tag{5.91}$$

where $a_n = g_0 c_{\lambda_n}$. The coefficients a_n can be determined from the initial condition $H_0 = \sum_{n=1}^{\infty} a_n J_0(\sqrt{\lambda_n} r)$ by applying the orthogonality of the eigenfunctions

$$a_n = \frac{\int_0^R H_0 J_0(\sqrt{\lambda_n} r) dr}{\int_0^R J_0^2(\sqrt{\lambda_n} r) r dr} \tag{5.92}$$

The coefficients a_n tend to zero for large n; typically not more than four terms are needed in the summation.

General solution (finite elements)

The Galerkin method can be used for a finite element solution. The finite element model can describe both the transient and steady-state response and can be implemented with a field and stress dependent permeability. Additionally, the flux density change due to a changing stress, uniform along the rod and over its cross section, can also be included. First the strong form (5.80) is multiplied by a kinematically admissible test function ϕ (it is zero where H is specified) and integrated to give the weak form,

$$\int_0^R \frac{\partial}{\partial r}\left(r \frac{\partial H}{\partial r}\right) \phi dr = \sigma \int_0^R r \left(\mu(H,T) \frac{\partial H}{\partial t} + d(H,T) \frac{\partial T}{\partial t}\right) \phi dr. \tag{5.93}$$

Integration by parts on the left side gives

$$r \frac{\partial H}{\partial r} \phi \Big|_0^R - \int_0^R r \frac{\partial H}{\partial r} \frac{\partial \phi}{\partial r} dr = \sigma \int_0^R r \left(\mu(H,T) \frac{\partial H}{\partial t} + d(H,T) \frac{\partial T}{\partial t}\right) \phi dr. \tag{5.94}$$

The boundary term is zero since at the left boundary $r = 0$ and at the right boundary the test function is zero where H is specified. The conversion $\tilde{H} = H - H_R \rightarrow \partial H/\partial r = \partial \tilde{H}/\partial r, \partial H/\partial t = \partial \tilde{H}/\partial t$ is useful so that the boundary condition is $\tilde{H}(R) = 0$. In the Galerkin method, the dependent variable $\tilde{H}$ is expanded on the test function basis,

$$- \int_0^R r \frac{\partial \tilde{H}}{\partial r} \frac{\partial \phi}{\partial r} dr = \sigma \int_0^R r \left(\mu(H,T) \frac{\partial \tilde{H}}{\partial t} + d(H,T) \frac{\partial T}{\partial t}\right) \phi dr, \tag{5.95}$$

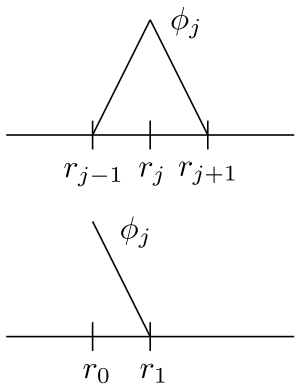

Figure 5.9: Hat functions used for linear finite element discretization over the radius of an infinite rod.

$$\tilde{H} = \sum_{j=0}^{N-1} (H_j - H_R)\phi_j, \tag{5.96}$$

where the nodal values H_j are the field at the node. There are N nodes and therefore $N-1$ elements.

Choosing hat functions (see Figure 5.9) for ϕ_j, the boundary condition is satisfied $\tilde{H}(r=R)=0$, since $\phi_j(r=R)=0$. Note that ϕ_0 is only the right half of the hat function. The derivatives are

$$\begin{aligned} \frac{\partial \tilde{H}}{\partial r} &= \sum_{j=0}^{N-1} (H_j - H_R)\frac{d\phi_j}{dr}, \\ \frac{\partial \tilde{H}}{\partial t} &= \sum_{j=0}^{N-1} \frac{dH_j}{dt}\phi_j. \end{aligned} \tag{5.97}$$

Substitution of (5.97) into (5.81) with test functions ϕ_i yields N equations

$$-\int_0^R r(H_j - H_R)\phi_i'\phi_j' dr = \sigma \int_0^R r\left(\mu(H_j,T)\frac{\partial H_j}{\partial t} + d(H_j,T)\frac{\partial T}{\partial t}\right)\phi_i\phi_j dr. \tag{5.98}$$

Performing the integrations and converting to matrix form, the finite element model is

$$\mathbf{C}\dot{\mathbf{B}} = -\mathbf{A}(\mathbf{H} - \mathbf{b}H_R), \tag{5.99}$$

where the system matrices with row index i and column index j are

$$\mathbf{C} = \sigma \Delta r^2 \begin{bmatrix} \frac{1}{12} & -\frac{1}{12} & 0 & \cdots & & & \\ -\frac{1}{12} & \frac{2}{3} & \frac{1}{4} & 0 & \cdots & & \\ \cdots & 0 & \frac{1}{6}(i-\frac{1}{4}) & \frac{2}{3}(i-1) & \frac{1}{6}(j-\frac{1}{4}) & 0 & \cdots \\ & & & \cdots & 0 & \frac{1}{6}N-\frac{1}{4} & \frac{2}{3}(N-1) \end{bmatrix} \tag{5.100}$$

and

$$\mathbf{A} = \begin{bmatrix} \frac{1}{2} & -\frac{1}{2} & 0 & \cdots & & & \\ -\frac{1}{2} & 2 & -\frac{3}{2} & 0 & \cdots & & \\ \cdots & 0 & -i+\frac{1}{2} & 2(i-1) & -j+\frac{1}{2} & 0 & \cdots \\ & & & & & -N+\frac{1}{2} & 2(N-1) \end{bmatrix}, \tag{5.101}$$

with input vector

$$\mathbf{b} = \begin{bmatrix} 1 \\ 1 \\ \vdots \\ 1 \end{bmatrix}. \tag{5.102}$$

In the construction of the system matrices it is assumed that all elements have length Δr. The components of the flux density rate $\dot{\mathbf{B}}$ are $\mu(H_j, T)\dot{H}_j + d(H_j, T)\dot{T}$. The system is therefore nonlinear for nonlinear magnetomechanical materials.

The N-degree system (5.99) can be reduced in order to characterize the time lag associated with eddy current losses. Using a single element, the system has a single degree of freedom, the field inside the rod, with two inputs, the field at the rod boundary and the stress rate. The matrix equations are reduced to a nonlinear, scalar equation

$$\mu(H, T)\dot{H} + d(H, T)\dot{T} = -\frac{6}{\sigma R^2}(H - H_R). \tag{5.103}$$

For small field and stress magnitudes, $\mu(H, T) = \bar{\mu}$ and the the equation becomes a linear system with time constant $\tau = \sigma R^2/\bar{\mu}$. The time constant from the finite element approach is very close to the first time constant in (5.91) $\tau_1 = (\sigma\bar{\mu})/\lambda_1 = (\sigma\bar{\mu})R^2/z_n^2 = (\sigma\bar{\mu})R^2/5.7832$.

Field diffusion simulations

A comparison of the finite element model (5.99), the lumped parameter method (5.103), and the analytic transient response (5.91) is shown in Fig. 5.10 for the transient response to an initial magnetic field $H(r,0) = H_c(1-r/R)$. For this comparison, the stress rate is zero and the permeability is constant since this allows for analytic solution. The field at varius points along the radius is shown where starting from the initial field, the field over the cross section decays to zero. The lumped parameter model from the finite element method can be used in lumped parameter electro-acoustic models.

A comparison with the analytic harmonic response (5.85) is shown in Fig. 5.11 where the error at the beginning is due to the fact that the numerical approaches capture both the transient and steady-state response whereas a general analytic solution is not possible. This comparison is also done with constant permeability and zero stress rate.

Magnetostructural dynamics

Here the coupled magnetostructural dynamics of a longitudinal actuator/sensor are described. Figure 5.12 depicts the transducer. Since the magnetic circuit is closed, the infinite rod assumptions used for deriving the field diffusion equation are accurate. An additional assumption made here is that the stress and strain are uniform in the rod.

The initial-boundary value problem governing displacements is from Newton's second law

$$\nabla \cdot \mathbf{T} = \rho \ddot{\mathbf{u}} + c\dot{\mathbf{u}}. \tag{5.104}$$

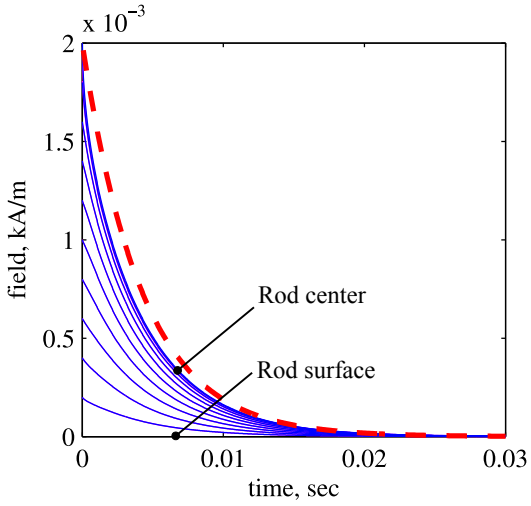

Figure 5.10: Transient response to initial field conditions in an infinite rod from the finite element method the analytic solution (they overlap) the lumped parameter model (dashed.)

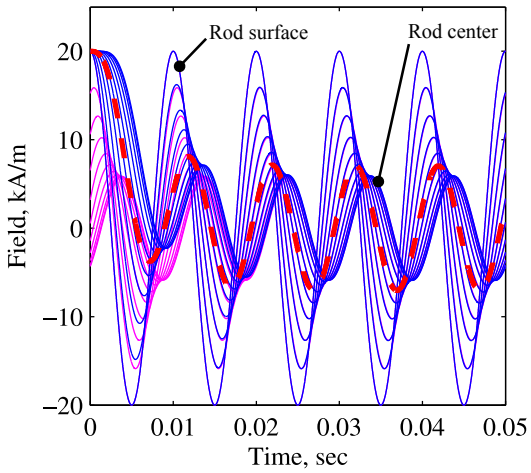

Figure 5.11: Comparison of the finite element model and lumped parameter model (dashed) with the harmonic analytic solution for magnetic field in an infinite rod.

With the uniform stress and strain assumption, this is reduced to a second-order differential equation for the rod tip displacement from equilibrium, driven by an external force f_{ext} at the rod tip and the average magnetostriction $\bar{S}_m$ calculated from the anhysteretic discrete energy-averaged model developed in Section 4.3,

$$(m_R + m_L)\frac{d^2u}{dt^2} + (c_R + c_L)\frac{du}{dt} + (k_R + k_L)u = EA\bar{S}_m(H,T) - f_{ext}, \quad (5.105)$$

$$u(0) = 0. \quad (5.106)$$

The mass $m_R = (1/3)\rho Al$ is the dynamic mass of the Galfenol rod with cross sectional area $A = \pi r_0^2$ and length l, $c_R = cA/l$ is the damping coefficient of the rod for its internal thermal-mechanical losses, and $k_R = EA/l$ is its stiffness. The parameters m_L, c_L, and k_L are the mass, damping, and stiffness of a load at the rod tip. The reduction (5.105) is made by using a single linear element for the z dimension. Details on the element definition can be found in the magnetostrictive transducer model of Dapino, Smith and Flatau [30]. The work here differs by coupling the structural model to the electromagnetic model (5.80) including eddy current losses. A consequence of using a single element for the mechanical domain is that structural modes higher than the fundamental are ignored. This simplification is necessary in order to couple to the 1-D electromagnetic model (5.80) since that model necessarily assumes that the magnetic field is uniform along the rod length. For the magnetic field to be uniform along the rod length, the stress and strain must also be uniform due to magnetomechanical coupling in the constitutive relationship. The constitutive relationship for stress in 1-D is

$$T = E(u/l - \bar{S}_m), \quad (5.107)$$

where E is the modulus of elasticity.

The outputs of the 1-D, magnetostructural model are the displacement u and the flux density $\bar{B}$ averaged over the cross section. The flux density is also calculated using the anhysteretic discrete energy-averaged model along with the coefficients $\mu(H,T)$ and $d(H,T)$ in (5.80). The anhysteretic model is used to illustrate delays due to magnetostructural dynamics only. The inputs are the magnetic field applied to the rod surface H_R and the externally applied force f_{ext}. A block diagram for the model is shown in Figure 5.13. The system is discretized in space with the finite element method and in time with backward differences and then solved iteratively, updating the stress with each iteration. The iterations continue until a convergence criterion is satisfied.

1-D Magnetostructural dynamic simulations

For all simulations the rod dimensions are $1/4 \times 1$ inches, $E = 60$ GPa, $\rho = 77.1$ Kg/m^3, $\lambda_{100} = 173e-6$, $\lambda_{111} = 20e-6$, $\mu_0 M_s = 1.62$ T, $K_{100} = 10$ kJ/m^3, $k_B\theta/V = 200$ kJ/m^3, and $\sigma = 1.4e6$ $(\Omega\text{m})^{-1}$. For a slowly-varying external magnetic field, the magnetic field is expected to be nearly uniform over the cross section and the average flux density is expected to follow the flux density at the rod surface $B(H_R)$.

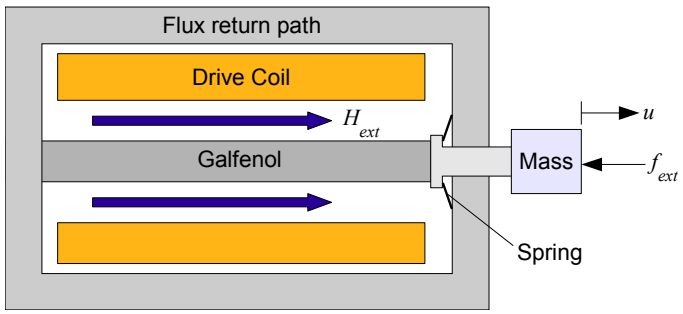

Figure 5.12: Longitudinal transducer operable for actuation/sensing.

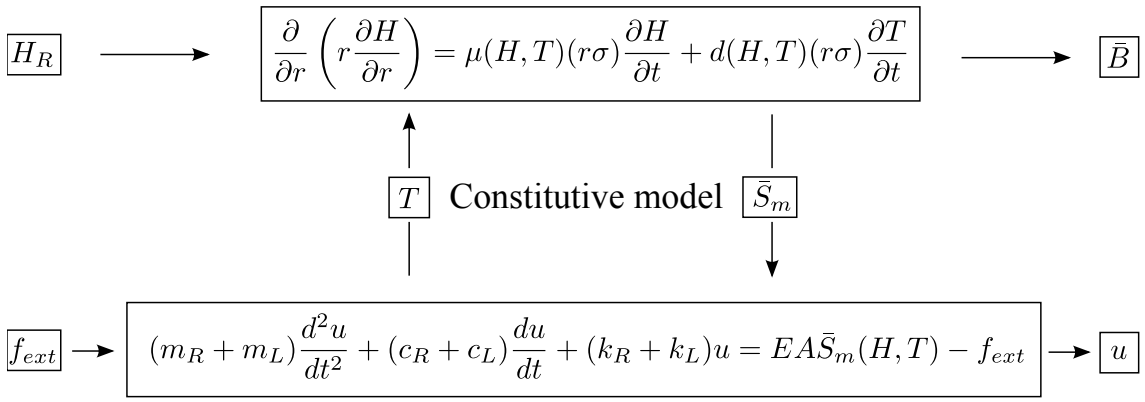

Figure 5.13: Block diagram for 1-D dynamic magnetostructural model.

Furthermore, if the spring load is zero and sufficient bias stress is applied to align domains 90^o to the rod axis, the stress should remain constant and the maximum free-strain $3/2\lambda_{100}$ should be reached. This is verified in Figure 5.14; Figure 5.14(a) shows that the magnetic field at all radius locations is the same; Figure 5.14(b) shows that the stress remains constant at the applied bias stress (-5 MPa); Figure 5.14(c) shows that the average flux density follows the surface flux density and Figure 5.14(d) shows that a rod elongation of $3/2\lambda_{100}$ is achieved.

If a spring of stiffness $k_l >> EA/l$ is now added, the rod displacement should be blocked and a blocking stress of $3/2\lambda_{100}E$ should be achieved in addition to the bias stress. Also, the flux density should be sheared because the magnetic field has to work against the stress-induced anisotropy. This is verified in Figure 5.15; Figure 5.15(b) shows that the stress varies from the bias stress to the sum of the bias stress and $3/2\lambda_{100}E$, and Figure 5.15(d) shows that the rod elongation is nearly zero.

As the transducer is actuated by a dynamic external magnetic field, eddy currents give rise to magnetic fields which oppose the applied field; this results in a spatial

distribution of the magnetic field. In addition, the magnetic field near the center of the rod is no longer purely sinusoidal because of the nonlinear and stress dependent permeability. Since the magnetic field near the center of the rod is delayed with respect to the external magnetic field, the average magnetic flux density and the rod elongation u/l plotted against the external applied field shows significant lag. These dynamic effects are shown in Figure 5.16 for a 100 Hz applied magnetic field.

When the transducer is used as a sensor, a dynamic force input results in a dynamic change in flux density due to stress-induced domain rotation. In response to this dynamic flux density, eddy currents arise which create magnetic fields in opposition to the flux density change (see Figure 5.17(a)). This results in dynamic hysteresis loss as seen in Figure 5.17(b) which shows the average magnetic flux density versus the force input and in Figure 5.17(c) which shows the rod elongation versus the force input.

5.3.5 2-D Static implementation with hysteretic constitutive law

A 2-D, magnetostatic (no eddy currents) analysis is performed in this section to study hysteresis in magnetostrictive transducers. The virtual work equations (5.43) and (5.44) are reduced under the following assumptions

- Spatially uniform stress
- Current density applied in z direction only
- Current density input varies slowly
- Zero magnetic field on the boundary of the air volume

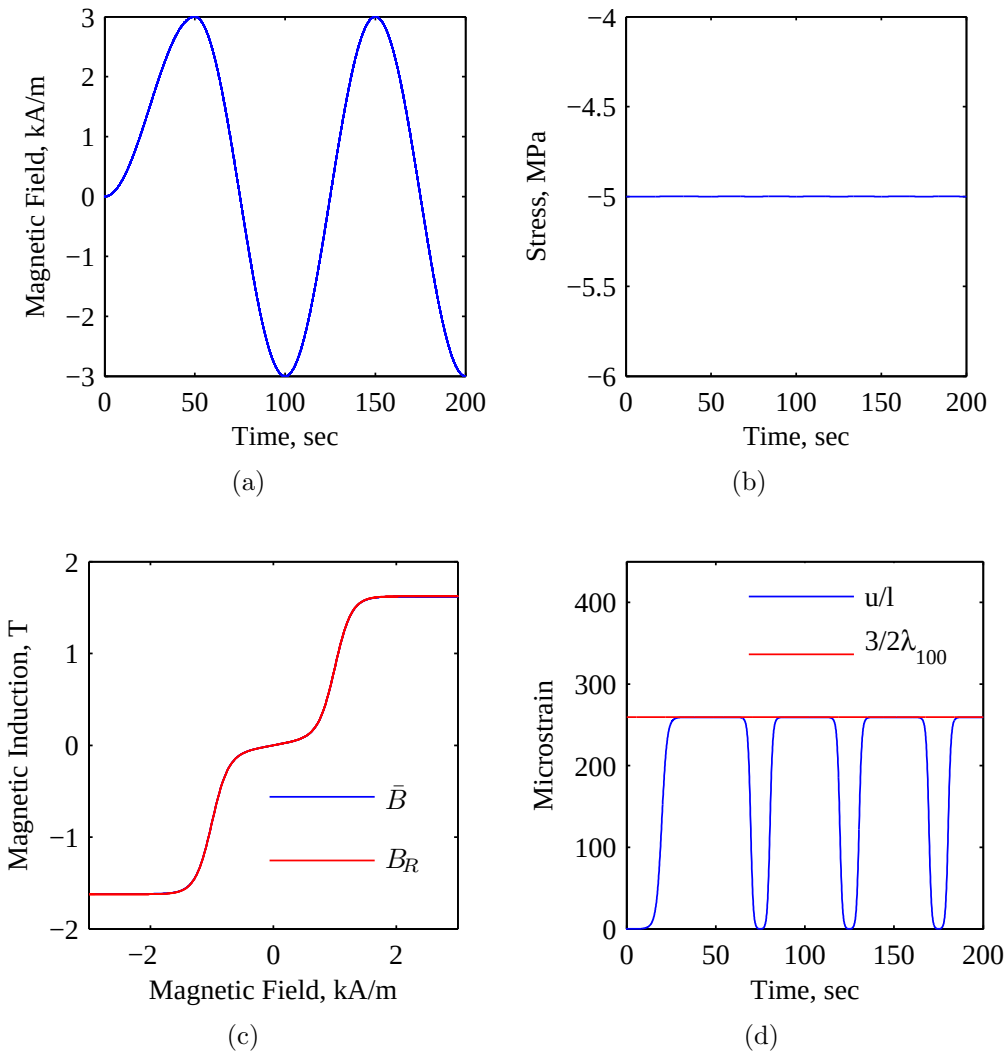

Figure 5.14: No-load model simulation with a constant bias stress of -5 MPa and a 100 mHz external field input with an amplitude of 3 kA/m.

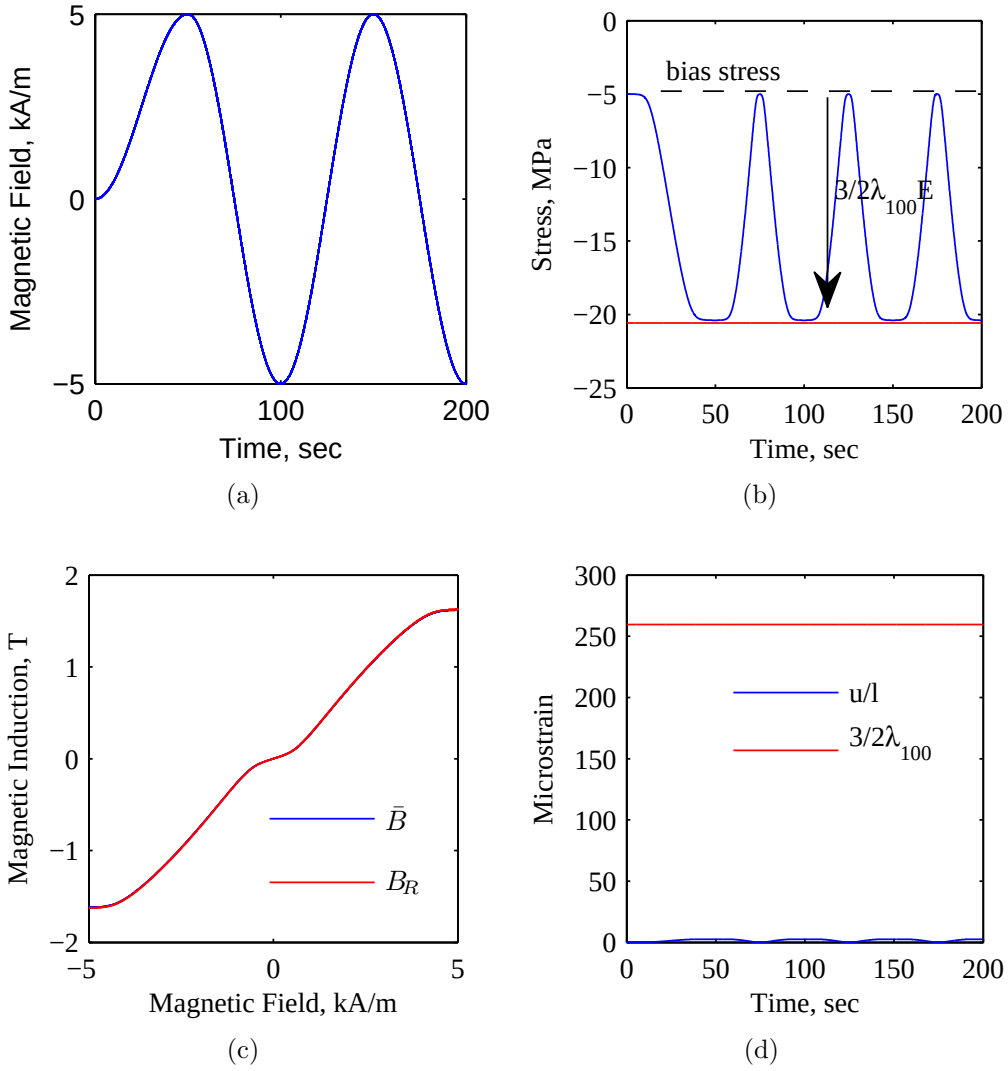

Figure 5.15: Blocked magnetostructural simulation with $k_L >> EA/l$, a constant bias stress of -5 MPa and a 100 mHz external field input with an amplitude of 3 kA/m

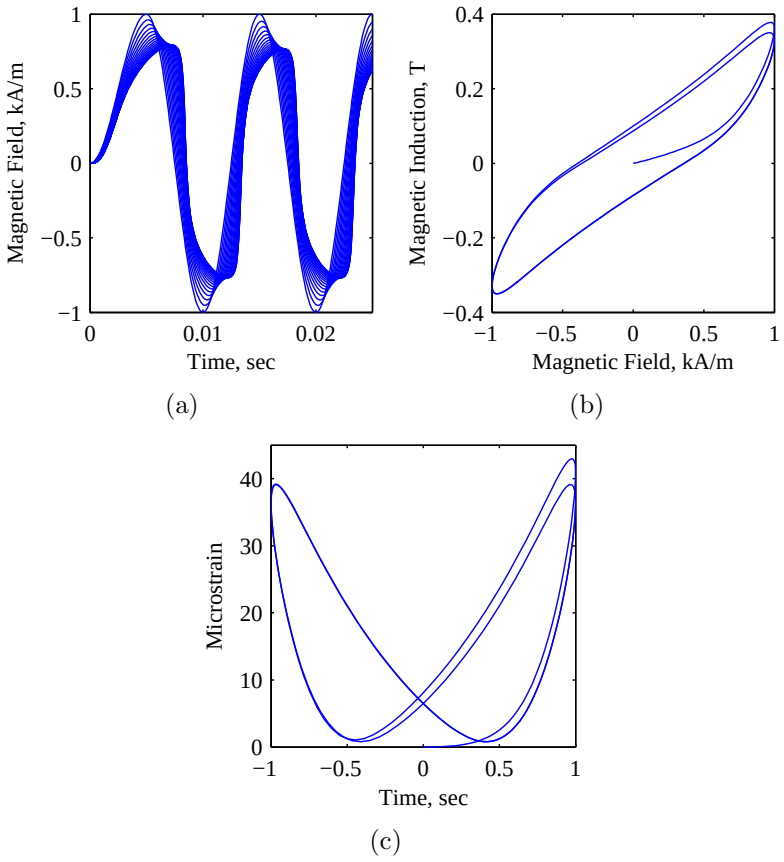

Figure 5.16: Dynamic actuation simulation with $k_L = (EA/l)/8$, a bias stress of -5 MPa and a 100 Hz external field input where (a) shows the spatial variation of the magnetic field with the smallest amplitude field at the center, (b) shows the average flux density versus applied magnetic field, and (c) shows the rod elongation u/l versus applied magnetic field.

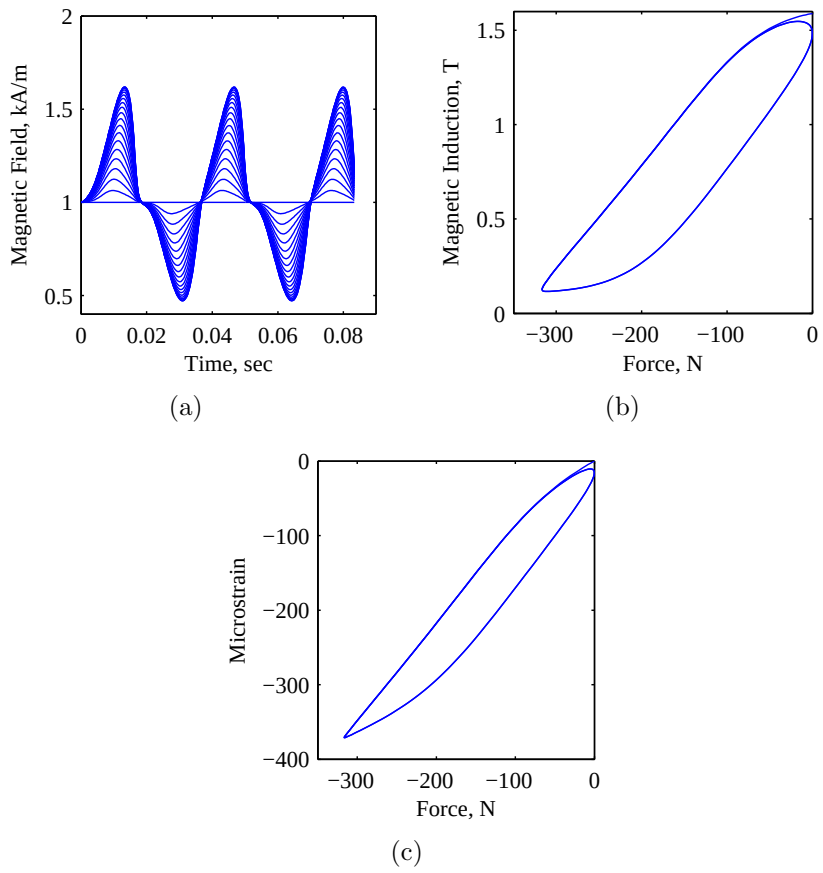

Figure 5.17: Dynamic sensing simulation with $k_L = EA/l/8$, a bias stress of -2 MPa, bias field of 1 kA/m and a 100 Hz external force input where (a) shows the eddy current induced spatial variation of the magnetic field with the largest amplitude field at the center (b) shows the average flux density versus applied force and (c) shows the rod elongation u/l versus applied force

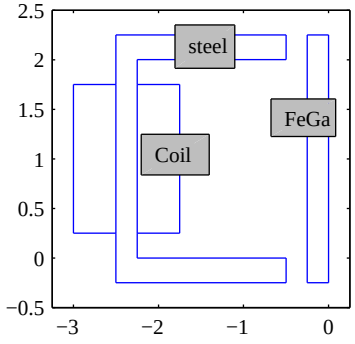

Figure 5.18: 2-D Geometry for quasi-static, nonlinear electromagnetic simulations.

With these assumptions the problem become planar; the virtual work is

$$\int_V \mathbf{H} \cdot \delta\mathbf{B} \; dV = \int_V J_z \delta A_z \; dV. \tag{5.108}$$

The magnetic field and flux density are the x and y components and A_z is the only nonzero component of the vector potential so that the flux density is,

$$B_x = \frac{\partial A_z}{\partial y}, \qquad B_y = -\frac{\partial A_z}{\partial x}. \tag{5.109}$$

For the air and copper subdomains, the constitutive relationship is simply $\mathbf{B} = \mu_0 \mathbf{H}$ and for the steel it is $\mathbf{B} = \mu_S \mathbf{H}$ where μ_S is the permeability of steel. For the Galfenol subdomain, the hysteretic discrete energy averaged model is used. The objective is to solve for the vector potential, from which all other quantities can be calculated $\mathbf{B}$, $\mathbf{H}$, $\mathbf{S}_m$ and the domain volume fractions ξ^k. The inputs are the current density J_z and the stress applied to the Galfenol.

Incremental solution method

An incremental or piece-wise linear solution method is employed to describe the planar system in Figure 5.18. The solution process begins from the known state $A_{z,0} = J_{z,0} = 0$ and $\mathbf{B}_0 = \mathbf{H}_0 = 0$. The current density is incremented $J_z = J_{z,0} + \Delta J_z$ resulting in an increment in all other quantities. Since the virtual work is balanced in the initial state, the increments must satisfy

$$\int_V \Delta\mathbf{H} \cdot \delta\mathbf{B} \; dV = \int_V \Delta J_z \delta A_z \; dV. \tag{5.110}$$

By taking small enough increments, the constitutive relationship between magnetic field and flux density, given by the discrete energy-averaged model, can be linearized

$$\Delta\mathbf{H} = \boldsymbol{\mu}^{-1}(\mathbf{B}_0, T)\Delta\mathbf{B}. \tag{5.111}$$

For each increment of applied current density, integration is performed over triangular elements with linear shape functions. Details of the element definition and matrices are not given since they follow directly from the 3-D definitions (5.53) and (5.65). This yields a matrix equation for the nodal values of the vector potential increments

$$\mathbf{K}^A\mathbf{Q}^A = \mathbf{F}^A. \tag{5.112}$$

The magnetic stiffness matrix and force vector are updated after each current density increment. This incremental solution method is implemented with Matlab's PDE toolbox; simulations follow in the next section.

2-D Magnetostatic simulations

The same Galfenol material properties are used in these simulations as are used in the 1-D magnetostructural model in addition to $k_p = 600$ and $c = 0.1$. The pinning coefficient is larger than expected for Galfenol in order to emphasize the effect of hysteresis. The Galfenol sample is mechanically unconstrained and loaded with a constant and spatially uniform compressive stress. The [010] crystal orientation is oriented along the Galfenol length directed up and the [100] is along the Galfenol width directed to the right. To analyze the effect of geometry and stress on the flux density, magnetostriction, and domain volume fractions, simulations were performed with and without air gaps between the steel flux path and Galfenol and with and without stress applied to the Galfenol sample.

Figure 5.19 depicts quantities calculated from the simulations. Figure 5.19(a) is the average magnetization over the cross section of the Galfenol sample at its center plotted against the magnetic field located 3.2 mm from the surface at the rod center.

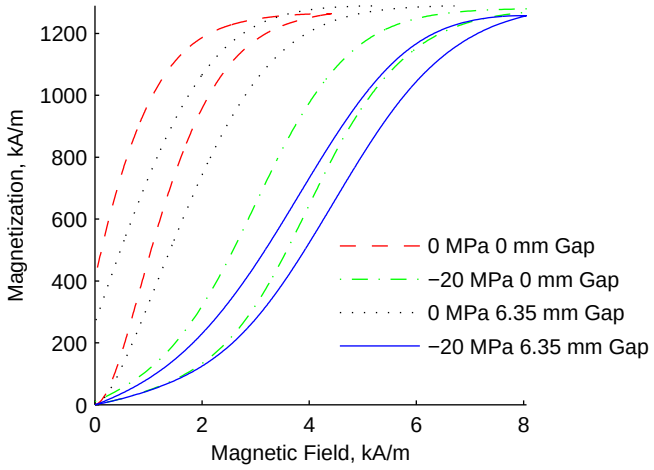

(a)

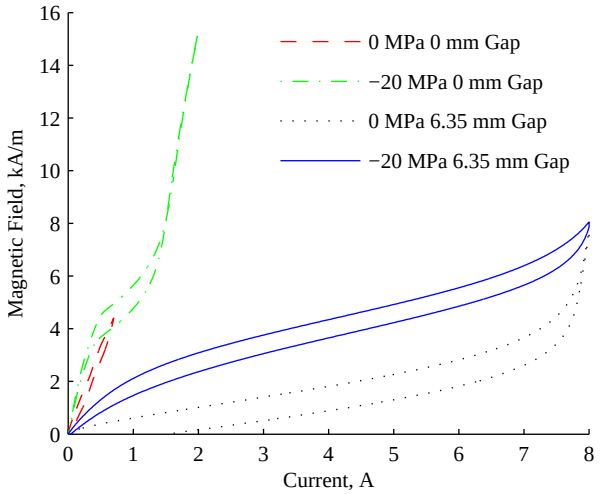

(b)

Figure 5.19: (a) Magnetization and (b) field simulations for applied current with and without stress and air gaps.

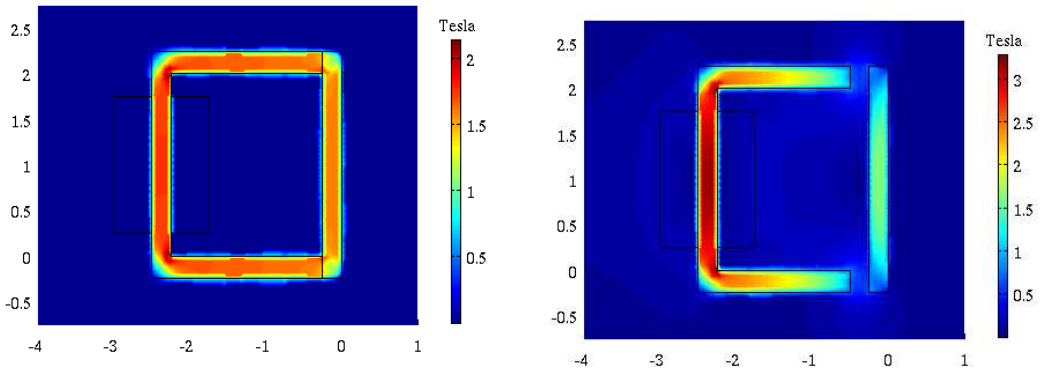

(a) (b)

Figure 5.20: Norm of flux density at saturation (a) without and (b) with air gaps.

Both quantities are for the [010] direction. Both air gaps and stress tend to shear the induction versus field behavior. Stress impedes domain rotation and favors the [100] and [$\bar{1}$00] directions which are perpendicular to the stress. Air gaps result in flux-leakage which shears the curve. This causes a change in the current-field behavior as well (see Figure 5.19(b)) where more current is needed in the presence of air gaps. Stress changes the current-field curves because it changes the permeability of Galfenol. This nonlinear behavior as well as saturation result in a nonlinear current-field relationship. The relationship is hysteretic as a result of the hysteresis in Galfenol's constitutive behavior which gives rise to a hysteretic permeability.

The cause of the sheared field-magnetization behavior for simulations with air gaps is illustrated in Figure 5.20 which plots the FEM solution for the norm of the induction at saturation. Here, saturation is defined as the point where the average magnetization over the cross section (Figure 5.19) reaches the material's saturation

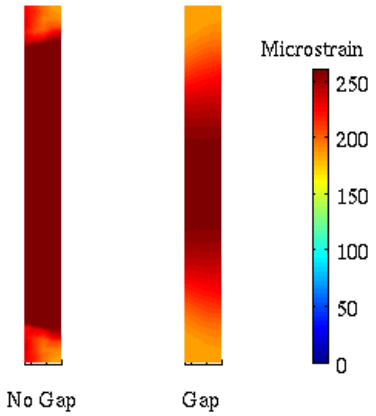

Figure 5.21: Norm of strain at saturation with no applied stress.

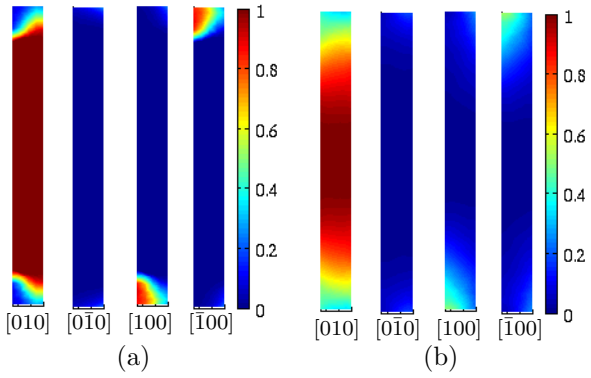

Figure 5.22: Domain volume fractions in Galfenol at saturation (a) without and (b) with air gaps.

magnetization. The difference in permeability between the air, steel and Galfenol regions gives a nonuniform induction from Gauss' law which can also be interpreted as the presence of a demagnetizing field which must be overcome by the current induced field. The non-uniformity for the case without air gaps (see Figure 5.20(a)) is much less because steel and Galfenol have similar permeability. This results in negligible demagnetizing fields and the Galfenol sample is easier to magnetize. Demagnetizing fields from Gauss' law also result in a nonuniform domain configuration. Although the modeling framework presented here does not encompass a microscopic description of domains including domain size, domain wall width and closure domains, the volume fraction of energetically favorable domain orientations in the material is calculated (see Figure 5.22.) Figure 5.22(a) shows a homogeneous domain distribution at saturation when there are no air gaps. The Galfenol consists almost entirely of [010] oriented domains except for the ends where [100] and $[\bar{1}00]$ domains are present to channel the flux through the steel return path. When air gaps are present (Figure 5.22(b)) the domain distribution is less homogeneous. Although saturation has been achieved at the center of the Galfenol sample, the rest of the material is not fully saturated as evidenced by the presence of domain orientations other than [010]. Because of the magnetomechanical coupling and non-uniformity in the magnetic state, the strain is nonuniform even though the stress is uniform (see Figure 5.21.)

Hysteresis in the domain volume fraction evolution results in a remanent induction and magnetostriction when the current is removed (see Figure 5.23.) Demagnetizing fields from air gaps and application of stress both tend to reduce the remanent induction. With no stress or air gaps, the remanent state has a significant fraction of domains in the [010] orientation (see Figure 5.24(a)) resulting in a net flux density

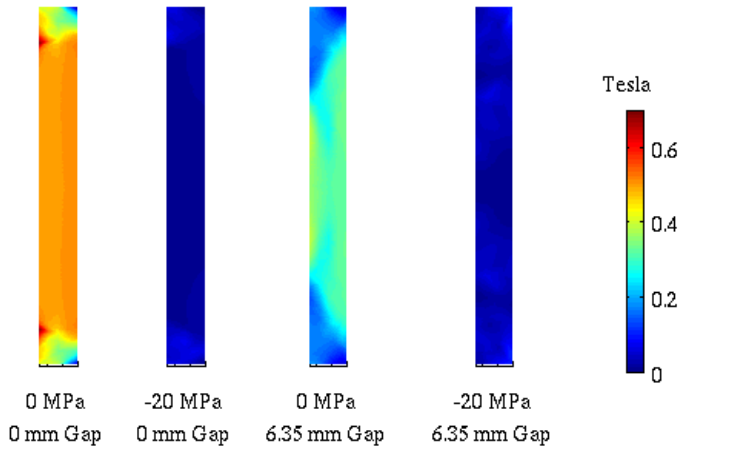

(a)

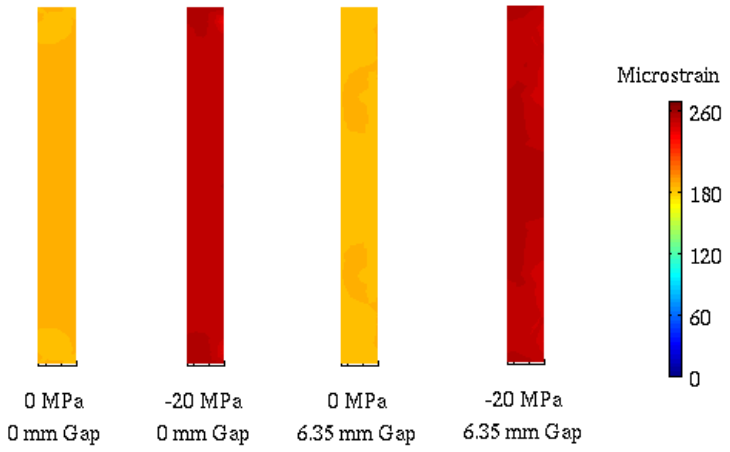

(b)

Figure 5.23: Remanent (a) flux density and (b) strain norms in Galfenol with and without stress and air gaps.

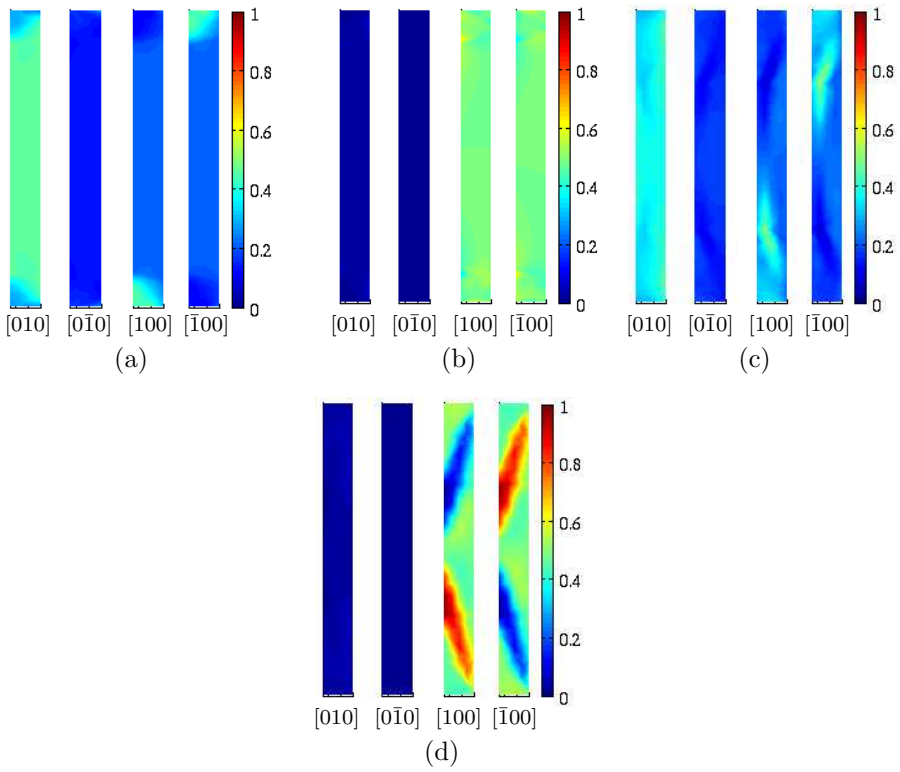

Figure 5.24: Domain volume fractions in Galfenol AT at remanence with (a) no stress and no gap (b) -20 MPa stress and no gap (c) no stress and 6.35 mm gaps (d) -20 MPa stress and 6.35 mm GAPS.

at remanence following a magnetization cycle. Applied stress tends to favor the [100] and [$\bar{1}$00] directions equally (see Figure 5.24(b) and 5.24(d)) resulting in negligible net flux density at remanence. Figure 5.24(c) shows a decrease in the volume fraction of [010] oriented domains at remanence resulting in less flux density. The norm of the magnetostriction exhibits behavior different from the norm of the induction because the magnetostriction of opposing directions (e.g., [100] and [$\bar{1}$00]) does not cancel. Demagnetizing fields result in less domain alignment which yields less magnetostriction (see Figure 5.23(b).) However, application of stress results in a high degree of alignment in the [100] and [$\bar{1}$00] directions which have the same magnetostriction and thus a net magnetostriction or widening and simultaneous shortening of the Galfenol region occurs. Thus the remanent magnetostriction in the case of applied stress is not due to the magnetic hysteresis but rather to stress-induced domain alignment.

5.3.6 2-D Dynamic implementation for composite beams

The objective of the work in this section is to provide a model for tip displacement and force in unimorph actuators. A unimorph actuator is a composite beam with a Galfenol layer and a substrate. Applying a magnetic field, the Galfenol attempts to elongate but the substrate constrains its horizontal deflection and causes a vertical deflection. The study of unimorph actuators provides a setting for understanding the structural dynamics that can occur as a result of magnetostrictive strains. Whereas the focus of previous sections is on dynamic electromagnetic effects and hysteresis in quasi-static operation, the emphasis here is on structural dynamics caused by nonlinear magnetostriction. In fact, the electromagnetic field equations are not solved—the magnetic field is assumed to be uniform in the Galfenol layer. This work differs from

the recent work from Zhou and Zhou [118] by using a hysteretic material model and coupling the actual stress to the magnetostriction as opposed to the bias stress only.

Geometric considerations

Consider a composite beam of length L and width b having a Galfenol layer of thickness t_G, elastic modulus E_G, density ρ_G, and internal damping c_G perfectly bonded to a substrate with thickness t_S, elastic modulus E_S, density ρ_S, and internal damping c_S (see Fig. 5.25.) The distance from the mid-plane to an infinitesimal area dA is y. The curvature κ is the inverse of the radius of curvature ρ (see Fig. 5.26) and is exactly

$$\kappa = \frac{1}{\rho} = \frac{d\theta}{ds}, \tag{5.113}$$

and for small deflections

$$\kappa = \frac{1}{\rho} = \frac{d\theta}{dx}. \tag{5.114}$$

The bending strain is determined from purely geometric considerations. For pure bending, sections mn and pq remain plane and normal to the longitudinal axis [42] (see Fig. 5.27.) Line segment ef then has an initial length dx and a final length of exactly

$$ef = (\rho - y)d\theta = ds - \frac{y}{\rho}ds, \tag{5.115}$$

and for small deflections

$$ef = dx - \frac{y}{\rho}dx. \tag{5.116}$$

Thus the bending strain is

$$S_B = -\frac{y}{\rho} = -\kappa y. \tag{5.117}$$

Additionally, for small rotations the angle θ is is the slope of the beam

$$\theta \approx \tan\theta = \frac{d\nu}{dx} \tag{5.118}$$

where ν is vertical deflection of the beam mid-plane and the bending strain is

$$S_B = -\frac{d^2\nu}{dx^2}y. \tag{5.119}$$

The total strain also has a contribution from the longitudinal strain $\partial u/\partial x$ where u is the horizontal displacement of the composite beam on the mid-plane. The total strain is

$$S = \frac{\partial u}{\partial x} - \frac{d^2\nu}{dx^2}y. \tag{5.120}$$

The strain displacement relation (5.119) is in most cases accurate for nonuniform bending as well. For a constant shear force along the axis of the beam, warping of the sections is the same for all beam elements and strain due to bending is still given by (5.119). The same expression is also accurate for a continuously varying shear force [44].

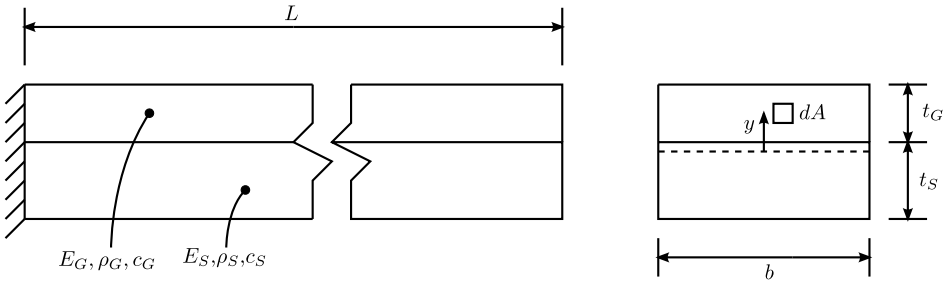

Figure 5.25: Composite beam, G:Galfenol, S:substrate.

Virtual work

The stress in the substrate is modeled with Hooke's law

$$T_S = E_S S. \tag{5.121}$$

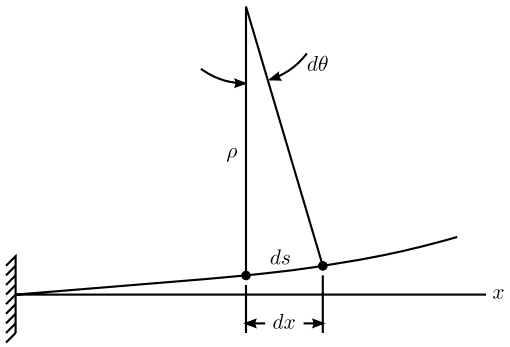

Figure 5.26: Curvature of a beam.

The total strain of the Galfenol is the sum of the purely elastic strain obeying Hooke's law and the magnetostriction

$$S = \frac{1}{E_G} T_G + \lambda(T_G, H), \tag{5.122}$$

and thus the stress is

$$T_G = E_G \left(S - \lambda(T_G, H) \right). \tag{5.123}$$

The magnetostriction is calculated using the hysteretic discrete energy-averaged model with a $\langle 100 \rangle$ direction oriented along the beam length.

By assuming that the magnetic field is uniform along the beam length, the virtual work is limited to mechanical quantities. The virtual work due to strain energy density is

$$\delta W_{TS} = \int_0^L \int_A T \delta S dA dx.$$

Here the implicit incremental solution method is demonstrated which involves iteration at each time step. The solution method for the 2-D magnetostatic implementation in the previous section employed an explicit scheme which has a tendency to

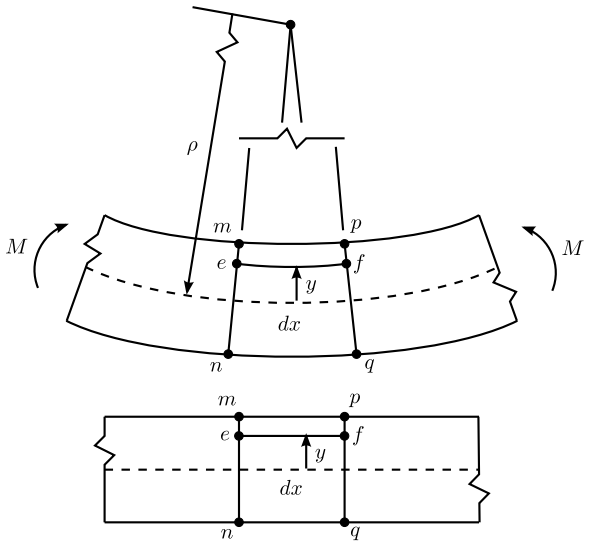

Figure 5.27: Strain of a beam in pure bending.

introduce drift error. The incremental forms of the variables are

$$
\begin{aligned}
u^{t+\Delta t} &= u^t + \Delta u, \\
\nu^{t+\Delta t} &= \nu^t + \Delta \nu, \\
T^{t+\Delta t} &= T^t + \Delta T, \\
S^{t+\Delta t} &= S^t + \Delta S, \\
&= \frac{\partial \left(u^t + \Delta u\right)}{\partial x} - \frac{\partial^2 \left(\nu^t + \Delta \nu\right)}{\partial x^2} y, \\
&= \frac{\partial u^t}{\partial x} - \frac{\partial^2 \nu^t}{\partial x^2} y + \frac{\partial \Delta u}{\partial x} - \frac{\partial^2 \Delta \nu}{\partial x^2} y, \\
\delta S^{t+\Delta t} &= \delta \Delta S = \frac{\partial \Delta u}{\partial x} - \delta \frac{\partial^2 \Delta \nu}{\partial x^2} y.
\end{aligned}
\tag{5.124}
$$

The virtual work from strain energy density in incremental form is

$$\begin{aligned}
\delta W_{TS} &= \int_0^L \int_A T^{t+\Delta t} \delta S^{t+\Delta t} dA dx, \\
&= \int_0^L \int_A T^t \delta \Delta S dA dx + \int_0^L \int_A \Delta T \delta \Delta S dA dx, \\
&= \int_0^L \int_{A_G} \Delta T_G \delta \Delta S_G dA_G dx + \int_0^L \int_{A_S} \Delta T_S \delta \Delta S_S dA_G dx + \int_0^L \int_A T^t \delta \Delta S dA dx, \\
&= E_G \int_0^L \int_{A_G} \left(\Delta S_G - \Delta\lambda\right) \delta \Delta S_G dA_G dx \\
&\quad + E_S \int_0^L \int_{A_S} \Delta S_S \delta \Delta S_S dA_G dx + \int_0^L \int_A T^t \delta \Delta S dA dx.
\end{aligned} \tag{5.125}$$

Substitution from the kinematic relations and material laws, and defining $EA \equiv E_G A_G + E_S A_S$, $EQ \equiv E_G Q_G + E_S Q_S$, $EI \equiv E_G I_G + E_S I_S$, where Q is the first moment of the area gives,

$$\begin{aligned}
\delta W_{TS} =& \delta W_{int} - \delta W_{ext}, \\
\delta W_{int} =& EA \int_0^L \frac{\partial \Delta u}{\partial x} \delta \frac{\partial \Delta u}{\partial x} dx + EI \int_0^L \frac{\partial^2 \Delta \nu}{\partial x^2} \delta \frac{\partial^2 \Delta \nu}{\partial x^2} dx \\
& - EQ \left(\int_0^L \frac{\partial \Delta u}{\partial x} \delta \frac{\partial^2 \Delta \nu}{\partial x^2} dx + \int_0^L \frac{\partial^2 \Delta \nu}{\partial x^2} \delta \frac{\partial \Delta u}{\partial x} dx \right), \\
\delta W_{ext} =& E_G \int_0^L \int_{A_G} \Delta\lambda \delta \frac{\partial \Delta u}{\partial x} dA dx - E_G \int_0^L \int_{A_G} \Delta\lambda \delta \frac{\partial^2 \Delta \nu}{\partial x^2} y dA dx \\
& - \int_0^L \int_A T^t \delta \frac{\partial \Delta u}{\partial x} dA dx + \int_0^L \int_A T^t \delta \frac{\partial^2 \Delta \nu}{\partial x^2} y dA dx.
\end{aligned} \tag{5.126}$$

The d'Alembert force, a function of the horizontal and vertical accelerations a^u and a^ν, and Kelvin-Voight damping, a function of the horizontal and vertical velocities v^u and v^ν also give rise to virtual work

$$\begin{aligned}
\delta W_\rho &= \int_0^L \int_A \rho a^u \delta u dA dx + \int_0^L \int_A \rho a^\nu \delta \nu dA dx, \\
\delta W_c &= \int_0^L \int_A c v^u \delta u dA dx + \int_0^L \int_A c v^\nu \delta \nu dA dx.
\end{aligned} \tag{5.127}$$

In incremental form, the accelerations, velocities, and displacements are related by

$$\begin{aligned} a^u &= \frac{\Delta v^u}{\Delta t}, \\ a^\nu &= \frac{\Delta v^\nu}{\Delta t}, \\ v^u &= \frac{\Delta u}{\Delta t}, \\ &= v^{t,u} + \Delta v^u, \\ v^\nu &= \frac{\Delta \nu}{\Delta t} \\ &= v^{t,\nu} + \Delta v^\nu. \end{aligned} \tag{5.128}$$

The virtual work from dynamic terms in incremental form is,

$$\begin{aligned} \delta W_\rho =& \int_0^L \int_A \rho \frac{\Delta v^u}{\Delta t} \delta u dA dx + \int_0^L \int_A \rho \frac{\Delta v^\nu}{\Delta t} \delta \nu dA dx, \\ =& \int_0^L \int_A \rho \frac{1}{\Delta t} \left(\frac{\Delta u}{\Delta t} - v^{t,u} \right) \delta u dA dx + \int_0^L \int_A \rho \frac{1}{\Delta t} \left(\frac{\Delta \nu}{\Delta t} - v^{t,\nu} \right) \delta \nu dA dx, \\ =& \frac{1}{\Delta t^2} \int_0^L \int_A \rho \left(\Delta u \delta u + \Delta \nu \delta \nu \right) dA dx - \frac{1}{\Delta t} \int_0^L \int_A \rho \left(v^{t,u} \delta u + v^{t,\nu} \delta \nu \right) dA dx \\ \delta W_c =& \int_0^L \int_A c \frac{\Delta u}{\Delta t} \delta u dA dx + \int_0^L \int_A c \frac{\Delta \nu}{\Delta t} \delta \nu dA dx, \\ =& \frac{1}{\Delta t} \int_0^L \int_A c \Delta u \delta u dA dx + \frac{1}{\Delta t} \int_0^L \int_A c \Delta \nu \delta \nu dA dx. \end{aligned} \tag{5.129}$$

Discretization

The beam is discretized into N elements of length l_e (see Figure 5.28) each with two nodes giving $N_n = 2N_e - 1$ nodes. Each node has three degrees of freedom. The first two are vertical displacement ν and rotation or slope $d\nu/dx$ giving a total of $N^\nu = 2N_n$ degrees of freedom associated with vertical displacement; the other degree of freedom is horizontal displacement which has $N^u = N_n$ degrees of freedom. The element values of the degrees of freedom associated with the vertical displacement are denoted $\mathbf{q}_e^\nu$ where the first two components are the vertical displacement and rotation

of the left node and the second two are the vertical displacement and rotation of the right node. The global notation is $\mathbf{Q}^{\nu}$. The element values of the degrees of freedom associated with horizontal displacement are denoted $\mathbf{q}_e^u$ with the first entry the horizontal displacement of the left node and the second entry the displacement of the right node. The global notation is $\mathbf{Q}^u$. The mesh definition includes a mapping between local and global variables which is used in the global assembly process.

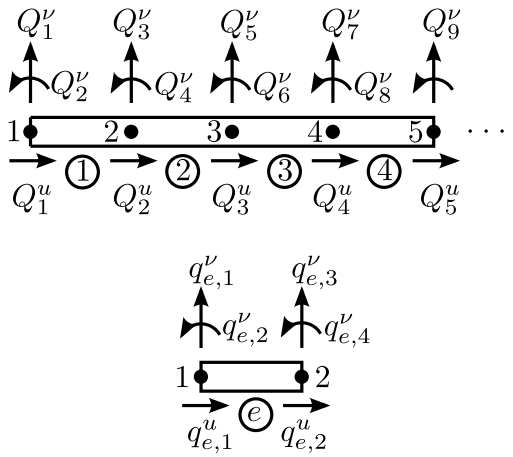

Figure 5.28: Finite-element discretization of beam.

The vertical displacement and its increments are interpolated over the element with Hermite shape functions, ensuring continuity of the first derivative (see Figure 5.29.) The horizontal displacement and its increments require only continuity of the zeroth derivative, so linear shape functions are used. The local spatial coordinate is ξ varying from negative one to one, the element vertical displacement and slope increments are $\Delta q_{e,1}^{\nu}$ and $\Delta q_{e,2}^{\nu}$ at the left element node and $\Delta q_{e,3}^{\nu}$ and $\Delta q_{e,4}^{\nu}$ at the right element node. The horizontal displacement increment is $\Delta q_{e,1}^{u}$ at the left node and $\Delta q_{e,2}^{u}$ at the right node. The vertical displacement increment of an element is

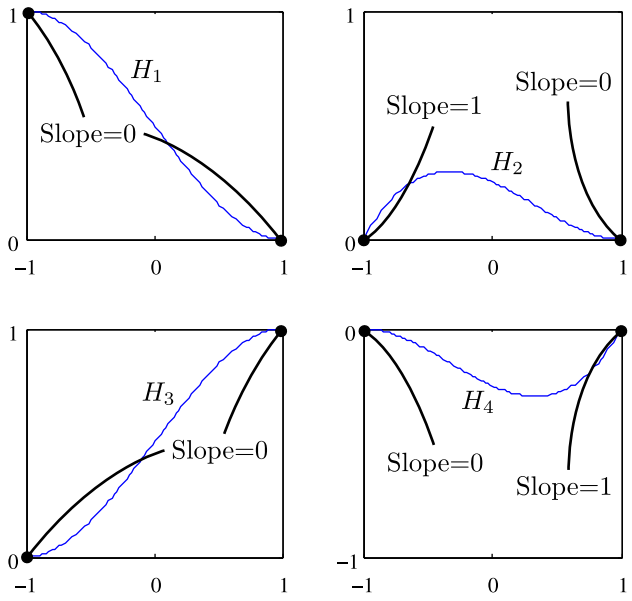

Figure 5.29: Hermite shape functions.

interpolated over the element according to

$$
\begin{aligned}
H_1 &= \frac{1}{4}(1-\xi)^2(2+\xi),\\
H_2 &= \frac{1}{4}(1-\xi)^2(\xi+1),\\
H_3 &= \frac{1}{4}(1+\xi)^2(2-\xi),\\
H_4 &= \frac{1}{4}(1+\xi)^2(\xi-1),
\end{aligned}
\tag{5.130}
$$

$$
\Delta\nu_e = \mathbf{H}\Delta\mathbf{q}_e^{\nu} = \left[\begin{array}{cccc} H_1 & \frac{l_e}{2}H_2 & H_3 & \frac{l_e}{2}H_4 \end{array}\right] \left[\begin{array}{c} \Delta q_{e,1}^{\nu} \\ \Delta q_{e,2}^{\nu} \\ \Delta q_{e,3}^{\nu} \\ \Delta q_{e,4}^{\nu} \end{array}\right].
$$

The horizontal displacement increment is linearly interpolated,

$$
\begin{aligned}
N_1 &= \frac{1-\xi}{2},\\
N_2 &= \frac{1+\xi}{2},
\end{aligned}
\tag{5.131}
$$

$$
\Delta u_e = \mathbf{N}\Delta\mathbf{q}_e^{u} = \left[\begin{array}{cc} N_1 & N_2 \end{array}\right] \left[\begin{array}{c} \Delta q_{e,1}^{u} \\ \Delta q_{e,2}^{u} \end{array}\right].
$$

The spatial coordinate x is interpolated in the same way as u. Derivatives are

$$\begin{aligned} dx &= \frac{l_e}{2} d\xi, \\ \frac{\partial \Delta u_e}{\partial x} &= \mathbf{B} \cdot \Delta \mathbf{q}_e^u = \frac{1}{l_e} \begin{bmatrix} -1 \\ 1 \end{bmatrix} \cdot \Delta \mathbf{q}_e^u, \\ \frac{\partial^2 \Delta \nu_e}{\partial x^2} &= \frac{4}{l_e^2} \frac{\partial^2 \mathbf{H}}{\partial \xi^2} \cdot \Delta \mathbf{q}_e^\nu. \end{aligned} \tag{5.132}$$

After discretization, the virtual work terms from strain energy density are

$$\begin{aligned} \delta W_{int} =& \sum_e \delta \mathbf{q}_e^u \cdot \left[\frac{EA}{l_e} \mathbf{B}^T \mathbf{B} \right] \Delta \mathbf{q}_e^u + \delta \mathbf{q}_e^\nu \cdot \left[\frac{8EI}{l_e^3} \int_{-1}^{1} \left(\frac{\partial^2 \mathbf{H}}{\partial \xi^2} \right)^T \frac{\partial^2 \mathbf{H}}{\partial \xi^2} d\xi \right] \Delta \mathbf{q}_e^\nu \\ & - \delta \mathbf{q}_e^\nu \cdot \left[\frac{2EQ}{l_e} \int_{-1}^{1} \left(\frac{\partial^2 \mathbf{H}}{\partial \xi^2} \right)^T \mathbf{B} d\xi \right] \Delta \mathbf{q}_e^u - \delta \mathbf{q}_e^u \cdot \left[\frac{2EQ}{l_e} \int_{-1}^{1} \mathbf{B}^T \frac{\partial^2 \mathbf{H}}{\partial \xi^2} d\xi \right] \Delta \mathbf{q}_e^\nu, \\ :=& \sum_{e=1}^{N} \delta \mathbf{q}_e^u \cdot \mathbf{k}_e^u \Delta \mathbf{q}_e^u + \delta \mathbf{q}_e^\nu \cdot \mathbf{k}_e^\nu \Delta \mathbf{q}_e^\nu - \delta \mathbf{q}_e^\nu \cdot \mathbf{k}_e^{u\nu} \Delta \mathbf{q}_e^u - \delta \mathbf{q}_e^u \cdot \left(\mathbf{k}_e^{u\nu} \right)^T \Delta \mathbf{q}_e^\nu, \\ \delta W_{ext} =& \sum_{e=1}^{N} \delta \mathbf{q}_e^u \cdot \left[\frac{E_G b l_e}{2} \left(\int_{-1}^{1} \int_G \Delta \lambda dy d\xi \right) \mathbf{B} \right] - \delta \mathbf{q}_e^\nu \cdot \left[\frac{2E_G b}{l_e} \int_1^{-1} \int_G \Delta \lambda \frac{\partial^2 \mathbf{H}}{\partial \xi^2} y dy d\xi \right] \\ & - \delta \mathbf{q}_e^u \cdot \left[\left(\frac{b l_e}{2} \int_{-1}^{1} \int_{-t/2}^{t/2} T^t dy d\xi \right) \mathbf{B} \right] + \delta \mathbf{q}_e^\nu \cdot \left[\frac{2b}{l_e} \int_0^L \int_{-t/2}^{t/2} T^t \frac{\partial^2 \mathbf{H}}{\partial \xi^2} dy d\xi \right], \\ :=& \sum_e \delta \mathbf{q}_e^u \cdot \mathbf{f}_e^{\lambda,u} - \delta \mathbf{q}_e^\nu \cdot \mathbf{f}_e^{\lambda,\nu} - \delta \mathbf{q}_e^u \cdot \mathbf{f}_e^{t,u} + \delta \mathbf{q}_e^\nu \cdot \mathbf{f}_e^{t,\nu}. \end{aligned} \tag{5.133}$$

The external virtual work is a function of the displacements since the magnetostriction depends on the strain increments. The integrals involving the magnetostriction are calculated numerically, with four-point Gauss-quadrature, since they are nonlinear functions of strain and therefore the displacement increments.

The velocities are interpolated with the same shape functions as displacements. After discretization and substitution of $\rho A = \rho_G A_G + \rho_S A_S$ and $cA = c_G A_G + c_S A_S$,

virtual work terms from dynamic effects are

$$\begin{aligned}
\delta W_\rho =& \sum_{e=1}^{N} \delta \mathbf{q}_e^u \cdot \frac{1}{\Delta t^2} \left[\frac{\rho A l_e}{2} \int_{-1}^{1} \mathbf{N}^T \mathbf{N} d\xi \right] \Delta \mathbf{q}_e^u + \delta \mathbf{q}_e^\nu \cdot \frac{1}{\Delta t^2} \left[\frac{\rho A l_e}{2} \int_{-1}^{1} \mathbf{H}^T \mathbf{H} d\xi \right] \Delta \mathbf{q}_e^\nu \\
& - \delta \mathbf{q}_e^u \cdot \frac{1}{\Delta t} \left[\frac{\rho A l_e}{2} \int_{-1}^{1} \mathbf{N}^T \mathbf{N} d\xi \right] \Delta \mathbf{q}_e^{v^u} - \delta \mathbf{q}_e^\nu \cdot \frac{1}{\Delta t} \left[\frac{\rho A l_e}{2} \int_{-1}^{1} \mathbf{H}^T \mathbf{H} d\xi \right] \Delta \mathbf{q}_e^{v^\nu} \\
:=& \sum_{e=1}^{N} \delta \mathbf{q}_e^u \cdot \left(\frac{1}{\Delta t^2} \mathbf{m}_e^u \Delta \mathbf{q}_e^u - \frac{1}{\Delta t} \mathbf{m}_e^u \Delta \mathbf{q}_e^{v^u} \right) + \delta \mathbf{q}_e^\nu \cdot \left(\frac{1}{\Delta t^2} \mathbf{m}_e^\nu \Delta \mathbf{q}_e^\nu - \frac{1}{\Delta t} \mathbf{m}_e^\nu \Delta \mathbf{q}_e^{v^\nu} \right) \\
\delta W_c =& \sum_{e=1}^{N} \delta \mathbf{q}_e^u \cdot \frac{1}{\Delta t} \left[\frac{c A l_e}{2} \int_{-1}^{1} \mathbf{N}^T \mathbf{N} d\xi \right] \Delta \mathbf{q}_e^u + \delta \mathbf{q}_e^\nu \cdot \frac{1}{\Delta t} \left[\frac{c A l_e}{2} \int_{-1}^{1} \mathbf{H}^T \mathbf{H} d\xi \right] \Delta \mathbf{q}_e^\nu, \\
:=& \sum_{e=1}^{N} \delta \mathbf{q}_e^u \cdot \frac{1}{\Delta t} \mathbf{c}_e^u \Delta \mathbf{q}_e^u + \delta \mathbf{q}_e^\nu \cdot \frac{1}{\Delta t} \mathbf{c}_e^\nu \Delta \mathbf{q}_e^\nu.
\end{aligned} \tag{5.134}$$

Combining with the virtual work terms from the strain energy and applying variational principles, the assembled system to solve is

$$\begin{bmatrix} \mathbf{K}^u + \frac{1}{\Delta t^2}\mathbf{M}^u + \frac{1}{\Delta t}\mathbf{C}^u & -\left(\mathbf{K}^{u\nu}\right)^T \\ -\mathbf{K}^{u\nu} & \mathbf{K}^\nu + \frac{1}{\Delta t^2}\mathbf{M}^\nu + \frac{1}{\Delta t}\mathbf{C}^\nu \end{bmatrix} \begin{bmatrix} \Delta \mathbf{Q}^u \\ \Delta \mathbf{Q}^\nu \end{bmatrix} = \begin{bmatrix} \mathbf{F}^{\lambda,u} + \mathbf{F}^{t,u} + \frac{1}{\Delta t}\mathbf{M}^u \mathbf{Q}^{t,v^u} \\ \mathbf{F}^{\lambda\nu} + \mathbf{F}^{t,\nu} + \frac{1}{\Delta t}\mathbf{M}^\nu \mathbf{Q}^{t,v^\nu} \end{bmatrix}, \tag{5.135}$$

$$\begin{bmatrix} \Delta \mathbf{Q}^{v^u} \\ \Delta \mathbf{Q}^{\Delta v^\nu} \end{bmatrix} = \begin{bmatrix} \Delta \mathbf{Q}^u / \Delta t - \mathbf{Q}^{t,v^u} \\ \Delta \mathbf{Q}^\nu / \Delta t - \mathbf{Q}^{t,v^\nu} \end{bmatrix}, \tag{5.136}$$

where the unknowns are the displacement and velocity increments. The form of these matrix equations with regards to the time increment is essentially backward Euler time integration, an implicit method. The load vectors $\mathbf{F}^{\lambda,u}$ and $\mathbf{F}^{\lambda,\nu}$ contain the magnetostriction which is a function of the strain and therefore the displacement increments; this makes the matrix system nonlinear. Broyden's algorithm, a quasi-Newton method, is used to solve for the increments. The advantage of this nonlinear solver is that the Jacobian does not need to be evaluated and it has super linear convergence. The stress from the previous time step appears in the load vectors $\mathbf{F}^{t,u}$

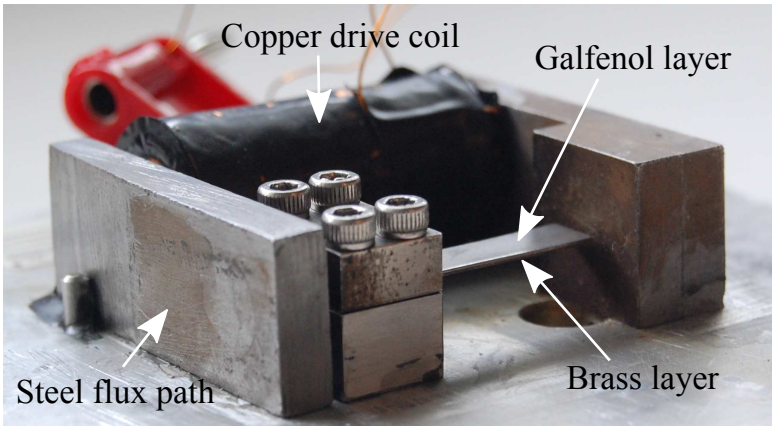

Figure 5.30: Unimorph actuator used for model validations.

and $\mathbf{F}^{t,\nu}$ and the velocity from the previous time step in the vectors $\mathbf{Q}^{t,v^u}$ and $\mathbf{Q}^{t,v^\nu}$. These correct the drift error associated with explicit methods.

Unimorph actuators are cantilevers. In the present model, the left end is clamped so that the displacements and rotations are zero. The elimination approach is taken to accommodate these conditions. The right end the beam is generally free but can be loaded with a force or a spring-mass-damper. The stiffness, damping coefficient, and mass of the load are added to the last diagonal components of the system mass, stiffness, and damping matrices.

Measurements and simulations

The composite beam, finite element model is implemented in Matlab with the m-script language and used to simulate the actuator pictured in Figure 5.30. The actuator was manufactured by Etrema Products Inc. The constitutive model for the magnetostriction increment is the hysteretic discrete energy-averaged model.

A Keyence laser displacement sensor was used in concert with a dSpace control system to simultaneously apply current to a solenoid, used to magnetically activate the Galfenol, and acquire the vertical tip displacement data. While the measurement system acquired the current to the coil, the model requires magnetic field as input. A simple linear model was used for the field-current relationship, $H = NI$ with $N = 2200$. The substrate is brass and both it and the Galfenol have a thickness of 15 mili-inch with a 1 inch length and 1/4 inch width. The Galfenol and substrate have density 7870 and 8400 kG/m^3, stiffness 60 MPa and 120 MPa, and internal damping 1×10^4 kG/s $\cdot$ m^3 (both). The internal damping was found from the decay in an impact test. The model parameters for the Galfenol constitutive behavior are $K_{100} = 30$ kJ/m^3, $\mu_0 M_s = 1.6$ Tesla, $(3/2)\lambda_{100} = 260$ microstrain, $3\lambda_{111} = -20$ microstrain, $\Omega = 1200$ kJ/m^3, $c = 0.1$ (reversibility coefficient), and $k_p = 200$ kJ/m^3. Figure 5.31 shows a comparison between the finite element beam model and measurements performed on the actuator (Figure 5.30). In the 0.5 Hz case, a full hysteresis loop was attained, demonstrating butterfly-type nonlinearity. The other three cases are for a biased input with an amplitude of 0.3 Amps. The hysteresis from the material constitutive behavior results in a delay between the input and the output which is frequency independent. At the higher frequencies of 150, 400, and 450 Hz, inertia and damping result in additional time lag. Measurements from an impact test indicate that the composite beam has a frequency of 620 Hz for the fundamental vibration mode which agrees with the model. Because the higher frequency tests are approaching the fundamental frequency, the displacement amplitudes increase and the associated phase lag causes a CCW rotation of the loop. For the 450 Hz test, there is significant negative deflection because of the beam inertia. As demonstrated

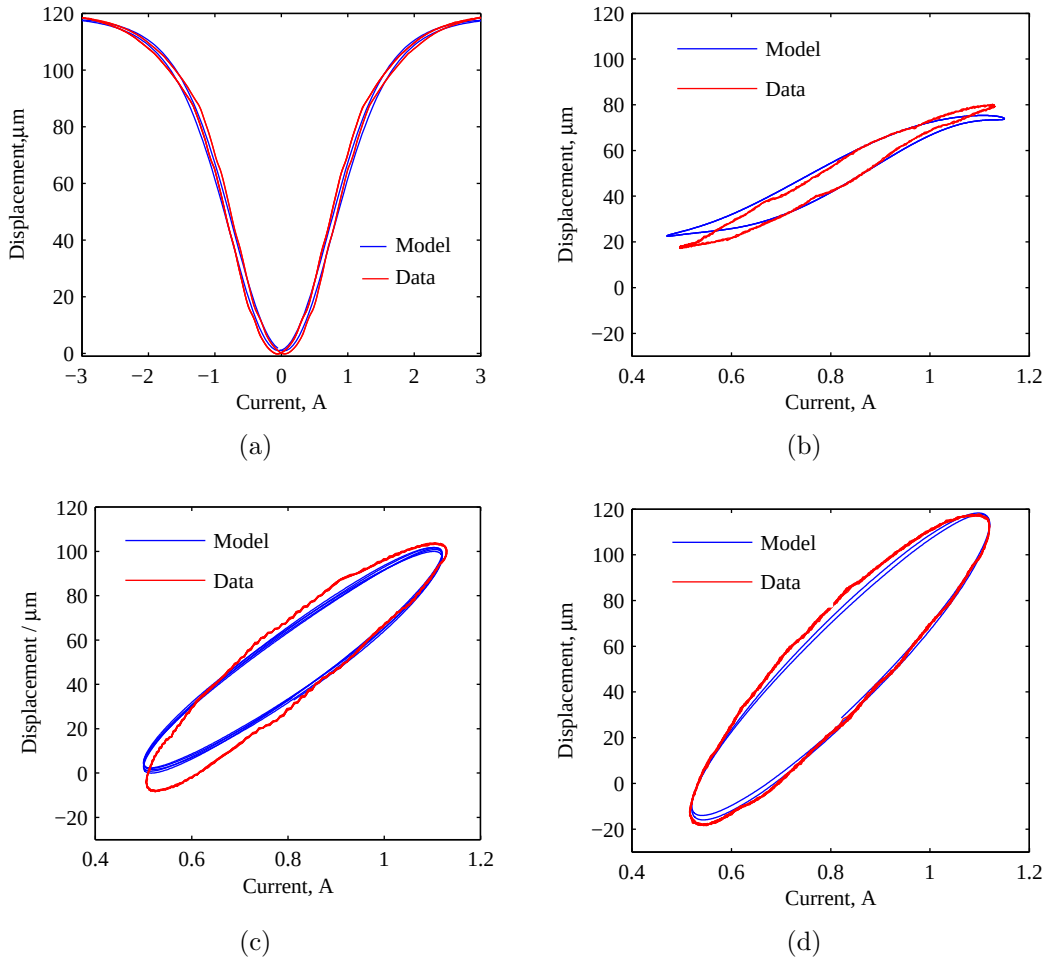

Figure 5.31: Model validation for nonlinear and dynamic finite element model of a composite beam actuator at (a) 0.5 Hz (b) 150 Hz (c) 400 Hz and (d) 450 Hz.

in the 0.5 Hz test, the deflection from the magnetostriction only cannot produce negative deflection because it is an even function of magnetic field.

Figure 5.32 shows the force that can be achieved when the tip works against a very stiff load with an alternated applied field. The blocked force is on the order of mili-newtons because displacement amplification has been used. If this Galfenol material were blocked in rod form, with no displacement amplification, it could produce a

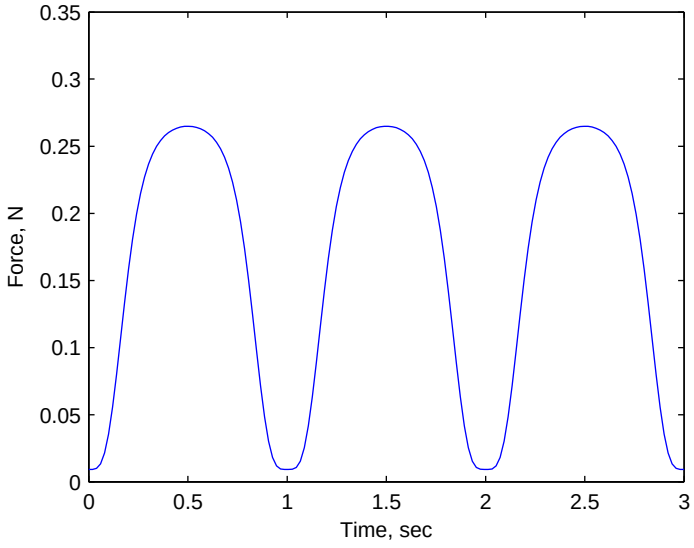

Figure 5.32: Blocked force of a unimorph actuator.

maximum stress of $(3/2)\lambda_{100}E = (260 \times 10^{-6})(60 \times 10^{9}) = 15.6$ MPa. With a sample of only 1/4 inch diameter, this for example is 494 N. However, the maximum strain is 260×10^{-6}, which would have a maximum displacement of just 6.6 micrometers with a 1 inch rod. The maximum displacement of the unimorph actuator is 120 micrometers.

5.3.7 3-D dynamic implementation

In this section the unimorph actuator (Figure 5.30) is again studied but with the fully 3-D and dynamic finite element model (5.77). The model is implemented in COMSOL Multiphysics which provides a meshing tool, local to global matrix assembly, and a post-processing and visualization toolbox. This is used because it allows the flexibility of partitioning the solution domain while allowing for the different subdomains to have different degrees of freedom. COMSOL Multiphysics also allows

specifying essential boundary conditions on internal boundaries, which is important because the mechanical constraints are inside the surrounding air volume.

The coefficient matrices in (5.60) and (5.61) can be calculated with the discrete energy-averaged model. The constitutive model is formulated as

$$\mathbf{B} = \mathbf{B}(\mathbf{H}, \mathbf{T}), \tag{5.137}$$

$$\mathbf{S} = \mathbf{S}(\mathbf{H}, \mathbf{T}). \tag{5.138}$$

The derivatives,

$$\begin{aligned} \boldsymbol{\mu} &= \frac{\partial \mathbf{B}}{\partial \mathbf{H}}(\mathbf{H}_0, \mathbf{T}_0), \qquad & \mathbf{d} &= \frac{\partial \mathbf{B}}{\partial \mathbf{T}}(\mathbf{H}_0, \mathbf{T}_0), \\ \mathbf{s} &= \frac{\partial \mathbf{S}}{\partial \mathbf{T}}(\mathbf{H}_0, \mathbf{T}_0), \qquad & \mathbf{d}^T &= \frac{\partial \mathbf{S}}{\partial \mathbf{H}}(\mathbf{H}_0, \mathbf{T}_0). \end{aligned} \tag{5.139}$$

can be calculated analytically. The coefficients relating $\Delta\mathbf{B}, \Delta\mathbf{S}$ to $\Delta\mathbf{H}, \Delta\mathbf{T}$ can then be calculated,

$$\begin{bmatrix} \boldsymbol{\mu}^{-1} & -\mathbf{a} \\ -\mathbf{a} & \mathbf{c} \end{bmatrix} = \begin{bmatrix} \boldsymbol{\mu} & \mathbf{d} \\ \mathbf{d} & \mathbf{s} \end{bmatrix}^{-1}. \tag{5.140}$$

A difficulty arising in this process is that the derivatives in (5.139) need to be calculated at $\mathbf{H}_0, \mathbf{T}_0$ which in the finite element model are functions of $\mathbf{B}$ and $\mathbf{S}$, the unknowns. The process of calculating the coefficient matrices in (5.60) and (5.61) is iterative because the discrete energy-averaged model does not have an analytic inverse. It is also therefore a vector process. All components of $\mathbf{H}_0$ and $\mathbf{T}_0$ must be calculated simultaneously with numerical inversion, using a technique such as the Newton-Raphson method. COMSOL Multiphysics does not have the capability of implementing vector functions so a single set of linear coefficients is used for the modeling in this section and the actuator is operated about a bias field applied by a permanent magnet. The boundary conditions are $\mathbf{A} = 0$ on the air boundary and $\mathbf{u} = 0$ on the bottom face of the block used for mounting the beam.

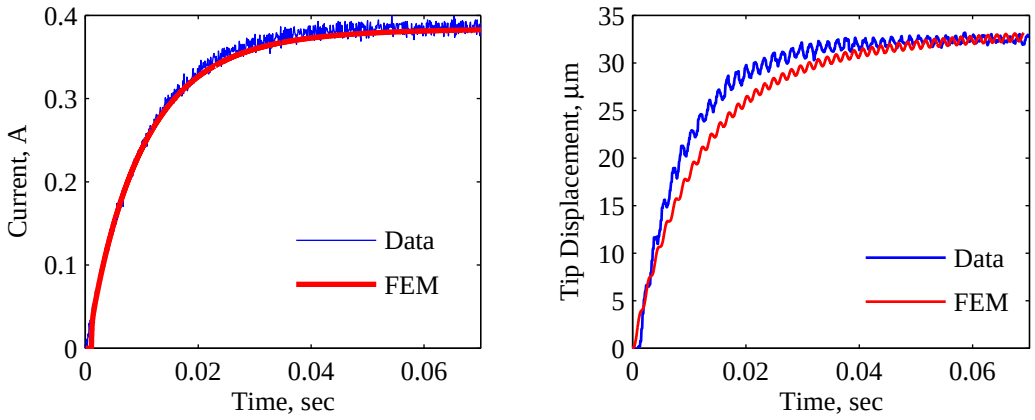

Figure 5.33: Step-response of unimorph with 8.22 input voltage.

Step response measurement and dynamic efficiency

First a step response is measured by supplying a step input voltage source $V_s = 8.19$ volts to the coil. The finite element model requires as input, a source current density $\mathbf{J}_s$. This can be calculated in the circumferential direction from the resistance of the coil R and the cross sectional area of the coil wire A_w, $J_s = V_s/(RA_w)$. The coil is modeled as a solid cylinder with its center on the x_1-axis, so the 3-D supplied current density can be calculated from the circumferential component according to,

$$\mathbf{J}_s = \begin{bmatrix} 0 \\ V_s/(RA_w) \times \left(-x_3/\sqrt{x_2^2 + x_3^2}\right) \\ V_s/(RA_w) \times \left(x_2/\sqrt{x_2^2 + x_3^2}\right) \end{bmatrix}. \tag{5.141}$$

Two quantities measured during the step-response are compared with the model, the wire current in the coil and the vertical displacement of the beam tip. The current is calculated as follows. The total current density is the sum of the source current density and the *back EMF*, or the opposing current/eddy current from the

Lenz-Faraday law, $-\sigma\partial\mathbf{A}/\partial t$. The total circumferential current density then is

$$J(\mathbf{x}) = J_s - \sigma\frac{\partial A_2}{\partial t}\left(-\frac{x_3}{\sqrt{x_2^2+x_3^2}}\right) - \sigma\frac{\partial A_3}{\partial t}\left(\frac{x_2}{\sqrt{x_2^2+x_3^2}}\right), \tag{5.142}$$

and the wire current I in the coil is then calculated from the average circumferential current density $\bar{J}$, averaged over the coil, $I = \bar{J}A_w$. The vertical displacement is calculated from the model by averaging the vertical displacement of the top edge of the Galfenol on the free end.

The same mechanical properties were used as in the 2-D beam model with the 3-D stiffness matrices calculated from the elastic modulus while using 0.33 for Poisson's ratio. The elastic modulus of the steel base is 200 GPa and its density 7860 kG/m^3. The electrical conductivity of copper is $\sigma_C = 59.6 \times 10^6$. However this is divided by π since there is void within the coil winding with a ratio of $1/\pi$ void to copper (the ratio of the area of a circle to the the area of a square.) The conductivity of the brass substrate is $0.28\sigma_C$ and the steel and Galfenol have conductivities $0.1\sigma_C$. The permeability of the steel flux path is isotropic, $10 \times 10^3\mu_0$. The steel base for clamping the beam is made of non-magnetic steel; a permeability of μ_0 is used. Brass is also non-magnetic.

Model and experiment are shown together in Figure 5.33. The voltage response is typical of a linear inductor-resistor electrical circuit and is described accurately by the model. The voltage step gives an impact-like input to the mechanical domain of the system through magnetomechanical coupling. As a result, the fundamental mode is excited and observed in both the measurement and the simulation. The fundamental frequency of the 3-D beam is the same as the measured frequency, 620 Hz, which also agrees with the 2-D beam model.

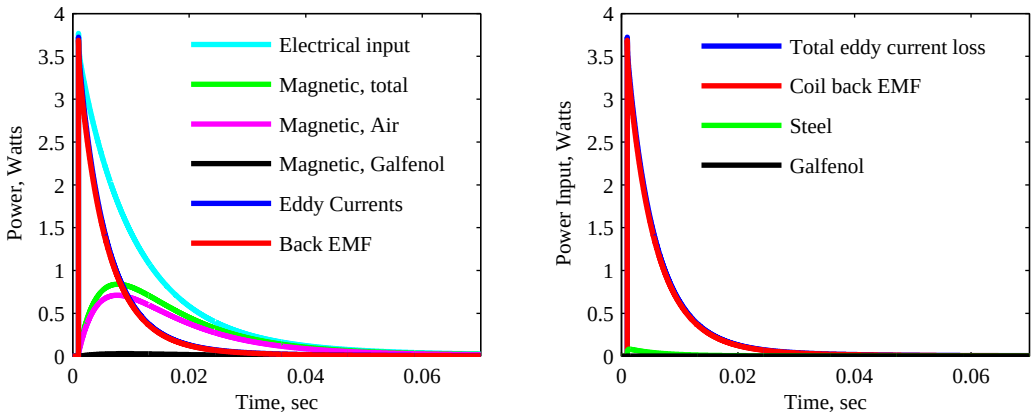

Figure 5.34: Power consumption in step-response to voltage.

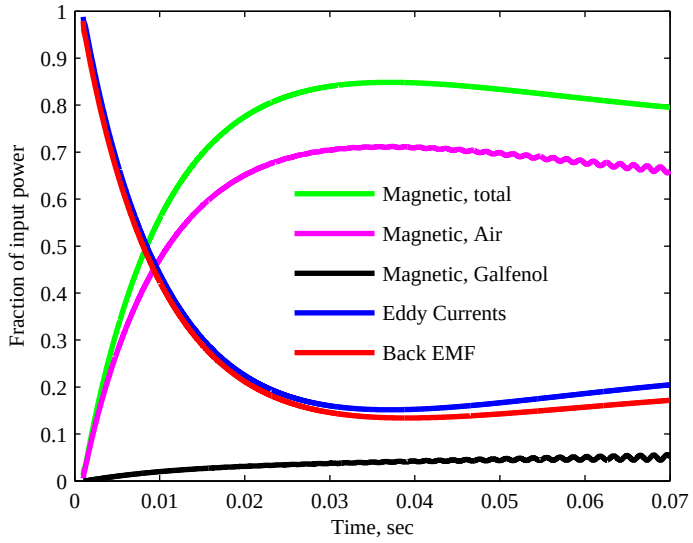

Figure 5.35: Power consumption as a fraction of input power during step-response to voltage.

A power efficiency study of the unimorph actuator shows that the two greatest sources of inefficiency are the power loss to the back EMF of the coil and the power loss due to flux leakage in the air. From (5.43), the input power to the system is

$$P_{input} = \int_{V_{coil}} \mathbf{J}_s \cdot \dot{\mathbf{A}} dV, \tag{5.143}$$

where the variation is replaced with a time derivative; this is the electrical power, IV_S from the power supply. The input power is expended in the magnetic power of each subdomain D,

$$P^D_{magnetic} = \int_{V_D} \mathbf{H} \cdot \dot{\mathbf{B}} dV, \tag{5.144}$$

and in the eddy current losses of each subdomain

$$P^D_{loss} = \int_{V_D} \sigma \dot{\mathbf{A}} \cdot \dot{\mathbf{A}} dV. \tag{5.145}$$

The most significant power sinks are plotted with the power source in Figure 5.34(a). At the beginning of the step response, nearly all of the power is lost through eddy currents. Figure 5.34(b) shows the total eddy current losses $\sum P^D_{loss}$ along with losses P^{coil}_{loss}, $P^{Galfenol}_{loss}$ and P^{steel}_{loss}. The most significant is in the coil which is the back EMF, followed by the steel and a negligible amount in the Galfenol. The most significant power sinks are shown as a fraction of input power in Figure 5.35. This shows that initially, the back EMF accounts for nearly all of the power consumption. As the system approaches steady-state $P^D_{magnetic}$ begins to dominate with $P^{air}_{magnetic}$ accounting for 65% of the power. The magnetic power supplied to the Galfenol, $P^D_{magnetic}$ accounts for at most 5% of the power consumption.

Quasi-static power efficiency

A quasi-static simulation (0.1 Hz) provides more detail regarding the power loss to flux leakage in the air $P^{air}_{magnetic}$. Additionally, it demonstrates the capability of the

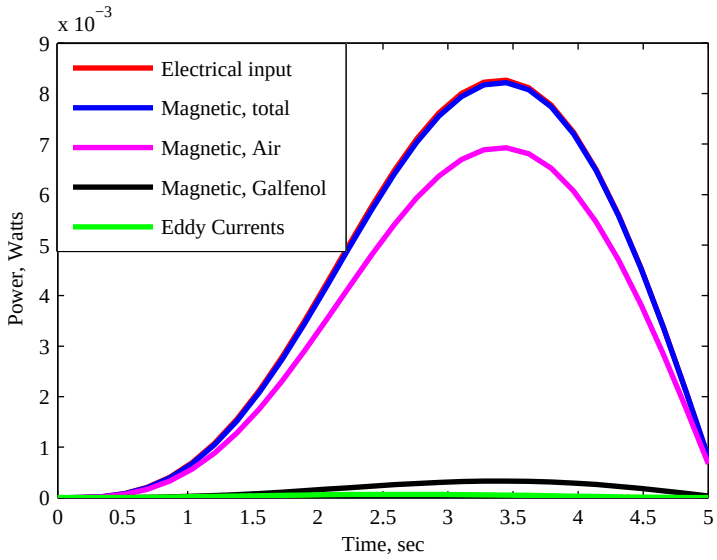

Figure 5.36: Quasi-static (0.1 Hz) power consumption.

3-D finite element model to calculate the spatial dependence of the flux density (Figure 5.39), strain (Figure 5.41), magnetic field (Figure 5.40), and stress (Figure 5.42).

The powers P_{input}, $\sum P^{D}_{magnetic}$, $P^{air}_{magnetic}$, $P^{Galfenol}_{magnetic}$ and $\sum P^{D}_{loss}$ are shown in Figure 5.36 and the same power sinks are shown as a fraction of P_{input} in Figure 5.37. Flux leakage to the air accounts for 82% of the input power while only 5% is supplied to the Galfenol. The conversion efficiency of magnetic energy into mechanical energy of the Galfenol is calculated from the magnetomechanical coupling

$$K = \frac{\int_{V_{Galfenol}} -\mathbf{aS}\cdot\dot{\mathbf{B}}dV + \int_{V_{Galfenol}} -\mathbf{a}^{T}\mathbf{B}\cdot\dot{\mathbf{S}}dV}{\sqrt{\int_{V_{Galfenol}} \boldsymbol{\mu}^{-1}\mathbf{B}\cdot\dot{\mathbf{B}}dV \int_{V_{Galfenol}} \mathbf{cS}\cdot\dot{\mathbf{S}}dV}}. \tag{5.146}$$

The conversion efficiency is a function of geometry, coupling matrix $\mathbf{a}$, the permeability $\boldsymbol{\mu}$ and the stiffness $\mathbf{c}$. This calculation is shown in Figure 5.38. The conversion efficiency is close to 50%, however this analysis shows that the efficiency of the overall system is poor since only 5% of the input power is supplied to the Galfenol, which in

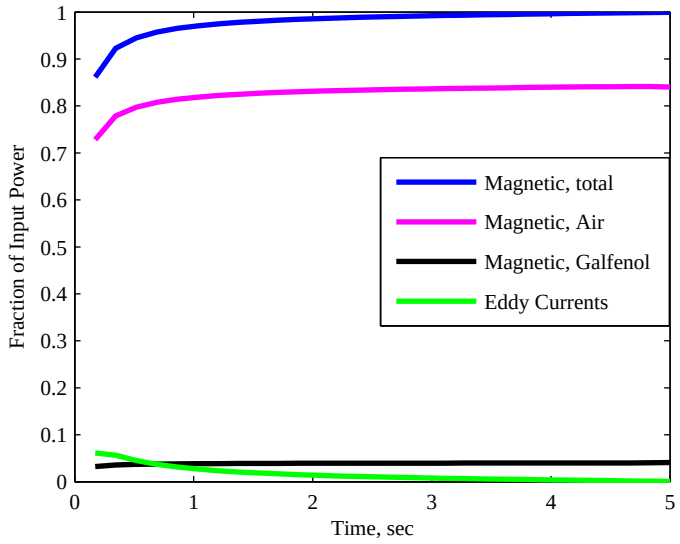

Figure 5.37: Quasi-static (0.1 Hz) power consumption as a fraction of power input.

turn has a near 50% conversion efficiency. The geometry of the actuator is therefore the chief reason for the poor efficiency. It can be improved by (1) reducing the air gap thereby reducing flux leakage and (2) improving the coil geometry to reduce the back EMF. Ideally, the flux path should not include air since its permeability is much lower than the Galfenol. Additionally, a long narrow coil is generally more efficient than a short wide coil.

5.3.8 Concluding remarks

The finite element method has been used in this section to describe a broad range of effects related to the spatial and temporal dependence of the flux density, strain or displacement, magnetic field and stress in magnetostrictive transducers. A general formulation was developed for magnetostrictive transducers which allows for subdomains to have different degrees of freedom. The virtual work was derived

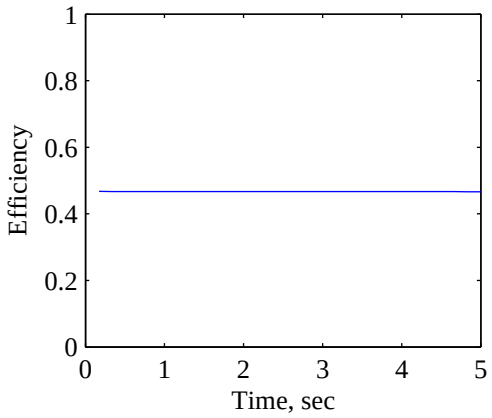

Figure 5.38: Magnetomechanical coupling efficiency.

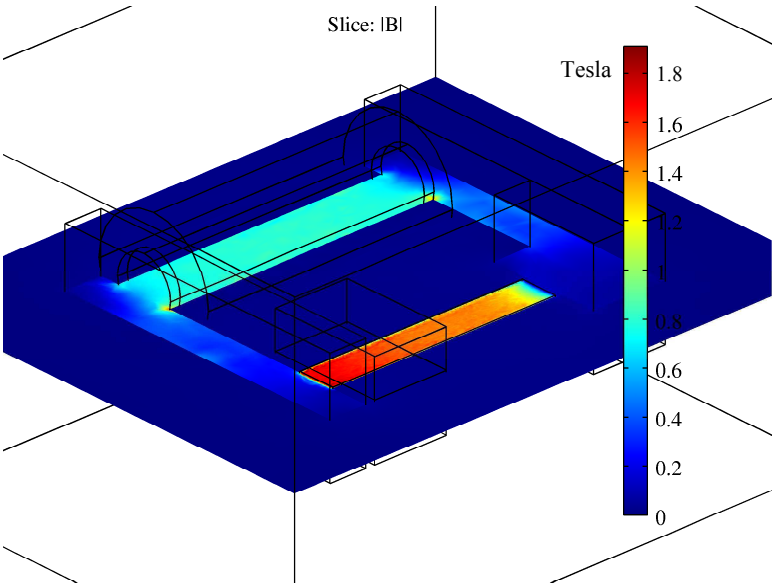

Figure 5.39: FEM solution for flux density.

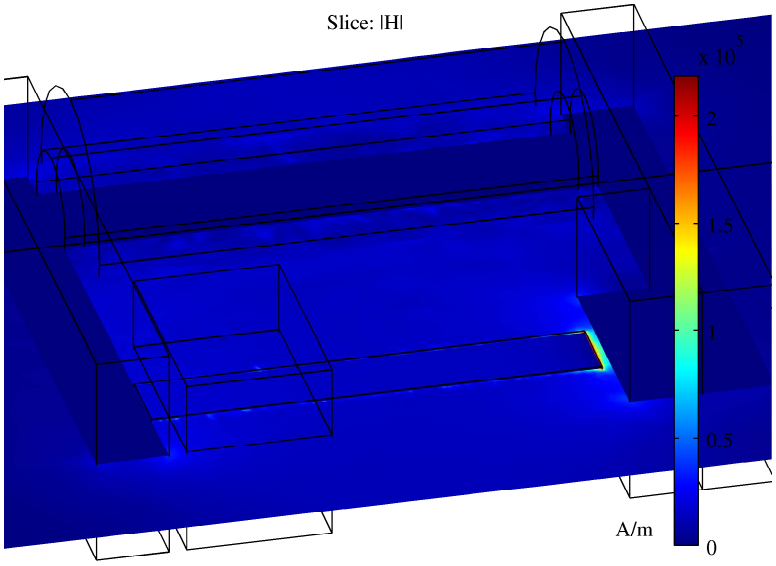

Figure 5.40: FEM solution for magnetic field.

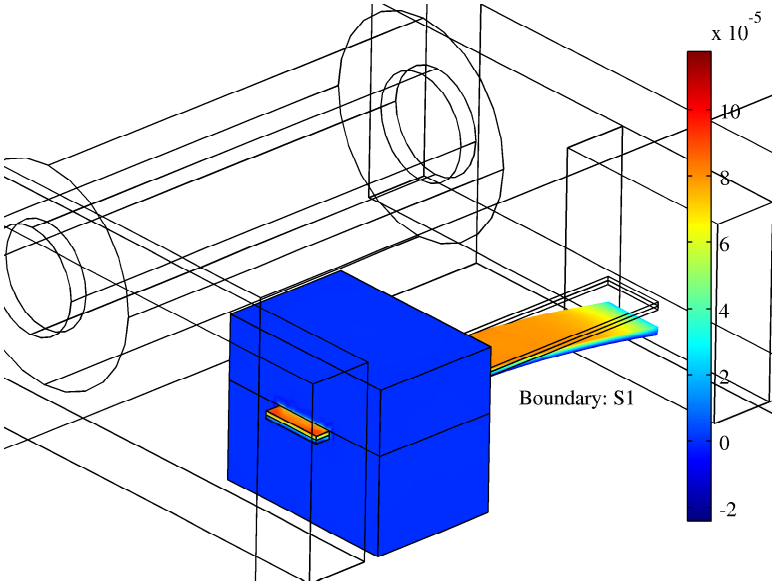

Figure 5.41: FEM solution for strain.

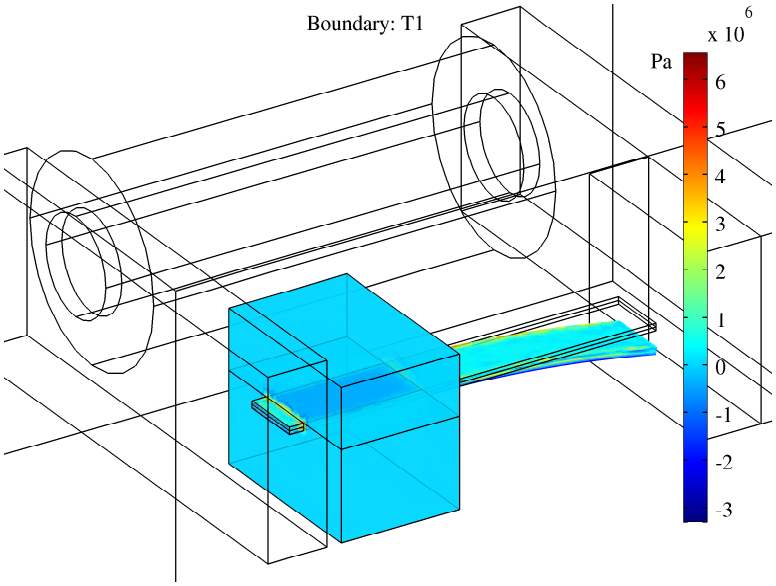

Figure 5.42: FEM solution for stress.

from the strong form or partial differential equation description, without the use of assumptions on the material constitutive behavior, for example, linearity.

A 1-D implementation was developed which provides a fully-coupled, dynamic model to characterize the nonlinear and dynamic strain and magnetization of Galfenol with longitudinal magnetic field and stress loading. Dynamic effects include eddy current losses and the mechanical dynamics of the transducer and load. The uncoupled finite element solution was validated against analytic solutions for the field diffusion in a rod. Important for dynamic actuation and sensing applications, this field diffusion was shown to cause delays in the input-output relationship of coupled, longitudinal, magnetostrictive transducers where the inputs are magnetic field applied to the surface and force applied at the free end and the outputs are the average flux density over the cross section and the displacement of the free end.

A 2-D implementation was developed for flux leakage or demagnetizing fields. It demonstrates the use of a nonlinear and hysteretic constitutive model in the context of the finite element solution of boundary value problems. In this implementation, the hysteretic discrete energy-averaged model is shown to be of particular utility for describing magnetic and strain remanence as well as the effect of changing the distribution of domain orientations.

The operation of a composite beam, unimorph actuator—an application unique to Galfenol—was described with a 2-D composite beam implementation. The implementation is an efficient means to describe the nonlinear, time-dependent input-output relationship between drive current and vertical tip displacement as well as the force at the tip of a loaded unimorph. It also illustrates the trade-off between maximum displacement and force encountered when amplification schemes are employed.

Finally, a fully 3-D and dynamic implementation was used to analyze the efficiency of the unimorph actuator. From the virtual work, expressions were developed for the input power, the magnetic field power, and the power lost to eddy currents. Furthermore, a method for calculating the magnetomechanical energy conversion efficiency was developed which includes geometry dependence. For this particular design, it was shown that the geometry of the transducer is not optimal compared to the coupling efficiency of Galfenol, shown to be nearly 50%. The implementation describes the adverse effects of back EMF, eddy currents, and flux leakage in 3-D which are emphasized in the unimorph application.

The framework developed in this section describes a broad range of 3-D nonlinear and dynamic effects related to magnetostrictive transducers. It is an enabling tool for

developing innovative and efficient designs for transducers capable of 3-D, combined magnetic field and stress loading.

CHAPTER 6

Conclusion

Design of Galfenol-based devices has not taken full advantage of its unique combination of high magnetostriction and robust mechanical properties, largely on account of its nonlinear constitutive behavior and the lack of a general transducer modeling framework with a dynamic and 3-D implementation. This dissertation was undertaken to advance the modeling of magnetostrictive materials and transducers. The research tasks presented in this dissertation were threefold: (1) study the nonlinear constitutive behavior of Galfenol through experiments, (2) construct a constitutive modeling framework for understanding this behavior, and (3) develop a transducer-level modeling framework for describing a broad range effects such as energy losses affecting device efficiency, dynamic magnetostructural effects, transducer-level consequences of using hysteretic materials, and eddy currents. Chapters 3 and 4 dealt with tasks (1) and (2) and Chapter 5 with task (3). Each chapter describes the important results and conclusions in detail. This chapter summarizes the entire research and lists the key contributions of this dissertation.

6.1 Work summary

6.1.1 Characterization and modeling of constitutive behavior

The purpose of this work was to characterize the nonlinear and hysteretic relationship between strain/magnetization and stress/magnetic field. In Part I, a 1-D model with a state-space implementation was developed. An efficient 3-D model was also developed; using similar statistical principles as the 1-D case but leveraging practical knowledge of the most probable domain orientations allowed for 3-D computations with minimal expense. These models relied on a limited set of measurements. In Part II additional measurements were performed and the modeling framework was refined in order to describe a broader range of observations from the measurements. Summaries of the work on characterization and modeling of Galfenol constitutive behavior follow.

Part I: State-space constitutive model for magnetization and magnetostriction of Galfenol alloys

A linear, time-variant, state-space constitutive model was presented which quantifies the nonlinear magnetization and magnetostriction of Galfenol alloys. The effects of external magnetic fields, stresses and stress annealing on the magnetization and magnetostriction of Galfenol were modeled by quantifying the coupling between magnetocrystalline anisotropy, magneto-elastic, Zeeman, and thermal energies. In the model, a triple-valued magnetization kernel characterized by a triple-well Gibbs energy potential provides an understanding of both the low permeability and burst regions of the major loop magnetization curve. Boltzmann statistics was used to describe the distribution and rotations of magnetic moments. This provides a physical basis for understanding the key features of the magnetization and magnetostriction

loops as well as the ability of a compressive stress to align magnetic moments 90^o from the z-axis for maximum magnetostriction. A small amount of hysteresis is naturally present in the model due to anisotropy and which agrees well with experimental measurements. Unaccounted-for effects such as pinning sites are likely to contribute to the magnetic hysteresis as well.

Part I: Efficient model for field-induced magnetization and magnetostriction of Galfenol

A low-order, 3-D constitutive model relating magnetization and strain to magnetic field and stress was developed by utilizing thermodynamic principles with an empirical smoothing operator. By directly minimizing the enthalpy to find the most likely domain orientations, smooth constitutive behavior was achieved with a summation of only six terms. As a result, the framework was readily extended to include irreversible domain wall motion and material texture, without making it too cumbersome for use in distributed parameter, general transducer models which are often solved with the finite-element method, requiring evaluation of the material constitutive model at each node. Comparison of the model to experiments showed it to accurately model field induced-magnetization and strain at constant stress. The model was also used to investigate how polycrystallinity affects the magnetization and magnetostriction behavior. Using a continuum of grain orientations characterized by a probability density function, smoothing of constitutive behavior along with a reduction in the magnetostriction was observed.

Part II: Measurement and modeling of magnetic hysteresis under field and stress in iron-gallium

In this work, magnetization measurements of production and research grade Galfenol from Etrema Products, Inc. were presented. Experiments include applied magnetic field at constant stress, applied stress at constant field, and alternately applied field and stress. The measurements show a remarkable degree of kinematic reversibility in the magnetomechanical coupling, even in the production grade sample. This is in contrast with the magnetomechanical coupling in steel which has been shown to exhibit stress and field induced magnetization that is both thermodynamically and kinematically irreversible [81, 26]. The kinematic reversibility in Galfenol was demonstrated by comparing a single stress-induced magnetization curve at constant magnetic field with a series of field-induced magnetization curves at constant stress. Minor loop measurements consisting of decreasing the field from a bias point, decreasing stress from a bias point, returning the field, and returning the stress showed that accommodation is insignificant in Galfenol. These measurements indicate that magnetic hysteresis for both applied field at constant stress and applied stress at constant field results from the same physical mechanism.

A formal thermodynamic development was undertaken to construct a relay or hysteron, representing magnetic domain orientation, which is applicable to magnetostrictive materials of arbitrary anisotropy. The hysteron depends on the 3-D field and stress and includes a small number of parameters, each with a clear physical interpretation. The number of hysteron states is dictated by material symmetry and anisotropy with one state for each easy axis. The criterion for switching was motivated by the second-law of thermodynamics and resulted in a unified hysteresis

model having the same properties as observed in the measurements. In the model description for macroscopic or bulk magnetization and magnetostriction, a statistically distributed interaction field is superimposed on the applied field. Rather than employ a 3-D, statistically distributed coercive field, a scalar coercive energy is used in the homogenization scheme resulting in fewer computations. This model enables accurate description of the measurements and is a vehicle for understanding hysteresis in ferromagnetic materials that exhibit kinematically reversible magnetomechanical coupling.

Part II: Efficient magnetic hysteresis model for field and stress application in magnetostrictive Galfenol

This work created a discrete energy-averaged model within the energy-weighted averaging class of constitutive models. A number of advancements were made to this class of models. First a new formulation for magnetocrystalline anisotropy energy was developed. This energy formulation is applicable to materials of any symmetry; it depends explicitly on the known easy crystal directions. Rather than seek a globally defined energy which includes the local energy minima or preferred orientations, the energy is defined locally about the known preferred orientations. Second, the magnetic hysteresis model used within this class of models was extended in a unified manner to account for hysteresis during both magnetic field and stress application, in 3-D. A single parameter characterizes the hysteresis delay for both field and stress. Finally, reversible domain volume fraction changes were included in the model which led to a better representation of minor hysteresis loops by eliminating unphysical regions of negative susceptibility. This model is particularly suited for adoption in transducer

level models because it describes magnetization and strain in nonlinear and hysteretic regimes with minimal computational expense.

6.1.2 Application of Galfenol to force sensing and 3-D dynamic transducer modeling

While the above work focused on the nonlinear and hysteretic relationship between strain/magnetization and stress/magnetic field, the focus of this work was on voltage, current, force, and displacement resulting from the spatial and temporal dependence of magnetic field, flux density, stress and strain. The application of Galfenol to force sensing was investigated. Additionally, a general framework was constructed to characterize device-level transduction between voltage/current and force/displacement.

Stress dependent susceptibility of Galfenol and application to force sensing

Magnetization measurements of $Fe_{79.1}Ga_{20.9}$ and $Fe_{81.6}Ga_{18.4}$ are linear with magnetic field in certain intervals of stress and magnetic field. These regions were shown to arise from coherent rotation of domains from the basal plane and to occur when a sufficient compressive stress aligns domains in the four easy crystal directions of the basal plane at zero magnetic field. A simple rotational model showed that the slope of the linear region is proportional to the field energy and inversely proportional to the anisotropy and magnetomechanical coupling energies. Energy minimization was used to interpret the differences in the magnetization processes of $Fe_{79.1}Ga_{20.9}$ and $Fe_{81.6}Ga_{18.4}$. It was found that magnetization of $Fe_{81.6}Ga_{18.4}$ is more strongly influenced by domain flipping and wall motion due to its higher anisotropy impeding domain rotation. As a result, its magnetization versus field curves at constant stress

have a distinctive kinked shape whereas the $Fe_{79.1}Ga_{20.9}$ curves are largely linear until saturation, having lower anisotropy which permits more domain rotation. The susceptibility of the $Fe_{79.1}Ga_{20.9}$ sample was shown to be more sensitive to stress. The stress dependence of the susceptibility in the linear or domain rotation region of both samples was accurately modeled with a simple expression derived from energy minimization. This expression motivates the use of Galfenol with Ga concentrations having high magnetostriction and saturation magnetization with a small, positive fourth-order anisotropy constant for transducers utilizing stress dependent susceptibility. This expression also shows that despite the nonlinear stress dependence of the susceptibility, a linear force transducer can be constructed with a transformer made from Galfenol.

Transducer-level modeling with the finite element method

The finite element method was used to describe a broad range of effects related to the spatial and temporal dependence of the flux density, strain, magnetic field and stress in magnetostrictive transducers. A general formulation was developed for magnetostrictive transducers which allows for subdomains to have different degrees of freedom. The virtual work was derived from the strong form or partial differential equation description, without the use of assumptions on the material constitutive behavior, for example, linearity.

A 1-D implementation was developed which provides a fully-coupled, dynamic model to characterize the nonlinear and dynamic strain and magnetization of Galfenol with longitudinal magnetic field and stress loading. Dynamic effects include eddy current losses and the mechanical dynamics of the transducer and load. The uncoupled finite element solution was validated against analytic solutions for the field diffusion in

a rod. Important for dynamic actuation and sensing applications, this field diffusion was shown to cause delays in the input-output relationship of coupled, longitudinal, magnetostrictive transducers where the inputs are magnetic field applied to the surface and force applied at the free end and the outputs are the average flux density over the cross section and the displacement of the free end.

A 2-D implementation was developed for flux leakage or demagnetizing fields. It demonstrates the use of a nonlinear and hysteretic constitutive model in the context of the finite element solution of boundary value problems. In this implementation, the hysteretic discrete energy-averaged model is shown to be of particular utility for describing magnetic and strain remanence as well as the effect of changing the distribution of domain orientations.

The operation of a composite beam, unimorph actuator—an application unique to Galfenol—was described with a 2-D composite beam implementation. The implementation is an efficient means to describe the nonlinear, time-dependent input-output relationship between drive current and vertical tip displacement as well as the force at the tip of a loaded unimorph. It also illustrates the trade-off between maximum displacement and force encountered when displacement amplification is employed.

Finally, a fully 3-D and dynamic implementation was used to analyze the efficiency of the unimorph actuator. Current, voltage, and displacement calculated by the model agree well with the measured step response. From the virtual work, expressions were developed for the input electrical power, the magnetic field power, and the power lost to eddy currents. Furthermore, a method for calculating the magnetomechanical energy conversion efficiency was developed which includes geometry

dependence. For this particular design, it was shown that the geometry of the transducer is not optimal compared to the coupling efficiency of Galfenol, shown to be nearly 50%. The implementation describes the adverse effects of back EMF, eddy currents, and flux leakage in 3-D.

6.2 Contributions and findings

Experimental characterization

- Magnetization and strain of Galfenol are thermodynamically irreversible and kinematically reversible
- The same magnetization trajectory can be obtained from applied field at constant stress and applied stress at constant field
- Energy loss (hysteresis) during domain rotation is negligible
- Hysteresis is greatest in the domain reconfiguration region of the magnetization process
- The slope or susceptibility at low fields is inversely proportional to stress
- The energy loss per cycle of major magnetization loops is 873 J/m^3 for research grade Galfenol and 1149 J/m^3 for production grade Galfenol

3-D and nonlinear framework for magnetization and strain

- Analytic expressions for the stress dependence of the burst region
- Analytic expressions for constitutive behavior dominated by domain rotation
- A state-space formulation for time-delay from thermal effects

- A discrete energy-averaged model that is 100 times faster than previous energy-averaged models
- A new hysteron for the homogenized energy class of constitutive models that is 3-D, anisotropic, and both stress and field dependent
- The integration order for Preisach-type, anisotropic, vector hysteresis models is reduced from six to four by replacing the coercive field with a coercive energy
- A new domain energy formulation that depends explicitly on the energy and direction of the easy axes applies to any material symmetry
- Hysteresis delay for stress application is greater than for magnetic field application because the magnetomechanical coupling energy generally has lower magnitudes than the Zeeman energy
- Negative piezomagnetic coupling observed at high fields in $\langle 110 \rangle$ oriented material is from negative λ_{111}

Applications to force sensing and 3-D dynamic transducer model

- A linear force sensor, operated with amplitude modulation, uses the stress dependence of the linear region in the magnetization versus field relationship
- The optimal Ga content for sensing applications is in the $19 - 22$ at.% range where magnetostriction is sacrificed for lower anisotropy
- The weak form of the field equations governing flux density, magnetic field, stress and strain is derived without assuming linear constitutive behavior

- Passive media are included in a 3-D and dynamic finite element model, allowing for the inclusion of flux leakage to air, fields from current carrying coils, and losses from eddy currents

- A method for characterizing the dynamic efficiency of magnetostrictive devices with 3-D geometry

- A method for calculating the magnetomechanical coupling factor of Galfenol that accounts for the transducer geometry

6.3 Future work

This research has resulted in a greater understanding of Galfenol constitutive behavior and greatly enhanced the capabilities of material and device level modeling for magnetostrictive materials. The following list enumerates possibilities for future work:

- The possibility of consolidating the tiered constitutive model can be investigated for the purpose of describing the hysteretic details of domain reconfiguration with sufficient efficiency for adoption in device-level models.

- Microscopic measurements can be performed to experimentally quantify the stress and field dependence of the domain volume fractions rather than rely on macroscopic magnetization measurements.

- The tensile behavior of nonlinear magnetomechanical coupling in Galfenol can be investigated.

- Identification of the interaction field and coercive energy density functions can be revisited, perhaps devising a method for direct experimental determination.
- New experimental setups can be investigated for full 3-D material characterization.
- Innovative devices with 3-D functionality can be investigated with the transducer-level model developed in this dissertation.
- The transducer-level model can be extended to include structural-acoustic interactions for characterization of sonar transduction devices.
- Fluid-structure interaction can also be added to the transducer-level model to investigate the potential use of Galfenol in electro-hydraulic actuators.
- In order to investigate hybrid magnetostrictive—moving-iron or moving-coil actuators/sensors, the Maxwell stress tensor, arising from electromagnetic body forces, can be added to the transducer-level model; this will require an Eulerian formulation.

BIBLIOGRAPHY

[1] A.A. Adly and I.D. Mayergoyz. A new vector preisach-type model of hysteresis. *Journal of Applied Physics*, 73(10):5824–5826, 1993.

[2] A.A. Adly, I.D. Mayergoyz, and A. Bergqvist. Preisach modeling of magnetostrictive hysteresis. *Journal of Applied Physics*, 69(8):5777–5779, 1991.

[3] D. Aeyels, R. Sepulchre, and J. Peuteman. Asymptotic stability conditions for time-variant systems and observability: uniform and non-uniform criteria. *Mathematics of Control, Signals, and Systems*, 11(1):1–27, 1998.

[4] C. Appino, M. Valsania, and V. Basso. A vector hysteresis model including domain wall motion and coherent rotation. *Physica B*, 275(1-3):103–106, 2000.

[5] W. D. Armstrong. An incremental theory of magneto-elastic hysteresis in pseudo-cubic ferro-magnetostrictive alloys. *Journal of Magnetism and Magnetic Materials*, 263:208, 2003.

[6] W.D. Armstrong. Magnetization and magnetostriction processes in $\mathrm{tb}_0.27 - 0.30\mathrm{dy}_0.73 - 0.70\mathrm{fe}_1.9 - 2.0$. *Journal of Applied Physics*, 81(5):23217–2326, 1997.

[7] J. Atulasimha, G. Akhras, and A.B. Flatau. Comprehensive 3-d hysteretic magnetomechanical model and its validation with experimental $\langle 110 \rangle$ singe-crystal iron-gallium behavior. *Journal of Applied Physics*, 103:07–336, 2008.

[8] J. Atulasimha and A.B. Flatau. Energy-based model for the magnetostrictive behavior of polycrystalline iron-gallium alloys. *Proceedings of SPIE*, 6170, 2006.

[9] J. Atulasimha, A.B. Flatau, and R.A. Kellogg. Sensing behavior of varied stoichiometry single crystal fe-ga. *Journal of Intelligent Material Systems and Structures*, 17:97–105, 2006.

[10] J. Atulasimha, A.B. Flatau, and E. Summers. Characterization and energy-based model of the magnetomechanical behavior of polycrystalline iron–gallium alloys. *Smart Materials and Structures*, 16:1265–1276, 2007.

[11] R.R. Basantkumar, B.J. Stadler, W.P. Robbins, and E.M. Summers. Integration of thin-film Galfenol with mems cantilevers for magnetic actuation. *IEEE Transactions on Magnetics*, 42(10):3102–3104, 2006.

[12] K. Bathe. *Finite Element Procedures*. Prentice Hall, Upper Saddle River, New Jersey 07458, 1996.

[13] A. Bergqvist and G. Engdahl. A phenomenological magnetomechanical hysteresis model. *Journal of Applied Physics*, 75(10):5496–5498, 1994.

[14] A.J. Bergqvist. A simple vector generalization of the jiles-atherton model of hysteresis. *IEEE Transactions on Magnetics*, 32(5):4213–4215, September 1996.

[15] G.V. Bolshakov and A.J. Lapovok. A Preisach model for magnetoelastic hysteresis. *Journal of Magnetism and Magnetic Materials*, 162:112–116, 1996.

[16] A.P. Boresi and R.J. Schmidt. *Advanced Mechanics of Materials*. John Wiley & Sons, Inc., 111 River Street, Hoboken, NJ 07030, 6th edition, 2003.

[17] O. Bottauscio, M. Chiampi, A. Lovisolo, P.E. Roccato, and M. Zucca. Dynamic modeling and experimental analysis of terfenol-d rods for magnetostrictive actuators. *Journal of Applied Physics*, 103:07F121, 2009.

[18] R.M. Bozorth. *Ferromagnetism*. D. Van Nostrand Company, Inc., New York, 1951.

[19] E. Cardelli, E. Della Torre, and E. Pinzaglia. Identifying the parameters of the reduced vector preisach model: theory and experiment. *IEEE Transactions on Magnetics*, 40(4):2164–2166, July 2004.

[20] T.R. Chandrupatla and A.D. Belegundu. *Introduction to Finite Elements in Engineering*. Prentice-Hall, Upper Saddle River, New Jersey 07458, 3rd edition, 2002.

[21] S. Chikazumi. *Physics of Magnetism*. John Wiley, New York, 1964.

[22] A.E. Clark, K.B. Hathaway, M. Wun-Fogle, J. B. Restorff, T. A. Lograsso, J. M. Keppins, G. Petculescu, and R.A. Taylor. Extraordinary magnetoelasticity and lattice softening in bcc fe-ga alloys. *Journal of Applied Physics*, 93(10):8621–8624, 2003.

[23] A.E. Clark, J.B. Restorff, M. Wun-Fogle, T.A. Lograsso, and D.L. Schlagel. Magnetostrictive properties of body-centered cubic fe-ga and fe-ga-al alloys. *IEEE Trans. Magn.*, 36(5):3238–3240, 2000.

[24] A.E. Clark, M. Wun-Fogle, J.B. Restorff, and T.A. Lograsso. Magnetostrictive properties of Galfenol alloys under compressive stress. *Material transactions*, 43(5):881–886, 2002.

[25] A.E. Clark, M. Wun-Fogle, J.B. Restorff, T.A. Lograsso, and J.R. Cullen. Effect of quenching on the magnetostriction of $Fe_{1-x}Ga_x(0.13 < x < 0.21)$. *IEEE Transactions on Magnetics*, 37(4):2678–2680, July 2001.

[26] D.J. Craik and M.J. Wood. Magnetization changes induced by stress in a constant applied field. *Journal of Physics D Applied Physics*, 3:1009–1016, jul 1970.

[27] J.R. Cullen, A.E. Clark, M. Wun-Fogle, J.B. Restorff, and T.A. Lograsso. Magnetoelasticity of Fe-Ga and Fe-Al alloys. *Journal of Magnetism and Magnetic Materials*, 226-223:948–949, 2001.

[28] B.D. Cullity. *Introduction to Magnetic Materials*. Addison-Wesley, Reading, MA, 1972.

[29] M.J. Dapino. On magnetostrictive materials and their use in adaptive structures. *Structural Engineering and Mechanics*, 17(3-4):303–329, 2004.

[30] M.J. Dapino, R.C. Smith, and A.B. Flatau. Structural magnetic strain model for magnetostrictive transducers. *IEEE Transactions on Magnetics*, 36(3):545–556, May 2000.

[31] S. Datta, J. Atulasimha, and A.B. Flatau. Modeling of magnetostrictive galfenol sensor and validation using four point bending test. *Journal of Applied Physics*, 101:09–521, 2007.

[32] S. Datta, J. Atulasimha, C. Mudivarthi, and A.B. Flatau. The modeling of magnetomechanical sensors in laminated structures. *Smart Materials and Structures*, 17:025010, 2008.

[33] S. Datta and A.B. Flatau. Magnetomechanical coupling factor and energy density of single crystal iron-gallium alloys. *Proceedings of SPIE*, 6929:6929–71, 2008.

[34] P.R. Downey and A.B. Flatau. Magnetoelastic bending of Galfenol for sensor applications. *J. App. Phys.*, 97:10–505, 2005.

[35] L.R. Dupré, R. Van Keer, and J.A. Melkebeek. Evaluation of magnetostrictive effects in soft magnetic materials using the Preisach theory. *Journal of Magnetism and Magnetic Materials*, 254-255:121–123, 2003.

[36] G. Engdahl. *Handbook of Giant Magnetostrictive Materials*. Academic Press, New York, 1st edition, 2000.

[37] G. Engdahl and A. Bergqvist. Loss simulations in magnetostrictive actuators. *Journal of Applied Physics*, 79(8):4689–4691, 1996.

[38] P.G. Evans and M.J. Dapino. State-space constitutive model for magnetization and magnetostriction of Galfenol alloys. *IEEE Transactions on Magnetics*, 44(7):1711–1720, 2008.

[39] P.G. Evans and M.J. Dapino. Efficient magnetic hysteresis model for field and stress application in magnetostrictive Galfenol. *Journal of Applied Physics*, page In Review, 2009.

[40] P.G. Evans and M.J. Dapino. Efficient model for field-induced magnetization and magnetostriction of Galfenol. *Journal of Applied Physics*, 105:113901, 2009.

[41] P.G. Evans and M.J. Dapino. Stress-dependent susceptibility of Galfenol and applications to force sensing. *Journal of Applied Physics*, in Review.

[42] G.A. Fazekas. A note on the bending of euler beams. *Journal of engineering education*, 57(5), 1967.

[43] M.V. Gandhi and B.S. Thompson. *Smart Materials and Structures*. Chapman and Hall, 1992.

[44] J.M. Gere. *Mechanics of materials*, chapter 5, page 351. Brooks/Cole, Pacific Grove, CA, USA, 5th edition, 2001.

[45] D. ter Haar. *Elements of Statistical Mechanics*. Butterworth-Heinemann, 3rd edition, 1995.

[46] W. Huang, B. Wang, S. Cao, Y. Sun, L. Weng, and H. Chen. Dynamic strain model with eddy current effects for giant magnetostrictive transducer. *IEEE Transactions on Magnetics*, 43(4):1381–1384, April 2007.

[47] N. Ida. *Numerical Modeling for Electromagnetic Non-Destructive Evaluation*. Chapman and Hall, London, 1st edition, 1995.

[48] D.C. Jiles. Modeling the effects of eddy current losses on frequency dependent hysteresis loops in electrically conducting media. *IEEE Transactions on Magnetics*, 30(6):4326–4328, 1994.

[49] D.C. Jiles. *Introduction to Magnetism and Magnetic Materials*. Chapman and Hall, London, UK, 1995.

[50] D.C. Jiles. Theory of the magnetomechanical effect. *Journal of Applied Physics*, 28:1537–1546, 1995.

[51] D.C. Jiles and D.L. Atherton. Theory of ferromagnetic hysteresis (invited). *Journal of Applied Physics*, 55(6):2115–2120, 1984.

[52] D.C. Jiles and D.L. Atherton. Theory of ferromagnetic hysteresis. *Journal of Magnetism and Magnetic Materials*, 61(1-2):48–60, 1986.

[53] D.C. Jiles, A. Ramesh, Y. Shi, and X. Fang. Application of the anisotropic extension of the theory of hysteresis to the magnetization curves of crystalline and textured magnetic materials. *IEEE Transactions on Magnetics*, 33(5):3961–3963, 1997.

[54] D.C. Jiles and J.B. Thoelke. Theoretical modelling of the effects of anisotropy and stress on the magnetization and magnetostriction of tb0.3dy0.7fe2. *Journal of Magnetism and Magnetic Materials*, 134(1):143–160, May 1994.

[55] D.C. Jiles, J.B. Thoelke, and M.K. Devine. Numerical determination of hysteresis parameters for the modeling of magnetic properties using the theory of ferromagnetic hysteresis. *IEEE Transactions on Magnetics*, 28(1):27–35, 1992.

[56] K.S. Kannan and A. Dasgupta. A nonlinear Galerkin finite-element theory for modeling magnetostrictive smart structures. *Smart Materials and Structures*, 6:341–350, 1997.

[57] R.A. Kellogg, A.B. Flatau, A.E. Clark, M. Wun-Fogle, and T.A. Lograsso. Quasi-static transduction characterization of Galfenol. *Journal of Intelligent Material Systems and Structures*, 16:471–479, 2005.

[58] R.A. Kellogg, A.B. Flatau, A.E. Clark, M. Wun-Fogle, and T.A. Lograsso. Temperature and stress dependencies of the magnetic and magnetostrictive properties of $Fe_{0.81}Ga_{0.19}$. *Journal of Applied Physics*, 91(10):7821–7823, 2006.

[59] R.A. Kellogg, A.M. Russell, T.A. Lograsso, A.B. Flatau, A.E. Clark, and M. Wun-Fogle. Tensile properties of magnetostrictive iron-gallium alloys. *Acta Materialia*, 52:5043–5050, 2004.

[60] J. Kim and E. Jung. Finite element analysis for acoustic characteristics of a magnetostrictive transducer. *Smart Materials and Structures*, 14:1273–1280, 2005.

[61] C. Kittel. Physical theory of ferromagnetic domains. *Review of Modern Physics*, 21(4):541–583, Oct 1949.

[62] D.K. Kleinke and H.M. Uras. A magnetostrictive force sensor. *Rev. Sci. Instrum.*, 65(5):1699–1710, 1994.

[63] E. Lacheisserie. *Magnetostriction*. CRC Press, Boca Raton, 1993.

[64] E. Lacheisserie. *Magnetostriction*. CRC Press, Boca Raton, FL, 1993.

[65] F. Liorzou, B. Phelps, and D.L. Atherton. Macroscopic models of magnetization. *IEEE Transactions on Magnetics*, 36(2):418–428, March 2000.

[66] T.A. Lograsso, A.R. Ross, D.L. Schlagel, A.E. Clark, and M. Wun-Fogle. Structural transformations in quenched Fe-Ga alloys. *Journal of Alloys and Compounds*, 350:95–101, 2003.

[67] T.A. Lograsso and E.M. Summers. Detection and quantification of do_3 chemical order in fe-ga alloys using high resolution x-ray diffraction. *Material Science and Engineering A*, 416:240–245, 2006.

[68] I.D. Mayergoyz and G. Friedman. Isotropic vector preisach model of hysteresis. *Journal of Applied Physics*, 61(8):4022–4024, 1987.

[69] P.D. McGary, L. Tan, J. Zou, B.J. Stadler, P.R. Downey, and A.B. Flatau. Magnetic nanowires for acoustic sensors. *Journal of Applied Physics*, 99:99–105, 2006.

[70] C. Mudivarthi, S. Datta, J. Atulasimha, and A.B. Flatau. A bidirectionally coupled magnetoelastic model and its validation using a galfenol unimorph sensor. *Smart Materials and Structures*, 17, 2008.

[71] J.M. Nealis and R.C. Smith. Model-based robust control design for magnetostrictive transducers operating in hysteretic and nonlinear regimes. *IEEE Transactions on Control Systems Technology*, 15(1):22–39, January 2007.

[72] L. Neél. *Annales Geophysicae*, 5:99, 1949.

[73] W.S. Oates. Multiscale constitutive model development and finite element implementation for magnetostrictive materials. In *Proceedings of IMECE*, November 2007.

[74] W.S. Oates and X. Peng. A multi-axial ferroelastic switching model using the homogenized energy approach. *Proceedings of SPIE*, 7286, 2009.

[75] R.C. O'Handley. *Modern Magnetic Materials: Principles and Applications*. John Wiley & Sons, Inc., 605 Third Avenue, New York, NY 10158-0012, 2000.

[76] F. Ossart, R. Davidson, and S.H. Charap. A 3D moving vector preisach hysteresis model. *IEEE Transactions on Magnetics*, 31(3):1785–1788, 1995.

[77] F. Ossart, O. Hubert, and R. Billardon. A new internal variables scalar hysteresis model respecting the wiping-out property. *Journal of Magnetism and Magnetic Materials*, 254-255:170–172, 2003.

[78] W. Panusittikorn and P.I. Ro. Modeling and control of a magnetostrictive tool servo system. *Journal of Dynamic Systems, Measurement, and Control*, 130:031003–1, May 2008.

[79] J.L. Pérez-Aparicio and H. Sosa. A continuum three-dimensional, fully coupled, dynamic, non-linear finite element formulation for magnetostrictive materials. *Smart Materials and Structures*, 13:493–502, 2004.

[80] G. Petculescu, K.B. Hathaway, T.A. Lograsso, M. Wun-Fogle, and A.E. Clark. Magnetic field dependence of Galfenol elastic properties. *Journal of Applied Physics*, 97:10M315, 2005.

[81] K.C. Pitman. The influence of stress on ferromagnetic hysteresis. *IEEE Transactions on Magnetics*, 26(5):1978–1980, 1990.

[82] F. Preisach. Uber die magnetische nachwirkung. *Zeitschrift fur Physik*, 94:277–302, 1935.

[83] S. Rafique, J.R. Cullen, M. Wuttig, and J. Cui. Magnetic anisotropy of fega alloys. *J. Appl. Phys.*, 95(11):6939–6941, 2004.

[84] A. Reimers and E. Della Torre. Fast preisach based magnetosriction model for highly magnetostrictive materials. *IEEE Transactions on Magnetics*, 35(3):1239–1242, may 1999.

[85] A. Reimers and E. Della Torre. Parameter identification of bimodal, magnetostrictive material model. *Journal of Applied Physics*, 85(8):4497, apr 1999.

[86] J.B. Restorff, M. Wun-Fogle, A.E. Clark, and K.B. Hathaway. Induced magnetic anisotropy in stress-annealed Galfenol alloys. *IEEE Transactions on Magnetics*, 42(10):3087–3089, 2006.

[87] N.N. Sarawate and M.J. Dapino. A dynamic actuation model for magnetostrictive materials. *Smart Materials and Structures*, 17:065013, 2008.

[88] S.Datta, J. Atulasimha, C. Mudivarthi, and A.B. Flatau. Modeling of magnetomechanical actuators in laminated structures. *Journal of Intelligent Material Systems and Structures*, 20(9):1121–1135, 2009.

[89] S. Seelecke and I. Muller. Shape memory alloy actuators in smart structures: Modeling and simulation. *Applied Mechanics Review*, 57(1), 2004.

[90] R.C. Smith. *Smart Material Systems: Model Development*. Frontiers in Applied Mathematics. SIAM, Philadelphia, PA, 2005.

[91] R.C. Smith and M.J. Dapino. A homogenized energy model for the direct magnetomechanical effect. *IEEE Transactions on Magnetics*, 42(8):1944–1957, 2006.

[92] R.C. Smith, M.J. Dapino, T.R. Braun, and A.P. Mortensen. A homogenized energy framework for ferromagnetic hysteresis. *IEEE Transactions on Magnetics*, 42(4):1747–1769, 2005.

[93] R.C. Smith, A.B. Hatch, B. Mukherjee, and S. Liu. A homogenized energy model for hysteresis in ferroelectric materials: general density formulation. *Journal of Intelligent Material Systems and Structures*, 16:713–732, 2005.

[94] R.C. Smith, S. Seelecke, M.J. Dapino, and Z. Ounaies. A unified framework for modeling hysteresis in ferroic materials. *Journal of Mechanics and Physics of Solids*, 54:46–85, 2006.

[95] R.C. Smith, S. Seelecke, Z. Ounaies, and J. Smith. A free energy model for hysteresis in ferroelectric materials. *Journal of Intelligent Material Systems and Structures*, 14:719, 2003.

[96] W.S. Oates R.C. Smith. Nonlinear optimal control techniques fro vibration attenuation using magnetostrictive actuators. *Journal of Intelligient Material Systems and Structures*, 19(2):193–209, 2007.

[97] E. Summers, T.A. Lograsso, J.D. Snodgrass, and J. Slaughter. Magnetic and mechanical properties of polycrystalline galfenol. *Proceedings of SPIE*, 5387:448–459, 2004.

[98] E.M. Summers, R. Meloy, and S. Na. Magnetostriction and texture relationships in annealed Galfenol alloys. *Journal of Applied Physics*, 105(7):07A922–07A922–3, 2009.

[99] T. Suzuki and E. Matsumoto. Magnetoelastic behavior of ferromagnetic materials using stress dependent preisach model based on continuum theory. *International Journal of Applied Electromagnetics and Mechanics*, 19:485–489, 2004.

[100] X. Tan and J.S. Baras. Modeling and control of hysteresis in magnetostrictive actuators. *Automatica*, 40:1469–1480, 2004.

[101] J.B. Thoelke and D.C. Jiles. Model calculation for determining local energy minima in the orientation of magnetic domains in terbium-dysprosioum-iron

single crystals. *Journal of Magnetism and Magnetic Materials*, 104-107:1453–1454, 1992.

[102] E. Della Torre. A preisach model for accommodation. *IEEE Transactions on Magnetics*, 30(5):2701–2707, Sept 1994.

[103] E. Della Torre, L.H. Bennett, R.A. Fry, and O.A. Ducal. Preisach-arrhenius model for thermal aftereffect. *IEEE Transactions on Magnetics*, 38(5):3409–3416, 2002.

[104] E. Della Torre and F. Vajda. Vector hysteresis modeling for anisotropic recording media. *IEEE Transactions on Magnetics*, 32(3):1116–1119, 1996.

[105] T. Ueno and T. Higuchi. Magnetostrictive bending micro actuator using iron-gallium alloy. *Proceedings of SPIE*, 6526:65262J–1, 2007.

[106] T. Ueno, C. Saito, N. Imaizumi, and T. Higuchi. Miniature spherical motor using iron–gallium alloy (Galfenol). *Sensors and Actuators A: Physical*, 154(1):92–96, 2009.

[107] T. Ueno, E. Summers, and T. Higuchi. Machining of iron-gallium for microactuator. *Proceedings of SPIE*, 6170:617000–7, 2006.

[108] T. Ueno, E. Summers, M. Wun-Fogle, and T. Higuchi. Micro-magnetostrictive vibrator using iron-gallium alloy. *Sensors & Actuators A: Physical*, 148(1):–280, 20081104.

[109] T. Ueno and H. Toshiro. Two-DOF micro magnetostrictive bending actuator for wobbling motion. *IEEE Transactions on Magnetics*, 44(11):4078–4083, 2008.

[110] W.K. Wilkie, D.J. Inman, J.M. Lloyd, and J.W. High. Anisotropic laminar piezocomposite actuator incorporating machined PMN–PT single-crystal fibers. *Journal of Intelligent Material Systems and Structures*, 17:14–28, 2006.

[111] R. Wu. Origin of large magnetostriction in Fe-Ga alloys. *Journal of Applied Physics*, 91(10):7358–7360, 2002.

[112] M. Wun-Fogle, J.B. Restorff, and A.E. Clark. Magnetomechanical coupling in stress-annealed Fe-Ga (Galfenol) alloys. *IEEE Transactions on Magnetics*, 42(10):3120–3122, October 2006.

[113] M. Wun-Fogle, J.B. Restorff, and A.E. Clark. Magnetostriction of stress-annealed Fe–Ga and Fe–Ga–Al alloys under compressive and tensile stress. *Journal of Intelligent Material Systems and Structures*, 17:117–122, 2006.

[114] M. Wuttig, L. Dai, and J. Cullen. Elasticity and magnetoelasticity of Fe-Ga solid solutions. *Applied Physics Letters*, 80(7):1135–1137, 2002.

[115] J. Yoo and A.B. Flatau. Measurement of field-dependence elastic modulus of iron-gallium alloy using tensile test. *Journal of Applied Physics*, 97:10M318, 2005.

[116] J.X. Zhang and L.Q. Chen. Phase-field microelasticity theory and micromagnetic simulations of domain structures in giant magnetostrictive materials. *Acta Materialia*, 53:2845–2855, 2005.

[117] Z. Zhang, T. Ueno, and T. Higuchi. Development of a magnetostrictive linear motor for microrobots using fe-ga (Galfenol) alloys. *IEEE Transactions on Magnetics*, 45(10):4598–4600, 2009.

[118] H. Zhou and Y. Zhou. Vibration suppression of laminated composite beams using actuators of giant magnetostrictive materials. *Smart materials and structures*, 16:198–206, 2007.